New electrodes for low temperature water electrolysis (PEMWE) based on doped tin dioxide aerogels (SnO2 Sb or Ta) as catalyst support

Lluis Sola Hernandez

HAL Id: tel-03235592
https://pastel.hal.science/tel-03235592

Submitted on 25 May 2021

THÈSE DE DOCTORAT
DE L'UNIVERSITÉ PSL

Préparée à MINES ParisTech

Nouvelles électrodes pour l'électrolyse de l'eau basse température (PEMWE) à base d'aérogels de dioxyde d'étain (SnO$_2$) dopé (Sb ou Ta) comme support de catalyseur.

New electrodes for low temperature water electrolysis (PEMWE) based on doped tin dioxide aerogels (SnO$_2$: Sb or Ta) as catalyst support.

Lluís SOLÀ-HERNÁNDEZ

Soutenance programmée

le 26 Janvier 2021

Ecole doctorale n° 621

ISMME – Ingénierie des Systèmes, Matériaux, Mécanique, Énergétique

Spécialité

Énergétique et Génie des Procédés

Composition du jury :

Stéphane, DANIELE
Professeur des Universités
Université de Lyon, France   *Président du jury*

Elena, SAVINOVA
Professeure des Universités,
Université de Strasbourg, France   *Rapporteur*

Hynd, REMITA
Directrice de recherche,
CNRS Université Paris Sud, France   *Rapporteur*

Fabien, AUPRETRE
Docteur
Areva H2gen, France   *Examinateur*

Arnaud, RIGACCI
Professeur
MINES ParisTech-PSL, France   *Examinateur*

Christian, BEAUGER
Maître de recherche
MINES ParisTech-PSL, France   *Directeur de thèse*

À mes deux étoiles,

Acknowledgements

Now that my adventure as a PhD student is coming to the end, I would like to express my gratitude to those who have walked with me among this journey:

Acordarme por supuesto de todas esas personas que me han acompañado a lo largo de estos años, que han estado ahí y con las que he compartido grandes vivencias: Lisa (ma belle niçois), Lara (Lady Madrid), Juanfran (el maquetador), Iván (l'andorrà bachatero), Reisa (mi compañera de bailes y chupitos), Anna (la psicòloga a temps complet), Vicky, María y Alicia (les meves valencianetes), Paula y Gemma (mis fisioterapeutas favoritas), Alejandro y David (los mousquetaires escaladores bailongos) y Diego (nos vemos en Medallo, hermano).

No tots els camins porten a Roma, alguns duen a Niça, que no és poc. M'és impossible no pensar i agrair a tota la gent que va acompanyar-me durant tant llarg trajecte.

Començar per tots aquells professors que em van ensenyar la química, la passió de la meva vida, des de l'institut fins a la universitat. També a aquells que em van ajudar a iniciar-me dins del "mundillu" de la investigació, i que possiblement sense ells no hagués arribat fins aquí: Roberto, Jordi, Javi, Jonathan i Marcos. A aquells amics de la Universitat i del poble, amb els quals, per més que ho intento, m'és impossible perdre el contacte: Josep, Belmez, Marc, Samanta, Esther, Gloria, Daniel, Sergi, Eric i Marcel.

Finalment a la meva família. A mi abuelo, el espejo donde mirarse, a mis tías, tíos, tiet i tieta. A mis primos: Noelia, Isabel, Iracema, Mariano, Eduardo, Diego, Javier i Marc, y a sus respectivas parejas. Gracias por acogerme siempre con los brazos abiertos cuando me acoplo en vuestras casas, y hacer siempre lo que sea por verme. A los pequeños Milos, Chloe, Jara y Jimena, ¡y a los que están por llegar! Al meu germà i a la Marina, per jugar-se la vida traficant ginebra per la frontera franco-catalana any rere any. Al meu pare i a la meva mare, per no ser cisells sinó cisalles, per obrir-me gàbies i donar-me ales, gràcies.

A tous, merci.

Table of contents

Index of abbreviations

Alkaline electrolysis cell	AEC
Alternating current	AC
Antimony-doped tin oxide	ATO
Atomic percentage	at. %
Barret-Joyner-Halenda	BHJ
Begging of life	BoL
Brunauer-Emmett-Teller	BET
Carbon capture, utilization and storage	CCUS
Catalyst coated membrane	CCM
Catalytic layers	CLs
Cell voltage	U_{cell}
Cetyltrimethylammonium bromide	CTAB
Chemical vapor deposition	CVD
Counter electrode	CE
Cyclic voltammetry	CV
Density functional theory	DFT
Dimethylformamide	DMF
Double-layer capacitance	C_{dl}
Electro-Chemically active Surface Area	ECSA
Electron	e^-
Electron paramagnetic resonance	EPR
End of life	EoL

Energy Dispersive X-ray Spectroscopy	EDX
Equation	Eq.
Extended X-Ray Absorption Fine Structure	EXAFS
Fluorine doped tin oxide	FTO
Fuel Cell Electric Vehicles	FCEV
Fuel Cells	FC
Gas diffusion layer	GDL
Glassy carbon	GC
Heteropolyacids	HPAs
High density polyethylene	HDPE
Higher Heating Value	HHV
Hydrogen evolution catalyst	HEC
Hydrogen evolution reaction	HER
Hydrogen oxidation reaction	HOR
Indium doped tin oxide	ITO
Inductively Coupled Plasma Mass Spectrometry	ICP-MS
Lattice Oxygen Evolution Reaction	LOER
Lower Heating Value	LHV
Mass activity	j_{mass}
Membrane electrode assemblies	MEAs
Metal Organic Frameworks	MOFs
Metal-metal oxide support interactions	MMOSI
Microporous	µ-porous

Millions of tons	Mt
Nanoparticles	NPs
Overpotential	η
Oxygen Evolution Reaction	OER
Oxygen Reduction Reaction	ORR
Perfluorosulphonated acid	PFSA
Photovoltaics	PVs
Polyether-etherketones	PEEK
Polyether sulfones	PES
Polyether sulfones	PES
Preferential Oxidation	PROx
Pressure Swing Adsorption	PSA
Proton coupled electron transfer	PCET
Proton Exchange Membrane Fuel Cells	PEMFC
Proton Exchange Membrane Water Electrolysis	PEMWE
Reversible voltage	E_{rev}
Rotating Disk Electrode	RDE
Roughness Factor	RF
Scanning Electron Microscope	SEM
Solid oxides electrolysis cell	SOEC
Specific activity	J_{spec}
Standard Hydrogen Electrode	SHE
Sequence	Seq.

Supercritical	SC
Tantalum-doped aerogels	TaTO
Thermoneutral voltage	E_{therm}
Tin oxide	TO
Transmission Electron Microscope	TEM
Water oxidation catalyst	WOCs
Wight in volume percentage	$Wt \cdot vol^{-1}$
Weight percentage	Wt. %
Working electrode	WE
X-ray Absorption Near Edge Structure	XANES
X-Ray diffraction	XRD
X-ray Photoelectron Spectroscopy	XPS

Introduction

Human society has relied mostly on energy sources for its development. To satisfy the global energy demand of our current economic model, fossil fuels (coal, petroleum and gas, **Figure 0.1**) are the main energy source, yet these reserves are decreasing as energy demand continues to rise.[1] Moreover, their indiscriminate use is clearly related to the increase in carbon dioxide emissions into the atmosphere, which is the major contribution to the greenhouse effect and climate change.[2] Furthermore, predicted energy demand by 2050 is about 300,000 TWh, which corresponds to an increase of about 100% compared to today's consumption (154,000 TWh, 2017).[3] Thus, given the expected increase in global energy consumption and the drawbacks of using fossil fuels (i.e. they are unevenly distributed, non-renewable and highly CO_2 emitting), it is vital to find a new non-carbon based, renewable source of energy to ensure the sustainable development of our society.
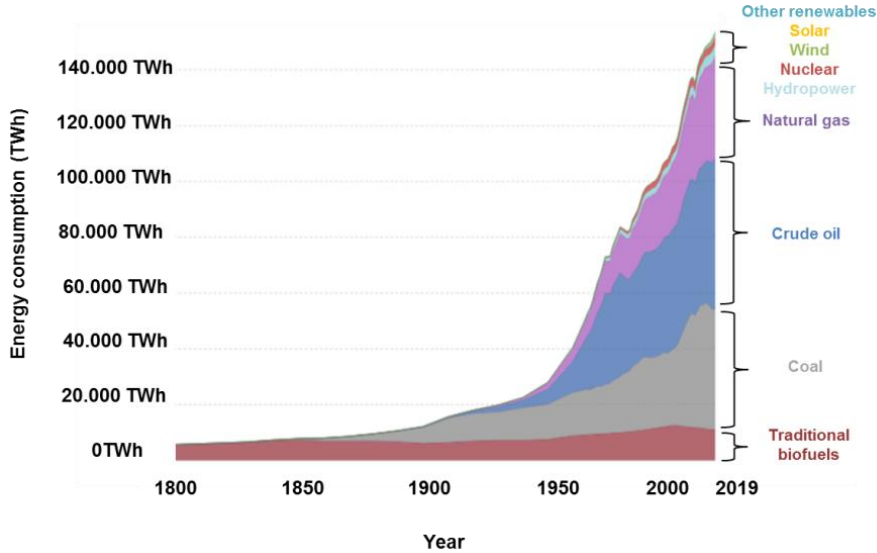
Figure 0.1 Structural change in world primary energy consumption, measured in terawatt-hours (TWh) per year, from 1800 – 2019, illustrating the substitution of traditional biomass (mostly non-commercial) by coal and later by oil and gas. The emergence of hydro, nuclear, solar, wind and other renewable energy sources is also shown.[3]

Fortunately, increasing interest is focused on replacing fossil fuels with cleaner, renewable products that can be widely used without damaging the environment. Different renewable sources now exist including biomass, wind and hydro powers, geothermal energy and solar energy.

Among all the renewable energy sources, solar energy is the most available, since in one hour of sunlight the Earth receives almost the same amount of energy as the world consumes in one year (120,000 TWh).[4] This means that only 0.35% of the total annual solar energy would be enough to fulfill all human energy requirements. As a result, researchers have focused investigation on this field, mainly in the conversion of solar energy into electricity by means of photovoltaic panels.[5] Although there is still room to improve their efficiency and decrease their price, photovoltaic cells are already a mature technology that is successfully implemented on the market.

However, photovoltaic panels generate electricity that has to be consumed immediately after production.[6] In order to store, transport and consume solar energy on demand (e.g., in automotive devices), it would need to be converted into a vector of energy that does not emit any greenhouse effect gases. Currently, devices using sunlight can be divided into two main categories:

a) **Solar thermal systems:** directly convert solar radiation into thermal energy for heating applications.

b) **Photovoltaics (PVs):** transform solar energy into electricity without the interface of a heating engine.
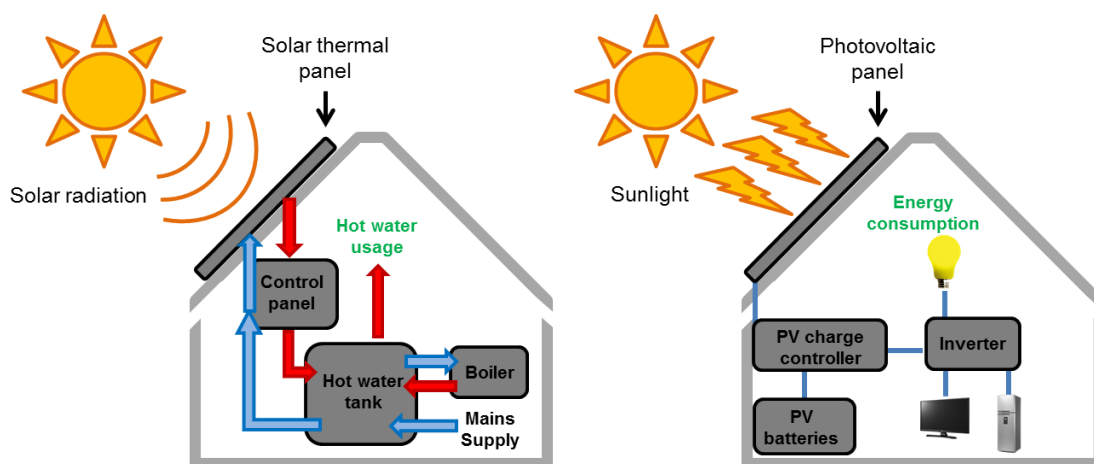
Figure 0.2 On the left, a diagram of a solar thermal system. On the right, a diagram of a photovoltaic (PV) system. The former is used to heat water from solar thermal energy, while the latter transform the sunlight received into electrical energy.

Producing an alternative to fossil fuels using sunlight as an energy source generates chemical products, which need to release only clean and environmentally friendly by-products into the

atmosphere. Synthesis processes are inspired by photosynthesis, whereby plants convert carbon dioxide and water into carbohydrates using the sun's energy.

Hydrogen is an interesting chemical product that can be used as an energy vector and produced from the surplus energy collected from renewable energy sources, such as solar energy. Once produced from surplus energy, hydrogen (or solar hydrogen) could be used to cover energy demand when it is not possible to produce electricity from renewable sources, or when energy is not distributed equally.

Producing hydrogen to use as a fuel makes a lot of sense. Although very few hydrogen deposits have been found on Earth, its presence is abundant in combination with other atoms, such as: oxygen (in the form of water), carbon (in the form of hydrocarbons and biomass), and nitrogen-based compounds, inter alia. Therefore, the development of hydrogen production technologies is a very interesting subject for future renewable energy development.

Hydrogen can be produced by non-renewable sources (derived from hydrocarbon products), such as methane, or by renewable ones such as biomass, vapor reforming or water electrolysis powered by renewable energies (solar, wind power, etc.). Water electrolysis is particularly interesting if the source of energy for converting water into hydrogen is renewable, such as wind or solar power. This method can be used to convert water into hydrogen by applying a voltage to PV panels for instance. The collected energy could then be converted into a fuel with interesting potential as discussed above.

Once hydrogen has been produced, using fuel cells it is possible to convert the chemical energy stored in the H — H covalent bonds into electricity and heat. Although the market is still quite small, some car manufacturers (Hyundai, Honda, Toyota, etc.) are already commercializing hydrogen fuel cell cars. Toyota Mirai and Hyundai Nexo are two of the Fuel Cell Electric Vehicles (FCEV) currently available.

Water electrolysis is the most mature choice of interest to produce clean hydrogen.

Three main technologies have been developed so far, based on alkaline, polymer membrane, or solid oxide electrolytes. Proton Exchange Membrane Water Electrolysis (PEMWE), operating at low temperatures (65°C) with a solid electrolyte is the anticipated technology for renewable energy storage. The main problem in developing large scale water electrolysis for clean hydrogen production is the high cost of many of the components (noble-metal-based electrode materials, selective permeable membranes, titanium porous layers) and the acid corrosive media.

In the case of PEMWE, iridium oxide is used at the anode to oxidize water, and platinum at the cathode side to recombine protons into hydrogen. As deployment of the technology develops, the pressure on both resources will increase their cost. Since both metals are very expensive,

USD 34,215 vs USD 34,744 per kg^{-1} (price November 2020), the objective is to decrease their amounts in the PEMWE anodes.

The main aim of this thesis is thus to identify a material capable of substituting the iridium oxide micro particles used in current PEMWE, and stable enough to operate at high potential in a liquid water environment. The research work consisted in mimicking the action in Proton Exchange Membrane Fuel Cells (PEMFC), while supporting catalyst nanoparticles on a stable, porous and electron-conductive support. As carbon supports are prohibited due to corrosion under the working conditions of PEMWE anodes, tin dioxide (SnO_2), which has already been studied as an alternative to carbon in PEMFC cathodes, was selected for its presumed stability at high potential.

Previous theses carried out by the MATPRO group at the MINES Paris-Tech PERSEE center have shown that carbon aerogels can be used effectively as a cathode catalyst support for PEMFC. Aerogels make it possible to maintain morphologies that are particularly suitable and interesting for such applications: high specific surface areas allow a homogeneous dispersion of the catalyst nanoparticles and pore size distribution, which enables good fluid management within the electrode. However, these carbon materials demonstrated limited corrosion resistance under PEMFC operating conditions, which is likely to be even worse in the case of PEMWE.

Considering problems of durability, especially the corrosion of the carbon catalyst support, other studies have focused on developing new aerogel-based supports, consisting of tin dioxide aerogels, which are known to be more resistant to corrosion. Such materials were designed to present suitable morphologies and high electronic conductivities. As SnO_2 is a dielectric metal oxide material, its conductivity was increased by doping the material with hypervalent cations (M^{5+}, such as Nb^{5+} or Sb^{5+}) in order to modify its electronic configuration. An improvement in durability (in high working potentials) was found when Pt nanoparticles were supported over such doped tin oxide materials and tested as cathode catalyst materials for PEMFC.

After promising results obtained on antimony-doped tin oxide aerogels (ATO aerogels) for PEMFC, it was decided to evaluate them as catalyst supports for anode materials in PEMWE.

Hence, the main objective of this work is to further develop doped tin oxide aerogels: improved electronic conductivity, specific surface area, corrosion resistance, etc. For this purpose, some modifications were applied to the aerogel synthesis protocol (sol-gel method). Aerogels were doped with different doping agents, such as Sb and Ta, in order to enhance their conductivity, specific surface area, porosity and corrosion resistance to the high operating potential of PEMWE cells.

Once a new catalyst support was developed, with improved properties, it was used for an Iridium catalyst deposition in order to perform electrocatalytic tests. The aim was to design an anode system for the Oxygen Evolution Reaction (OER) that displays high activity, long durability and low noble metal (catalyst) loading to reduce total costs.

This document consists of five chapters.

The first chapter corresponds to a bibliographic study of the state of the art of the thesis subject. First of all, the different types of technology for hydrogen production are presented, with an ultimate focus on Proton Exchange Membrane Water Electrolysis cells. The subject of the thesis mainly centers on presenting the anode materials of devices of this kind that have been studied to date. In addition, the materials composition of the cathode and membrane parts of the cell is presented. A second aspect of the bibliographic study concerns the physicochemical properties of doped tin dioxide and the synthesis of aerogel materials.

The second chapter describes the materials, methods and characterization techniques used during the experimental part of this study.

The third chapter of the thesis is dedicated to the experimental results concerning the development of tin oxide-based materials during the study. This begins with a discussion of the influence of modifying some synthesis parameters from the sol-gel method previously established by our group for ATO aerogels synthesis. It is followed by a presentation of the development of novel Ta-doped aerogels (TaTO).

The fourth chapter presents the deposition of the Ir noble metal catalyst over the developed tin oxide-based aerogels. This part features a discussion of the nanocatalysts' shape, structure and chemical composition, as well as the influence of the deposition on the Oxygen Evolution Reaction, studied by Rotating Disk Electrode (RDE) tests.

CHAPTER 1: State of the Art

I Hydrogen energy

Hydrogen is a very powerful energy carrier, since it is the fuel with highest known energy content (in mass), as shown in **Table 1.1**. No greenhouse gases, particulates, NO_x or sulfur oxides or ozone are produced from the use of hydrogen. Its reaction with oxygen (reaction **1**) simply releases water and a huge amount of energy, making this gas very interesting for the future (from an energetic point of view). However, hydrogen can emit high CO_2 concentrations to the atmosphere if produced from fossil fuels such as coal, oil or natural gas (**section I.3** of this chapter).

$$2\ H_2 + O_2 \rightarrow 2\ H_2O \ \textbf{(Eq. 1.1)}$$
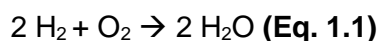
Table 1.1. Energy content in MJ per kg of different known fuels.[7]

Fuel	Lower Heating Value (LHV), MJ·kg^{-1}
Coal	22
Diesel	43
Butane	46
Methane	50
HYDROGEN	**120**

The main advantage of hydrogen over electricity is that hydrogen is a chemical energy carrier that can be stored and carried in a stable way, like for example oil, coal or natural gas. It can also be combined with other elements, such as carbon or nitrogen, in order to make hydrogen-based fuels that are easier to handle and can be used as feedstock in industry.

The main advantages of hydrogen as an energy carrier result from its attributes, making it a promising alternative to fossil fuels:

1. Hydrogen presents an LHV value 2.8 times higher than diesel.

2. It can be obtained sustainably from abundant chemical products on Earth, such as H_2O or biomass.

3. Its reaction with oxygen only produces steam and/or liquid H_2O, which is highly valuable from an environmental point of view.

4. It is light.

5. It is nontoxic.

6. In fuel cells (FCs), the chemical energy of the hydrogen bond (H—H) is directly transformed into electricity and heat without any heat requirement and with enhanced efficiency.

7. Hydrogen's long-distance energy transport is more economical than through high-voltage alternating current (AC) lines.[8,9]

Due to all of these advantages, there is a growing interest in the widespread use of hydrogen for clean energy systems.

As discussed in the following section, employing hydrogen as a chemical fuel produces electricity that can be used for many applications. Therefore, low-carbon-emitting energy can be supplied over very long distances, and electricity can be stored to make up weekly or monthly imbalances in supply and demand.

Many of the disadvantages of using hydrogen as a fuel instead of gasoline, or other fossil fuels, are related to its high price when produced by renewable energies; to its low energy density (9 $MJ·L^{-1}$ for liquid hydrogen vs. 32 $MJ·L^{-1}$ for gasoline);[7] and the strict, careful measures required for its storage and transport. These disadvantages are discussed below.

I.1 Use of hydrogen

Hydrogen production for industrial purposes is a major business in today's world. Demand for hydrogen has grown more than a 300% since 1975, mainly used in oil refining and chemical production.

As seen in **Figure 1.1**, the current demand for pure hydrogen (2018) is around 74 million tons (Mt) per year, compared to 38 Mt for oil refining, 31 Mt for ammonia production (mainly used to make fertilizer), and less than 5 Mt for other applications, such as transport, or for energy purposes.

A further 45 Mt of hydrogen are used in industry without prior separation of hydrogen from other gases. The main uses of this type of hydrogen are ethanol production, steel production (via direct reduction of iron ore), and other mixed applications that use hydrogen as a part of a mixture of gases (such as synthesis gas, for fuel or feedstock).[9]
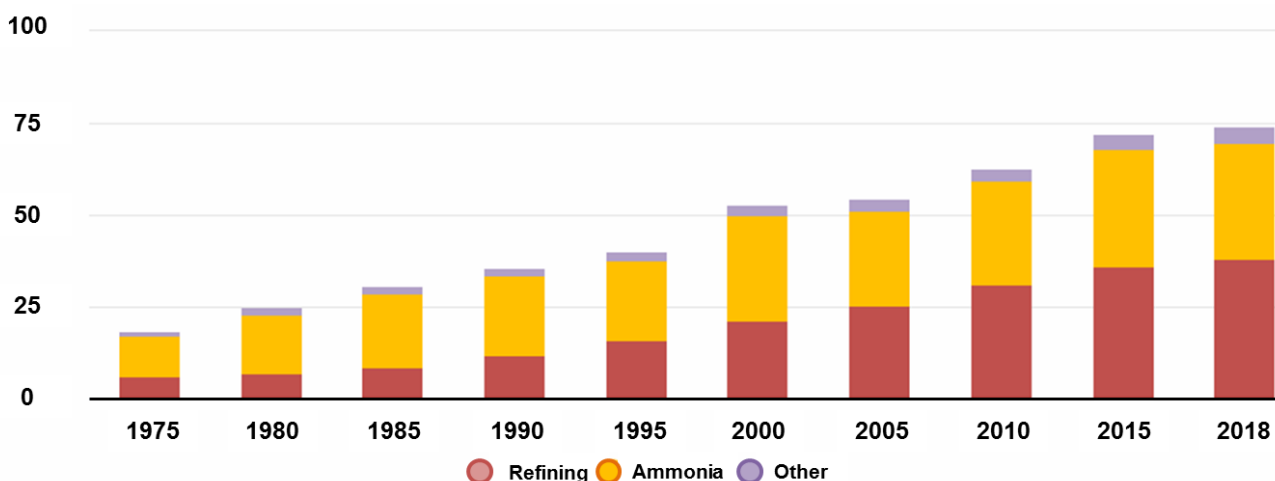
Figure 1.1 Global demand for pure hydrogen in millions of tons (Mt) per year, 1975 – 2018.[9]

In the energy sector, hydrogen currently plays a negligible role, as it accounts for less than 0.2% of electricity generation. This is mostly linked to the use of the gas for petrochemical plants and refineries, but there is potential for this to change in the near future. The use of hydrogen-fired gas turbines or fuel cells can provide a source of flexibility in electricity systems featuring increasing shares of variable renewables.

In recent times, the proportion of renewable energy supply in demand has become increasingly problematic. In fact, as deployment meets and exceeds 20% capacity (an oversupply of electricity to the grid), as already experienced in many countries, grid balancing issues become acute, leading to the curtailment of wind or solar energy sources. This is driving a need for long-term, large-scale energy storage solutions, as for example by hydrogen production.

Hydrogen production can lead to long-term energy storage from renewable sources (e.g., solar or wind power, green hydrogen). Therefore, seasonal energy surpluses of renewable energy could be used to provide energy during periods of several days featuring no or very little wind or sunshine. Such energy reserves could also be exported or imported into regions with lower renewable sources or reserves to cover their energy demand.

It is well known that hydrogen-based storage options suffer from low round-trip efficiency: in the process of converting electricity through electrolysis into hydrogen and then the hydrogen back into electricity, around 60% of the original electricity is lost, compared to storage cycle losses of about 15% for lithium-ion batteries. Nevertheless, batteries are unlikely to be used for long-term, large-scale storage partly because they self-discharge, and partly because of the immense number of batteries/cells that would be needed. On the other hand, for shorter discharge durations, under a few hours, hydrogen storage is a much more expensive, unlikely option than these current batteries.

Several other options are also considered with regard to using hydrogen as part of energy storage. One of these is to inject hydrogen directly into urban gas networks. However, for safety reasons, the hydrogen concentration must be kept below a certain threshold. To be able to introduce more hydrogen, a methanation process can be used to transform the hydrogen into methane. By using fuel cells (FC), it is possible to use hydrogen for electricity, and heat production for mobile, stationary, and transport applications. Although currently the fuel cell market remains quite small, this technology is becoming more accessible with more competitive prices, as is already the case for the forklift market. Major car manufacturers are increasingly investing in hydrogen as the energy carrier of the future. For example, Hyundai, Honda and Toyota have recently launched cars equipped with fuel cells, but their price remains very high.

I.2 Hydrogen storage and transport

Nowadays, several kinds of hydrogen storage technologies are available. Hydrogen can be stored (1) physically: as liquid, compressed gas or adsorbed on the surfaces of solids; or (2) chemically: absorbed in metal hydrides or maintained in hydrogen vectors (such as in ammonia, or related compounds, and in organic hydrogen carriers).

- **Physical methods:**

  The simplest method is compressed hydrogen gas. Compressed hydrogen is a storage form where hydrogen gas is kept under high pressure (in high-density polyethylene (HDPE) or stainless-steel high-pressure vessels) in order to increase its storage density. Hydrogen is compressed in tanks at 350 bars or 700 bars, and used for hydrogen tank systems in vehicles, based on type IV carbon-composite technology. Car manufacturers such as Honda and Nissan have been developing this solution.

  Liquid hydrogen storage is also possible: from 25% to 45% of the stored energy is required to liquefy the hydrogen. With this method, the density of hydrogen storage is very high, but hydrogen boils at about -253ºC and it is necessary to maintain this low temperature (otherwise the hydrogen will boil away), which requires bulky insulation.

  Currently, a neither new method is carbon adsorption. At applied pressure, hydrogen bonds with porous carbon materials such as fibers, nanotubes, graphene, fullerenes, etc.[7,10] Other porous materials, such as zeolites or metal-organic Frameworks (MOFs), are also being investigated for hydrogen adsorption.[11]

- **Chemical methods:**

  In metal hydride storage, powdered metals absorb hydrogen under high pressure. During this process, heat is produced upon insertion, while the process is reversed with pressure release and applied heat. The main problem with this method is the weight of the absorbing material – a tank's mass would be about 600 kg compared to 80 kg for a comparable compressed hydrogen gas tank.[12]

  Hydrogen storage in chemical bonds is another option. Some hydrogen carrier molecules can be used for this purpose, such as: amino boranes, carbohydrates, synthetic methane or ammonia.[13] Such products can make use of the existing infrastructure for transport, storage and distribution. However, the potential benefits and opportunities of these

hydrogen-based fuels and feed-stocks should be weighed against the costs of conversion from hydrogen to these products.

In summary, hydrogen storage is currently not competitive with hydrocarbon fuels. It will need to become a great deal more economical in order to be produced on a large scale.

I.3 Hydrogen production

Hydrogen can be produced from many different sources and in various ways that are described hereafter. Currently, 94% of hydrogen production comes from non-renewable sources such as steam-reforming of natural gas (steam methane reforming) and coal gasification (**Figure 1.2**).[14] The other 6% of production comes either from biomass (around 1%), a renewable technology with a neutral carbon footprint, or as a by-product of chlor-alkali electrolysis in the production of chlorine and caustic soda electrolysis (around 5%).[9]
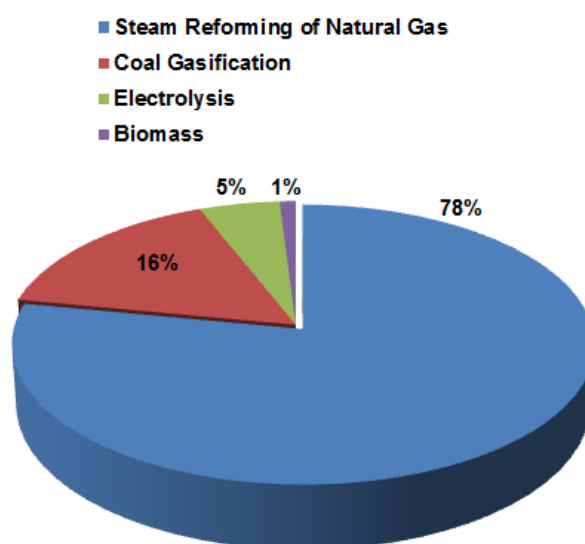
Figure 1.2 Percentage of hydrogen production methods in 2015. [14]

Steam methane reforming is currently the process most commonly used for hydrogen production, and consists in converting the natural gas or methane into hydrogen and carbon dioxide through a reaction with water steam in the presence of a catalyst (reactions **2**, steam methane reforming, and **3**, water gas-shift).

$$CH_4 + H_2O \text{ (+ heat)} \rightarrow 3\ H_2 + CO \textbf{ (Eq. 1.2)}$$

$$CO + H_2O \rightarrow H_2 + CO_2 \textbf{ (Eq. 1.3)}$$
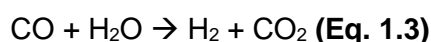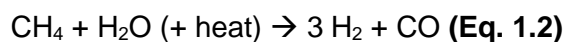
The hydrogen produced is not pure, consisting of around 70-75% hydrogen with smaller amounts of methane (2-6%), carbon monoxide (7-10%), carbon dioxide (6-14%), and hydrogen sulfide. The hydrogen is then purified or separated from the other gases by different methods:

- Flowing the feed produced through a hydrogen-permeable or proton-conductive membrane.

- Condensing the gas mixture at different temperatures.

- Using pressure swing adsorption (PSA), which consists in adsorbing impurities from the gas steam to leave pure hydrogen gas.

- Using preferential oxidation (PROx), which works to remove trace amounts of CO from H_2/CO/CO_2 mixtures produced by steam reforming and water-gas shift. Then, a catalyst (usually Pt or Au nanoparticles supported over ceramic supports) oxidizes the CO, which poisons PEMFC catalysts into CO_2 and hydrogen, creating a hydrogen-rich gas ready for use. Currently, the preferred and most common method for hydrogen purification.

The main disadvantage of the steam reforming process is that it emits significant amounts of greenhouse gases into the atmosphere, such as carbon dioxide and carbon monoxide.

Coal gasification, also known as partial oxidation process, can produce hydrogen from coal, water and air, or oxygen. In this process, carbon reacts with low amounts of oxygen, CO_2 and water to yield a mixture of carbon monoxide and hydrogen at 1,200ºC to 1,350ºC (reactions **4** to **7**). The hydrogen is then separated from the other gases, as in steam methane reforming.

$$C + \tfrac{1}{2}O_2 \rightarrow CO \textbf{ (Eq. 1.4)}$$

$$C + CO_2 \rightarrow 2\ CO \textbf{ (Eq. 1.5)}$$

$$C + H_2O \rightarrow H_2 + CO \textbf{ (Eq. 1.6)}$$

$$CO + H_2O \rightarrow H_2 + CO_2 \textbf{ (Eq. 1.7)}$$
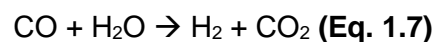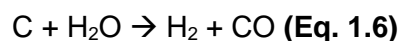
Plasma reforming produces hydrogen from non-renewable hydrocarbons, such as natural gas or methane. The most commonly used processes are the Kværner process and the Kværner carbon black and hydrogen process (CB&H), where hydrocarbons (such as methane, natural gas or biogas) are decomposed into carbon black and hydrogen in a plasma burner at around 1,600 °C, equation **8**:[15]

$$C_nH_m \rightarrow nC_{(s)} + \tfrac{m}{2}H_{2\ (g)}\ T = 1070\ K \textbf{ (Eq. 1.8)}$$
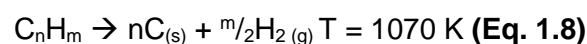
In comparison to other reforming processes, such as steam methane reforming or partial oxidation, the natural gas is efficiently and completely transformed into pure carbon (carbon black) and hydrogen. The total obtained energy of the reformation is approximately distributed as: 48% in the produced hydrogen, 40% in the by-produced activated carbon, and 10% in a superheated steam.

A variation of this process using a plasma arc has been used since 1957, whereby methane or natural gas or organic matter are converted into a hydrogen and carbon. A plasma torch powered by an electric source is used to ionize the gas and create a plasma, and to catalyze the decomposition of methane into syngas, with slag as a byproduct. This system is commercially used in waste treatment procedures and has been tested for the gasification of municipal waste such as solids, biomass, industrial waste, hazardous waste and solid hydrocarbons (like coal, oil sands, etc.).

Other industrial methods exist to produce hydrogen from renewable sources, such as biomass. Biomass plants constitute one of the best solutions for converting organic matter into chemicals, energy or materials in order to maximize the economic and environmental benefits, while minimizing waste and pollution. The conversion of biomass into hydrogen can be achieved using two different technologies: thermo-chemical processes and biochemical processes. For the first of these, hydrogen-rich gas can be obtained by heating biomass at high temperature in the absence of oxygen, producing an aqueous bio-oil phase after a water treatment. In biochemical processes, a digestion of sugars using enzymes is required to produce bio-ethanol (**Figure 1.3**). Once the aqueous bio-oil and the bio-ethanol are produced, a thermal treatment followed by steam reforming releases hydrogen gas and other hydrocarbons.
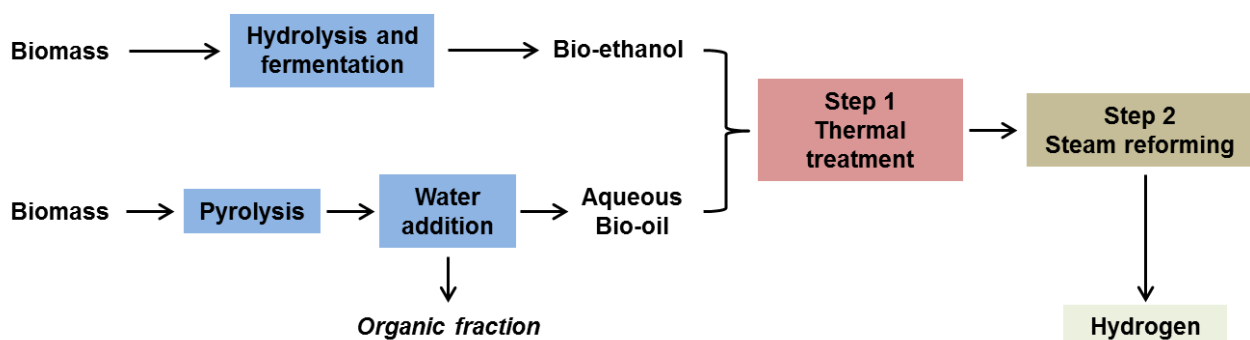
Figure 1.3 Diagram of hydrogen production by biochemical processes, adapted from Remiro *et al.*.[16]

Another method for hydrogen production consists in splitting thermal water into oxygen and hydrogen. As the required temperatures for the single-step decomposition of water reach values over 4,700 K,[17] an alternative method, based on a multi-step procedure at around 1,100 K, is used to produce hydrogen:

$$2H_2O_{(g)} + I_{2(g)} + SO_{2(g)} \rightarrow 2HI(g) + H_2SO_{4(g)} \quad T = 300 \text{ K} \textbf{ (Eq. 1.9)}$$

$$H_2SO_{4(g)} \rightarrow H_2O_{(g)} + SO_{2(g)} + \tfrac{1}{2} O_2 \quad T = 510 \text{ K} \textbf{ (Eq. 1.10)}$$

$$Ni_{(s)} + 2HI_{(g)} \rightarrow NiI_{2(s)} + H_{2(g)} \quad T = 570 \text{ K} \textbf{ (Eq. 1.11)}$$

$$NiI_{2(s)} \rightarrow Ni_{2(s)} + I_{2(g)} \quad T = 1070 \text{ K} \textbf{ (Eq. 1.12)}$$
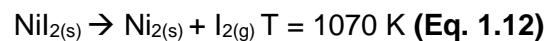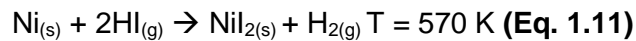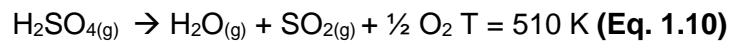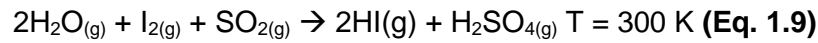
Most of these hydrogen production methods present many disadvantages, such as sustainability of the non-renewable sources, CO_2 emissions, and the low purity of the hydrogen obtained.[18]

Hence, a different strategy needs to be considered to overcome these difficulties. To achieve this, researchers have taken inspiration from nature, and particularly the photosynthetic processes of plants, which store solar energy in the form of chemical bonds through photosynthesis. Plants are capable of using water, sunlight and CO_2 to form sugars and other carbohydrate molecules, with an efficiency of between 3% and 6 % of total collected solar radiation. Such carbohydrates can be consumed later as fuels for the plants' mitochondrial respiration or used for their own growth.

Therefore, during the last decades, the scientific community has been trying to mimic nature in order to store sunlight energy by developing systems for hydrogen generation, known as water electrolysis devices.

For this purpose, the starting reaction always involves cleaving a water molecule to produce electrons, protons and oxygen. The generated current can be used for reducing protons and generating hydrogen that can be stored and used afterwards to produce heat and energy in a clean manner.[19]

I.4 Focus on water electrolysis

Water electrolysis is an electrochemical process that splits water into hydrogen and oxygen. Most of the hydrogen produced by electrolysis, around 5% of global hydrogen production, is created as a by-product of chlor-alkali electrolysis in the production of chlorine and caustic soda.[9] Today, less than 1% of pure hydrogen global production comes from water electrolysis and the hydrogen produced by this means is mostly used in markets where high-purity hydrogen is necessary (e.g., electronics).

As mentioned, the water electrolysis process consists in splitting water into hydrogen and oxygen molecules (equation **13**) using energy, which can be provided from a renewable source powering an electrolyzer device. On the one hand, water electrolysis offers the advantage of not being directly dependent on fossil fuels, if coupled with renewable energies. On the other hand, the purity of the hydrogen produced is close to 100%, without requiring any purification. These electrolyzer devices or cells are composed of two electrode compartments, an anode compartment and a cathode one, where the water oxidation and proton reduction occur respectively. They are separated by a selective permeable membrane in order to avoid mixing of generated gases. Both electrodes are connected to the power supply.

$$2\ H_2O \rightarrow O_2 + 2\ H_2 \textbf{ (Eq. 1.13)}$$
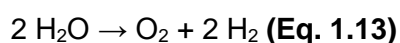
The global reaction of water electrolysis can occur under different conditions: aqueous alkaline or aqueous acidic conditions at temperatures lower than 100°C, or using solid oxide electrolytes at temperatures higher than 700°C. Water electrolysis cells are thus classified into three main categories:[20]

1. **Alkaline electrolysis cells (AEC):** for this type of cell, the working temperature is lower than 80°C and the ionic species are hydroxyl ions (OH^-). Aqueous KOH or NaOH solutions are used as the electrolytic medium.

2. **Proton exchange membrane water electrolysis (PEMWE) cells** or water electrolysis PEM cells**:** in this case, the working temperature is below 80°C, and the ionic species are hydronium ions (H^+). They comprise solid electrolyte membranes made of perfluoro sulfonic acid (PFSA).

3. **Solid oxide electrolysis cell (SOEC):** this cell works at temperatures above 700°C, and the ionic species are oxide ions (O^{2-}). It uses solid electrolytes made of yttrium stabilized zirconia (YSZ).

Independently from the electrolytic media, the standard anode potential ($E^0_{(O2/H2O)}$), at pH=0, for the anodic reaction of water oxidation into dioxygen is 1.23 V vs SHE (standard hydrogen electrode), while the standard cathode potential ($E^0_{(H2O/H2)}$) for all cathode reactions of water reduction into dihydrogen is 0.0 V vs SHE. Therefore, the standard cell voltage for the global reaction of water dissociation presented in reaction **13** is always 1.23 V independently from the electrolysis system.

The total energy required to split 1 mole of water (H_2O) into 1 mole of hydrogen (H_2) and ½ moles of oxygen (O_2), is the standard molar enthalpy of water decomposition, $\Delta H° = 285.8$ kJ/mol. Part of this energy corresponds to the thermal energy that the reaction needs to take place, which entails increasing the system's temperature (thermal energy) to reduce the required electrical energy. The thermodynamic relation is given by equation **14**:

$$\Delta H° = \Delta G° + T\Delta S° = 285{,}8 \; kJ/mol \quad \textbf{(Eq. 1.14)}$$

$\Delta G°$ is the standard molar Gibbs energy for water decomposition ($\Delta G° = 237{,}2$ kJ·mol^{-1}), and $\Delta S°$ corresponds to the standard molar-free entropy of the reaction ($\Delta S° = 0{,}2$ kJ·mol^{-1}).

The standard Gibbs energy ($\Delta G°$) represents the minimum electric energy that is needed, while $T\Delta S°$ is the minimum heat that the water-splitting reaction needs in order to take place. The electric energy ($\Delta G°$) is provided by an external electric generator, while the heat energy ($T\Delta S°$) is provided by the temperature of working conditions or an external source of heat. Once equation **14** is established, two electrolysis voltages can be defined: the first one, from $\Delta G°$, is the thermodynamic or reversible voltage (E_{rev}); the second one is the enthalpy or thermoneutral voltage (E_{therm}), and takes into account the global energy that the reaction requires. Both voltages can be calculated from the following equations (**15** and **16**):

$$E rev \; = \frac{-\Delta G°}{nF} = 1{,}23 \; V \quad \textbf{(Eq. 1.15)}$$

$$Etherm \; = \frac{-\Delta H°}{nF} = 1{,}48 \; V \quad \textbf{(Eq. 1.16)}$$

Where F is the Faraday constant (96.485 C·mol^{-1}) and n is the number of electrons exchanged in the water electrolysis reaction (here $n = 2$). Both $\Delta G°$ and $\Delta H°$ are given for standard conditions ($p = 1$ bar $= 10^5$ Pa) and 25°C (298K), where water is in a liquid phase, while oxygen

and hydrogen are gases, meaning that both E_{rev} and E_{therm} voltages are dependent on the system's pressure and temperature, **Figure 1.4**.

According the electrolysis cell voltage (U_{cell}) applied, three scenarios are possible:

1. $U_{cell} < U_{rev} \rightarrow$ the reaction will not occur; hydrogen generation is impossible.

2. $U_{rev} < U_{cell} < U_{therm} \rightarrow$ endothermic water splitting, heat or extra energy is required. Cell efficiency is 100%.

3. $U_{therm} < U_{cell} \rightarrow$ exothermic water-splitting, heat is produced and released.

Therefore, and as seen in **Figure 1.4**, a supplementary voltage (overpotential) of 0.25 V could be defined, derived from the entropy change ($\Delta S°$), which is the heat required for the reaction to occur. This corresponds to the minimum voltage with respect to the U_{rev} (1,23 V) that has to be applied by the electrocatalytic cell (U_{cell}) in order to start the water decomposition reaction for 100% efficiency. If the reaction takes place at 1.48 V, the efficiency of the cell will still be 100%, and water-splitting will take place without any heat exchange with the environment.

Apart from this overpotential of 0.25 V to reach the thermoneutral potential (U_{therm}), the reaction kinetics of both electrodes present limitations, i.e., the appearance of oxidation and reduction overpotentials on both electrodes, $\eta_{cathode}$ and η_{anode} respectively, leading to an overvoltage. These activation overpotentials are increased by augmenting the current density of the cell, but can be lowered using electrodes with a catalytic action over the desired reaction, such as Ruthenium or Iridium through the water oxidation on the anode, and Pt through hydrogen production on the cathode.[21] Moreover, some other irreversible losses contribute to the increase in cell voltage, involving more over-voltages: the different elements that constitute the electrolysis cell (connections, interfaces, electrolyte materials, electrodes, current collectors, etc.) and the interfaces between them are responsible for the appearance of ohmic resistances (R_{cell}) or losses; in addition, losses linked to mass transport, where reagents cannot reach the electrode in order to react (formation of hydrogen and oxygen bubbles during the electrolysis), contribute to the increase in mass transport losses (R_{mass}).

As a consequence, the cell voltage U_{cell} must be higher than the reversible voltage (1.23 V, $U_{rev} = E°_{rev}$) for the final production of hydrogen on the cathode side, but should be kept as close as possible to 1.48 in order to maximize the efficiency of the cell and minimize the production of heat (waste energy). On the other hand, the lower the overpotential, the slower the reaction that occurs (**Figure 1.4**), so a compromise is needed. Materials development and cell design are key ways to obtain this compromise, like for example increasing the contact areas between the electrodes and the liquid, which increases the cell current (and the hydrogen production) without increasing the overpotential.
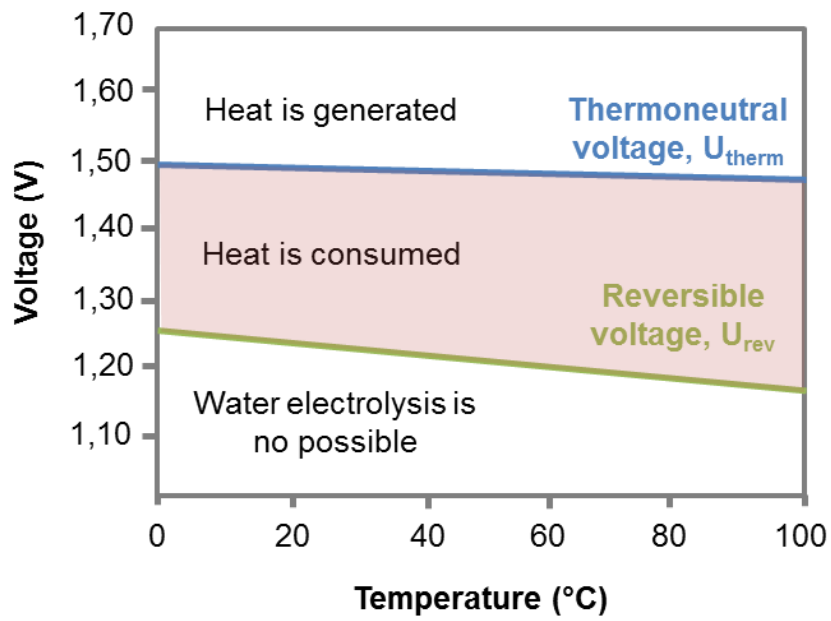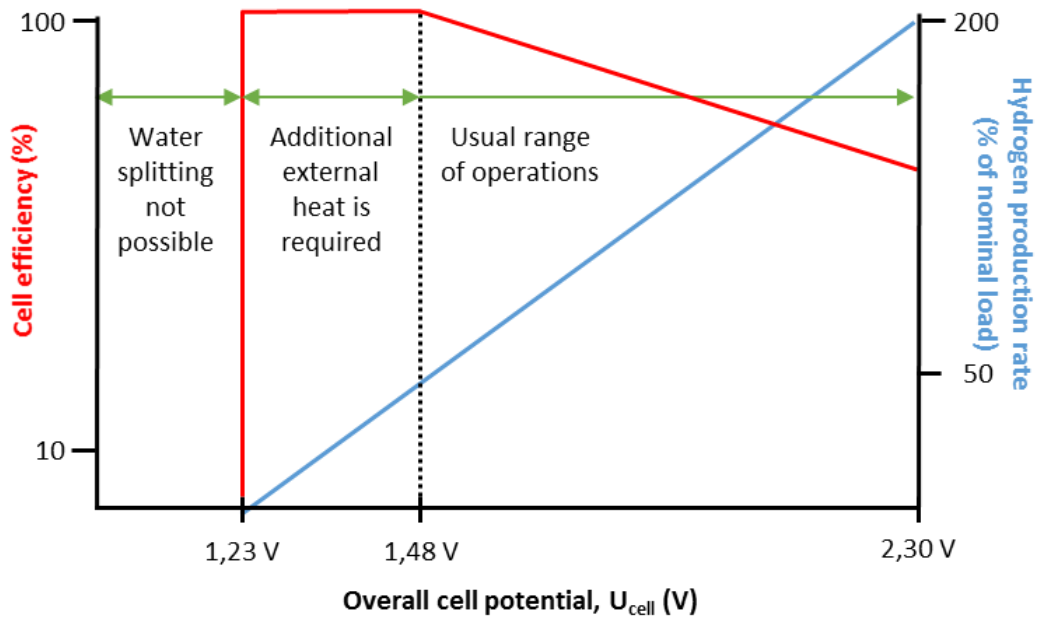
Figure 1.4 Top graph: illustrative cell efficiency and hydrogen production rate as a function of voltage. Bottom graph: reversible and thermo-neutral voltage for water electrolysis as a function of temperature at pressure of 1 bar. Adapted from Neagu *et al.* [21]

I.4.1 Alkaline electrolysis cells (AEC)

Alkaline electrolysis is a mature, commercial technology that is currently the electrolysis technology most used by industry for hydrogen production. The electrolyte of AEC systems is an aqueous solution of NaOH or KOH (which are not as corrosive as acids), where potassium or sodium hydroxide concentrations are in the 25 to 30 wt.% range for pressures between 1 to 30 bar and temperatures between 70 and 100°C.[22] During AEC operations, electrons are consumed by water to form hydrogen on the cathode (equation **19**, $E^0_{(H2O/H2)}$ = -0.83 V vs SHE) while hydroxyl anions are transferred through the electrolyte solution to the anode (equation **20**, $E^0_{(OH/O2)}$ = 0.40 V vs SHE), releasing electrons and oxygen as products:[23]

Cathode reaction: $4H_2O + 4e^- \rightarrow 2H_2 + 4OH^-$ $E^0_{(H2O/H2)}$ = -0.83 V vs SHE **(Eq. 1.19)**

Anode reaction: $4OH^- \rightarrow 2H_2O + 4e^- + O_2$ $E^0_{(OH/O2)}$ = 0.40 V vs SHE **(Eq. 1.20)**
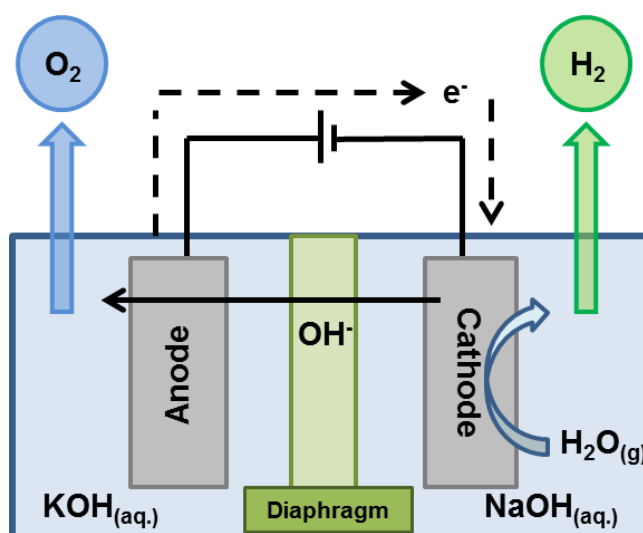
Figure 1.5 Working principle of an alkaline electrolysis cell (AEC) illustrating the different compartments (anode and cathode).

On the one hand, the AEC diaphragm needs to be highly permeable to water and resistant to corrosion due to the strongly alkaline media, and must also feature a high ionic conductivity for hydroxyl ions, high efficiency and low cost.[24] Different types of diaphragm have been studied, such as ceramic materials composites and microporous materials, e.g. NiO based porous materials, reinforced microporous polyethersulfones (PES) membranes and glass reinforced polyphenylene sulfide compounds.[25]

On the other hand, the electrode materials for AEC are made of highly stable materials in alkaline media such as nickel, cobalt and iron.[22] Nickel oxide-based materials are currently used in commercial systems due to their high stability.[26] The best catalytic performances for anodes have been found in nanostructured cobalt cobaltite systems, but need to be doped by Li or La in order to increase conductivity.[27] Commercial alkaline electrolysis systems generally use mild steel recovered by a nickel layer as cathode materials.[28]

Although AEC is currently used by industry, its efficiency is lower than that of acidic cells (e.g., PEMWE cells). This is due to the higher resistance of alkaline cells, which can be attributed to the macroporous electrodes employed and the thicker separator between compartments (in comparison to acidic water electrolyzer membranes).[20] Large ohmic resistance limits the hydrogen production flow rates.

I.4.2 Proton exchange membrane water electrolysis (PEMWE)

As seen in **Figure 1.6**, in PEMWE cells, ultrapure water is fed into the cell's anode, which is normally made from or coated with a noble metal oxide (Ruthenium or Iridium). In the anode, water molecules are oxidized (equation **22,** $E^0_{(O2/H2O)}$ = 1,23 V vs SHE) generating oxygen and protons. A membrane conducts hydrated protons from the anode side to the cathode side, where the protons are reduced into hydrogen (equation **21,** $E^0_{(H2O/H2)}$ = 0,0 V vs SHE). This technology can operate in the temperature range where water is in a liquid phase (lower than 100°C).

Currently, PFSA polymer membranes, such as the brand Nafion®, are the solid electrolytes most frequently used solid electrolytes in PEMWE, due to their excellent chemical and thermal stabilities, mechanical strength and high proton conductivity.

PEMWE membrane materials present lower ohmic resistances, which means they can be worked at higher current densities than AEC (0.6 to 2.0 A cm^{-2}_{geo} against 0.2 to 0.6 A cm^{-2}_{geo}, respectively).[29] In addition, they react faster to power fluctuations, and this aspect is very interesting from the point of view of combining PEMWE devices with renewable energy sources. It is also possible to produce hydrogen at relatively high pressures, 30 bars or even 100. The energy efficiency of ideal cells is 80%.[30] However, working conditions are very aggressive due to the acidic environment, making the use of non-noble catalysts impossible, which induces a relatively high cost (€ 1,860 - € 2,320 kWel^{-1} against € 1,000 - € 1,200 kWel^{-1} in alkaline electrolysis) and a shorter lifespan.[31]

Cathode reaction: $4H^+ + 4e^- \rightarrow 2H_2$ $\qquad$ $E^0_{(H2O/H2)}$ = 0,0 V vs SHE **(Eq. 1.21)**

Anode reaction: $2H_2O \rightarrow 4H^+ + 4e^- + O_2$ $\qquad$ $E^0_{(O2/H2O)}$ = 1,23 V vs SHE **(Eq. 1.22)**
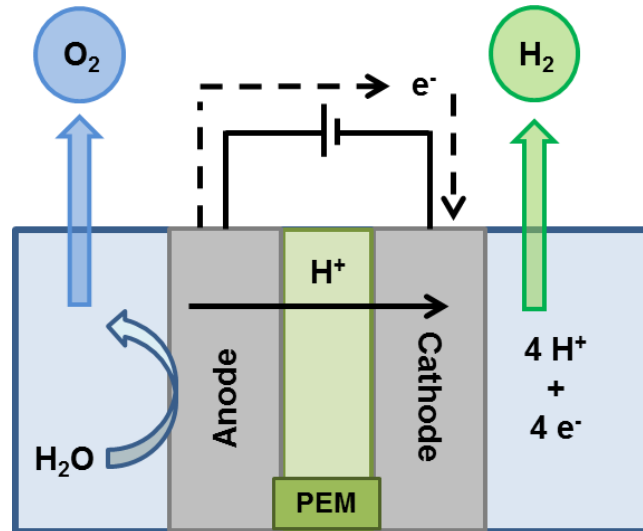
Figure 1.6 Working principle of a PEMWE cell, illustrating anode and cathode compartments.

The cathodes in this type of electrolyzer normally consist of Pt/C or other mixed oxides such as electrocatalysts. Anode, cathode and membrane materials are further discussed in **section II.2.4** of this chapter.

I.4.3 Solid oxide electrolysis cells (SOEC)

The electrochemical reactions that take place at high temperatures, between 500 and 1,000°C, are completely different from those occurring in PEMWE's and AEC's that operate at temperatures lower than 100°C. In SOECs, the cathode (equation **17**) is fed with steam water, which is reduced to hydrogen and the oxide ion species O^{2-}. These oxide ions migrate to the anode through an anion-conducting electrolyte, where they are oxidized to produce oxygen (equation **18**).[32]

Cathode reaction: $2H_2O + 4e- \rightarrow 2H_2 + 2O^{2-}$ $\quad$ $E^0_{(H2/O2-)}$ = -0.83 V vs SHE **(Eq. 1.17)**

Anode reaction: $2O^{2-} \rightarrow 4e^- + O_2$ $\qquad$ $E^0_{(O2-/O2)}$ = 0.40 V vs SHE **(Eq. 1.18)**
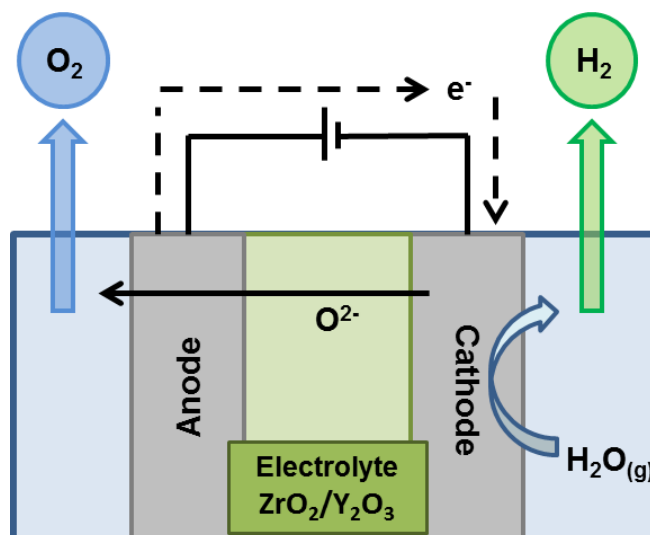
Figure 1.7 Working principle of a SOEC, illustrating the different compartments (anode and cathode) and the solid electrolyte.

The components of SOEC cells must be thermally stable (usually made of solid oxides) and feature electron-conducting porous ceramic materials in order to facilitate the electron and mass transportation (oxygen and hydrogen). In addition, they must present high ionic conductivity in order to allow the migration of oxide anion species (O_2^-). For example, electrode materials generally consist in conducting mixed oxides with a perovskite structure (ABO_3). Mixing different metals at different ratios has been shown to improve the stability and activity of both electrodes.[33] Anode catalysts are mostly based on La, Sr and Mn oxides, while the composition of cathode catalysts is based on Ni or Zr oxides.[34] Meanwhile, the solid electrolyte is generally based on a mixed oxide comprising ZrO_2/Y_2O_3.[35]

Loss of cell performance is normally caused by the delamination of different layers of the electrodes and the electrolyte, induced by high-temperature working conditions and the presence of water steam.[34]

I.4.4 Advantages and drawbacks of the different technologies

Regarding the operating conditions, or the reactions that evolve at the electrode's surface, the materials used in these different systems must have specifics properties. Each type of electrolysis cell has its own advantages and drawbacks, as summarized in **Table 1.2**:

Table 1.2. Main advantages and drawbacks of electrolysis cell systems.

	Alkaline electrolysis (AEC)	PEM electrolysis (PEMWE)	Solid oxide electrolysis (SOEC)
Advantages	Commercial technology Non-noble catalysts Long-term stability Relatively low cost MW range stacks Cost effective	Near-term technology High current densities High voltage efficiency Good partial load range Rapid system response Compact system design Easy coupling to Renewable energies High gas purity with relatively high H_2 pressures Dynamic operation	Efficiency up to 100% Thermoneutral voltage Non-noble catalysts High-pressure operation
Drawbacks	Low current densities Low degree of gas purity Low partial load range Low operational pressures Caustic electrolyte	High costs of components Acid corrosive media Low durability Stacks below MW range	Startup time Mediate-term technology Bulky system design Durability Brittle ceramics

38

The main advantages of AECs are the possibility of using non-noble electrocatalyst materials and their long-term stability in stationary mode. On the other hand, the highly corrosive electrolytic alkaline medium corrodes the system. Moreover, the diaphragm used as a separator cannot totally avoid gas permeation during long-term hydrogen production, and the lower mobility of hydroxyl ions (compared with protons) limits the conductivity and the cell's efficiency.

For PEMWE cells, the compactness of the system allows operations at high-current densities while preserving the purity of the hydrogen produced under high pressures (30 bars to the date). Their rapid voltage response induced by the nature of the solid electrolyte and the protons migrating through the electrolyte means that these systems can be coupled with intermittent renewable energy sources. The main drawbacks of this type of electrolyzer are the high cost of the main components and the anode materials corrosion under the acidic environment.

For SOECs, the high operation temperature means that non-noble metals can be used in ceramic oxides serving as electrodes and electrolyte. Moreover, hydrogen production results in a decrease in electric energy consumption, at the expense of the need to heat the system. However, because of the compactness of these systems and the thinness of their ceramic materials, membrane electrode assemblies (MEAs) can be easily damaged. On the other hand, ceramic materials can also be broken during long-term hydrogen production. Despite this, due to the high operation temperature requirement, this technology is quite interesting for the development of reversible, so-called unitized fuel-cell technology.

In summary, each technology has an application depending on the domain considered: SOECs for the recovery of excess energy production, e.g., the heat produced in nuclear power plants; AECs for industrial stationary applications; and finally PEMWE cells for their ability to be specifically coupled with renewable energy systems (wind, solar, tidal, etc.), which makes them the most interesting technology for future renewable energy storage. A significant reduction in the cost of the active components of PEMWE cells (which currently make up about 70% of MEA production costs),[36] could allow a considerable scale-up of these systems, making them highly competitive and promising as green hydrogen production devices.

II PEMWE cells

II.1 Current situation and perspectives

There are many commercial PEMWE systems available from different international manufacturers: Hydrogenics, Proton Onsite, Siemens, ITM power, Giner, ArevaH2Gen (recently bought by GTT), H-TEC Systems, Kobelco-eco solutions, SylaTech, NEL ASA, etc. Of these, the most powerful electrolyzer is the HyLYZER-3000, manufactured by Hydrogenics, a 15 MW plant with 10 cell stacks (cell area < 0.3 m^2) capable of producing 3,000 Nm^3 (normal cubic meters) of hydrogen per hour. Electricity consumption, which is very similar in all systems available, is around 5.5 kWh per Nm^3 of hydrogen produced (which means an energy yield of 55 or 65%, LHV or HHV respectively).[37]

Hydrogen production costs present huge regional variations, and their economic future depends on factors that will continue to vary regionally, including the prices of fossil fuels, electricity and carbon (due to CO_2 taxes). If we compare the price per kg of H_2 produced by current commercial PEM electrolyzers with the price of hydrogen produced by non-renewable sources such as coal or natural gas, we observe huge differences (**Figure 1.8**). For example, in the Middle East, it is possible to produce 1 kg of H_2 from natural gas for less than USD 1 (without CCUS, carbon capture, utilization and storage).
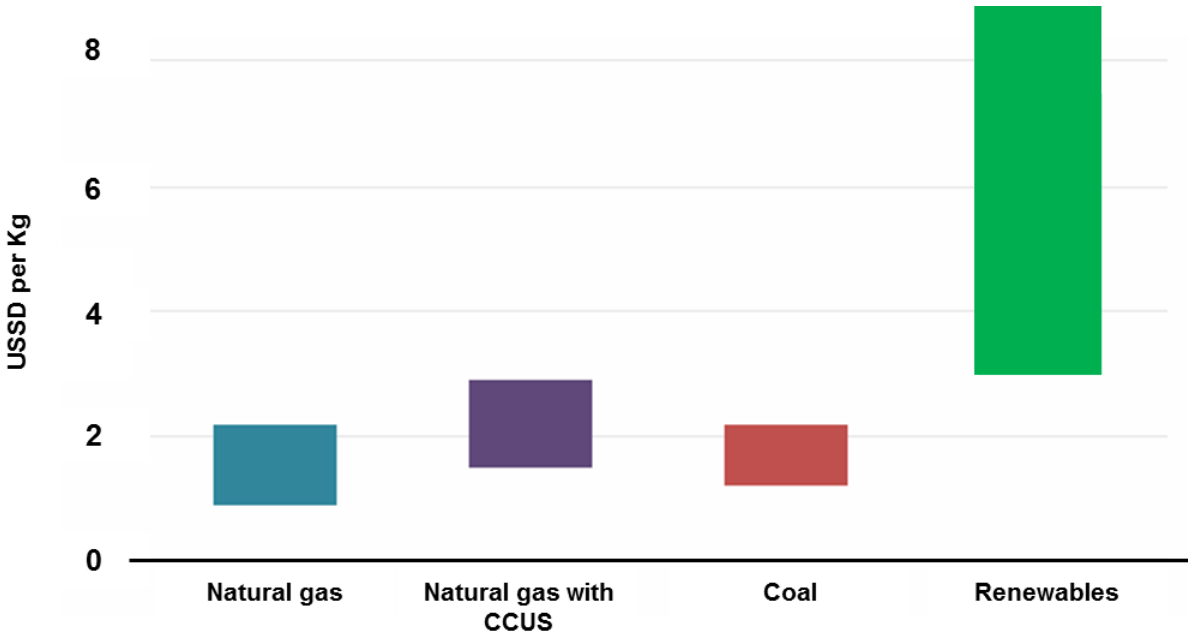
Figure 1.8 World average hydrogen production costs, 2018. [9]

Therefore, the price of hydrogen production using PEMWE cells needs to be reduced by around 4-5 times in order to be competitive with production by non-renewable sources. One way to reduce production costs is to bring down the cost of the stacks in the system, which are responsible for 53% of the overall system expenses, see **Figure 1.9**. By decreasing the total cost of each single cell, the overall expenses would be reduced.
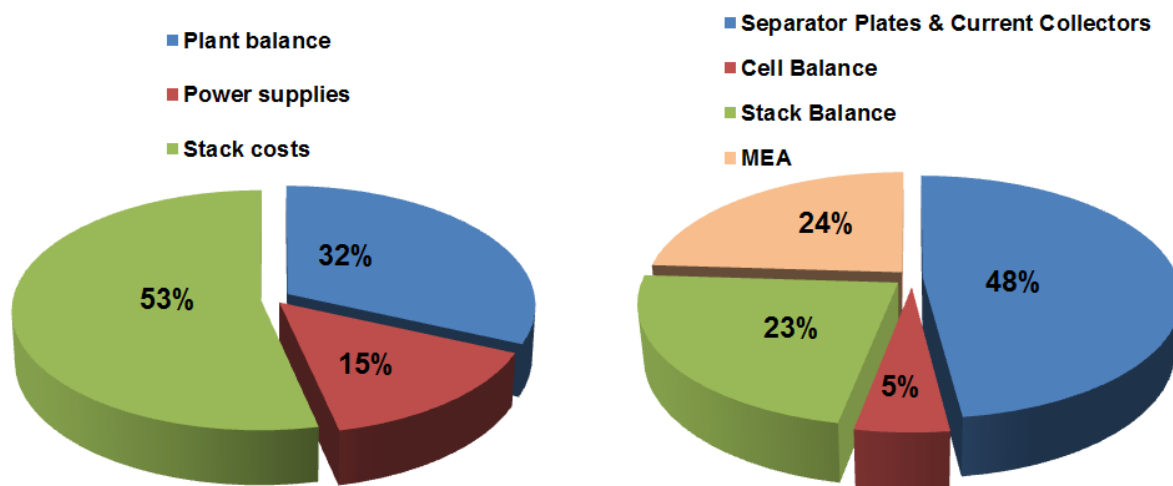
Figure 1.9 Left: breakdown of the system cost of a PEMWE cell. Right: breakdown of the cost of a single cell.[36]

Presently, research efforts are addressed at reducing these stack costs by improving the efficiency and durability of active materials, which contribute to about 70% of MEA production costs.[38] The main ways to reduce these costs involve developing low-cost electrocatalysts, low-noble-metal-content electrodes and cost-effective alternative membranes. For example: the current anode loading of iridium oxide is between 1.5 and 3 mg·cm^{-2},[38] and the cathode loading of platinum is 0.5 mg·cm^{-2}; thus it is essential to reduce these amounts of expensive noble metal electrocatalyst in the electrode by at least one order of magnitude.[38]

Other crucial research area focuses on surface treatment of titanium-based separator plates and current collectors in order to reduce contact resistance and improve corrosion resistance.[40] Decreasing the costs of separators plates and current collectors is of great importance, as it corresponds to a 48% of the cell costs.

Another strategy for cost reduction is to develop larger electrolyzers, which can be obtained by assembling several stacks. In this way, it is possible to save cost on auxiliaries while increasing the overall capacity of the system,[9] **Figure 1.10**. The strategy of scaling-up production devices is suitable for both alkaline and PEM water electrolyzers.
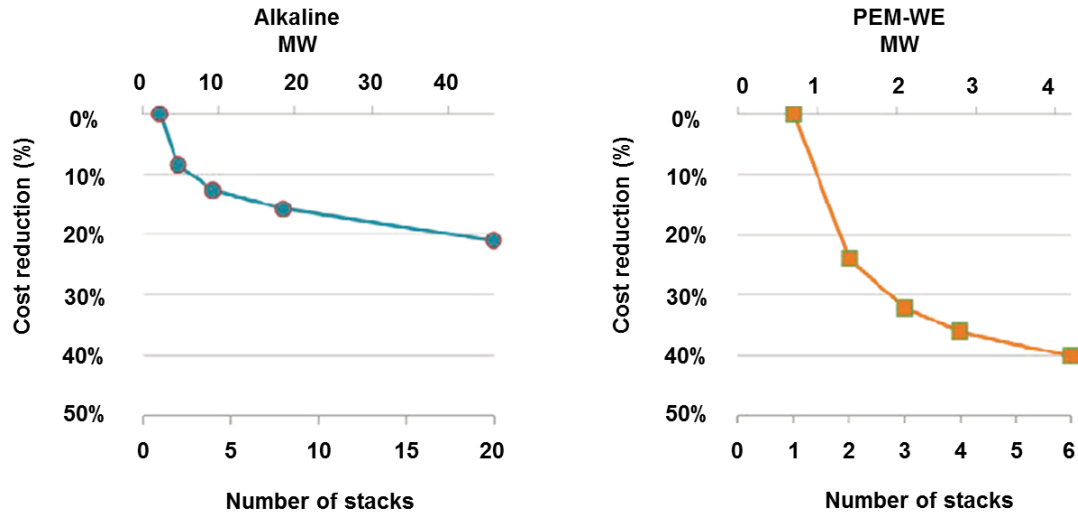
Figure 1.10 Expected reduction in electrolyzer costs from using multi-stack systems.[9]

In the long term, as well as lower electrolyzer costs and improved performance of solar photovoltaics and wind technologies for electricity generation, another potential low-cost supply option for hydrogen production is to build electrolyzers at locations with excellent renewable resource conditions. With this solution, hydrogen from renewable power would become competitive with (or even cheaper than) all forms of hydrogen produced from fossil fuels. Data from the International Energy Agency predict that hydrogen produced from electrolysis using solar or wind power will be cheaper than natural gas by 2030 in the best locations,[9,39] and cost less than USD 1.6 per kg (**Figure 1.11**).
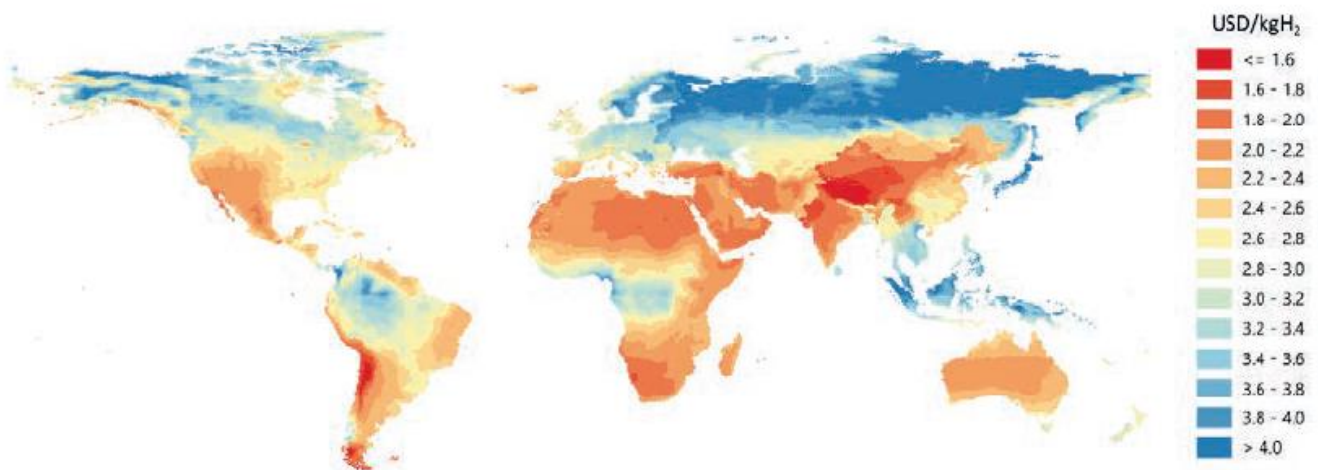
Figure 1.11 Hydrogen costs from hybrid solar PV and onshore systems in the long term.[9]

The main drawbacks for market applications are that: (1) larger electrolyzers have to be operated at multi A·cm^{-2} current densities with extended durability (a minimum of 10 kgH$_2$·h^{-1} is required in the short term to supply hydrogen in refueling stations), and (2) market requirements are calling for systems in the range of USD 500 kW^{-1}. State-of-the-art performances, short-term targets and the ultimate potential of PEM water electrolyzers are plotted in **Figure 1.12**. This is a fast-evolving field and milestones may be reached faster than expected with appropriate R&D efforts financially supported by public funding agencies and industry.

Property	State of the art	Target 2020–2030	Ultimate goal
Operating current density (A cm^{-2})	0–1	0–2	0–5
Operating temperature (°C)	50–80	80–120	100–150
Operating pressure (bar)	1–50	1–350	1–700
Enthalpic efficiency with PGM catalysts	80% at 1 A cm^{-2}	80% at 2 A cm^{-2}	80% at 4 A cm^{-2}
Enthalpic efficiency with non-PGM catalysts	30–40% at 1 A cm^{-2}	60% at 1 A cm^{-2}	60% at 1 A cm^{-2}
SPE voltage drop (mV at 1 A cm^{-2})	150	100	67
SPE ionic conductivity (S cm^{-1} at 80 °C)	0.17	0.20	0.30
SPE gas permeability to H$_2$ (cm^2 s^{-1} Pa^{-1}) (80 °C, full humidity)	10^{-11}	10^{-9}	10^{-9}
Cathodic PGM (Pt) content (mg cm^{-2})	1.0–0.5	0.5–0.05	<0.05
Anodic PGM (Ir, Ru) contents (mg cm^{-2})	1.0–2.0	0.5–0.1	<0.1
Durability (h)	10^4	10^4–5.10^4	>10^5
Production capacity of electrolysis units	1 kg h^{-1} ($\approx$10 Nm^3 h^{-1})	>10 kg h^{-1} ($\approx$100 Nm^3 h^{-1})	>100 kg h^{-1} ($\approx$1000 Nm^3 h^{-1})
Energy (kWh kg^{-1} H$_2$ at 80 °C, 1 A cm^{-2})	56	<50	48
Non-energy cost (€ kg^{-1} H$_2$)	5	2	1

Figure 1.12 State-of-the-art, short-term target and ultimate goals for PEM water electrolysis specification.[40]

For example, in 2007 (revised in 2015) the EU presented a Strategic Energy Technology Plan (SET Plan). This plan aims to coordinate the research and innovation activities of EU Member States in order to achieve decarbonisation by 2050. The Commission granted € 1.34 billion to 396 projects related to energy storage on the grid and low-carbon mobility, with 37% of total investments targeting hydrogen or fuel cell projects in order to ensure a common, strong, competitive hydrogen market for future.

Other projects have been initiated in Germany by Siemens and H-TEC, in Italy (European REMOTE project), in Denmark by Air Liquide (European HYBalance project) and in France (MYRTE or Jupiter 1000 projects).

II.2 PEMWE cell main constituents

A PEM electrolyzer consists of several series of elementary cells forming a stack, with each elementary PEM cell (**Figure 1.13**) containing several components. The electrochemically active central component is a membrane electrode assembly (MEA), composed of a proton-conducting polymer electrolyte membrane (**Figure 1.13c-3**), coated on each side with two porous layers of electrocatalysts; one at the anode for the oxygen evolution reaction (OER) or water splitting, and the other at the cathode for the hydrogen evolution reaction (HER). The MEA is usually clamped between two porous current collectors (**Figure 1.13c2,4**) made of titanium. Two bipolar separator plates (**Figure 1.13c-1**) are used to convey the electric current to the cell and to separate two adjacent cells that are used to carry, through channels, water to the anode while collecting liquid–gas mixtures in each cell compartment. Two end plates are joined to copper or aluminum current collectors installed for the electrical connection (**Figure 1.13a**). Thick endplates made of steel, together with several bolts and sets of stacked flat springs, are used to ensure optimal compression of the cells.
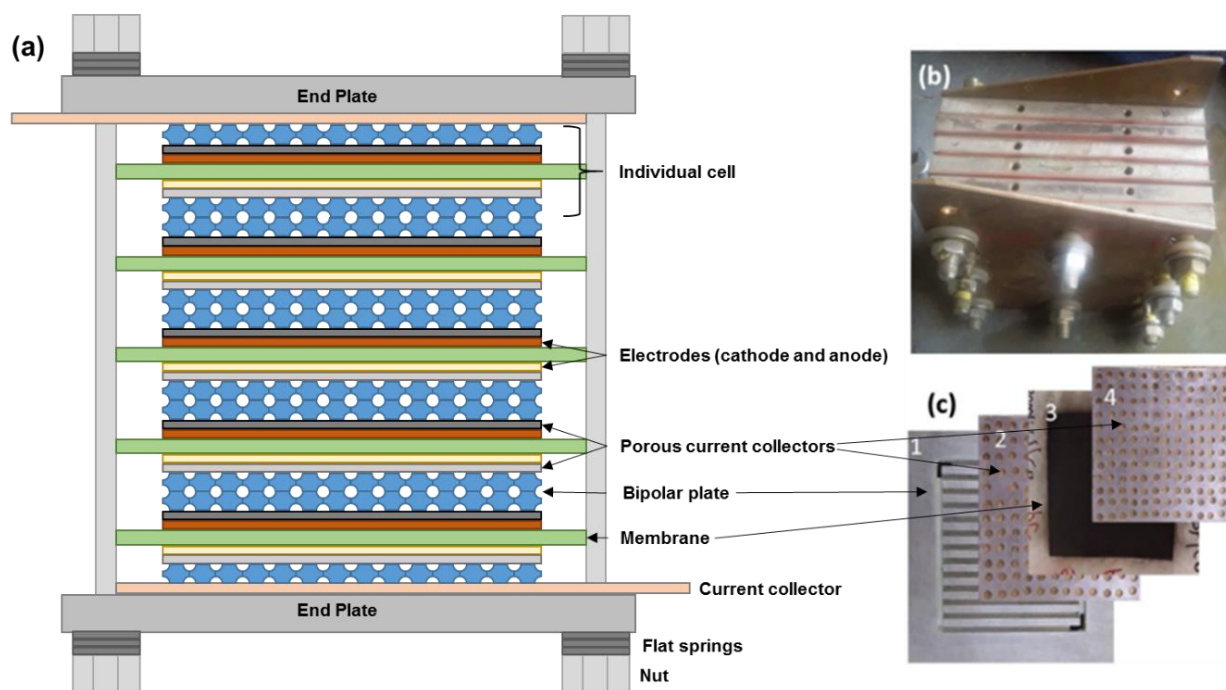
Figure 1.13 (a) Overview scheme of typical PEM water electrolyzer (b) PEM cell stack (c) Cell components; 1-Bipolar plate, 2-Anode current collector, 3-MEA, 4-Cathode current collector.[36]

II.2.1 Separator plates and current collectors

In the PEMWE process, water is pumped to the anode side of the cell, where an oxygen evolution reaction (OER) occurs. The water feed travels through the separator plates (or bipolar plates) and diffuses via current collectors (also called gas diffusion layers). The water feed then reaches the anode electrode surface, where water molecules are decomposed into oxygen, protons and electrons. The oxygen produced returns to the outside of the cell via the electrodes, current collectors and then separator plates. Protons move from the anode to the cathode side through the proton-conducting membrane, and electrons travel from the current collectors to separator plates and finally to the cathode side, where they are recombined with protons giving hydrogen through a hydrogen evolution reaction (HER). The hydrogen obtained then leaves the cell via the cathode current collector and separator plates. Therefore, the components, separator plates and current collectors must all present high corrosion resistance (due to the acidic environment, high potential working conditions and presence of oxygen) and good electrical conductivity. The reason is that they are made of expensive, resistant materials that constitute 48% of the overall cell cost, **Figure 1.9**.

Current collectors also offer good mechanical strength to the membrane and optimized porosity (for gas management, such a gas diffusion layer, GDL, in PEMFC). For PEMWE cells, titanium plates are typically used, as they present unique properties, such as good electrical conductivity, high mechanical stability to ensure support to the membrane, and high corrosion resistance under acidic environments.[36] In order to prevent titanium surface passivation, they are normally coated with an anticorrosion loading made of Pt, Ar or Ir.[41]

Although separator plates made of titanium, stainless steel and graphite exist, these materials are expensive and present different operational drawbacks, for example corrosion at the anode side in the case of titanium. To address this issue and protect the plates, precious metal coatings and alloys are used, at the expense of increasing the total cost of the stack. Therefore, cost-effective separator plates are still under investigation.[36, 42]

II.2.2 Polymer electrolyte membrane (PEM)

At the center of the MEA is a polymer electrolyte membrane, or proton exchange membrane (PEM), which is designed to conduct protons, H^+, while acting as an electronic insulator and reactant barrier, e.g., to oxygen and hydrogen gases. Protons pass through the polymeric electrolyte membrane (PEM), from the anode side, to the cathode and combine with electrons to form hydrogen. These membranes comprise solid electrolyte instead of the liquid electrolytes used in alkaline water electrolyzers. They are responsible for 24% of the overall cell cost, **Figure 1.8**.

Membranes should display:

- High proton conductivity.

- No electronic conductivity.

- High thermal and chemical stability in acid media.

- Mechanical properties combining high strength and flexibility.

- Good thermal and viscoelastic properties.

- Low permeability to the hydrogen and oxygen gases produced.

- An important aspect of PEMWE operations is related to the cross-over of the gases produced (oxygen and hydrogen). When cross-over occurs, hydrogen and oxygen react directly on the catalytic sites of the cathode or anode. The reaction is extremely exothermic, producing a level of heat that can damage the membrane or cause strong catalyst sintering over time. Therefore, low levels of gas cross-over are necessary for PEMWE application for possible operation at high-pressure that may reach 50–100 bars. Thus, the polymer electrolyte separator should be of an appropriate thickness.

- PEMs can be made of sulfonated fluoropolymers (perfluorosulfonic acid, PFSA) such as the brands Nafion®, Fumapem®, Flemion®, Aciplex®,[43] or composite membranes (where other materials are embedded in a polymer matrix).

- PFSA polymer is composed of a tetrafluoroethylene backbone with chains terminated with a sulfonic acid group ($-SO_3$-H). An essential property of this sulfonic acid group is that it attracts water, and the conductivity of the membrane is dependent on hydration. Mixing water with the sulfonic acid group enable protons to move through the hydrated molecular structure of the membrane via sulfonic groups. A high hydration rate is important to maintain high proton conductivity in the membrane. These membranes are usually between 50 and 250 µm thick. The selection of the appropriate thickness results from a compromise between low-area specific resistance, low cross-over (gas mixtures), and suitable mechanical stability requirements.

The main disadvantages of these PFSA polymer membranes are:

- Their high cost, over USD 120 per m^{-2}, which increases the final cost of the MEAs.[44]

- The presence of fluorine in the polymer structure.

- Their thickness (which increases the ohmic resistance).

- Their loss of mechanical strength and proton conductivity at high temperatures (>100°C) due to membrane dehydration.[45]

This kind of PFSA-based proton-conducting membrane is quite similar to those used in PEMFC, where proton exchange membranes are also needed. PEMFCs are similar to PEMWEs in this respect, since a polymer electrolyte membrane separates both compartments, the anode and cathode. They allow the protons produced to flow on the anode side, following the hydrogen oxidation reaction (HOR, equation **23**), through the cathode, where the oxygen reduction reaction (ORR, equation **24**) occurs. In PEMFCs, hydrogen and oxygen are used as reactants for energy production, generating water as a byproduct of the overall procedure, equation **25**.

Anode reaction: $2 H_2 \rightarrow 4H^+ + 4e^-$ $E^0_{(H/H+)} = 0.00$ V vs SHE **(Eq. 1.23)**

Cathode reaction: $O_2 + 4e^- + 4H^+ \rightarrow 2H_2O$ $E^0_{(H2O/O2)} = 1.23$ V vs SHE **(Eq. 1.24)**

Overall reaction: $2 H_2 + O_2 \rightarrow 2H_2O$ $E^0 = 1.23$ V vs SHE **(Eq. 1.25)**
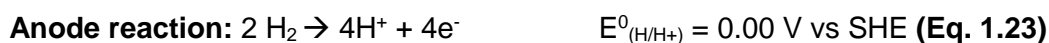
Using this kind of membrane in PEMWEs should also result in good proton conductivity, no electron conductivity (to avoid a short circuit effect in the cell), optimal and mechanical stabilities, and low permeability to oxygen and hydrogen gases (in order to avoid cross-over procedures). Similar weaknesses are found in PEM membranes used for PEMFC, for example concerning working temperatures: working at higher temperatures than 100°C leads to a dry membrane.

Compared to PEMFC, in electrolysis cells the membrane is thicker (between 50 and 250 μm vs 15 μm) and fully hydrated. The different operation pressure conditions between both cells is another point that explains the thickness of the membrane; while in PEMWEs the operating pressure can be up to 100 bar, in PEMFCs it operates at lower pressures.[46]

Currently investigations are focused either on improving membrane properties or on finding alternative materials. For example, Nafion® membranes have been modified with novel oxide particles (composite membranes) to improve their thermal properties.[47] Composite-based

membranes have emerged as alternative membranes that are more suitable for work at high temperatures (120-150°C) and have good mechanical properties. This type of composite membrane is based on hygroscopic ceramic oxide fillers (such as SiO_2, ZrO_2 or ZrO_2/SO_4^{2-} NPs) embedded in a polymer matrix (such as PFSA), which enhances the water retention inside the membrane, allowing the system to operate at high temperatures. Moreover, cross-over is decreased thanks to the presence of nanoparticles inside the membrane. Alternative hydrocarbon-based membranes, such as polybenzimidazoles, polyether-etherketones (PEEK), polyethersulfones (PES), and sulfonated polyphenyl quinoxaline, have been developed in order to decrease the cost of the materials.[48] The proton-conductivity in all membranes of this type is also provided by the presence of sulfonic acid groups and optimal hydration.

II.2.3 Catalyst layers

Catalyst layers are the key components of MEAs, as they are where the OER occurs at the anode and the HER occurs at the cathode. They are composed of electrocatalysts with the addition of an ionomer solution (typically Nafion®) in order to provide ionic conductivity and allow better mechanical stability.

Catalysts offer an alternative, energetically favorable pathway for a reaction and allow selective routes to produce fewer or no by-products.[49]

The electrocatalysts most commonly used at the cathode are platinum nanoparticles (NPs) supported on carbon (Pt/C, loaded between 0.5 - 1.0 mg·cm^{-2}).[50] The anode catalyst is iridium dioxide (IrO_2) in the form of microparticles with a loading of around 1.5 - 3 mg·cm^{-2}.[38]

The catalytic layers are deposited either on the current collectors, or directly on the membrane (catalyst coated membrane, CCM). To be effective, they must be in close contact with three elements at the same time:

- The current collectors, in order to be able to conduct the electrons exchanged during the OER and the HER.

- The polymer electrolyte, in order to be able to exchange the protons from the anode to the cathode.

- Water, a reagent of the OER.

Unlike HER, which is a rapid reaction, OER is kinetically slow and more complex, involving several reaction steps.[51] The study and improvement of the kinetics of this reaction are crucial to increase the energy efficiency of PEMWE cells.

II.2.3.1 Cathode electrocatalysts for hydrogen evolution reaction

The hydrogen evolution reaction (HER) is one of the most investigated electrochemical reactions in catalysis. In HER, protons combine with electrons at the cathode electrode surface to form chemisorbed species which then desorb as free hydrogen gas molecules. HER involves the formation of two H—H bonds by the reduction of two H^+ cations, Equation **23**:

$$2H^+ + 2e^- \rightarrow H_2 \textbf{ (Eq. 1.23)}$$
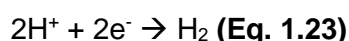
In heterogeneous catalysis, HER has been described as occurring through two different reaction pathways, namely Volmer-Heyrovsky and Volmer-Tafel. The steps followed are given in **Figure 1.14** and described hereafter (Eq. 24-26):[52]

Volmer: $H_3O^+ + M + e^- \rightarrow M\text{-}H + H_2O$ **(Eq. 1.24)**

Heyrovsky: $H_3O^+ + M\text{-}H + e^- \rightarrow M + H_2O + H_2$ **(Eq. 1.25)**

Tafel: $M\text{-}H + M\text{-}H \rightarrow 2M + H_2$ **(Eq. 1.26)**
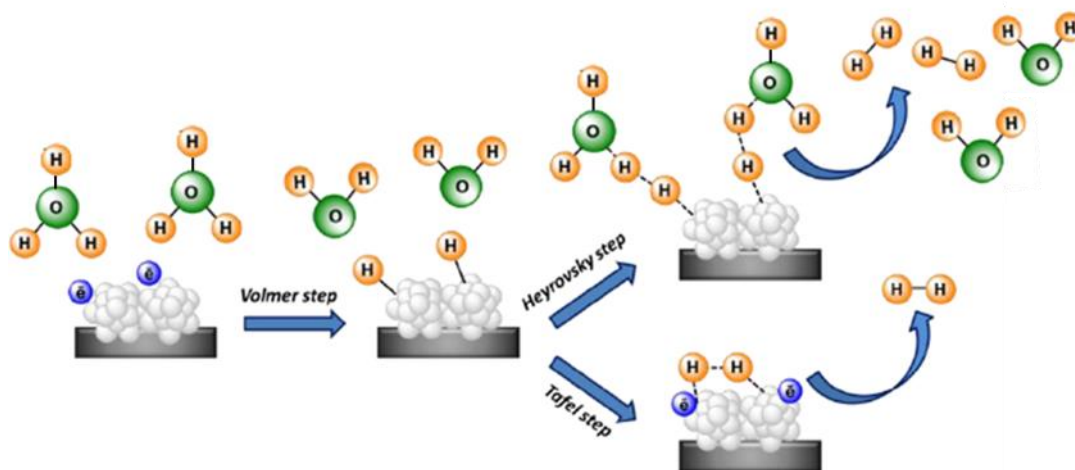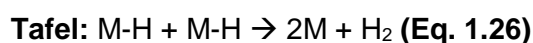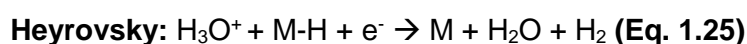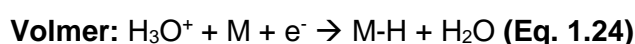
Figure 1.14 Representation of the three steps involved in the HER mechanism on heterogeneous catalysis.[52]

The Volmer step (**24**) involves the adsorption of one proton onto the catalyst surface, and is common for all hydrogen evolution catalysts (HEC). It is considered as a proton coupled electron transfer (PCET) on the surface of the catalyst, and is also known as a discharge reaction. The desorption step either involves the electro-desorption of the adsorbed hydride

with an H^+ in solution (Heyrovsky, **25**), which is also a PCET process; or the recombination of two metal-hydride groups (M-H), from a single particle or two different ones (**26**).

Pt black was initially used as a standard HEC on the cathode side; following experience gained in the development of PEMFC, researchers started using Pt nanoparticles supported on carbon-based materials (Pt/C),[53] such as nanotubes, graphene, carbon fibers, etc.

However, despite its lower Pt loadings, the cathode catalyst still represents a considerable portion of the total stack cost (price of Pt around USD 34.744 per kg^{-1}, November 2020), especially if degradation of the carbon-based supports occurs. Currently, the cathode-side Pt loading is approximately between $0.5 - 1$ $mg \cdot cm^{-2}$, but loading values lower than 0.2 $mg \cdot cm^{-2}$ are targeted.

The great majority of current studies are concentrated on this reduction of Pt loadings and on identifying potential Pt substitutes (Pt-free catalysts). Taking in account that the catalytic activity order for the HER was: Pd > Pt > Rh > Ir > Re > Os > Ru > Ni, studies that are focused on Pt loading reduction or substitution also look for longer catalyst durability.[54]

Some of these research directions where researchers use alternative catalysts are: MoS_2 supported on carbon-based materials (with similar performances to Pt, but cheaper),[55] $CuNiWO_4$,[56] WO_3 Nano-rods,[57] Co- and Ni-based nanomaterials.[58] Other studies use advanced materials such as core-shell NPs: Pt layer over Cu NPs,[59] Pt-Cu NPs,[60] or mixed metal alloys like $Pt_{65}Co_{32}Mn_3$.[61] Despite the low activity of the noble metal Ru in HER, recent studies have found that cathodes prepared with Ru-nanosized species could be potential substitutes for Pt-based electrodes.[8,62] This novel Ru-based HEC would constitute an alternative to reduce the cost of the catalyst, as the price of Ru (8.000 $USD \cdot kg^{-1}$) is around quarter that of Pt. Unfortunately, Ru resources are between 3 and 5 times lower than Pt ones on Earth's crust.[8]

Nowadays Pd-based electrocatalysts have increased the interest in the hydrogen evolution reaction due to its higher activity and stability, despite its higher costs in comparison with Pt (48.600 $USD \cdot kg^{-1}$ vs. 34.744 $USD \cdot kg^{-1}$). Most studies that used Pd as an HER electrocatalyst employed carbon-based materials (such as carbon nanotubes,[63] doped carbon materials, [64] graphene,[65] etc.).

In summary, in the family of Pt-free electrocatalysts developed, MoS_2 electrocatalysts appear to be the most suitable alternatives in terms of electro catalytic activity and stability compared to Pt based catalysts.

II.2.3.2 Anode electrocatalysts for oxygen evolution reaction

The Oxygen Evolution Reaction (OER) is considered to be one of the major roadblocks for hydrogen production, due to the low efficiency of current electrocatalysts. In OER (Equation **27**), water molecules are split into oxygen, protons and electrons (which are later recombined in the cathode side for hydrogen production):

$$H_2O \rightarrow 2H^+ + 2e^- + {}^1/_2 O_2 \textbf{ (Eq. 1.27)}$$
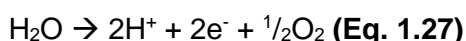
In electrochemical catalysis, this reaction takes place at high anode potentials (>1.4 V), where metal corrosion and passivation are observed. Due to high anode potentials, all anode catalytic materials take the form of oxide (at least on the surface). These oxide species have to display good electrical conductivity and must be stable enough to avoid further oxidation, which causes erosion/corrosion and impedes the activity of the catalyst over time.

Contrary to HER, OER is a more complex process, as four H-O bonds have to be broken and a O=O double bon formed. HER just involves the formation of two H—H bonds by the reduction of two H^+ cations. This divergence is evidenced with the overpotentials that catalysts require in each semi-reaction, in general being inferior to 100 mV for hydrogen evolution catalysts (HECs) and superior to 200 mV for water oxidation catalyst (WOCs).

The main steps of the OER process are:

1. The adsorption of water molecules forming intermediate species.

2. The reaction between adsorbed species

3. The oxygen desorption.

For the OER to take place in the most efficient way possible, the reaction intermediates (O *, OH *, OOH *) must have a certain affinity with the active sites of the electrocatalyst in order to be adsorbed.[66] However, they must not be adsorbed too strongly so that the reaction products can desorb, leaving the active site free for new reactant molecules. The speed of the OER is limited either by excessively strong adsorption of OH* species or by excessively weak adsorption of O* species,[67] while the OER activation overvoltage is linked to the kinetic constraints of each of the elementary steps.[68]

Many different reaction mechanisms have been proposed for the OER based on kinetic studies or DFT calculations, some of which are shown in **Figure 1.15**. Despite all of these proposed mechanisms, it is very difficult to determine which one is used by each catalyst, as current in situ techniques are not sufficiently developed to study the mechanism of bulk materials.

I) Oxide Path		II) Electrochemical Oxide Path	
1)	$H_2O + M \rightarrow M\text{-}OH + H^+ + e^-$	1)	$H_2O + M \rightarrow M\text{-}OH + H^+ + e^-$
2)	$2\,M\text{-}OH \rightarrow M\text{-}O + M + H_2O$	2)	$M\text{-}OH \rightarrow M\text{-}O + H^+ + e^-$
3)	$2\,M\text{-}O \rightarrow 2\,M + O_2$	3)	$2\,M\text{-}O \rightarrow 2\,M + O_2$
III) Electrochemical Metal Peroxide Path		**IV) DFT-predicted Peroxide Path**	
1)	$H_2O + M \rightarrow M\text{-}OH + H^+ + e^-$	1)	$H_2O + M \rightarrow M\text{-}OH + H^+ + e^-$
2)	$2\,M\text{-}OH \rightarrow M\text{-}O + M + H_2O$	2)	$M\text{-}OH \rightarrow M\text{-}O + H^+ + e^-$
3)	$M\text{-}O + H_2O \rightarrow M\text{-}OOH + H^+ + e^-$	3)	$M\text{-}O + H_2O \rightarrow M\text{-}OOH + H^+ + e^-$
4)	$2\,M\text{-}OOH \rightarrow M\text{-}O + H_2O + O_2 + M$	4)	$M\text{-}OOH \rightarrow M + O_2 + H^+ + e^-$

Figure 1.15 Proposed reaction mechanisms for the oxygen evolution reaction. Reaction mechanisms I–III are according to reference,[69] whereas reaction mechanism IV is according to reference.[70]

The main explanations for the difficulty in understanding the OER mechanism occurring on catalytic materials, such the ones described above, have been enunciated by Trasatti and coworkers: (1) the high activation energies of the intermediates formed during the OER pathways are sensitive to electrode surface properties; (2) the electrode surface undergoes modifications due to the high anode potentials required for the OER; and (3) the surface changes of the electrodes under a controlled potential cause the OER kinetic to modify over time.[71]

Unlike for heterogeneous catalysts, a detailed understanding of the OER mechanism has been established for homogeneous catalysts. Most homogeneous OER catalysts are well suited to in-situ studies, for instance using resonance Raman spectroscopy, EPR, XANES or EXAFS, which can establish relatively deep mechanistic insights that are not available for heterogeneous OER catalysts.[8,51] Despite this, their lifespan and stability are much lower than those of heterogeneous catalysts.

It has been found that the activity towards OER, or water oxidation reaction, follows the following order: Os > Ru > Ir > Pd > Rh > Pt > Au > Nb, where Os can hardly be called a catalyst as it presents very low stability. On the other hand, the stability follows the order: Pt > Rh > Nb > Ir > Au > Ru.[72] Numerous studies have been performed on ruthenium and iridium oxides as heterogeneous catalysts due to their high activities towards the OER. RuO_2 is the most active material for OER (except Os) but presents poor stability and can be further oxidized and decomposed into RuO_4.[73] On the other hand, IrO_2 is slightly less active but more stable,[74] with the result that it is the state-of-the-art electrocatalyst for OER in PEMWE electrolyzers.

Thermally prepared oxides are found to provide higher stability than electrochemically prepared ones through OER at around 2-3 orders of magnitude, but with lower activity (due to the loss of Ir-bound hydroxyl groups, the oxohydroxide phase).[75] Some authors have suggested that calcining Ir-based catalysts between 400 and 500°C establishes a good compromise between electrocatalytic activity and stability.[75b,c] The properties of electrochemically prepared catalysts (Ru or Ir oxides) strongly depend on: the metallic precursor, the voltammetry parameters used, the electrolyte or working temperature.[76] On the other hand, oxides prepared by thermal decomposition only depend on: the precursor, the gas atmosphere and more importantly, the calcination temperature.[77] Many authors have found that the higher the calcination temperature for catalyst preparation, the higher the stability of the oxide for OER applications, but the lower the activity. A relationship between the activity and crystallinity is then established, where more active catalysts are obtained for amorphous oxide phases (low calcination temperatures) than for crystalline ones (higher calcination temperatures).[78] It has been established that the M-OH species (i.e., with a high level of hydration) in amorphous oxide surfaces allows the presence of a considerable amount of Ir/Ru(III) besides Ir/Ru(IV). This generates O 2p hole states attributable to O^{-1} species that facilitate a nucleophilic attack by water molecules enhancing the OER activity.[79]

Given that Ir and Ru oxides have been established as high-performing catalysts for OER, most studies have focused on these particular catalysts. It is of great importance to increase their long-term stability and decrease the noble metal content, by at least one order of magnitude (typical anode loadings range between 1.5 and 3 mg·cm^{-2} IrO$_2$ microparticles in present PEMWE anodes).[38] One approach to achieve the latter goal is to use nanometric Ir or Ru materials, such as metal or metal oxide nanoparticles (NPs), nanostructures, or thin layers. Other approaches for both goals involve mixing these noble metals together (mixed Ir-Ru oxide catalysts) or with other non-noble metals.

Firstly, the most obvious approach to tune the performance of Ru and Ir oxides is to form a mixture of both. The addition of RuO$_2$ to IrO$_2$ oxides enhances its OER activity, while the oxidation of RuO$_2$ to RuO$_4$ is suppressed by the presence of IrO$_3$ generated during OER, which populates the t$_{2g}$ band of the mixed oxide, thus avoiding RuO$_4$ generation and Ru dissolution.[80] Many authors have found that mixing IrO$_2$ with small amounts of RuO$_2$ increases the activity of the former, and that doped RuO$_2$ with around 20% of IrO$_2$ decreases the activity of the oxide, but increases the stability of pure RuO$_2$.[81]

Other approaches in which Ru and Ir are mixed with non-noble and cheaper metals have been reported (e.g., Ni,[82] La,[83] Ce,[84] Ti,[85] Nb,[86] Ta,[87] Pb,[88] Sn,[89] Co,[90] Zn,[91] Pt [92] and Fe[93]). Most of these studies show that the addition of a nonprecious metal oxide primarily dilutes the active catalysts sites number (Ru or Ir) so that the mixed oxides present a similar catalytic activity to

pure IrO$_2$ or RuO$_2$, resulting in a reduction in noble metal content without scarifying the activity. Furthermore, the addition of inert oxides has a slight positive effect on active pure IrO$_2$ or RuO$_2$ materials against corrosion. Despite this, a maximum addition of non-noble oxide seems to be in the range of 50-60%, after which additional dilution reduces the activity of the catalyst because there are far fewer active sites.[94]
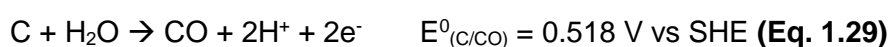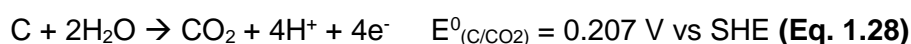
The previously mentioned optimization concepts for OER catalysts mostly rely on the optimization of synthesis conditions and the substitution of Ru or Ir by other metal cations. However, anion substitution also appears to be workable in this context, if the anion bound in the catalyst has a higher oxidation potential than the potentials applied during the OER. For example, doping IrO$_2$ with fluorine atoms (F$^-$) has a beneficial effect on OER performance, and in particular an improvement in activity by about 20% without affecting the stability of the catalyst.[95] F$^-$ ions have a smaller effective charge than O$^-$ ions, leading to a reduced electrostatic repulsion between oxygen surface intermediates and the fluorine-doped IrO$_2$ surface, resulting in stronger adsorption.[96] The approach of fluorine doping has also been extended to mixed oxides like Ir-Sn, Ir-Sn-Nb and Ru-Sn oxide, in which the noble metal content is appreciably reduced.[97]

Secondly, another path to optimize the performance of electrocatalysts concerns general nanostructuring, which includes controlling the size and shape of the catalyst particles. The preparation of small particles provides large surface to bulk ratios and reduces the amount of Ru and Ir catalysts by dispersion. Additionally, the high ratio between surface and volume makes nanoparticles (NPs) a very promising material for catalysis applications, such as OER. Properties and synthesis methods for nanomaterials are further discussed in **section III** of this chapter.

These nano-scaled catalysts can only reveal their full potential if they are dispersed on an appropriate support material. A catalyst support is by definition a solid material with a large surface area where the catalyst nanomaterials can be anchored. As the reactivity of heterogeneous catalysts occurs on the surface atoms, great efforts are made to maximize the surface area of a catalyst by nano-scaling them and distributing them over a support. Therefore, in the case of costly materials, such as noble metals, obtaining smaller particles is necessary. If the metal nanoparticles are well dispersed over this kind of catalyst support, the agglomeration of the catalyst can be inhibited, more homogenous distribution. This support material ideally have to combine: (1) high electrical conductivity, so that the support can act as a simpler path for electrons transfer; (2) a large surface area, which may be obtained through extended mesoporosity; (3) sufficient porosity and pore size to allow water to access the reaction sites and gases to be transported out of the electrode; (4) excellent stability to

corrosion under the highly corrosive acidic OER reaction conditions; (5) reasonable cost; and (6) either an inert state or participation in the catalytic reaction.[98]

For many electrocatalytic applications, carbon-based support materials such as nanotubes, nanofibers, carbon black and mesoporous carbon are widely used since they provide high electrical conductivity and a large surface area.[99] For example, the carbon support Vulcan® XC-72, which is common carbon support material, presents a conductivity of several $S \cdot cm^{-1}$ and a surface area of 252 $m^2 \cdot g^{-1}$.[99] Unfortunately, for PEMWE cells, carbon materials are not appropriated on the anode side, due to high corrosion conditions (Equations **28** and **29**).

$$C + 2H_2O \rightarrow CO_2 + 4H^+ + 4e^- \quad E^0_{(C/CO2)} = 0.207 \text{ V vs SHE } \textbf{(Eq. 1.28)}$$

$$C + H_2O \rightarrow CO + 2H^+ + 2e^- \quad E^0_{(C/CO)} = 0.518 \text{ V vs SHE } \textbf{(Eq. 1.29)}$$

Hence, carbon-based supports face sintering and detachment of the noble-metal nanoparticles (NPs),[100] which in turn results in depreciated electrocatalytic performance.[101] So far, very few carbon-based materials displaying stability under the required potential for the OER have been found.[102] On the contrary, metal oxides feature excellent corrosion resistance on top of exhibiting strong interactions with noble metal catalysts.[103]

Metal oxides are highly interesting materials in diverse applications due to their wide variety of electronic and chemical properties. Many metal oxide materials have two unique structural features: mixed cation valences, and an adjustable oxygen deficiency, which are the basis for creating and tuning many chemical and physical properties. Metal oxide materials span a wide range of electrical properties from those of wide band gap insulators to those of metals and superconductors. They also are found to be interesting materials because of their acid-base and redox properties, as the surface of metal oxides may terminate with M-OH, M-O-M, M = O, or M–(O-vacancy) functionalities.[104] Due to such properties, and their higher corrosion resistance compared to carbon, some metal oxides are used as catalyst supports for dispersed metal catalysts, but they also exhibit catalytic activity of their own.

Furthermore, when mixing two different metal oxides (the catalyst and the catalyst support), some properties are enhanced, for example the acidic or basic strength, the surface area and sometimes the activity strength of the catalyst in comparison with single metal catalysts. These improvements are produced by the synergistic effect of the various possible types of metal—oxygen chains that are found on the edges or corners between the two oxide materials. For example: the two different metal cations represented as M_A^{n+} and M_B^{m+} can be connected as M_A–O–M_B–O, M_A–O–M_A–O, or M_B–O–M_B–O by metal—oxygen chains. This different chain

order can give the binary material the mentioned synergistic effects.[104] The metal oxides most frequently used as catalyst supports for OER are based on: Ti, W, In, Sb, Nb and Sn, due to their good stability under PEM electrolyzer conditions:[105]

For example, Tungsten oxide (WO_3) has been used widely as a photo-catalyst for OER, as already demonstrated by Butler *et al.* in 1976.[106] Furthermore, tungsten oxide shares many attributes with TiO_2 in terms of chemical inertness and exceptional photo and chemical stability in acidic aqueous media over a relatively wide pH range (pH < 8).[107] This material is known to be able to form hydrogen tungsten bronze (H_xWO_3) compounds in acidic solution that are nonstoichiometric and electro-conductive, which can facilitate the dehydrogenation process.[108] Tungsten has a large number of stable oxidation states, which enable a variety of properties for many chemical and electrochemical applications, such as electrocatalyst support at the PEMFC cathode or PEMWE anode, or for methanol oxidation.[109]

Ti-based oxide is a cheap material that has been largely studied, especially for application in solar cells,[110] or for its photocatalytic properties.[111] Different morphologies have already been reported: nanoparticles, nanotubes and aerogels.[112] Examples include Wang *et al.* who obtained improved Ir utilization compared to the commercial Ir-black by deposition of metallic Ir(0) nanoparticles (NPs) on Ti_4O_7 without any thermal treatment.[113] Chen and co-workers also demonstrated enhanced OER activity in acid media when using Ti_4O_7 as an Ir catalyst support.[114] Siracusano *et al.* also obtained better performances when depositing IrO_2 electrocatalysts on Ti based suboxides.[115] It was found that by doping the catalyst supports, such as TiO_2, with polyvalent cations (such as Sb^{5+}, Nb^{5+} or Ta^{5+}), the electrical conductivity and specific surface area were enlarged. [112L,116] For example, Xia *et al.* studied $Nb_{0.05}Ti_{0.95}O_2$ as a potential non-carbon support for IrO_2 catalyst in PEMWE. They found that with 26% of IrO_2 loading, the provided mass-based activity at 1.6 vs. RHE and the catalyst stability were greater than that of unsupported IrO_2.[117] TiO_2-based materials employed as a catalyst support have also been widely used for PEMFC, on the cathode side for oxygen reduction, as the working conditions also corrode carbon supports.[118]

Besides Ti, W or In-based oxides, SnO_2-based materials are considered a promising alternative to carbon support materials for electrocatalysts.[119] The main applications of SnO_2 as a catalyst support, and its properties and synthesis methods, are further discussed in **section IV** of this manuscript.

Other OER catalysts based on non-noble transition metals constitute promising alternatives, mostly used in alkaline catalysis, because of their low-cost, reasonable activity and long-term stability under oxidation conditions.[120] Among these, cobalt oxide is one of the earliest oxides to be used as an OER catalyst in an alkaline medium due to its high stability and good catalytic

activity.[121] Numerous kinds of mixed-transition metal oxide catalysts present superior OER activity, such as: Co-Fe-O/rGO,[122] Ni-Co-O,[123] Ni-Fe-O,[124] along with various spinel-type oxides such as M-Mn-O, M-Co-O and M-Fe-O (where M corresponds to divalent metals).[125] The low price and performance advantages of Cu-based catalysts has made them a popular choice for non-noble metal OER catalysts.[126] Other metallic nitrides or phosphides, among others, have been also developed.[127]

II.3 Cell stacking

Individual PEM cells are limited by their own production capacity, so normally cells are stacked together in order to adjust the production capacity of the electrolyzer to the process requirements, and (as previously mentioned) for final cost reduction.[128]

The main challenges for the stacking are: (1) to establish a design that ensures the homogeneous distribution of liquid water over the entire surface area of anodic catalytic layers, (2) to efficiently collect the gas produced in view of a later separation from liquid, and (3) to establish a homogeneous distribution of current lines across the stack in order to avoid undesirable high degradation rates.

In order to avoid many of the described issues, current PEMWE electrolyzers require a period of activation. This activation period is devised to reach the thermal equilibrium of the cell, hydrate the clamped MEAs, and allow gases to find their way across current distributors. At the end of this period, the system operates more homogeneously.

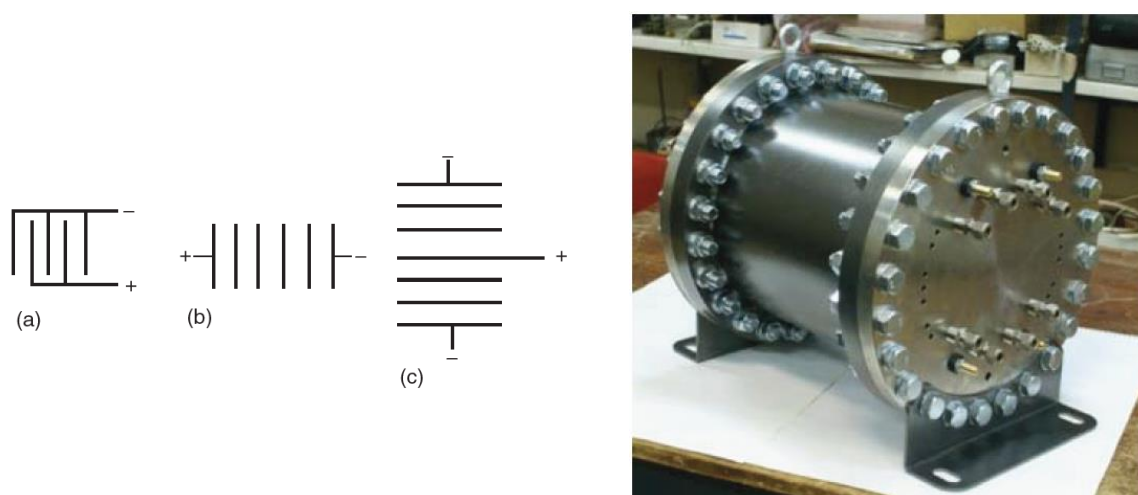The main stack connection designs are plotted in **Figure 1.16**.

Figure 1.16 Left: different series connections of electrolysis cells: (a) monopolar; (b) bipolar; (c) bipolar with central anode.[40] Right: photograph of a pressurized PEM water electrolysis bi-stack [129]

In PEMWE electrolyzer stacks, a polymer-based sealant is used to adjust compression forces between individual cells and delineate the volumes. They are also used to support the different pressure between the cells and the atmosphere, allowing operation at several bars. For safety reasons, a flow of pressurized insert gas across the pressurization vessels during operation its applied. This ensures the elimination of any traces of leaking hydrogen or oxygen that tend to accumulate inside vessels, causing damage to the system (especially on MEAs).

II.4 Cell performance

In PEM cells, water travels through spacers and flow disrupters (4' on **Figure 1.17**) and diffuses via porous current collectors (3' on **Figure 1.17**). Once water reaches the anode catalytic layer surface (2' on **Figure 1.17**) it is decomposed into oxygen, protons and electrons (Equation **21**). Then the oxygen is returned back out of the cell through the electrode surface, porous current collectors, and lastly flow disrupters. Protons migrate from the anode electrode surface to the cathode side through the proton-conducting membrane (1 on **Figure 1.17**). An external DC power supply moves the electrons from current collectors to the separator plates and to the cathode side; once they reach the cathode surface they recombine with protons, producing hydrogen (Equation **20**). Hydrogen then leaves the cell via the cathodic porous current collectors and flow disrupters (3 and 4 on **Figure 1.17**).
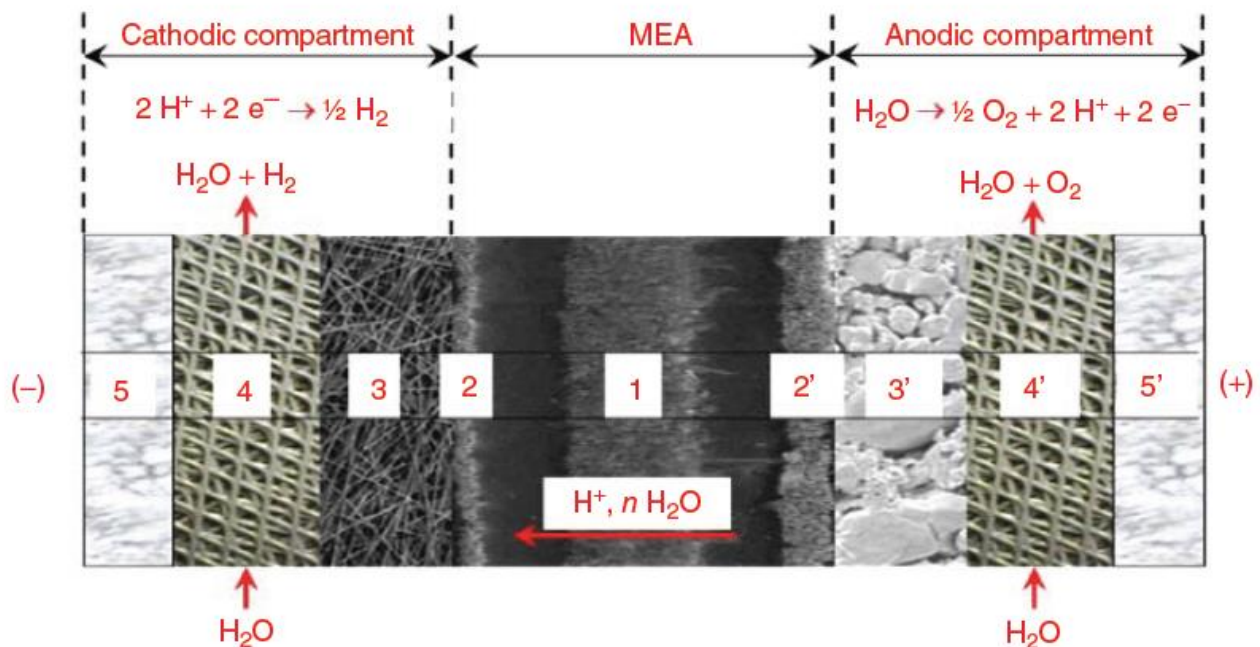

Figure 1.17 Cross section of a PEM water electrolysis cell: 1- membrane; 2-2' catalytic layers (CLs); 3-3' porous current collectors or gas diffusion layers; 4-4' spacers and flow disrupters; 5-5' end-plates. Image from Millet *et al.*: PEM Water Electrolysis, 2018.[130]

As discussed above (in **section II.2**), in conventional PEMWE cells, carbon-supported Pt nanoparticles are used as an electrocatalyst for the HER, and Ir (metal or oxide) is used for the OER. The best reported electrolysis efficiencies are around 80% at 1 mA/cm^2, using noble metal loading of about 0.5 mg·cm^{-2} Pt for the HER and about 1.5 -3 mg·cm^{-2} Ir for the OER.

As previously said, for an ideal PEMWE electrolyzer (not a theoretical cell, a real PEMWE cell with optimized cell components), the efficiency would be around 80% at 1 mA·cm^{-2}.

Ideal cells would also:

1. Produce high purity gas (4N of hydrogen at 50-60 bar).

2. Be scalable in size to several hundred cells without any efficiency or durability impact.

3. Maintain high-level efficiency without degradation over time.

Nevertheless, degradation and ageing mechanisms occur in the cells, resulting in a decrease in cell performance in time.

II.5 PEMWE Cell Ageing

PEMWE aging occurs during operation, and can severely impact performance. The main degradation causes are listed below: [130]

- Pt cathode catalysts enduring corrosion in open-circuit conditions

- Formation of H_2O_2 inside the membrane, causing deleterious effects on PFSA chains.

- H_2 and O_2 gases cross-over.

- Loss of catalytic sites because of corrosion in both anodes and cathodes.

- Local membrane swelling differences.

- Heterogeneous distributions of current lines.

- Oxidation at metal-metal interfaces.

The main consequences of degradation are:

- Chemical or physical alteration of the membrane, leading to either an increase in ionic resistivity or a chemical oxidation that leads to membrane thinning.

- Loss of energy and columbic efficiency, and gas purity

- Increasing safety issues and risk of irreversible breakdown.

II.5.1 Separator plate degradation

Separator or bipolar plates are usually bulk metallic cell components. They are mainly vulnerable to surface modification because of oxidation and corrosion as a result of contact with deionized water or active hydrogen. In the short term, this usually leads to increased electronic resistivity and contact resistances, and different or heterogeneous current distributions. In the longer term, it might also lead to mechanical failure.

II.5.2 Porous current collector degradation

Current collectors are used in PEMWE cells for the dual purpose of carrying electric current between bipolar plates and catalytic layers (CLs), and transporting fluids (reactant or reaction products) to/from catalyst layers. Made from titanium, they can lose some of their bulk mechanical properties due to hydrogen or hydrofluoric acid attack (formed by PFSA membrane degradation). However, metallic cell components in PEMWE cells are more sensitive to surface and interface degradation than to bulk degradation. Titanium cell components are prone to surface passivation which is responsible for large cell resistances. Therefore, as surface oxide layers are unfavorable to the optimal operation of PEMWE cells, surface treatments are required to avoid greater contact resistances. Many surface treatments have been described in the literature, including platinum sputtering and the formation of surface titanium nitrides/carbides.[131]

II.5.3 Polymer membrane degradation

Polymer membrane degradation or performance loss can be attributed to different causes:

1. **Reversible modification of membrane bulk ionic conductivity:**

   For optimal (efficient and durable) operation, a PEMWE cell requires the use of highly purified water. Water quality degradation can be caused by pollutants: I) biological contamination or II) metallic cations released by corrosion of the catalyst layers or metallic components. If the water used in the process does not have the appropriate level of purity, then impurities tend to accumulate within the membranes thus decreasing membrane performance. The process is reversible but cleaning is not an easy task and, in most cases, requires dismantling the cells. In commercial systems, this can be avoided by using online conductivity monitoring and ion-exchange resin beds that can adsorb foreign ions and other impurities and maintain the residual conductivity at appropriate levels.

2. **Irreversible chemical degradation and membrane thinning:**

PFSA materials used as solid polymer electrolyte membranes in PEMWE cells are subjected to chemical attack and corrosion. Polymer-side chains are prone to chemical corrosion via various mechanisms, reducing the concentration of membrane charge carriers and resulting in an increase in the membrane's electrical resistance. The most spectacular consequence of this degradation is a gradual and irreversible reduction in the membrane thickness. Normally, degradation and chemical corrosion result from the formation of hydrogen peroxide (H_2O_2), which attacks some weak chemical bonds (for example acid -COOH groups of the PFSA chains) leading to the formation of carbon dioxide and hydrofluoric acid. This hydrofluoric acid can have significant damaging effects, like the corrosion of titanium-based cell components, as mentioned above.

3. **Membrane perforation:**

A combination of various factors can accelerate membrane degradation. For example, the catalytic recombination of hydrogen and oxygen, can have quite dramatic consequences, and ultimately lead to membrane perforation.[132] Continuous monitoring of hydrogen and oxygen purity constitutes appropriate safety and prevention management.

II.5.4 Degradation of catalysts and catalyst layers

The degradation of catalysts and catalyst layers can be caused by multiple factors. On the one hand, catalyst layer degradation can originate in a heterogeneous current distribution on the PEMWE cell (causing faster aging of the catalytic layers), or in a structure modification of the layer. On the other hand, two main causes of catalyst degradation result in a performance loss for the PEMWE cell: loss of intrinsic activity and loss of active sites.

In all of these degradation mechanisms, the stability and performance of the PEMWE cells are negatively affected.

1. **Catalyst layer structure modification:**

As already discussed in this manuscript, catalytic layers are critical elements of PEMWE cells. Several factors, such as acidic and corrosive environments, thermal cycling, local drying, heterogeneous distribution of current lines, gas formation and accumulation, etc., are suspected to impact the structure and stability of catalytic layers, and hence their performance. For example, differential water swelling and heterogeneous gas formation induce a stress that can cause the formation of craters or cracking on the catalytic layer.

2. **Catalyst layer surface poisoning:**

This degradation mechanism is caused by surface poisoning by metallic cations in the other cell components, or by deposition of previously diluted metallic catalyst ions. This process is reversible by equilibration in an aqueous acidic solution; however, as for reversible membrane modification, cleaning is not an easy task.

3. **Loss of active sites:**

Catalyst degradation means that the population of the active sites tends to decrease during the PEMWE cell's operation. This decrease in the active site's population (represented on **Figure1.18**) can be related to: (a) catalyst corrosion or dissolution (in water or in the polymer electrolyte); (b) Ostwald ripening (dissolution of small particles inside bigger ones); (c) sintering of catalyst particles; or (d) detachment of catalyst particles due to the presence of bubbles (mechanical action). Therefore, it is very important to achieve an optimized morphology of the catalytic layer to remove gas bubbles as quickly as possible. The reduction of active sites can be easily detected by cyclic voltammetry, as shown on **Figure 1.19**, where the difference between the cyclic voltammograms at the begging of life (BoL) and the end of life (EoL) of the catalyst are plotted and compared (for both the anode and cathode).
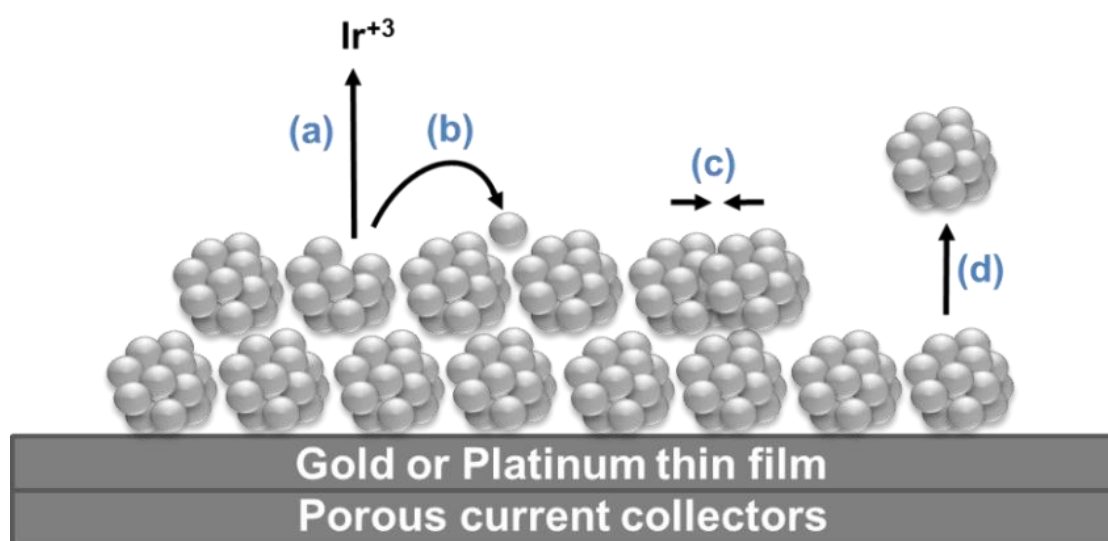

Figure 1.18 OER electrocatalysts degradation mechanisms: (a) dissolution of metal oxide catalyst, (b) Ostwald ripening process, (c) particle sintering, and (d) particle detachment (mechanical action).[133]
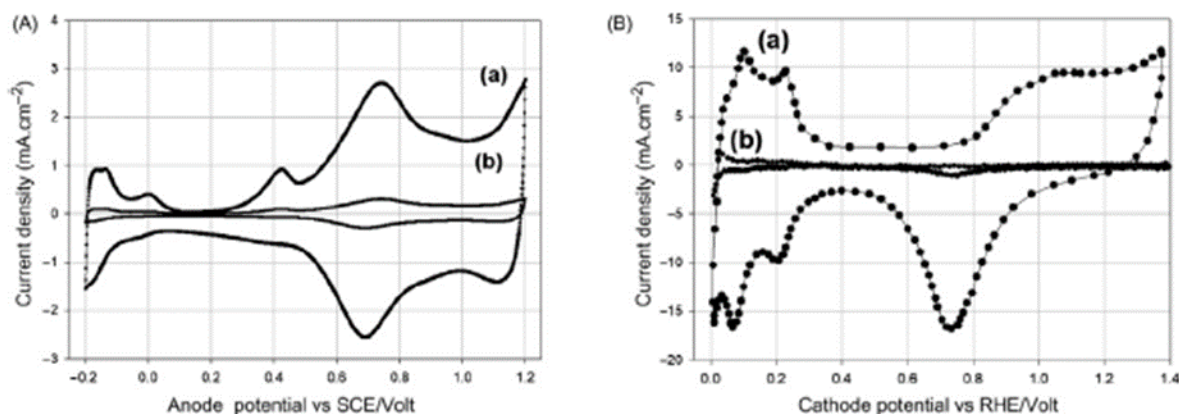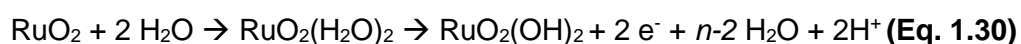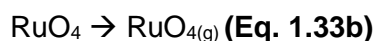
Figure 1.19. Left: A, CV curves measured on a PEMWE anode at (a) BoL and (b) EoL. Right: B, CV curves measured on C/Pt PEM cathodes at (a) BoL and (b) EoL.[130]

Most new insights into Ru and Ir dissolution come from recent ICP-MS studies.[75b-c,134] It has been found that the dissolution rate is two orders of magnitude higher for metallic catalysts than for metal oxides,[134a,e] with the overall stability order as follows: Ru << RuO_2 < Ir << IrO_2.

In recent years, significant progress has also been made in the mechanistic understanding of the degradation and dissolution of Ir and Ru during the OER, as well as other non-noble-based metal catalysts.[135] This higher dissolution of noble metal catalysts results from the participation of oxygen atoms from the crystal lattice in the OER, called the Lattice Oxygen Evolution Reaction (LOER) mechanism. This has been observed for IrO_2 and RuO_2 but not for Pt. The metals in which such LOER mechanisms take place suffer from more dissolution under the application of a constant current.
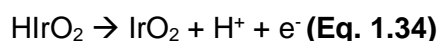
The low stability of ruthenium catalysts has generally been attributed to the OER mechanism (**Figure 1.20**), which involves the formation of RuO_4 species (Equation **32**) at potentials above 1.4 V.[136] In this mechanism, leaching of the RuO_4 intermediate from the electrode and further diffusion into the electrolyte results in a macroscopically electrode mass loss or dissolution that can be measured by ICP-MS techniques, Equation **33b**.

$$RuO_2 + 2\,H_2O \rightarrow RuO_2(H_2O)_2 \rightarrow RuO_2(OH)_2 + 2\,e^- + \textit{n-2}\,H_2O + 2H^+ \textbf{(Eq. 1.30)}$$

$$RuO_2(OH)_2 \rightarrow RuO_3(OH) + H^+ + e^- \textbf{(Eq. 1.31)}$$

$$RuO_3(OH) \rightarrow RuO_4 \textbf{(Eq. 1.32)}$$

$$RuO_4 + H_2O \rightarrow RuO_2(OH)_2 + \frac{1}{2} O_{2(g)} \text{ (Eq. 1.33a)}$$

$$RuO_4 \rightarrow RuO_{4(g)} \text{ (Eq. 1.33b)}$$

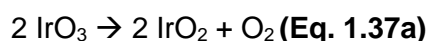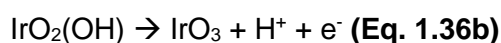$$RuO_4 + H_2O \rightarrow H_2RuO_5 \rightarrow RuO_2(H_2O)_2 + O_2 \text{ (Eq. 1.33c)}$$

As seen on **Figure 1.20** and from the OER reactions presented above, the OER mechanism involves the formation of RuO_4, which can either be converted again into $RuO_2 \cdot (OH)_2$ species when reacting with water (starting the cycle again), or transformed into $RuO_{4(g)}$, causing electrode erosion and dissolution.[136a]

For iridium-based catalysts, different OER mechanisms are possible depending on catalysts properties. On the other hand, the OER mechanism in hydrous iridium oxide-based catalysts consists of three steps forming a closed circle, Equations **34-36**:[134b,c]

$$HIrO_2 \rightarrow IrO_2 + H^+ + e^- \text{ (Eq. 1.34)}$$

$$IrO_2 + H_2O \rightarrow IrO_2(OH) + H^+ + e^- \text{ (Eq. 1.35)}$$

$$2\ IrO_2(OH) \rightarrow 2\ HIrO_2 + O_2 \text{ (Eq. 1.36a)}$$

The main dissolution procedures for iridium catalysts are proposed for Ir(III) species, by formation of aquo-ions $[Ir(H_2O)_6]^{3+}$ or instable complexes such as $Ir(OH)_3$ from $HIrO_2$ species.[137] Despite this, oxidation of $HIrO_2$ to IrO_2 (Equation **34**) is very fast, explaining why iridium catalyst dissolution is much slower than that of ruthenium in OER catalysis.

If IrO_2 is proposed as the initial stage species, Ir(III) species is less prone to dissolution and, therefore, some corrosion is avoided. This is the case for thermally prepared oxides, which have been shown to be less active but more resistant to the OER, where the different initial stage species leads to a different OER mechanism (**Figure 1.20**):

$$IrO_2 + H_2O \rightarrow IrO_2(OH) + H^+ + e^- \text{ (Eq. 1.35)}$$

$$IrO_2(OH) \rightarrow IrO_3 + H^+ + e^- \text{ (Eq. 1.36b)}$$

$$2\ IrO_3 \rightarrow 2\ IrO_2 + O_2 \text{ (Eq. 1.37a)}$$

However, recent studies have revealed the possible degradation of IrO_3 species into soluble IrO_4^- (Equation **37b**) at potentials over 1.6 V in parallel with a reduction to IrO_2 initial stage species and oxygen (Equation **37a**).[138]
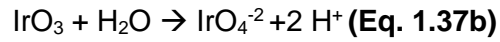
$$IrO_3 + H_2O \rightarrow IrO_4^{-2} + 2\ H^+ \textbf{ (Eq. 1.37b)}$$

Figure 1.19 plots both OER and degradation mechanisms for Ru and Ir based catalysts.
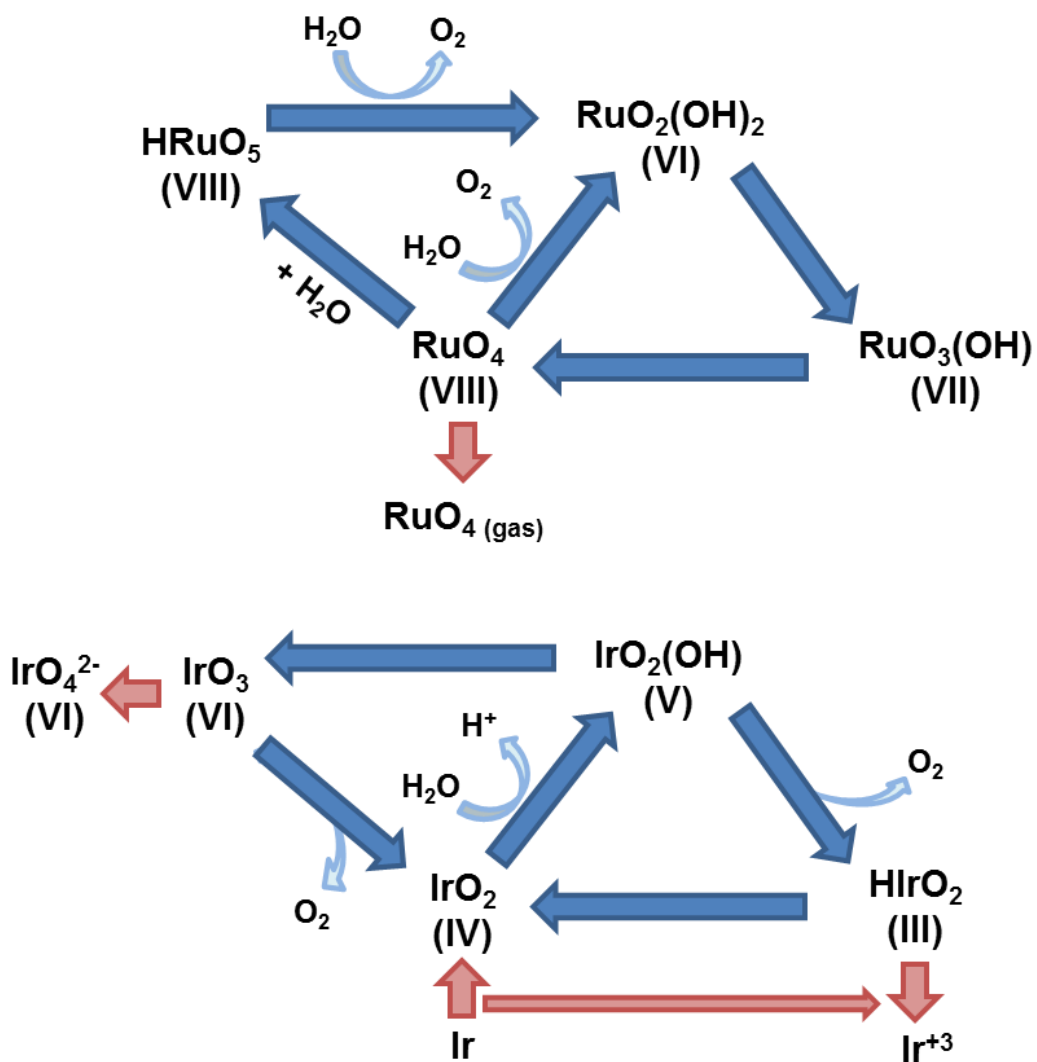
As mentioned above, the structure of Ir and Ru oxide catalysts can be modified when a metal oxide support is incorporated due to metal-metal oxide support interactions (MMOSI).[79c] By supporting catalyst NPs on catalyst supports (such as TiO_2, WO_3, SnO_2, etc.), an increase is observed in both catalyst utilization, and more important, stability. These catalyst and support interactions decrease the d-electron vacancy of catalysts due to interfacial electron charge donations from the catalyst to the support, suppressing the growth of the oxidation state that leads to dissolution, (Ir(VI) or Ru(VIII)).[139]

III Nanomaterials

A material is considered to be a nanomaterial when it measures between 1 and 100 nm in at least one dimension. Different nanomaterials can be classified depending on their dimensions (**Figure 1.21**). Nanomaterials whose dimensions are all measured within the nanoscale are called zero-dimensional, e.g., nanoparticles (NPs). If only one dimension is outside the nano-scale they are called one-dimensional, e.g., nanotubes, nanorods and nanofilaments. Finally, nanomaterials that have two dimensions outside the nanoscale are two-dimensional, e.g., nanofilms and nanolayers. If all dimensions exceed the nanoscale (three-dimensional), a material cannot be called a nanomaterial and is considered a bulk material. For information, nanotextured materials also exist, which exceed the nanoscale in all three dimensions, but either present nanoscaled structures on their surface or are made of nanomaterials. Examples are aerogels, fibers, columns and cones.
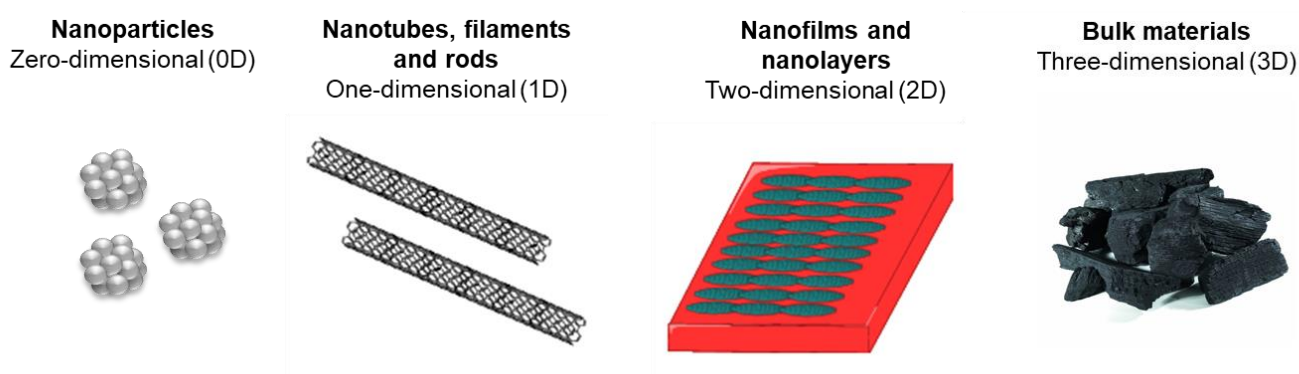

Nanoparticles
Zero-dimensional (0D)

Nanotubes, filaments and rods
One-dimensional (1D)

Nanofilms and nanolayers
Two-dimensional (2D)

Bulk materials
Three-dimensional (3D)

Figure 1.21 Different type of nanomaterials: 0D (zero-dimensional) nanoparticles; 1D (one-dimensional) nanotubes, filaments and rods; 2D (two-dimensional) films and layers; 3D (three-dimensional) bulk materials.

Nanomaterials are crystalline or amorphous and can be constituted by organic or inorganic materials. They are the link between bulk materials and atomic or molecular structures (**Figure 1.22**), presenting different physical and chemical properties. For example, due to their high surface-to-volume ratio, metal nanoparticles have many applications such as biological and chemical sensor fabrication,[140] information storage[141] and especially catalysis applications.[142]
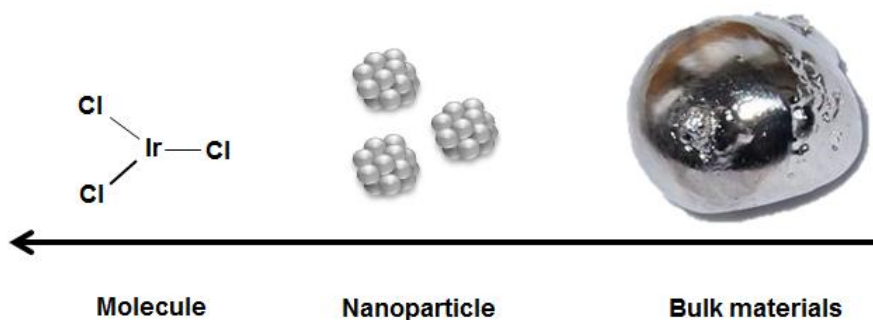
Figure 1.22 Comparison between bulk materials, nanoparticles and molecular complexes.

In catalysis, metal NPs are at the frontier between homogeneous and heterogeneous catalysts, as they display properties from both families.[143] In homogeneous catalysis, the reactants and the catalyst are in the same phase, ensuring good interaction but a difficult recovery of the catalytic species. Each entity acts as an active site, allowing the understanding of the mechanistic pathways and providing high activities and stabilities. On the other hand, heterogeneous catalysts are in a different phase to the reactants (normally rugged solid catalysts vs. gas/solution reactants) permitting easy recovery and recycling of the catalysts. They require high surface areas to achieve high populations of active sites, and different active sites can act in different ways, which complicates the mechanistic understanding and the selectivity of the catalytic reaction. NPs can present different selectivity by tuning their surface composition, and can be supported on solid supports to be recycled and reused, as mentioned above for the HER and OER catalysts in PEMWE electrolyzers (**section II.2.4** of this chapter).

III.1 Nanomaterials properties

Nanomaterials properties (e.g., physical, electrical, optical or mechanical) are significantly different from those of their bulk counterparts. These properties are due to the material size and the large percentage of their atoms in grain boundary environments. The most common properties of nanomaterials are quantum confinement and surface-to-volume ratio:[144]

- **Surface-to-volume ratio:**

    When a material is reduced to the nanoscale, the ratio between the total surface and the total volume of the material increases (**Figure 1.23**), modifying its properties (e.g., thermodynamic, electronic, spectroscopic, electromagnetic and chemical properties). Since in catalysis the reactive part of the material is the surface, nanomaterials are more reactive
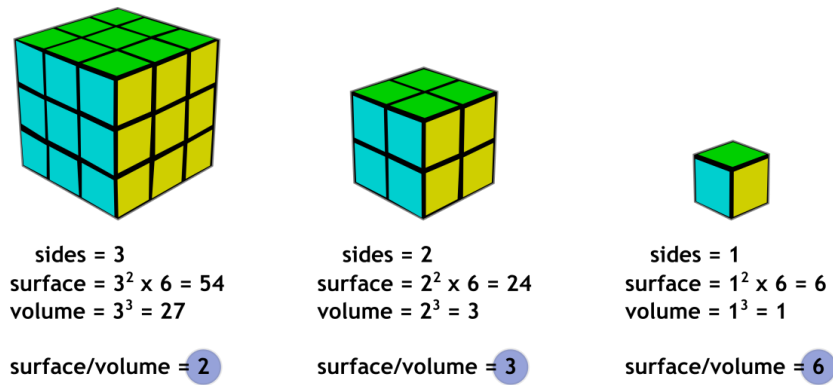
Figure 1.23 Reduction of a 3^3 cube into cubes of 1^3 and the effect on the total surface-volume ratio.[145]

- **Quantum confinement:**

  Quantum confinement corresponds to a change in electronic and optical properties when the material sample is sufficiently small - typically 10 nm or less. The bandgap increases as the size of the nanostructure decreases. Specifically, this phenomenon results from electrons and holes being squeezed into a dimension that approaches a critical quantum measurement, called the exciton Bohr radius.[144]

III.2 Nanomaterials synthesis methods

Metal-based nanomaterials are clusters formed by a few tens to several thousands of metal atoms. They can be obtained by several preparation methods, with different advantages and disadvantages regarding key parameters such as size, shape, dispersion, surface control and oxidation state. These methodologies are classified into two main categories, **Figure 1.24**:[146]

- **Physical methods (top-down):**
  This consists in the subdivision of large metallic structures using physical or mechanical energy. The main drawback is the lack of control of the final structure, comprising irregular nanocrystals with no uniformity in size or shape. This approach comprises well-developed techniques (e.g., ball milling) which are dominant in microfabrication.

- **Chemical methods (bottom-up):**
  This is based on the growth or nucleation of small units such as atoms, molecules or clusters, by means of chemical reactions. This approach is less effective in terms of quantitative production than the previous one, but it allows extensive control of the reaction conditions, allowing the size, surface and dispersion of the particles to be tuned; in other words, it results in better defined nanomaterials.

It is very difficult, even impossible, to obtain the same material with similar properties following these two different routes.

Figure 1.24 Bottom-up and top-down approaches to nanomaterials construction.

Most of the strategies used for the synthesis of metal-based nanomaterials are derived from the second category, because of easier size and dispersion control. The main used methods are:

a) Chemical reduction of transition-metal salts:

This is the most commonly used method for NP preparation, and consists in the chemical reduction of a metal salt precursor (by a reducing agent, such as: hydrogen, carbon monoxide, alcohols, hydrazine or borohydrides) to its zero-valent single atom. The naked atoms then start nucleating by agglomerating with other metallic atoms until they form stable nuclei. There are advantages of using such precursor salts, such as their high solubility in water and many organic solvents, and the reproducible formation of monodispersed particles and clusters. However, the main disadvantage of this procedure is the counter-ions that remain, both from the precursor and the reducing agent, which are difficult to eliminate and can end up coordinated on the surface of the particles, modifying the sought-after reactivity or selectivity. [147]
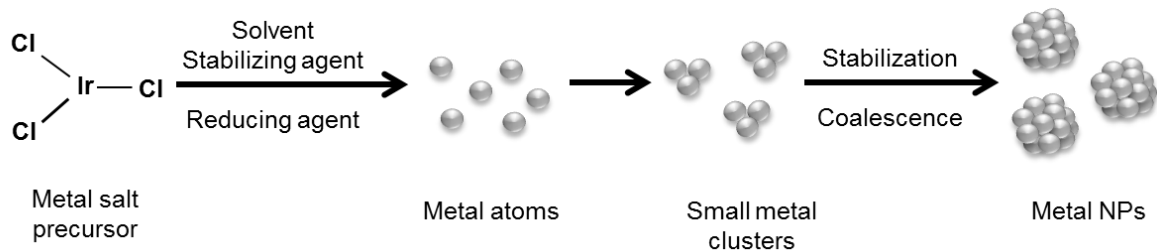
Figure 1.25 Synthesis of metal nanoparticles by reduction of a transition metal salt precursor.

b) Thermal, photochemical or sonochemical decomposition:

Using this method, temperature, light or ultrasound radiations are used to foster the vaporization of a metal precursor complex. This methodology can be used to obtain large amounts of particles, or other shaped materials, without using other chemical reagents, but with poor control of the size and shape of the obtained material.

c) Chemical vapor deposition (CVD):

This methodology consists in the vaporization of metal precursors and their decomposition onto a surface to form different shaped nanomaterials. This reaction requires an activation energy to vaporize the precursor, which can be provided thermally, by plasma or by laser. Thus, the precursors in the gas phase react with a substrate (surface) where their atoms are deposited.[148]

d) Electrochemical reduction:

This method consists in the oxidative dissolution of a sacrificial bulk metal anode. The leached metal ions then migrate to the cathode where they are reduced to zero-valent metal atoms that nucleate and grow to yield many different shaped metal nanomaterials. Its advantage is that there are no remaining secondary products from the reducing agents or salts, and the colloidal product is easy to isolate as a precipitate or deposit onto the electrode (electrodeposition).[149]

e) Sol-gel process:

As seen on **Figure 1.26**, many different metal and metal oxide-based nanomaterials can be produced by the sol-gel method. The term sol-gel is the abbreviation for "solution-gelation". After hydrolysis, condensation and polymerization reactions of an initial metal precursor, in acidic or basic medium, a dispersion of oligomers of few nanometers is formed (a sol). One option is to employ this sol to directly obtain different materials such as: ceramic fibers or uniform NPs. Over time, the sol will evolve into a gel. A gel consists in a three-dimensional network of organized particles in which the

71

solvent is trapped. It is important for the initial colloidal suspension formation that the nucleation rate of the generated oligomers is greater than the growing rate of the colloids. Without this condition, a precipitation of big clusters or particles will be observed on the solution, and no gelation will be obtained. Once the sol is gelled, xerogels or aerogels can be obtained after solvent elimination (drying for xerogels and extraction for aerogels).

The other option is to obtain dense films by coating materials with the initial metal precursor solution, before sol-gel reactions start taking place.
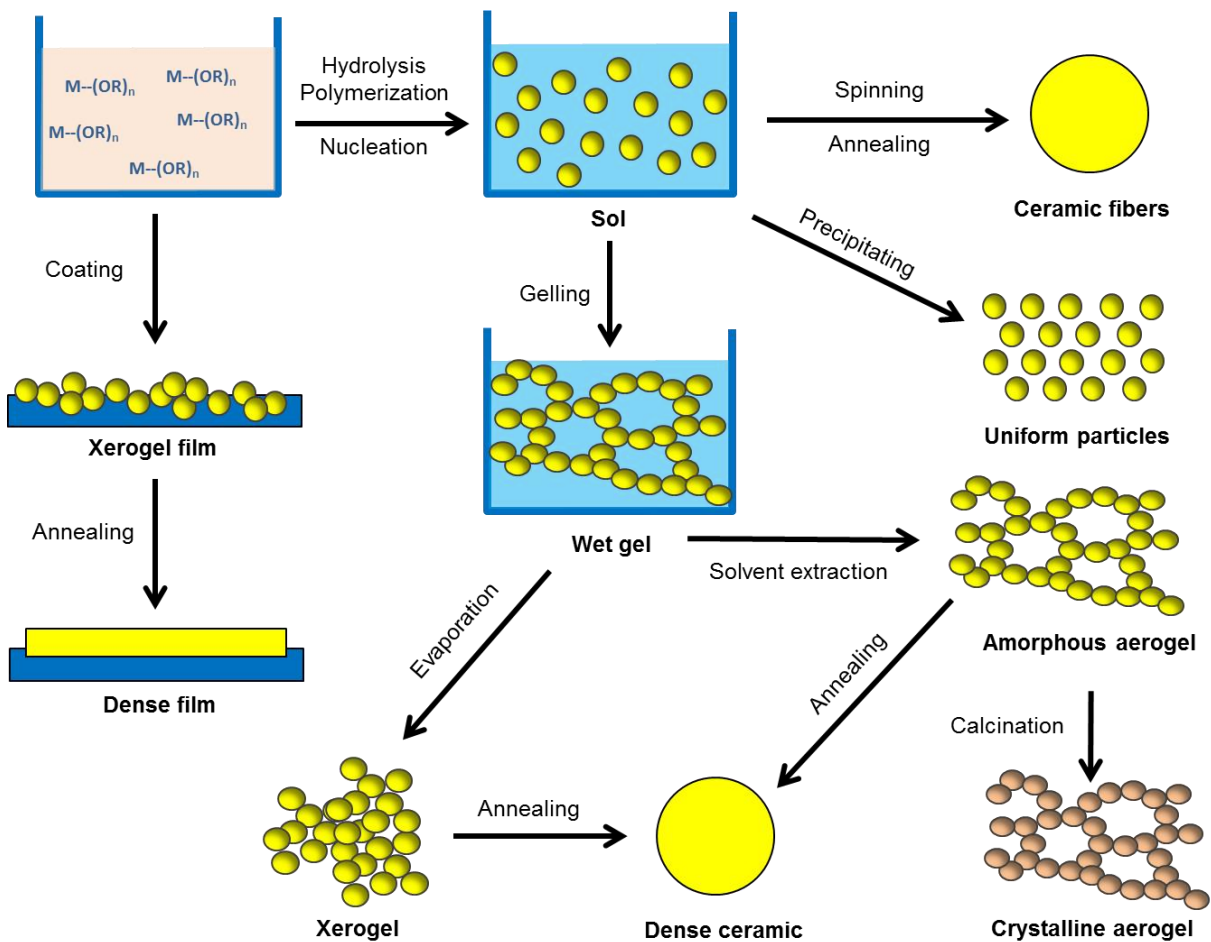

Figure 1.26 Representation of the sol-gel process and technologies and their products.

Among all the possible materials or nanomaterials that can be produced by the sol-gel process, aerogels are especially interesting. Aerogels are composed by a network of interconnected nano-sized particles, allowing large air-filled cavities inside the material. They exhibit many, and sometimes unusual, properties of interest for chemistry and other applications, such as:[150]

- High specific surface areas.

- Very high porosities, which means low-density materials.

- Low thermal conductivity.

- Good structural stability during heat treatment at high temperatures.

- They can easily be crystallized if calcined at high temperatures.

All of these properties of aerogels make them an ideal material as a catalyst support for catalysis applications, such as OER or HER (as previously mentioned).

Figure 1.27 Image of a graphene aerogel illustrating the low density of the material.[151]

IV SnO$_2$ as catalysts supports for PEMWE cells

IV.1 SnO$_2$ presentation and properties

Tin oxide is an inorganic compound that exists in two main forms: stannic oxide (SnO$_2$) and stannous oxide (SnO). The possible formation of these two oxides shows the double valence property of tin, with oxidation states (IV) and (II), respectively.

SnO presents a less common litharge structure, while stannic oxide possesses a rutile structure in which cassiterite is the main SnO$_2$ mineral found in nature. SnO$_2$ is the most abundant form of tin oxide, exhibiting two different crystalline phases; rutile or orthorhombical structures. At atmospheric pressure and at a temperature of 25 °C, this material crystallizes into the rutile type structure with a tetragonal crystalline system, (**Figure 1.28**), where Sn atoms present a coordination number of 6, and O atoms 3.[152] In contrast, the orthorhombical structure is stable and formed at high pressures.
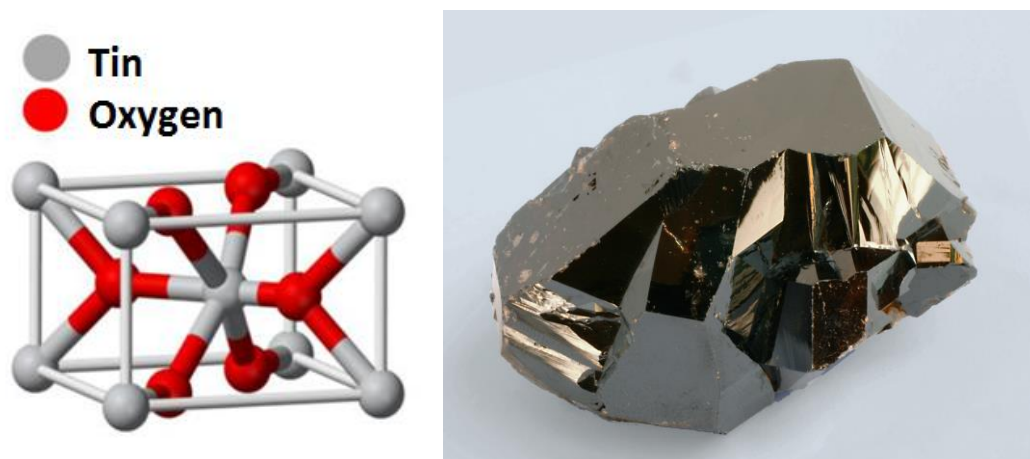

Figure 1.28 Left: rutile structure of SnO$_2$, where grey atoms correspond to tin (Sn) and red atoms correspond to oxygen (O). Right: the Cassiterite mineral from the Musée de minéralogie MINES ParisTech.[153]

Tin oxide is a chemically inert, mechanically hard, thermodynamically stable, white, diamagnetic and amphoteric solid oxide material. It is considered as an n-type semiconductor, with a wide band gap of 3.6 eV.[154] The electrical resistivity of this compound can vary depending on the temperature, the stoichiometry and the morphology of the oxide.

Tin dioxide properties can be tailored by extrinsic doping atoms. For example, doping the material with different atoms, such as fluorine (F$^-$) or with hypervalent cations (Sb(V), Ta(V), Nb(V), V(V) or Mo(V)) can increase the electronic conductivity of SnO$_2$, and induce a high n-type conductivity.[155] On the one hand, fluorine-doping replaces O$_2^-$ with F$^-$ anions, giving free electrons to the solid matrix, which significantly increases the conductivity. On the other hand,

when doping with cations (replacement of Sn^{4+}) two scenarios are possible: (1) if the cation presents greater valence than Sn(IV), as for example M^{5+}, free electrons will be released for charge compensation, increasing the material conductivity; (2) when the doping cation presents lower valence than Sn(IV), the compound will present an oxygen deficiency ($VO^{\circ\circ}$), which will have a negative effect on the bulk conductivity of the material. In addition, when doping, for example, with niobium[156] or vanadium,[155] the SnO_2 morphology is modified, as these elements inhibit the growth of primary particles, resulting in larger specific surface areas.

Due to its properties, SnO_2 is used for many applications:

- **Transparent conductive oxide (TCO):**

  Like In_2O_3 and ZnO, pure SnO_2 combines significant transparency in the visible part of the electromagnetic spectrum with low electrical resistance. These properties make it suitable for many applications for optoelectronic devices, such as: solar cell electrodes, light-emitting diodes, thin film transistors, active glazing, etc.
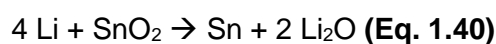
  The combination of high electronic conductivity and optical transparency of the oxide is due to a specific characteristic in its band structure, i.e. (1) an optical gap of 3.6 eV. (absorption below 344 nm), that prevents any charge transfer between bands in the visible domain and (2) the presence of charge carriers, induced by intrinsic and/or extrinsic defects, injecting electrons into the conduction band. The presence of impurities results in the introduction of energy levels in the bandgap, which facilitates different electron transfer to the conduction band. However, such transitions could occur in the visible domain.[157] For this type of application, SnO_2 is generally doped with antimony (ATO, antimony tin oxide) or fluorine (FTO, fluorine tin oxide).

- **Electrode material for lithium-ion batteries:**

  The operation of lithium-ion batteries is based on the reversible exchange of ions between a positive electrode and a negative electrode. The first Li-ion batteries on the market consisted of a negative graphite electrode. The structure of graphite allows lithium to be stored between its hexagonal sheets up to a stoichiometry of LiC_6. However, due to the formation of passivation layers during the initial charge, the graphite used in commercially manufactured lithium cells results in reversible capacities significantly lower than the theoretical amount.

  Electrodes composed of SnO_2 offer specific capacities much higher than those made from carbon graphite (993 vs 372 mA·h·g^{-1}, respectively), and reach a higher potential than Li, which contributes to a greater safety margin against the formation of metallic lithium dendrites.[158]

Reactions (**1.40**) and (**1.41**) represent the first steps of the electrochemical reaction of lithium with tin oxide. In the first reaction, the tin oxide partially irreversibly converts into tin enclosed into a Li_2O matrix. The tin particles can then form different alloys with lithium up to the theoretical limit of $Li_{4.4}Sn$ by following equation **1.41**. This last reversible mechanism drives the electrochemical activity and allows the battery to operate.[159]

$$4 \; Li + SnO_2 \rightarrow Sn + 2 \; Li_2O \; \textbf{(Eq. 1.40)}$$

$$x \; Li + Sn \leftrightarrow SnLi_x \; \text{where: } 0 \leq x \leq 4.4 \; \textbf{(Eq. 1.41)}$$

It has been found that using SnO rather than SnO_2 reduces the loss of Li ions during the first step of the electrochemical reactions (Equation **1.40**), Equation **1.42**:

$$2 \; Li + SnO \rightarrow Sn + Li_2O \; \textbf{(Eq. 1.42)}$$
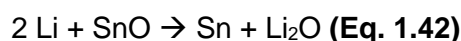
Tin-based materials including oxides, sulfides, intermetallic alloys, etc. have attracted a great deal of attention and been intensively studied in the past decades. However, only a few articles compare their performances in the same electrochemical conditions, with a significant lack of data on Sn(II) oxide. The members of our group have been working with SnO-based materials as negative electrodes for lithium-ion batteries.[159]

- **Gas sensors:**

Gas sensors consist in materials whose properties can be modified in contact with a gas, usually their electronic conductivity. The most frequently used materials for this type of application are ZnO and SnO_2.[160] Tin oxide has shown good detection efficiency for gases such as CO, H_2, NO_2, etc.

Doping gas sensors with other elements can improve sensor sensitivity for some gases. For example, the deposition of Pd or Pt particles over a metal oxide surface improves the sensitivity and detection of CO and CH_4.[161]

- **Glass coatings:**

SnO_2 coatings can be prepared using a chemical vapor deposition technique that employs $SnCl_4$ or organotin trihalides. This technique is used to coat glass bottles with a thin layer of SnO_2 (<0.1 µm), which facilitates the subsequent adhesion of, e.g., polyethylene, as a protective polymer coating.

Thicker layers doped with Sb or F ions conduct electricity and are used in electroluminescent devices.[162]

- **Polishing**

SnO_2 can be used as a polishing powder, sometimes in mixtures with lead oxide, for jewelry, marble or silver.[163]

- **Ceramic glazes:**

Tin oxide has also long been used as an opacifier and as a white pigment in ceramic glazes.[164] Mixing SnO_2 with other metallic oxides obtains other colors such as: V_2O_5 (yellow), Cr_2O_3 (pink), and Sb_2O_5 (grey blue). [165] Tin oxide is commonly used in glazes for earthenware, sanitary ware and wall tiles. Tin oxide remains in suspension in a vitreous matrix of the fired glazes; due to its high refractive index, light is scattered, which increases the opacity of the glaze. The higher the firing temperature, the higher the degree of dissolution of the tin oxide powder in the firing glaze. [166] The solubility of tin oxide in glaze melts is generally low, but can be increased by adding other oxides such as Na_2O, K_2O and B_2O_3, or reduced by adding CaO, BaO, ZnO, Al_2O_3.[167]

- **Catalysis applications:**

Among the different metal oxides, SnO_2 is found to be an active and versatile catalytic material due to the higher oxidation state 4+ of Sn and its lower ionic character.[49]

SnO_2-based materials have been widely used as catalysts in various processes of interest in the chemical industry, for example: condensation,[168] acetylation, ketalization and carbonylation reactions,[169] catalytic hydrogenation reactions,[170] catalytic oxidation of CO, hydrocarbons and alcohols,[171] and as catalysts for the Oxygen Reduction Reaction in PEM-FC.[171c] Due to its semiconductor behavior, this type of material is also used as a photo-catalyst for degradation of organic compounds.[172]

Mixing SnO_2 with other metal oxides (composite oxides) demonstrates excellent and improved catalytic behaviors compared to those of individual metal oxides. [49] For example, ZnO-SnO_2 composites present a highly active and selective character for carbonylation reactions.[173] WO_3-SnO_2 composites have been used for many organic acid-catalyzed reactions such as: cyclization, ethylation, hydration, carbonylation, isomerization, etc.[49] Apart from the above-mentioned applications of SnO_2 as a catalyst or co-catalyst, it can also be used as a catalyst support as an alternative to carbon materials.

IV.2 SnO₂-based materials as catalyst supports

Tin oxide (SnO_2) has been used as a potential catalyst support in catalysis by inserting or depositing other M/SnO_2 metal particles (where M = Ca, Si, WO_3, MoO_3, Pd, Ru, Ir, among others). The strong interactions between catalysts and the tin oxide supports (metal-metal oxide support interactions, MMOSI), and the high stability and inertness of this kind of material in many catalysis environments and conditions make this oxide a promising material for such applications.

For example, CaO has been revealed as a promising solid base catalyst for the synthesis of biodiesel at mild temperatures and at atmospheric pressure. However, CaO undergoes particle dissolution of the solid in the reaction medium. By supporting calcium oxide nano-catalysts on tin oxide materials, both catalytic activity and stability were found to improve.[174] Palladium nanoparticles supported onto tin oxide aerogels have demonstrated higher performances as catalysts in Suzuki coupling reactions than non-supported ones.[175] Another example is the deposition of WO_3 on SnO_2 for transesterification reactions, where the WO_3 deposited onto SnO_2 shows better catalytic activity than for single WO_3 catalysts.[176] Other organic reactions such as etherification, esterification and benzylation of many organic compounds are catalyzed with higher performance and durability by Heteropoly acids (HPAs) supported onto tin oxide materials.[49]

In recent years, doped tin oxide materials have attracted significant attention from the research community for their increased electronic conductivity,[177] resulting in an improvement of the electrocatalytic activity associated with charge transfer processes. As the intrinsic conductivity of SnO_2 is very low, doping is a prerequisite for forming a degenerate semi-conductor and enables sufficient electronic conductivity for practical use. As a result, many other catalysis applications featuring doped tin oxide as a catalyst support have been reported. For example, fluorine-doped tin oxide supports (FTO) have been tested as catalyst supports for glycerol conversion to 1,2-propanediol using many different metal catalysts;[178] and antimony-doped tin oxide (ATO) nanofibers have been used as catalyst support structures for the methanol oxidation reaction in direct methanol fuel cells, ethanol oxidation and oxygen reduction reactions (ORR) in PEM-FC.[179]

Despite the fact that many other metal oxides have been used as catalyst supports for OER (such as Ti, W, In, Sb, Nb, as seen in **section II.2.4**), doped tin oxide materials are considered promising materials due to their high stability and conductivity. Significant efforts have been made to optimize the morphology, conductivity and corrosion resistance of tin oxide-based supports by doping: antimony-doped tin oxide (ATO),[180] indium tin oxide (ITO),[119a,181] fluorine tin oxide (FTO),[184g] tantalum tin oxide (TaTO),[182] etc. Many of these doped materials have been

coated with scarce noble metals, significantly reducing the use of metal. Doped tin oxides have also been widely used as a catalyst support, as for example in oxygen reduction reactions (ORR) for PEM-FC cathodes, to reduce the Pt catalyst loading.[183]

Because of its high conductivity, over the past five years, antimony-doped tin oxide (ATO) has received significant attention as an anodic catalyst support material in OER applications, ahead of other doped tin oxide materials.[180b-d,184] ATO-supported iridium electrocatalysts have been found to be highly effective OER catalysts; they can exhibit high OER mass-specific activity, while simultaneously using much less iridium than that required for unsupported catalysts. NPs of different iridium phases (Ir metal, partially-oxidized oxohydroxides (IrO_x) or rutile structure iridium oxide (IrO_2)) have been deposited onto ATO supports by different methods: Adams fusion,[184h,o] the colloidal method,[184a] hydrothermal synthesis,[184g] *in situ* synthesis and deposition over ATO supports by chemical reduction,[184c,184j,192] or using the solvothermal technique for the deposition of IrO_2 onto macroporous ATO supports.[184d] Most important studies on deposited Ir-based nanocatalysts on ATO supports are shown on **Table 1.3**.

One of the main advantages of using tin oxide-based supports is the metal/metal oxide support interactions (MMOSI) between the noble metal catalyst and the doped tin oxide.[185] As explained above regarding titanium-based supports, such interactions result in an enhancement of the intrinsic OER activity of the catalyst. Strasser and co-workers demonstrated the influence of this kind of interaction by developing a highly active catalyst consisting in $IrNiO_x$ supported on mesoporous ATO.[119,184d-e] Similar MMOSI interactions, together with a high catalyst dispersion, were also a key factor identified in the highest OER activity catalyst (1100 $A \cdot g_{Ir}^{-1}$ at 80ºC, at 1.45 V_{RHE}), reported in the literature until the date by Hartig-Weiss *et al.*.[184f] In their work, authors supported controlled size Iridium oxide NPs over a high surface area and highly conductive ATO materials. This enhanced activity allows a significant reduction (ca. 75-fold) in the precious metal catalyst loading if this catalyst is implemented in the anode of a PEMWE. R. Schlögl *et al.*, [184b] used the hydrothermal method to deposit an Ir oxohydroxide phase catalyst over a high surface area ATO NPs (154 $m^2 \cdot g^{-1}$). Interactions between the oxohydroxide phase of the Ir catalyst and ATO support enhanced the activity (up to 1300 $A \cdot g_{Ir}^{-1}$ at 25ºC, at 1.58 V_{RHE}) and stability through the OER compared to the non-supported catalysts.

Table 1.3. Comparison of catalytic performance, on RDE configuration, between most important studies on deposited Ir-based nanocatalysts on ATO supports

Reference	Group	Deposition method	ATO morphology	Dominant Ir phases	Ir loading (wt. %)	OER mass activity (A·g^{-1}) (25°C)
101d	F. Maillard	Polyol	ATO aerogels	Oxohydroxide IrO_x	17 %	100 A·g^{-1} 1.51 V_{RHE}
180c	X. Wang	Adams' fusion	ATO nanowires	Rutile IrO_2	43 %	240 A·g^{-1} 1.55 V_{RHE}
180d	D. Fattakhova-Rohlfing	Solvothermal	ATO microparticles	Rutile IrO_2	25 %	63 A·g^{-1} 1.53 V_{RHE}
182	H. Uchida	Colloidal	Fused-aggregate	Amorphous IrO_2	11 %	22 A·g^{-1} 1.55 V_{RHE}
184a	Q. Wu	Colloidal	Mesoporous ATO particles	Rutile IrO_2	26 %	240 A·g^{-1} 1.55 V_{RHE}
184b	R. Schlögl	MW-assisted hydrothermal	ATO nanoparticles	Oxohydroxide IrO_x	33 %	1300 A·g^{-1} 1.58 V_{RHE}
184e	P. Strasser	Polyol	Mesoporous ATO particles	Ir metal	20 %	90 A·g^{-1} 1.51 V_{RHE}
184f	A. Hartig-Weiss	Polyol synthesis	ATO particles	Ir metal with Oxohydroxide IrO_x shell	11 %	185 A·g^{-1} 1.50 V_{RHE} Also at (80°C) 1100 A·g^{-1} 1.45 V_{RHE}
184g	S. Cherevko	Hydrothermal	ATO particles	Oxohydroxide IrO_x	22 %	41.3 A·g^{-1} 1.55 V_{RHE}
184i	R. Mohamed	OMCD	ATO nanopowder	Rutile IrO_2	9 %	70 A·g^{-1} 1.52 V_{RHE}
192	A. Friedrich	Chemical reduction	ATO aerogels	Oxohydroxide IrO_x	30 %	95 A·g^{-1} 1.51 V_{RHE}

The main drawbacks of doped-tin oxides, especially all type of Sb-doped materials, is the dopant dissolution under OER and ORR conditions.

The stability of doped tin oxide-based materials used as a catalyst support for PEMWE cells has been discussed widely in the literature.[101c,186,187] Although these oxides are generally considered to be more stable than carbon, in harsh electrochemical conditions they also degrade. Similar to carbon, a corrosion of the tin-based oxide support may lead to a detachment of the catalyst. The most crucial issue is dopant leaching. Since the conductivity of tin-based oxides depends on the concentration of dopants, even a small decrease in their amount may lead to a significant increase in ohmic losses, along with a decrease in energy efficiency and catalytic performance. Moreover, the dissolution products of tin, dopant metals and catalyst detachment can end up in the membrane or on the counter electrode, causing a deterioration in their performance.

Geiger *et al.*,[186b] investigated the corrosion stability of tin oxide-based catalysts (ATO, ITO, and FTO) in acidic media under applied potentials (harsh electrochemical conditions), and showed that these materials possess a critical dissolution rate under certain potential. They found that ITO (In-doped) was the material with the fastest dopant dissolution rate between the potential limits -0.1 to 2.35 V, with the result that this support is not recommended for electrolysis applications. For ATO materials (Sb-doped), Sb and Sn are relatively stable within 0.36 to 1.1 V and -0.29 to 1.45 V respectively. This was also shown by Cognard *et al.*,[187b] where a preferential Sb dissolution in comparison with Sn was observed after accelerated stress tests (1.0 – 1.5 V_{RHE}). Fabbri and coworkers also reported a decrease in the Sb amount after potential cycling (0.05 – 1.6 V_{RHE}).[186a] Da Silva et al.,[184g] also studied the dopant elements dissolution, observing that it was especially critical for Sb (**Figure 1.29a**), which critically destabilize the IrO_x phase. Dubau *et al.*,[188] detected a major dissolution of the Sb doping agent compared with Nb atoms when operating in a real PEM-FC, although the ORR performance of Pt/ATO was greater than for Pt/NTO due to the lower conductivity of the latter. Therefore, according to many authors, the stabilization of the doping element is a key issue for ATO to be implemented in PEMWE anodes or PEM-FC cathodes.[186c] Finally, FTO materials (F-doped) showed a stability window from -0.34 to 2.7 V_{RHE} with no indication of any measurable dissolution between such limits. In contrast to other tin oxide-based materials, F anions replaces O ones instead of other metal cations, thus avoiding the formation of less stable oxides. Based on these studies, FTO demonstrates the best stability and is therefore considered as a good candidate for many electrochemistry applications, such as catalyst support for electrolysis cells. However, FTO shows the poorest intrinsic conductivity, meaning a decrease in performance that can be detrimental when operating in real PEMWE cell conditions.[186b]

Similar results were obtained by Uchida *et al.*,[182] who reported interesting results when depositing IrO$_x$ catalysts over M-SnO$_2$ supports, where M = Nb, Ta and Sb (NTO, TaTO and ATO respectively). They measured similar stabilities and activities for all prepared catalysts on half-cell measurements, but on single cell tests, with MEAs, the lower conductivity of TaTO and NTO supports induced higher resistances and therefore, lower cell performances.
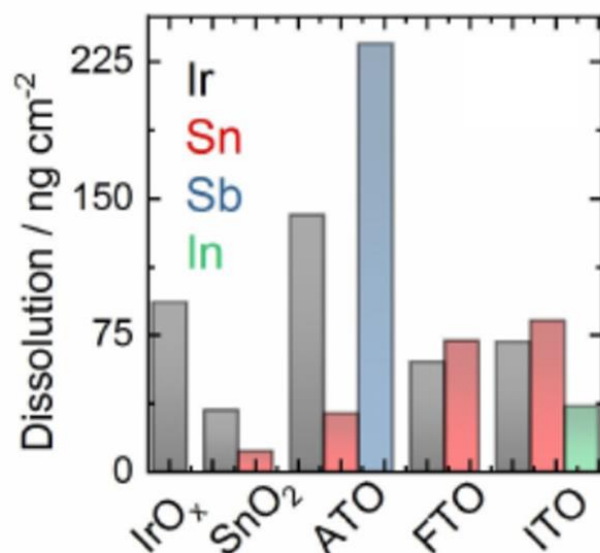

Figure 1. 29 IrO$_x$/SnO$_2$ dissolution profiles during 1,000potential cycles between 1.1–1.6 V, at 400 mV·s^{-1}, in 0.1 M H$_2$SO$_4$.[184g]

Further works should be dedicated to the improvement of FTO and TaTO conductivity, or to the improvement of Sb stability for ATO materials by homogenizing its dispersion onto the SnO$_2$ matrix.

As seen in **Table 1.3**, Many different ATO morphologies or materials have been used for this kind of IrO$_x$ deposition: commercial ATO NPs,[184h,i] mesoporous ATO materials prepared hydrothermally,[184b,f,g] by electrospinning,[184o] or by a soft template method,[184a] or macroporous ATOs.[180d] Challenges in developing supported catalysts concern synthesizing ideally conductive and corrosion-stable supports with an optimized morphology and optimum conductivity.

For PEMWEs in particular, the morphology of catalyst supports plays an important role. Supports should present a high surface area based on large mesoporosity with optimal pore size to allow water to access the active sites of the catalyst, and allow gas diffusion and optimal catalyst dispersion. Optimization of the supports can contribute towards higher mass-activity values.[184i]

Our group has been involved in the improvement of TO-based aerogels synthesis, and their utilization for energy applications, for many years. Our materials have been evaluated by many groups as catalysts supports for PEMFC or PEMWE.[101c,184j,187] For example, previous PhD student of our group, G. Ozouf, show an improvement of Pt utilization and stability when supporting Pt catalysts over ATO aerogels.[187a,b] Other studies, such as Cognard et al., have shown an increase in the activity and stability of Pt catalysts for ORR when supporting onto Nb-doped tin oxide aerogels (NTO).[187b] For OER catalysis in PEMWE, Wang et al. supported an IrO_x catalyst over a SnO_2:Sb aerogel modified with V, showing an improvement of Iridium stabilization and OER activity compared with non-supported Ir catalysts.[192] Abbou et al., also improved the Ir utilization when depositing IrO_x catalysts over ATO and TaTO (Ta-doped tin dioxide) aerogels.[189]

IV.3 SnO_2-based aerogel synthesis

As mentioned above, metal oxide aerogels have shown excellent capacities for catalysis applications,[49] and are particularly interesting due to their pore size diameter of between 2 and 50 nm, known as mesopores. The presence of mesopores in catalysts can overcome the diffusion constraints which are observed in microporous catalysts (pore size < 2 nm). In addition, the presence of large surface areas makes it easier for the reactant molecules to access active sites, leading to improved catalytic performance. In addition to their wide range of applications in the field of catalysis, mesoporous materials have also been used in adsorption, sensors, lithium-ion batteries, drug delivery, and nanodevices.[190]

Mesoporous tin oxide can be synthesized using numerous different synthesis methods, such as:[191] the template method followed by hydrothermal treatment,[119,187a] the flame pyrolysis method,[187b] the Doctor Blade method,[187c] the co-precipitation procedure,[191d] and the sol-gel method.[191e] Especially interesting materials are tin oxide aerogels, prepared using the sol-gel method, which present many of the aerogel properties mentioned in section III.2, such as large surface areas and mesoporosity. Doping such tin oxide-based aerogels with polyvalent cations (such as Sb(V), Ta(V), Nb(V), etc.) improves conductivity. Many authors have used doped SnO_2 aerogels as catalysts supports for both ORR in PEM-FC,[187] and OER in PEMWE cells,[192] for low Pt and Ru or Ir loadings respectively.

Therefore, using SnO_2 aerogels as a catalyst support presents many advantages due to its properties, which can be modulated depending on the synthesis conditions. Several precursors have been used in literature for tin oxide aerogel synthesis: (1) $SnCl_4 \cdot 5H_2O$,[193] (2) $SnCl_4$ anhydrous,[194] (3) $SnCl_2 \cdot 2H_2O$,[195] (4) Sn granulated,[196] (5) $Sn(OBu)_4$,[197] and (6) $Sn(OiPr)_4$.[191e,198] It has been reported that using chlorine precursors reduces the catalytic activity of the catalysts

due to Cl absorption over the surface.[199] It is also well known that *sol-gel* synthesis with chlorine precursors leads to reproducibility problems. Despite this, Correa *et al.* synthetized ATO aerogels with chlorine precursors for Sn and Sb.[200] They found that when using NH_4F with a molar ratio of 1:1 vs an Sn precursor, the chlorine content of the aerogels decreased along with the degree of shrinkage during aging and calcination.

All of the as-prepared aerogels in this report have been prepared following the already reported *sol-gel* method,[198f] using the $Sn(OiPr)_4$ alkoxide as the metal precursor.

Once the colloidal suspension is stable, in our case a colloidal suspension of oligomers from the $Sn(OiPr)_4$ metal-alkoxide initial precursor, the colloids tend to agglomerate with each other forming a 3D network structure. The whole transformation mechanism, from a metal-alkoxide precursor into a metal oxide gel, can be broken down into several steps:[201]

1. **Hydrolysis reactions:**

$$Sn(OiPr)_4 + H_2O \rightarrow Sn(OiPr)_3(OH) + iPrOH \textbf{ (Eq. 1.43)}$$
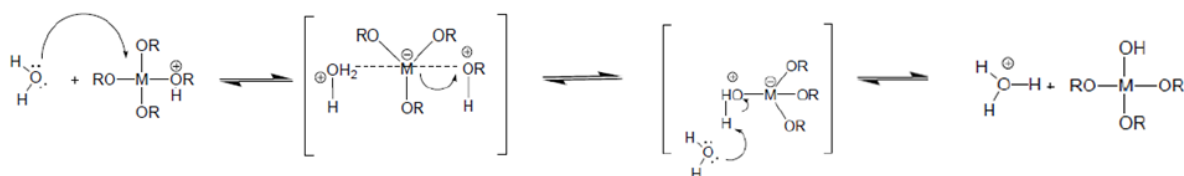
Figure 1.30 Hydrolysis mechanism in acid media.[202]

The pH of the medium determines the growth mechanisms of the network:

Acid hydrolysis, **Figure 1.30**, allows the protonation of an alkoxide group (the better leaving group); however, once an alkoxide group is substituted by a hydroxide, the metal-alkoxide intermediate becomes less stable, which implies a decrease in the hydrolysis kinetics rate. Acidic catalysis leads to the formation of weakly cross-linked polymers/gels.
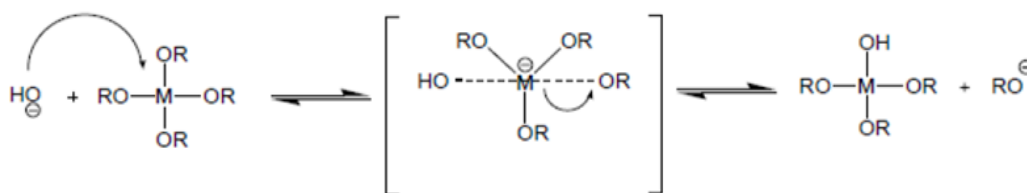
Figure 1.31 Hydrolysis mechanism in basic media.[202]

In basic hydrolysis, **Figure 1.31**, the hydroxyl ion, which is a very nucleophilic group, attacks the metal center more easily, and the stable negative intermediate allows successive hydrolysis reactions with the different hydroxyl groups that attacked the metal center. Therefore, basic catalysis favors the formation of highly branched polymers, which results in more porous and permeable aerogels.

2. **Condensation reactions:**

After hydrolysis, condensation reactions take place via the hydroxide group, which attacks another hydrolyzed precursor to form a metalloxane bridge M-OM. Two condensation reactions with different mechanisms are possible:

a) Oxolation: where the leaving group after the nucleophilic attack is a water molecule, **Figure 1.32** right.

$$2\ Sn(OiPr)_3(OH) \rightarrow (OiPr)_3Sn\text{-}O\text{-}Sn(OiPr)_3 + H_2O \textbf{ (Eq. 1.44)}$$
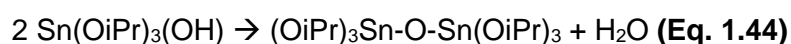
b) Alcoxolation: where the leaving group after the nucleophilic attack is an alcohol, **Figure 1.32** left.

$$Sn(OiPr)_3(OH) + Sn(OiPr)_4 \rightarrow (OiPr)_3Sn\text{-}O\text{-}Sn(OiPr)_3 + iPrOH \textbf{ (Eq. 1.45)}$$
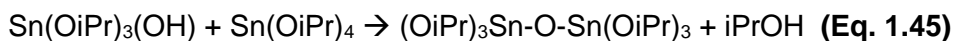
These successive reactions form longer chains whose size varies depending on the polymerization and depolymerization kinetics.
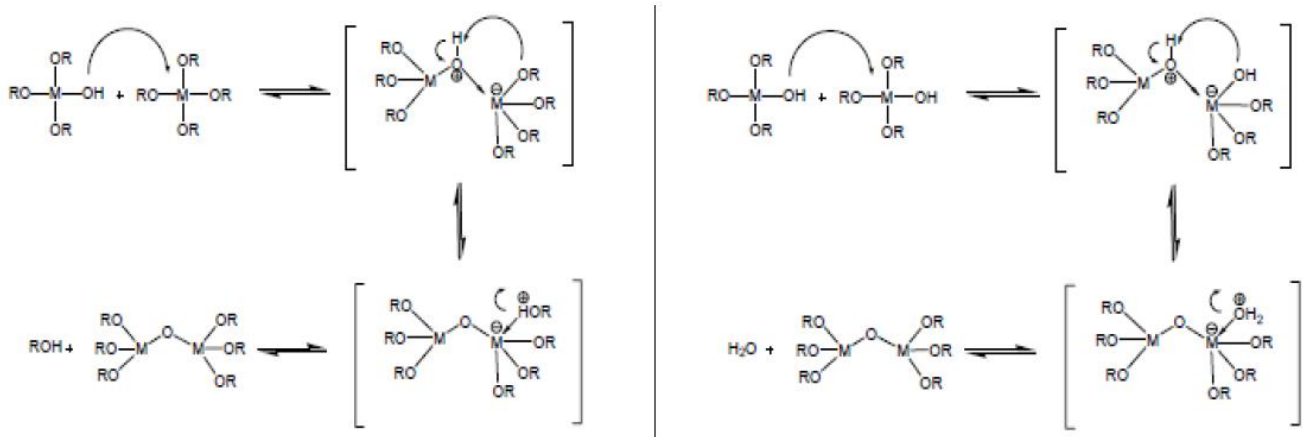
Figure 1.32 Condensation mechanism for alkoxylation (left) and oxolation (right).[202]

3. Gelation:

When the first particles or clusters are generated after hydrolysis and condensation reactions, a sol is generated. On the one hand, if there is a saturation of polymer particles or clusters, a gel is formed. These clusters are stable and do not aggregate as long as there is an electrostatic or steric repulsion; however, when this impedance disappears due to a change in the media or because van der Waals forces are higher, particles or clusters tend to aggregate, generating denser structures. The gelation process then features the formation of a spanning cluster, giving a network, which entraps the remaining solution. On the other hand, if the colloidal suspension is destabilized before the gelation, a precipitate with a non-gel shape is obtained. The polymerization and depolymerization mechanism will then modify the shape of this material.

4. Aging:

During aging, hydrolysis and condensation reactions still take place, featuring crosslinking between different chains of the network. At this point, the gel is being contracted and the solvent is expelled (syneresis), while some properties of the gel, such as specific surface and pore size distribution, are still being modified. Dissolution and re-precipitation procedures (polymerization and depolymerization) also occur during the aging of the gel.

5. **Drying:**

Once a solid network with an entrapped solvent is formed, if this solvent is then removed by conventional evaporation, cracking and densification of the material usually appear. This phenomenon is due to the appearance of high capillary tensions in the pores resulting from the presence of a liquid-gas interface. This results in the formation of a *xerogel*, a material with a low specific surface area and pore size.

To avoid solid network contractions, in 1931 Kistler *et al.*[203] introduced supercritical drying, where the solvent of the gel is removed by a supercritical solvent in order to prevent destruction of the network.[204] This type of drying preserves the morphology with a high porosity and high specific surface area of the gel, obtaining a solid network of empty cavities: an *aerogel*.

6. **Densification:**

Thermal treatment leads to the crystallization of the aerogel, obtaining a porous and crystalline ceramic

V Conclusions

Hydrogen can be produced from water by electrolysis. Proton Exchange Membrane Electrolysers (PEMWE), if powered by clean energy sources, such as solar or wind power, are considered a clean and sustainable way to produce hydrogen and store energy. However, one of the major challenges when designing PEMWE devices is the anode material. The catalysts must be able to cope with high electrochemical potentials (> 1.6 V with respect to SHE), in the presence of oxygen, in very acidic environments and moderate temperatures (around 80 °C).

Previous studies have determined that the precious metal oxides, ruthenium and iridium, have been shown to be the best electrocatalysts for the oxygen production reaction (OER). Current anodes use particles of micrometric size, charged between 1.5 - 3 mg·cm^{-2}. A reduction in the precious metal content is therefore desired in anticipation of the deployment of high power electrolyzers to come. One possible solution for reducing the total amount of catalyst consists in using nanometric sized catalysts (Ir or Ru) supported on electron-conducting support materials with large specific surface areas. Carbon blacks (CB) have been widely used as a support material in electrochemical applications, due to their large specific surface area, high electrical conductivity, and low cost. However, the high potentials required for OER make it impossible to use these carbon-based materials on PEMWEs.

Materials based on metal oxides exhibit excellent stability and resistance to corrosion while exhibiting strong interactions with metal catalysts. These are promising materials for use as catalyst supports for PEMWE devices. Previous work has shown the potential of using mesoporous doped tin oxide airgels as catalyst supports for OER, where the use of noble metals has been improved. Such noble metal use is attributed to an absence of Ir (III) species when the catalysts are supported on ATO materials, avoiding the formation of intermediate species involved in the dissolution process. Therefore, tin oxide aerogels with a three-dimensional mesoporous structure are particularly useful materials as catalyst supports on PEMWEs. Like carbon aerogels, which have already proven their worth for other catalysis applications, their morphology can be adjusted and modulated by adjusting the sol-gel parameters for higher specific surfaces or an improvement in conductivity by doping with different elements.

VI Résumé

L'hydrogène peut être produit à partir d'eau par électrolyse. Les électrolyseurs à membrane échangeuse de protons (PEMWE), s'ils sont alimentés par des sources d'énergie propres, telles que l'énergie solaire ou éolienne, sont considérés comme un moyen propre et durable de produire de l'hydrogène et stocker l'énergie. Cependant, l'un des défis majeurs lors de la conception des dispositifs PEMWE est le matériau d'anode. Les catalyseurs doivent être capables de faire face à des potentiels électrochimiques élevés (>1,6 V par rapport à SHE), en présence d'oxygène, dans des environnements très acides à température modérée (environ 80°C). Des études antérieures ont déterminé que les oxydes de métaux précieux, le ruthénium et l'iridium, se sont avérés être les meilleurs électrocatalyseurs pour la réaction de production d'oxygène (OER). Les anodes actuelles utilisent des particules de taille micrométrique, chargées entre 1.5 - 3 mg·cm^{-2}. Une réduction de la teneur en métal précieux est donc souhaitée en prévision du déploiement d'électrolyseurs de forte puissance à venir. Une solution possible pour diminuer la quantité totale de catalyseur consiste à utiliser des catalyseurs de taille nanométrique (Ir ou Ru) supportés sur des matériaux support conducteurs d'électrons présentant une grande surface spécifique. Les noirs de carbone (CB) ont été largement utilisés comme matériau de support dans les applications électrochimiques, en raison de leur grande surface spécifique, de leur conductivité électrique élevée et de leur faible coût. Cependant, les potentiels élevés requis pour l'OER rendent impossible l'utilisation de ces matériaux à base de carbone.

Les matériaux à base d'oxydes métalliques présentent d'excellentes stabilités et résistances face à la corrosion tout en présentant de fortes interactions avec les catalyseurs métalliques. Ce sont des matériaux prometteurs à utiliser comme supports de catalyseur pour les dispositifs PEMWE. Des travaux antérieurs ont montré le potentiel de l'utilisation d'aérogels d'oxyde d'étain dopés mésoporeux comme supports de catalyseurs pour l'OER, où l'utilisation de métaux nobles a été améliorée. Une telle utilisation de métal noble est attribuée à une absence d'espèces Ir(III) lorsque les catalyseurs sont supportés sur des matériaux ATO, évitant la formation d'espèces intermédiaires impliquées dans le processus de dissolution. Par conséquent, les aérogels d'oxyde d'étain à structure mésoporeuse tridimensionnelle sont des matériaux particulièrement intéressants comme supports de catalyseurs. A l'image des aérogels de carbone, qui ont déjà fait leurs preuves pour d'autres applications de catalyse, leur morphologie peut être ajustée et modulée en jouant sur les paramètres sol-gel pour des surfaces spécifiques plus élevées ou une amélioration de la conductivité par dopage par différents éléments.

VII References

[1] N. Armatoli, Balzani, V. *Angew. Chem. Int. Ed.* **2007**, *46*, 52-66.

[2] (a) T. Karl, K. Trenberth, *Science* **2003**, *302*, 1719-1723 (b) I. Omae, *Coord. Chem. Rev.* **2012**, *256*, 1384-1405 (c) Wang, W.; Wang, S.; Ma, X.; Gong, J.; *Chem. Soc. Rev.* **2011**, *40*, 3703-3727.

[3] (a) *Exhausting profiles of oil products*, Exxon-Mobile, **2004**; (b) *Solar Energy Utilization Workshop* U.S. Department of Energy, Washington DC, **2005**; (c) *New Science for a Secure and Sustainable Energy Future* U.S. Department of Energy, **2008**; (d) *Research Needs and Impacts in Predictive Simulation for Internal Combustion Engines (PreSICE)* U.S. Department of Energy, **2011**. (e) O. Edenhofer, R. Pichs-Madruga, Y. Sokona, E. Farahani, S. Kadner, K. Seyboth, A. Adler, I. Baum, S. Brunner, P. Eickemeier, B. Kriemann, J. Savolainen, S. Schlömer, C. Von Stechow, T. Zwickel, J. Minx, *Climate Change 2014: Mitigation of Climate Change. Contribution of Working Group III to the Fifth Assessment Report of the Intergovernmental Panel on Climate Change.;* Cambridge Univerity Press: Cambridge, UK, **2014**.

[4] (a) *BP Statistical Review of World Energy*, **2015**. (b) Q. Schiermeier, J. Tollefson, T. Scully, A. Witze, O. Morton, *Nature* **2008**, *454*, 816-823. (c) S. Styring, *Faraday Discuss.*, **2012**, *155*, 357–376.

[5] Branker, K.; Pathak, M. J. M.; Pearce, J. M. *Renew. Sust. Energ. Rev.* **2011**, *15,* 4470-4482.

[6] S. Karlsson, J. Boixel, Y. Pellegrin, E. Blart, H. Becker, F. Odobel, Hammarstrom, L. *Faraday Discuss.*, **2012**, *155*, 233-252.

[7] B. Viswanathan, *Hydrogen Storage*, Energy Sources, Fundamentals of Chemical Conversion Processes and Applications. Elseiver, **2017**, Chapter 10, 185-212.

[8] Jordi Creus Casanovas, **2018**, *Electrocatalytic Water Splitting with Ruthenium Nanoparticles*, Universitat Autònoma de Barcelona, Departament de Química, Cerdanyola del Vallés.

[9] *The future of hydrogen*, IEA, 2019

[10] (a) H. M. Lee, Y. J. Heo, K. H. An, S. C. Jung, D. C. Chung, S. J. Park, B. J. Kim, *Int. J. Hydrogen Energy* **2018**, *43,* 5894-5902; (b) L. Luo, T. Chen, W. Zhao, M. Fan, *BioResources,* **2017**, *12*, 6237-6250; (c) N. Thaweelap, P. Thongtana, C. Sitthiwet, S. Thiangviriya, P. Eiamlamai, R. Utke, *Int. J. Hydrogen Energy,* **2017**, *42*, 24915-24926; (d) A. Yadava, N. Verma, *Int. J. Hydrogen Energy,* **2017**, *42*, 27139-27153; (e) R. S. Rajauraa, S. Srivastavaa, P. K. Sharmab, S. Mathurb, R. Shrivastavac, S. S. Sharmad, Y. K. Vijay, *Nano-Structures & Nano-Objects,* **2018**, *14*, 57-65

[11] (a) N. Bimbo, W. Xu, J. E. Sharpe, V. P. Ting, T. J. Mays, *Mater. Des.,* **2016**, *89*, 1086-1094; (b) Y. Liu, J. Lu, J. Yang, Y. Zhang, J. Wang, C. Li, L. Xia, *Mater. Lett.,* **2018**, *214*, 91-94.

[12] (a) M. H. Kowsaria, S. Naderlou, *Microporous Mesoporous Mater.* **2017**, *240*, 39-49; (b) P. Roy, N. Das, *Ultrason. Sonochem.,* **2017**, *36*, 466-473.

[13] M. Zahmakiran, S. Ozkär, *Top. Catal.,* **2013**, *56*, 1171-1183.

[14] I. Dincer, C. Acar, *Int. J. Hydrogen Energy,* **2015**, *40*, 11094-11111.

[15] Process and system for generating synthesis gas - worldwide.espacenet.com

[16] A. Remiro, B. Valle, L. Oar-Arteta, A. Aguayo, J. Bilbao, A. Gayubo, *Int. J. Hydrogen Energy,* **2014**, *39*, 6889-6898.

[17] B. Viswanathan, *Hydrogen as an Energy carrer*, Energy Sources, Fundamentals of Chemical Conversion Processes and Applications. Elseiver, **2017**, Chapter 9, 161-183

[18] N. Lewis, D. Nochera, *Proc. Natl. Acad. Sci. U.S.A.* **2006**, *103*, 15729-15735.

[19] (a) J. Hurst, *Science.* **2010**, *328*, 315-316. (b) K. Sanderson, K. *Nature*, **2008**, *452*, 400- 402.

[20] C. Coutanceau, S. Baranton, T. Audichon, *Hydrogen Electrochemical Production*, (Ed) Bruno G. Pollet, 2017

[21] C. Neagu, H. Jansen H, H. Gardeniers, M. Elwenspoek, *Mechatronics,* **2000**, *5*, 571-581.

[22] Ø. Ulleberg, *J. Hydrogen Energy*, **2003**, *28*, 2133.

[23] D. Santos, C. Sequeira, *Quim. Nova,* **2013**, *36*, 1176-1193.

[24] V.M. Rosa, M.B.F. Santos, E.P. Da Silva, *Int. J. Hydrogen Energy*, **1995**, *20*, 697-700.

[25] T. Ohmori, K. Tachikawa, K. Tsuji, K. Anzai, *Int. J. Hydrogen Energy*, **2007**, *32*, 5094-5097.

[26] M.E.G. Lyons, M.P. Brandon, *Int. J. Electrochem. Sci.,* **2008**, *3*, 1386-1424.

[27](a) Y. Liang, Y. Li, H. Wang, J. Zhou, J. Wang, T. Regier, *Nat. Mater.*, **2011**, *10*, 780-786; (b) M. Hamdani, M.I.S. Pereira, J. Douch, A. Ait Addi, Y. Berghoute, M.H. Mendonça, *Electrochim. Acta*, **2004**, *49*, 1555-1596; (c) R.N. Singh, D. Mishra, Anindita, A.S.K. Sinha, A. Singh, *Electrochem. Comm.*, **2007**, *9*, 1369 - 1373.

[28] (a) M. dos Santos Andrade, M. Aciolia, J. Ginaldo da Silva Jr, J. Pereira Silva, E. Vilar, J. Tonholo, *Int. J. Hydrogen Energy*, **2004**, *29*, 235-241; (b) J.M. Olivares-Ramírez, M.L. Campos-Cornelio, J. Uribe Godínez, E. Borja-Arco, R.H. Castellanos, *Int. J. Hydrogen Energy*, **2007**, *32*, 3170-3173; (c) D. Marcelo, A. Dell'Era, D. Marcelo, A. Dell'Era, *Int. J. Hydrogen Energy*, **2008**, *33*, 3041-3044.

[29] M. Carmo, D. Fritz, J. Mergel, D. Stolten, *Int. J. Hydrogen Energy*, **2013**, *38 (12)*, 4901-4934.

[30] F. Barbir, *Solar Energy*, **2005**, *78 (5)*, 661-669.

[31] O. Schmidt, A. Gambhir, I. Staffell, A. Hawkes, J. Nelson, S. Few, *Int. J. Hydrogen Energy*, **2017**, *42 (52)*, 30470-30492

[32] M.A. Laguna-Bercero, *J. Power Sources*, **2012**, *203*, 4-16.

[33] (a) S. Li, R. Yan, G. Wu, K. Xie, J. Cheng, *Int. J. Hydrogen Energy*, **2013**, *38*, 14943-14951; (b) X. Yang, J.T.S. Irvine*, J. Mater. Chem.*, **2008**, *18*, 2349-2354.

[34] P. Moçoteguy, A. Brisse, *Int. J. Hydrogen Energy*, **2013**, *38*, 15887-15902.

[35] A. Brisse, J. Schefold, M. Zahid, *Int. J. Hydrogen Energy*, **2008**, *33*, 5375-5382.

[36] S. Shiva, V. Himabindu, *Materials Science for Energy Technologies*, **2019**, *2*, 442-454

[37] Proton Exchange Membrane Water Electrolysis as a Promising Technology for Hydrogen Production and Energy Storage, R. Maric, H. Yu, *Nanostructures in energy generation, transmission and storage*, **2018**.

[38] A. Aricò, S. Siracusano, N. Briguglio, V. Baglio, A. Di Blasi, V. Antonucci, *J. Appl Electrochem*, **2013**, *43*, 107-118.

[39] (a) S. O'Neil, Fuel Cell & Hydrogen Energy Association, **2019** (b) M. Rees, D. King, J. Browne, R. Layard, G. O'Donnell, N. Stern, A. Turner A global apollo programme to combat climate change, **2015**.

[40] Hydrogen Production: by Electrolysis, P. Millet, A. Godula-Jopek, Wiley-VCH Verlag GmbH & Co. KGaA, **2015**.

[41] (a) C. Rakousky, G. Keeley, K. Wippermann, M. Carmo, D. Stolten, *Electrochim. Acta*, **2018**, *278*, 324-331; (b) C. Rakousky, U. Reimer, K. Wippermann, M. Carmo, W. Lueke, D. Stolten, *J. Power Sources*, **2016**, *326*, 120-128; (c) S. Siracusano, V. Baglio, S. Grigoriev, L. Merlo, V. Fateev, A. Aricò, *J. Power Sources*, **2017**, *366*, 105-114; (d) S. Siracusano, S. Hodnik, P. Jovanovic, F. Ruiz-Zepeda, M. Šala, V. Baglio, A. Aricò, *Nano Energy*, **2017**; (e) C. Liu, M. Carmo, G. Bender, A. Everwand, T. Lickert, J. Young, T. Smolinka, D. Stolten, W. Lehnert, *Electrochem. Com.*, **2018**, *97*, 96-99.

[42] (a) H. Jung, S. Huang, P. Ganesan, B. Popov, *J. Power Sources*, **2009**, *194 (2)*, 972-975.

[43] (a) S. Siracusano, V. Baglio, C. D'Urso, V. Antonucci, A.S. Arico, *Electrochim. Acta*, **2009**, *54,* 6292-6299. (b) J. Cheng, H. Zhang, G. Chen, Y. Zhang*, Electrochim. Acta*, **2009**, *54,* 6250-6256.

[44] V.F.3 Fuel Cell Vehicle and Bus Cost Analysis., J. Brian, DOE Hydrogen and Fuel Cells Program, **2015**.

[45] (a) K. Ayers, E. Anderson, C. Capuano, B. Carter, L. Dalton, G. Hanlon, *ECS Trans.,* **2012**, *33*, 315. (b) Y. Kawano, Y. Wang, R.A. Palmer, S.R. Aubuchon, *Polim.: Cienc. Tecnol.*, **2002**, *12*, 96-101. (c) S. Grigoriev, V. Porembsky, V. Fateev, *Int. J. Hydrogen Energy*, **2006**, *31*, 171-175.

[46] A. S. Arico, S. Siracusso, N. Briguglio, V. Baglio, A. Di Blasi, V. Antonucci, *J. App. Electrochem.*, **2013**, *43*, 107-1118.

[47] (a) V. Antonucci, A. Di Blasi, V. Baglio, R. Ornelas, F. Matteucci, J. Ledesma-Garcia, L. Arriaga, A. Arico, *Electrochim. Acta*, **2008**, *53*, 7350-7356. (b) S. Siracusano, V. Baglio, M.A. Navarra, S. Panero, V. Antonucci, A.S. Arico, *Int. J. Electrochem. Sci.*, **2012,** *7*, 1532-1542.

[48] (a) A. Marshall, **2005**, *Electrocatalysts for the oxygen evolution electrode in water electrolysers using proton exchange membranes: synthesis and characterization*, Department of Materials Technology, Norwegian University of Science and Technology (NTNU), Trondheim; (b) Q. Feng, X. Yuan, G. Liu, B. Wei, Z. Zhang, H. Li, H. Wang, *Journal of Power Sources*, **2017**, *366*, 33e55; (c) F.Khati, T. Wilberforce, O. Ijaodola, E.Ogungbemi, Z.El-Hassan, A. Durrant, J. Thompson, A. Olabi, *Renewable and Sustainable Energy Reviews*, **2019**, 111, 1–142

[49] Synthesis, Properties, and Applications Metal Oxides, P. Manjunathan, G. Shanbhag, Tin Oxide Materials, **2020**.

[50] K. Ayers, E. Anderson, C. Capuano, An industrial perspective on challenges and opportunities for low temperature water electrolysis. In EFCF, Lucerne, **2019**.

[51] T. Reier, H. Nong, D. Teschner, R. Schlögl, P. Strasser, *Adv. Energy Mater.*, **2017**, *7*, 1601275

[52] T. Shinagawa, A. T. Garcia-Esparza, K. Takanabe, *Sci. Rep.* **2015**, *5*, Article nº 13801; B. E. Conway, B. V. Tilak, *Electrochim. Acta,* **2002**, *47*, 3571-3594.

[53] F.I. Mattos-Costa, P. Lima-Neto, S.A.S. Machado, L.A. Avaca, *Electrochim. Acta*, **1998**, *44*, 1515-1523.

[54] PEM Electrolysis for Hydrogen Production: Principles and Applications, M. Carmo, W. Maier, D. Stolten, Ed. CRC Press, **2017**.

[55] Y. Yu, Y. Li, S. Steinmann, W. Yang, *Nano Letters,* **2014**, *14*, 553-558

[56] R. Selvan, A. Gedanken, *Nanotechnology*, **2009**, *20*

[57] J. Rajeswari, P. Viswanathan, T. Varadarajan, *Nanoscale Research Letters*, **2007**, *2,* 496 - 503

[58] O. Pantini, E. Anxolabehere-Mallart, A. Aukauloo, P. Millet, *Electrochemistry Communications*, **2007**, *9*, 54-58

[59] S. Alayoglu, A. Nilekar, M. Mavrikakis, B. Eichhorn, *Nature Materials*, **2008**, *7*, 333-338

[60] S. Kohn, T. Anniyev, K. More, C. Yu, H. Ogasawara, M. Toney, P. Strasser, *Nature Chemistry*, **2010**, *2*, 454-460

[61] M. Debe, *Journal of the Electrochemistry Society*, **2012**, *159*, 165-176

[62] (a) Z. Chen, J. Lu, Y. Ai, Y. Ji, T. Adschiri, L. Wan, *ACS Appl. Mater. Interfaces*, **2016**, *8*, 35132−35137; (b) E. Demir, S. Akbayrak, A. Önal, S. Özkar, *ACS Appl. Mater. Interfaces*, **2018**, *10*, 6299−6308; (c) R. Ye, Y. Liu, Z. Peng, T. Wang, A. Jalilov, B. Yakobson, S. Wei, J. Tour, *ACS Appl. Mater. Interfaces*, **2017**, *9,* 3785−3791; (d) Y, Zheng, Y. Jiao, Y. Zhu, L. Li, Y. Han, Y. Chen, M. Jaroniec, S. Qiao, *J. Am. Chem. Soc.*, **2016**, *138*, 16174−16181; (e) J. Mahmood, F. Li, S. Jung, M. Okyay, I. Ahmad, S. Kim, N. Park, H. Jeong, J. Baek, *Nat. Nanotechnol.*, **2017**, *12*, 441−446.

[63] (a) P. Millet, D. Dragoe, S. Grigoriev, V. Fateev, C. Etievant, *Int. J. Hydrogen Energy*, **2009**, *34,* 4974-4982; (b) S. Grigoriev, M. Mamat, K. Dzhus, G. Walker, P. Millet, *Int. J. Hydrogen Energy*, **2011**, *36,* 4143-4147

[64] (a) J. Wua, Z. Yang, Q. Sun, X. Li, P. Strasser, R. Yang, *Electrochim. Acta*, **2014**, *127*, 53-60; (b) Y. Zhou, R. Maa, S. Candelaria, J. Wang, Q. Liu, E. Uchaker, P. Li, Y. Chen, G. Cao, *J. Power Sources*, **2016**, *314*, 39-48.

[65] S. Shiva Kumar, S. Ramakrishna, B. Rama Devi, V. Himabindu, *Int. J. Green Energy,* **2018**, *15*, 558-567

[66] 44. Willsau, J.; Wolter, O.; Heitbaum, J., J. Electroanal. Chem. Interfacial Electrochem. 1985, 195 (2), 299-306.

[67] Rossmeisl, J.; Qu, Z. W.; Zhu, H.; Kroes, G. J.; Nørskov, J. K., J. Electroanal. Chem. 2007, 607 (1-2), 83-89.

[68] (a) Dau, H.; Limberg, C.; Reier, T.; Risch, M.; Roggan, S.; Strasser, P., ChemCatChem 2010, 2 (7), 724-761; (b) Fabbri, E.; Habereder, A.; Waltar, K.; Kötz, R.; Schmidt, T. J., Catal. Sci.Technol. 2014, 4 (11), 3800-3821

[69] J. O. Bockris, *J. Chem. Phys.* **1956**, *24*, 817.

[70] J. Rossmeisl, Z. W. Qu, H. Zhu, G. J. Kroes, J. K. Norskov, *J. Electroanal. Chem.* **2007**, *607*, 83.

[71] (a) S. Trasatti*, Electrochim. Acta*, **1984**, *29*, 1503-1512. (b) G. Lodi, E. Sivieri, A. Battisti, S. Trasatti, *J. Appl. Electrochem.*, **1978**, *8,* 135-143. (c) L.M. Doubova, A. De Battisti, S. Daolio, C. Pagura, S. Barison, R. Gerbasi, et al., *Russ. J. Electrochem.*, **2004**, *40*, 1115-1122.

[72] (a) M.H. Miles, M.A. Thomason, *J. Electrochem. Soc.*, **1976**, *123*, 1459-1461. (b) M.H. Miles, E.A. Klaus, B.P. Gunn, J.R. Locker, W.E. Serafin, S. Srinivasan, *Electrochim. Acta*, **1978**, *23*, 521-526.

[73] (a) R. Kötz, S. Stucki, D. Scherson, D.M. Kolb, *J. Electroanal. Chem.,* **1984**, *172*, 211-219. (b) C. Iwakura, K. Hirao, H. Tamura, *Electrochim. Acta,* **1977**, *22*, 329-334.

[74] A. Minguzzi, F.R.F. Fan, A. Vertova, S. Rondinini, A.J. Bard, *Chem. Sci.*, **2012**, *3*, 217.

[75] (a) N. Danilovic, R. Subbaraman, K. C. Chang, S. H. Chang, Y. J. J. Kang, J. Snyder, A. P. Paulikas, D. Strmcnik, Y. T. Kim, D. Myers, V. R. Stamenkovic, N. M. Markovic, *J. Phys. Chem. Lett.* **2014**, *5*, 2474. (b) S. Cherevko, S. Geiger, O. Kasian, N. Kulyk, J. P. Grote, A. Savan, B. R. Shrestha, S. Merzlikin, B. Breitbach, A. Ludwig, K. J. J. Mayrhofer, *Catal. Today,* **2016**, *262*, 170. (c) S. Geiger, O. Kasian, B. R. Shrestha, A. Mingers, K. J. J. Mayrhofer, S. Cherevko, *J. Electrochem. Soc.* **2016**, *163*, F3132.

[76] E. Fabbri, A. Habereder, K. Waltar, R. Kotz, T. J. Schmidt, *Catal. Sci. Technol.* **2014**, *4*, 3800.

[77] (a) T. Reier, D. Teschner, T. Lunkenbein, A. Bergmann, S. Selve, R. Kraehnert, R. Schlogl, P. Strasser, *J. Electrochem. Soc.* **2014**, *161*, F876. (b) A. de Oliveira-sousa, M. A. S. da Silva, S. A. S. Machado, L. A. Avaca, P. de Lima-Neto, *Electrochim. Acta,* **2000**, *45*, 4467.

[78] (a) T. Reier, I. Weidinger, P. Hildebrandt, R. Kraehnert, P. Strasser, *ECS Trans.* **2013**, *58*, 39. (b) S. Cherevko, T. Reier, A. R. Zeradjanin, Z. Pawolek, P. Strasser, K. J. J. Mayrhofer, *Electrochem. Commun.* **2014**, *48*, 81.

[79] (a) V. Pfeifer, T. E. Jones, J. J. Velasco Vélez, C. Massué, M. T. Greiner, R. Arrigo, D. Teschner, F. Girgsdies, M. Scherzer, J. Allan, M. Hashagen, G. Weinberg, S. Piccinin, M. Hävecker, A. Knop-Gericke, R. Schlögl, *Phys. Chem. Chem. Phys.* **2016**, *18*, 2292. (b) V. Pfeifer, T. E. Jones, J. J. V. Velez, C. Massue, R. Arrigo, D. Teschner, F. Girgsdies, M. Scherzer, M. T. Greiner, J. Allan, M. Hashagen, G. Weinberg, S. Piccinin, M. Havecker, A. Knop-Gericke, R. Schlogl, *Surf. Interface Anal.* **2016**, *48*, 261.

[80] E. Antolini, *ACS Catalysis*, **2014**, *4* (*5*), 1426-1440

[81] (a) R. Kotz, S. Stucki, *J. Electrochem. Soc.* **1985**, *132*, 103. (b) H. H. Pham, N. P. Nguyen, C. L. Do, B. T. Le, *Adv. Nat. Sci.: Nanosci. Nanotechnol.* **2015**, *6*, 025015. (c) N. Mamaca, E. Mayousse, S. Arii-Clacens, T. W. Napporn, K. Servat, N. Guillet, K. B. Kokoh, *Appl. Catal.* B, **2012**, *111*, 376. (d) T. Audichon, E. Mayousse, S. Morisset, C. Morais, C. Comminges, T. W. Napporn, K. B. Kokoh, *Int. J. Hydrogen Energy* **2014**, *39*, 16785. (e) R. Kotz, S. Stucki, *Electrochim. Acta,* **1986**, *31*, 1311. (f) L. E. Owe, M. Tsypkin, K. S. Wallwork, R. G. Haverkamp, S. Sunde, *Electrochim. Acta,* **2012**, *70*, 158. (g) N. Danilovic, R. Subbaraman, K. C. Chang, S. H. Chang, Y. J. Kang, J. Snyder, A. P. Paulikas, D. Strmcnik, Y. T. Kim, D. Myers, V. R. Stamenkovic, N. M. Markovic, *Angew. Chem. Int. Ed.* **2014**, *53*, 14016; (h) J. Cheng, H. Zhang, G. Chen, Y. Zhang, *Electrochemical Acta,* **2009**, *54*, 6250-6256.

[82] (a) T. Reier, Z. Pawolek, S. Cherevko, M. Bruns, T. Jones, D. Teschner, S. Selve, A. Bergmann, H. N. Nong, R. Schlogl, K. J. J. Mayrhofer, P. Strasser, *J. Am. Chem. Soc.* **2015**, *137,* 13031. (b) H. N. Nong, L. Gan, E. Willinger, D. Teschner, P. Strasser, *Chem. Sci.* **2014,** *5*, 2955. (c) V. Petrykin, Z. Bastl, J. Franc, K. Macounova, M. Makarova, S. Mukerjee, N. Ramaswamy, I. Spirovova, P. Krtil, *J. Phys. Chem. C* **2009**, *113*, 21657. (d) R. B. Moghaddam, C. Wang, J. B. Sorge, M. J. Brett, S. H. Bergens, *Electrochem. Commun.* **2015**, *60,* 109. (e) J. Lim, S. Yang, C. Kim, C. W. Roh, Y. Kwon, Y. T. Kim, H. Lee, *Chem. Commun.* **2016**, *52*, 5641.

[83] M. Abreu-Sepulveda, P. Trinh, S. Malkhandi, S. R. Narayanan, J. Jorne, D. J. Quesnel, J. A. Postonr, A. Manivannan, *Electrochim. Acta,* **2015**, *180*, 401.

[84] T. Audichon, S. Morisset, T. W. Napporn, K. B. Kokoh, C. Comminges, C. Morais, *Chemelectrochem* **2015**, *2*, 1128.

[85] (a) S. Trasatti, *Electrochim. Acta,* **2000**, *45*, 2377; (b) M. H. P. Santana, L. A. De Faria, *Electrochim. Acta* **2006**, *51*, 3578; (c) J. Aromaa, O. Forsen, *Electrochim. Acta* **2006**, *51*, 6104; (d) L. A. Naslund, C. M. Sanchez-Sanchez, A. S. Ingason, J. Backstrom, E. Herrero, J. Rosen, S. Holmin, *J. Phys. Chem. C* **2013**, *117*, 6126

[86] V. K. Puthiyapura, S. Pasupathi, S. Basu, X. Wu, H. N. Su, N. Varagunapandiyan, B. Pollet, K. Scott, Int. *J. Hydrogen Energy,* **2013**, *38,* 8605.

[87] (a) J. Ribeiro, A. R. de Andrade, *J. Electroanal. Chem.* **2006**, *592*, 153; (b) J. Ribeiro, M. S. Moats, A. R. De Andrade*, J. Appl. Electrochem.* **2008**, *38*, 767; (c) S. Aridizzone, C. L. Bianchi, G. Cappelletti, M. Ionita, A. Minguzzi, S. Rondinini, A. Vertova, *Journal of Electroanalytical Chemistry*, **2006**, *589*, 160-166.

[88] M. Musiani, F. Furlanetto, R. Bertoncello, *J. Electroanal. Chem.* **1999**, *465*, 160.

[89] (a) J. Gaudet, A. C. Tavares, S. Trasatti, D. Guay, *Chem. Mater.* **2005**, *17*, 1570. (b) X. Wu, J. Tayal, S. Basu, K. Scott*, Int. J. Hydrogen Energy,* **2011**, *36*, 14796.

[90] (a) M. V. Makarova, J. Jirkovsky, M. Klementova, I. Jirka, K. Macounova, P. Krtil, *Electrochim. Acta* **2008**, *53*, 2656; (b) L. M. Da Silva, J. F. C. Boodts, L. A. De Faria, *Electrochim. Acta* **2001**, *46*, 1369; (c) L. M. Da Silva, J. F. C. Boodts, L. A. DeFaria, *Electrochim. Acta* **2000**, *45*, 2719; (d) R. Forgie, G. Bugosh, K. C. Neyerlin, Z. C. Liu, P. Strasser, *Electrochem. Solid-State Lett.* **2010**, *13*, D36;

(e) V. Petrykin, K. Macounova, M. Okube, S. Mukerjee, P. Krtil, *Catal. Today* **2013**, *202*, 63.

[91] (a) V. Petrykin, K. Macounova, O. A. Shlyakhtin, P. Krtil, *Angew. Chem. Int. Ed.* **2010**, *49*, 4813; (b) V. Petrykin, K. Macounova, J. Franc, O. Shlyakhtin, M. Klementova, S. Mukerjee, P. Krtil, *Chem. Mater.* **2011**, *23*, 200.

[92] K. C. Neyerlin, G. Bugosh, R. Forgie, Z. C. Liu, P. Strasser, *J. Electrochem. Soc.*, **2009**, *156*, B363

[93] K. Macounova, M. Makarova, J. Franc, J. Jirkovsky, P. Krtil, *Electrochem. Solid-State Lett.* **2008**, *11*, F27.

[94] K. Kadakia, MK. Datta, *Int. Journal of Hydrogen Energy*, **2012**, *37*, 3001-3013.

[95] K. Kadakia, M. K. Datta, P. H. Jampani, S. K. Park, P. N. Kumta, *J. Power Sources*, **2013**, *222*, 313.

[96] O. I. Velikokhatnyi, K. Kadakia, M. K. Datta, P. N. Kumta, J*. Phys. Chem. C,* **2013**, *117*, 20542.

[97] a) K. S. Kadakia, P. Jampani, O. I. Velikokhatnyi, M. K. Daita, S. J. Chung, J. A. Poston, A. Manivannan, P. N. Kumta, *J. Electrochem. Soc.*, **2014**, *161*, F868; b) K. Kadakia, M. K. Datta, O. I. Velikokhatnyi, P. H. Jampani, P. N. Kumta, *Int. J. Hydrogen Energy,* **2014**, *39*, 664; c) K. Kadakia, M. K. Datta, O. I. Velikokhatnyi, P. Jampani, S. K. Park, S. J. Chung, P. N. Kumta, *J. Power Sources,* **2014**, *245,* 362.

[98] D. Bessarabov, H. Wang, H. Li, N. Zhao, **2016**, *PEM Electrolysis for Hydrogen Production: Principles and Applications*, CRC Press

[99] E. Antolini, E. R. Gonzalez, *Solid State Ionics,* **2009**, *180*, 746

[100] (a) H. Oh, K. Kim, H. Kim, *Int. J. Hydrogen Energy*, **2011**, *36*, 11564-71; (b) H. Huang, S. Chen, C. Yua, *J. Power Sources*, **2008**, *175*, 166-74; (c) X. Yu, S. Ye, *J. Power Sources*, **2007**, *172*, 133-44.

[101] (a) H. Oh, K. Kim, B. Roh, I. Hwang, H. Kim, *Electrochim. Acta*, **2009**, *54*, 6515-21; (b) H. Oh, J. Oh, S. Haam, K. Arunabha, B. Roh, I. Hwang, H. Kim, *Electrochem. Commun.*, **2008**, *10*, 1048-51; (c) S. Maass, F. Finsterwalder, G. Frank, R. Hartmann, C. Merten, *J. Power Sources*, **2008**, *176*, 444-51; (d) F. Claudel, L. Dubau, G. Berthomé, L. Sola-Hernandez, C. Beauger, L. Piccolo, F. Maillard, *ACS Catal.*, **2019**, *9(5)*, 4688-98.

[102] (a) E. Antolini, E. Gonzalez, *Solid State Ionics*, **2009**, *180*, 746-63; (b) Y. Lu, Y. Jiang, X. Gao, X. Wang, W. Chen, *J. Am. Chem. Soc.*, **2014**, *136*, 11687-97; (c) F. Luo, S. Liao, D. Dang, Y. Zheng, D. Xu, H. Nan, T. Shu, Z. Fu, *ACS Catal.*, **2015**, *5*, 2242-49; (d) R. Badam, M. Hara, H. Huang, M. Yoshimura, *Int. J. Hydrogen Energy*, **2018**, *43 (39)*, 18095-18104.

[103] (a) D. Resasco, G. Haller, *J. Catal.*, **1983**, *82*, 279-288; (b) S. Huang, P. Ganesan, S. Park, B. Popov, *J. Am. Chem. Soc.*, **2009**, *131*, 13898-13899; (c) Y. Liu, W. Mustain, *J. Am. Chem. Soc.*, **2013**, *135*, 530-533.

[104] M. Gawande, R. Pandey, R. Jayaram, *Cat Sci Technol.*, **2012**, *2*, 1113–25.

[105] a) H. Chhina, S. Campbell, O. Kesler, *J. Power Sources*, **2006**, *161*, 893; b) X. Z. Cui, J. L. Shi, H. R. Chen, L. X. Zhang, L. M. Guo, J. H. Gao, J. B. Li, *J. Phys. Chem. B*, **2008**, *112*, 12024;

c) R. Ganesan, J. S. Lee, *J. Power Sources*, **2006**, *157*, 217; d) T. Ioroi, Z. Siroma, N. Fujiwara, S. Yamazaki, K. Yasuda, *Electrochem. Commun.*, **2005**, *7*, 183; e) K. W. Park, K. S. Seol, *Electrochem. Commun.* **2007**, *9*, 2256; f) Y. Liu, S. Shrestha, W. E. Mustain, *ACS Catal.*, **2012**, *2*, 456; g) J. Suffner, S. Kaserer, H. Hahn, C. Roth, F. Ettingshausen, *Adv. Energy Mater.*, **2011**, *1*, 648. (h) J. Y. Xu, Q. F. Li, M. K. Hansen, E. Christensen, A. L. T. Garcia, G. Y. Liu, X. D. Wang, N. J. Bjerrum, *Int. J. Hydrogen Energy*, **2012**, *37*, 18629. (i) Y. Liu, W. E. Mustain, *J. Am. Chem. Soc.*, **2013**, *135*, 530

[106] M.A. Butler, R.D. Nasby, R.K. Quinn, *Solid State Communications*, **1976**, *19*, 1011–1014

[107] (a) C. Bignozzi, S. Caramori, V. Cristino, R. Argazzi, L. Meda, A. Tacca, Chem. *Soc. Rev.*, **2013**, *42*, 2228; (b) C. Janáky, W. Chnmanee, K. Rajeshwar, *Electrocatalysis*, **2013**, *4*, 382; (c) H. Zheng, J. Ou, M. Strano, R. Kaner, A. Mitchell, K. Kalantar-Zadeh, *Adv. Func. Mater.*, **2011**, *21*, 2175; (d) N. de Tacconi, C. Chenthamarakshan, G. Yogeeswaran, A. Watcharenwong, R. de Zoysa, N. Basit, K. Rajeshwar, *J. Phys. Chem.*, **2006**, *110*, 25347.

[108] (a) P. Kulesza, L. Faulkner, *Electroanal. Chem.* **1989**, *259*, 81. (a) A. Tseung, K. Chen, *Catal. Today.* **1997**, *38*, 439.

[109] (a) J. Suntivich, K. May, H. Gasteiger, J. Goodenough, Y. Shao-Horn, *Science*, **2011**, *334*, 1383. (b) L. Roen, C. Paik, T. Jarvi, *Electrochem. Solid-State Lett.* **2004**, *7*, A19. (c) S. Tauster, S. Fung, R. Garten, *J. Am. Chem. Soc.*, **1978**, *100*, 170. (d) Q. Fu, T. Wagner, *Surf. Sci. Rep.*, **2007**, *62*, 431.

[110] (a) B. O'Regan, M. Gratzel, *Nature*, **1991**, *353*, 737 - 740. (b) M. Gratzel, *Photochem. Rev.*, **2003**, *4*, 145 - 153.

[111] (a) A. Fujishima, K. Honda, *Nature*, **1972**, *238*, 37 - 38. (b) J. Nowotny, T. Bak, M.K. Nowotny, L.R. Sheppard, *Int. J. Hydrogen Energy*, **2007**, *32*, 2609 - 2629.

[112] (a) L. Znaidi, R. Seraphimova, J.F. Bocquet, C. Colbeau-Justin, C. Pommier, *Mater. Res. Bull.*, **2001**, *36*, 811 - 825. (b) T. Kasuga, M. Hiramatsu, A. Hoson, T. Sekino, K. Niihara, *Langmuir*, **1998**, *14*, 3160 - 3163. (c) G.K. Mor, O.K. Varghese, M. Paulose, K. Shankar, C.A. Grimes, *Sol. Energy Mater. Sol. Cells*, **2006**, 90, 2011 - 2075. (d) D. Kowalskia, D. Kimb, P. Schmuki, *Nano Today*, **2013**, *8*, 235 - 264. (e) Y. Suzuki, B. Pichon, D. D'Elia, C. Beauger, S. Yoshikawa, *J. Ceram. Soc. Jpn.*, **2009**, *117*, 381 - 394. (f) M. Schneider, A. Baiker, *J. Mater. Chem.*, **1992**, *2 (6)*, 587 - 589. (g) J.J. Pietron, A.M. Stux, R.S. Compton, D.R. Rolison, *Sol. Energy Mater. Sol. Cells*, **2007**, *91*, 1066 - 1074. (h) S. Boujday, F. Wünsch, P. Portes, J.-F. Bocquet, C. Colbeau-Justin, *Sol. Energy Mater. Sol. Cells*, **2004**, *83*, 421 - 433. (i) Y. Suzuki, M.-H. Berger, D. D'Elia, P. Ilbizian, C. Beauger, A. Rigacci, J.- F. Hochepied, P. Achard, *Nano*, 2008, *3 (4)*, 1 - 7. (j) D. D'Elia, C. Beauger, J.-F. Hochepied, A. Rigacci, M. Berger, N. Keller, V. Keller-Spitzer, Y. Suzuki, J. Valmalette, M. Benabdesselam, P. Achard, *Int. J. Hydrogen Energy*, **2011**, *36*, 14360 - 14373. (k) M. Popa, D. Macovei, E. Indrea, I. Mercioniu, I.C. Popescu, V. Danciu, *Microporous Mesoporous Mater.*, **2010**, 132, 80 – 86; (l) R. Genova-Koleva, F. Alcaide, G. Álvarez, P. Cabot, H. Grande, M. Martínez-Huerta, O. Miguel, *Energy Chem.*, **2019**, *34*, 227-239; (m) S. Schlicht, P. Büttner, J. Bachmann, ACS Appl. *Energy Mater.*, **2019**, *2 (3)*, 2344-2349.

[113] L. Wang, P. Lettenmeier, U. Golla-Schindler, P. Gazdzicki, N. Canas, T. Morawietz, R. Hiesgen, R. Hosseiny, A. Gago, K. Friedrich K, *Phys. Chem. Chem. Phys.*, **2016**, *18*, 4487-95.

[114] G. Chen, S. Bare, T. Mallouk, *J. Electrochem. Soc.*, **2002,** *149*, 1092 - 99.

[115] S. Siracusano, V. Baglio, C. D'Urso, V. Antonucci, A. Aricò, *Electrochemical Acta*, **2009**, *54 (26)*, 6292-6299.

[116] (a) X. J. Lu, W. G. Yang, Z. W. Quan, T. Q. Lin, L. G. Bai, L. Wang, F. Q. Huang, Y. S. Zhao, *J. Am. Chem. Soc.*, **2014**, *136*, 419. (b) W. Liu, A. K. Herrmann, N. C. Bigall, P. Rodriguez, D. Wen, M. Oezaslan, T. J. Schmidt, N. Gaponik, A. Eychmuller, *Acc. Chem. Res.*, **2015**, *48*, 154.

[117] W Hu, S. Chen, Q. Xia, *Int. J. Hydrogen Energy*, **2014**, *39*, 6967.

[118] C. Beauger, L. Testut, S. Berthon-Fabry, F. Georgy, L. Guetaz, *Microporous and Mesoporous Materials,* **2016**, *232*, 109 – 118

[119] H. S. Oh, H. N. Nong, P. Strasser, *Adv. Funct. Mater.*, **2015**, *25*, 1074.

[120] Y. Nannan, J. Qianqian, L. Jie, T. Jianguo, Arabian Journal of Chemistry, 2019 (in press)

[121] (a) L. Krishtalik, *Electrochimal Acta*, **1981**, *26 (3)*, 329-337; (b)Y. Li, F. Meng, S. Li, J. Zeng, Y. Chen, *ASC Catalysis*, **2018**, *8 (3)*, 7b-03949; (c) Y. Tong, P. Chen, T. Zhou, K. Xu, W. Chu, C. Wu, Y. Xie, *Angew. Chem. Int. Ed.*, **2017**, *56 (25)*, 7121; (d) J. De Tovar, N. Romero, S. A. Denisov, R. Bofill, C. Gimbert-Suriñach, D. Ciuculescu-Pradines, S. Drouet, A. Llobet, P. Lecante, V. Colliere, Z. Freixa, N. McClenaghan, C. Amiens, J. Garcia-Anton, K. Philippot, X. Sala, *Mater. Today Energy*, **2018**, *9*, 506 – 515.

[122] J. Geng, L. Kuai, E. Kan, Q. Wang, B. Geng, *Chemsuschem*, **2015**, *8 (4)*, 659-664

[123] T.N. Lambert, J.A. Vigil, S.E. White, D.J. Davis, S.J. Limmer, P.D. Burton, E.N. Coker, T.E. Beechem, M.T. Brumbach, *Chem. Commun.*, **2015**, *51 (46)*, 9511-9514

[124] D. Zhang, L. Meng, J. Shi, N. Wang, S. Liu, C. Li, *Electrochim. Acta*, **2015**, *169*, 402-408

[125] T. Chinnusamy, V. Rodionov, F.E. Kühn, O. Reiser*, Nat. Chem.*, **2011**, *3 (1)*, 79-84

[126] (a) M.D. Koninck, S.C. Poirier, B. Marsan, *J. Electrochem. Soc.*, **2006**, *153 (12)*, 381-A388; (b) R. Berenguer, A.L. Rosatoro, C. Quijada, E. Morallón, *J. Phys. Chem. C*, **2008**, *112 (43)*, 16945-16952; (c) A.L. Rosatoro, R. Berenguer, C. Quijada, F. Montilla, E. Morallón, J.L. Vazquez, *J. Phys. Chem. B*, **2006**, *110 (47)*, 24021-24029; (d) S.K. Bikkarolla, P. Papakonstantinou, *J. Power Source*, **2015**, *281*, 243-251.

[127] (a) P. Chen, K. Xu, Y. Tong, X. Li, S. Tao, Z. Fang, W. Chu, X. Wu, C. Wu, *Cheminform*, **2016**, *3 (2)*, 236-242; (b) K. Xu, P. Chen, X. Li, Y. Tong, H. Ding, X. Wu, W. Chu, Z. Peng, C. Wu, Y. Xie, J. Am. *Chem. Soc.*, **2015**, *137 (12)*, 4119-4125; (c) C.G. Read, J.F. Callejas, C.F. Holder, R.E. Schaak, *ACS Appl. Mater. Interfaces*, **2016**, *8 (20)*, 12798-12803 (d) T. Liu, L. Xie, J. Yang, R. Kong, G. Du, A.M. Asiri, X. Sun, L. Chen, *ChemElectroChem*, **2017**, *4 (8)*, 840-1845.

[128] (a) Electrochemical Process Engineering: A Guide to the Design of Electrolytic Plant, F. Goodridge, and K. Scott, Plenum Publishing Corporation (Eds.), **1995.** (b) Electrochemical Engineering: Science and Technology in Chemical and Other Industries, H. Wendt, G. Kreysa, Springer, **1999.**

[129] P. Millet, S. Grigoriev, V. Porembskiy, *Int. J. Energy Res.*, **2013**, *37*, 449–456.

[130] PEM Water Electrolysis, D. Bessarabov, P. Millet, Elsevier Ltd, **2018**, pp 61-94 (Chapter 3)

[131] P. Millet, 2008. Final report of the GenHyPEM FP6 research project, FCH-JU. European Commission, Brussel, Belgium, **2008**.

[132] P. Millet, F. de Guglielmo, S. Grigoriev, V. Porembskiy, *Int. J. Hydrogen Energy*, **2012**, *37*, 17478-17487.

[133] S. Cherevko, *Current Opinion in Electrochemistry*, **2018**, *8*, 118–125

[134] (a) S. Cherevko, S. Geiger, O. Kasian, A. Mingers, K. Mayrhofer, *J. Electroanal. Chem.*, **2016**, *774*, 102–110. (b) S. Cherevko, S. Geiger, O. Kasian, A. Mingers, K. Mayrhofer, *J. Electroanal. Chem.*, **2016**, *774*, 69–78. (c) S. Siracusano, N. Hodnik, P. Jovanovic, F. Ruiz-Zepeda, M. Šala, V. Baglio, A. Aricò, *Nano Energy*, **2017**, *40*, 618–632. (d) N. Hodnik, P. Jovanovic, A. Pavlišic, B. Jozinovic, M. Zorko, M. Bele, V. Šelih, M. Šala, S. Hocevar, M. Gaberšcek, *J. Phys. Chem. C*, **2015**, *119*, 10140–10147. (e) O. Kasian, S. Geiger, P. Stock, G. Polymeros, B. Breitbach, A. Savan, A. Ludwig, S. Cherevko, K. Mayrhofer, *J. Electrochem. Soc.*, **2016**, *163*, F3099–F3104.

[135] S. Cherevko, A. Zeradjanin, A. Topalov, N. Kulyk, I. Katsounaros, K. Mayrhofer, *ChemCatChem*, **2014**, *6*, 2219–2223.

[136] (a) E. Fabbri, A. Habereder, K. Waltar, R. Kotz, T. Schmidt, *Catal. Sci. Technol.*, **2014**, *4*, 3800–3821. (b) R. Kötz, H. Lewerenz, P. Brüesch, S. Stucki, *J. Electroanal. Chem.*, **1983**, *150*, 209–216.

[137] Cobalt, rhodium and iridium, in: N.N. Greenwood, A. Earnshaw (Eds.), Chemistry of the Elements (Second Edition), Butterworth-Heinemann, Oxford, **1997**. pp. 1113–1143 (Chapter 26).

[138] O. Kasian, J. Grote, S. Geiger, S. Cherevko, K. Mayrhofer, *Angew Chem. Int. Ed. Engl.*, **2018**, *57*, 2488–2491.

[139] (a) H. Oh, H. Nong, T. Reier, A. Bergmann, M. Gliech, J. Ferreira de Araújo, *Journal of the American Chemical Society*, **2016**, 138, 12552-12563. (b) E. Oakton, D. Lebedev, M. Povia, D. Abbott, E. Fabbri, A. Fedorov, *ACS Catalysis*, **2017**, *7*, 2346-2352

[140] (a) P. Shiny, A. Mukherjee, N. Chandrasekaran, *Int. J. Pharm. Pharm. Sci.*, **2013**, *5*, 239-241. (b) R. Ladj, A. Bitar, M. Eissa, Y. Mugnier, R. Le Dantec, H. Fessi, A. Elaissari, *J. Mater. Chem. B*, **2013**, *1*, 1381-1396.

[141] (a) K. Momose, S. Takayama, E. Hata, Y. Tomita, *Opt. Lett.*, **2012**, *37*, 2250-2252. (b) A. Stalmashonak, A. Abdolvand, G. Seifert, *Appl. Phys. Lett.*, **2011**, *99*, 26765-26775.

[142] (a) A. Tkachenko, H. Xie, D. Coleman, W. Glomm, J. Ryan, M. Anderson, S. Franzen, D. Feldheim, *Am. Chem. Soc.*, **2003**, *125*, 4700-4701; (b) A. Templeton, W. Wuelfing, R. Murray, *Acc. Chem. Res.*, **2000**, *33,* 27-36; (c) L. Peyser, A. Vinson, A. Bartko, A. Dickson, *Science*, **2001**, *291*, 103-106 ; (d) D. Astruc, F. Lu, J. Aranzaes, *Angew. Chem. Int. Ed.*, **2005**, *44*, 7852-72; (e) M. Moreno-Manas, R. Pleixats, *Acc. Chem. Res.*, **2003**, *36*, 638-643; (f) J. Aiken, R. Finke, *J. Mol. Cat. A: Chem.*, **1999**, *145*, 1-44; (g) A. Roucoux, J. Schulz, H. Patin, *Chem. Rev.*, **2002**, *102*, 3757-3778; (h) P. Duran, G.

Rothenberg, *App. Organomet. Chem.*, **2008**, *22*, 288-99; (i) J. Durand, E. Teuma, M. Gomez, *Eur. J. Inorg. Chem.*, **2003**, *191*, 187- 207.

[143] a) R. Crabtree, E. F. Peris, Química Organometálica de los Metales de Transición, Publicaciones de la Universitat Jaume I, Castellón, **1997**; b) R. Whyman, Applied Organometallic Chemistry and Catalysis, Oxford University Press, Oxford, **2001**

[144] (a) P. Edwards, R. Johnston, C. Rao, On the Size-Induced Metal-Insulator Transition in Clusters and Small Particles, Metal Clusters in Chemistry, Ed., Wiley, Weinheim, **1999**. (b) E. Roduner, Chem. Soc. Rev., **2006**, 35, 583-592. (c) B. Teo, N. Sloane, *Inorg. Chem.*, **1985**, *24*, 4545-4558. (d) J. Aiken III, R. Finke, *Mol Catal. A: Chem.*, **1999**, *145*, 1-44. (e) C. Poole, F. Owens, Introducción a la Nanotecnología, Reverté, Barcelona, **2007**.

[145] OBEN Science website

[146] A. Roucoux, J. Schulz, H. Patin, *Chem. Rev.*, **2002**, *102*, 3757-3778.

[147] H. Bönemman, G. Braun, W. Brijoux, R. Brinkmann, A. Schulze, K. Seevogel, K. Siepen, *J. Organomet. Chem.,* **1996**, *520*, 143-162.

[148] F. Benfield, M. Green, J. Odgen, D. J. Young, *J. Chem. Soc. Chem. Commun.* **1973**, 866-867.

[149] M. Reetz, W. Heilbig, *J. Am. Chem. Soc.* **1994**, *116*, 7401-7402.

[150] G. Pajonk, *Applied Catalysis,* **1991**, *72*, 217-266.

[151] W. Lei, N. Mochalin, D. Liu, S. Qin, Y. Gogotsi, Y. Chen, *Nature comm.*, **2015**, *6*, 8849

[152] H. Von Werner, *Acta Cryst.*, **1956**, *9*, 515-520

[153] J. M. Le Cleac'h, Musée de minéralogie MINES ParisTech Cassitérite 16652, Gitebe, Rwanda.

[154] C. Kilic, and A. Zunger, *Physical Review Letters*, **2002**, *88,* 9.

[155] (a) V. Gokulakrishnan*, Journal of Materials Science*, **2011**, *46*(16), 5553-5558. (b) D. Szczuko, *Applied Surface Science*, **2001**, *179(1-4),* 301-306

[156] E. Leite, I. Weber, E. Longo, J. A. Varela, *Advanced Materials*, **2000**, *12(13),* 965.

[157] C. Kilic, A. Zunger, *Physical Review Letters*, **2002**. *88 (9)*.

[158] J. Harreld, J. Sakamoto, B. Dunn, *Journal of Power Sources*, **2003**, *115(1)*, 19-26.

[159] (a) C. Gervillié, A. Boisard, J. Labbéc, S. Berthon-Fabry, K. Guérin, *Synthetic Metals*, **2020**, *267*, 11647-11657; (b) C. Gervillié, A. Boisard, J. Labbéc, K. Guérin, S. Berthon-Fabry, Materials Chemistry and Physics, 2021, 257, 123461-123473.

[160] (a) J. Viricelle, *et al.*, *26th European Conference on Solid-State Transducers*, Eurosensor **2012**, *2012* (*47),* 655-658. (b) S. Shukla, *Sensors and Actuators B-Chemical*, **2003**. *96(1-2)*, 343-353. (c) M. D'Arienzo, *et al.*, *Chemistry of Materials*, **2010**, *22(13)*, 4083-4089. (c) A. Gaddari, *et al.*, *Sensors and Actuators B-Chemical*, **2013**, *176*, 811-817.

[161] G. Tournier, C. Pijolat, R. Lalauze, B. Patissier, *Sensors and Actuators B-Chemical*, **1995**, *26(1-3)*, 24-28.

[162] N. Greenwood, A. Earnshaw, Chemistry of the Elements. Oxford: Pergamon Press, **1984**

[163] Material Name: stannic oxide. Museum of Fine Arts, Boston, **2007**.

[164] A. B. Searle, The Glazer's Book. The Technical Press Limited. London. **1935**.

[165] Hermann Kühn, Blei-Zinn-Gelb und seine Verwendung in der Malerei, Farbe und Lack 73, **1967**.

[166] E. Bourry, A Treatise On Ceramic Industries, Fourth edition. Scott, Greenwood & son. London, **1926**.

[167] C. Parmelee, C. Harman. Ceramic Glazes, Third edition. Cahners Books, Boston, Massachusetts, **1973**.

[168] A. Ahmed, S. El-Hakam, A. Khder, W. Abo ElYazeed, *J. Mol. Catal. A: Chem.*, **2013**, *366*, 99–108.

[169] V. S. Marakatti, P. Manjunathan, A. B. Halgeri, G. V. Shanbhag, Catal. *Sci. Technol.*, **2016**, *6*, 2268–2279

[170] D. Mohanta, M. Ahmaruzzaman, *RSC Adv.*, **2016**, *6*, 110996–111015.

[171] (a) Z. Zhang, L. Wang, Y. Jin, F. Xiao, S. Wang, *Part. Part. Syst. Charact.*, **2016**, *33*, 519–523. (b). Y. Sun, F. Lei, S. Gao, B. Pan, J. Zhou, Y. Xie, *Angew. Chem., Int. Ed. Engl.*, **2013**, *52*, 10569-10572. (c) J. Xu, D. Aili, Q. Li, C. Pan, E. Christensen, J. O. Jensen, W. Zhang, G. Liu, X. Wang, N. J. Bjerrum, *J. Mater. Chem. A*, **2013**, *1*, 9737

[172] (a) A. Bhattacharjee, M. Ahmaruzzaman, T. Sinha, Spectrochim. *Acta, Part A*, 2015, *136*, 751–760. (b) A. Bhattacharjee, M. Ahmaruzzaman, *Mater. Lett.*, **2015**, *145*, 74–78.

[173] P. Manjunathan, R. Ravishankar, G. Shanbhag, *ChemCatChem*, **2016**, *8*, 631–639.

[174] W. Xie, L. Zhao, *Energ Conver Manage*, **2013**, *76*, 55–62.

[175] G. Collins, M. Bl¨omker, M. Osiak, J. D. Holmes, M. Bredol, C. O'Dwyer, *Chem. Mater.*, **2013**, *25*, 4312–4320

[176] W. Xie, T. Wang, *Fuel Process Technol*, **2013**, *109*, 150–5.

[177] (a) R. Kötz, S. Stucki and B. Carcer, *J. Appl. Electrochem.*, **1991**, *21*, 14-20. (b) F. Vicent, E. Morallón, C. Quijada, J. L. Vázquez, A. Aldaz and F. Cases, *J. Appl. Electrochem.*, **1998**, *28*, 607-612.

[178] (a) W. Samad, W. Wan Roslam, N. Nordin, M. Yarmo, M. Yusop, *Malaysian Journal of Analytical Sciences*, **2015**, *19(1)*, 55-64. (b) W. Samad, W. Wan Isahak, M. Yarmo, M. Yusop, *Materials Science Forum*, **2017**, *888*, 496–502.

[179] (a) G. Liu, A. Bonakdarpour, X. Wang, *Electrocatalysis*, **2019**, *10*, 262–271. (b) J. Ayoub, R. De Souza, J. Silva, R. Piasentin, E. Spinacé, M. Santos, A. Oliveira, Int. J. Electrochem. Sci., 2012, 7, 11351 – 11362.

[180] (a) A. Marshall, R. Haverkamp, *Electrochemical Acta*, **2010**, *55*, 1978-1984 (b) H.-S. Oh, H. N. Nong, T. Reier, M. Gliech, P. Strasser, *Chem. Sci.*, **2015**, *6*, 3321. (c) G. Liu, J. Xu, Y. Wang, X. Wang, *J.*

Mater. Chem. A, **2015**, 3, 20791-20800. (d) D. Böhm, M. Beetz, M. Schuster, K. Peters, A. G. Hufnagel, M. Döblinger, B. Böller, T. Bein, D. Fattakhova-Rohlfing, *Adv. Funct. Mater.*, **2019**, *19*, 6670.

[181] K. Puthiyapura, S. Pasupathi, H. Su, X. Liu, B. Pollet, K. Scott, *Int. J. of Hydrogen Energy*, **2014**, *39* (5), 1905-1913.

[182] H. Ohno, S. Nohara, K. Kakinuma, M. Uchida, H. Uchida, *Catalysts*, **2019**, *9*, 74-86.

[183] (a) I. Savych, S. Subianto, Y. Nabil, S. Cavaliere, D. Jonesa, J. Rozièrea, *Phys. Chem. Chem. Phys.*, **2015**, *17*, 16970 -16976; (b) E. Fabbri, A. Rabis, Y. Chino, M. Uchida, T. J. Schmidt, *Electrochemistry Communications*, **2017**, *83*, 90-95; (c) P. Mohanta, C. Glökler A. Orozco, L. Jörissen, *International Journal of Hydrogen Energy*, **2017**, *42 (46)*, 27950-2796; (d) Y. Liu, W. E. Mustain, *J. Am. Chem. Soc.* **2013**, *135*, 530−533; (e) H. Chhina, S. Campbell, O. Kesler, *Journal of Power Sources*, **2006**, *27*, 893-900; (f) P. Zhang, S. Huang, B. N. Popov, *J. Electrochem. Soc.*, **2010**, *157 (8)*, B1163-B1172; (g) Y. Senoo, K. Taniguchi, K. Kakinuma, M. Uchida, H. Uchida, S. Deki, M. Watanabe, *Electrochemistry Communications*, **2015**, *51*, 37-40; (h) E. Fabbri, A. Rabis, Y. Chino, U. Uchida, T. Schmidt, *Electrochemistry Communications*, **2017**, *83*, 90-95.

[184] (a) J. Tong, Y. Liu, Q. Peng, W. Hu, Q. Wu, *J. Mater. Sci.*, **2017**, *52*, 13427–13443; (b) C. Massué, V. Pfeifer, X. Huang, J. Noack, A. Tarasov, S. Cap, R. Schlögl, *ChemSusChem*, **2017**, *10*, 1943–1957. (c) L. Sola-Hernandez, F. Claudel, F. Maillard, C. Beauger, *International Journal of Hydrogen Energy*, **2019**, *44 (45)*, 24331-24341. (d) H. N. Nong, H.-S. Oh, T. Reier, E. Willinger, M.-G. Willinger, V. Petkov, D. Teschner, P. Strasser, *Angew. Chemie Int. Ed.*, **2015**, *54*, 2975–2979; (e) H.-S. Oh, H. N. Nong, D. Teschner, T. Reier, A. Bergmann, M. Gliech, J. Ferreira de Araújo, E. Willinger, R. Schloegl, P. Strasser, *J. Am. Chem. Soc.*, **2016**, *138*, 12552-12563; (f) A. Hartig-Weiss, M. Miller, H., A. Schmitt, A. Siebel, A.T. S. Freiberg, H. A. Gasteiger, H.A El-Sayed, *ACS Appl. Nano Mater,* **2020**, *3*, 2185–2196; (g) G. da Silva, S. Venturini, S. Zhang, M. Löffler, C. Scheu, K. J. J. Mayrhofer, E. Ticianelli, S. Cherevko, *ChemElectroChem*, **2020**, *7*, 2330; (h) V. Puthiyapura, M. Mamlouk, S. Pasupathi, B. Pollet, S. Scott, *J. Power Sources*, **2014**, *269*, 451−460; (i) Z. Rajan, T. Binninger, P. Kooyman, D. Susac, R. Mohamed, *Catal. Sci. Technol.*, **2020**, *10*, 3938-3948; (j) V. Saveleva, L. Wang, O. Kasian, M. Batuk, J. Hadermann, J.-J. Gallet, F. Bournel, N. Alonso-Vante, A. Gago, G. Ozouf, C. Beauger, K. J. J. Mayrhofer, S. Cherevko, A. S. K. A. Friedrich, S. Zafeiratos, E. R. Savinova, *ACS Catal.*, **2020**, *10*, 2508−2516.

[185] (a) S. Yang, D. Chung, Y. Tak, J. Kim, H. Han, J. Yu, A. Soon, Y. Sung, H. Lee, *Appl. Catal., B*, **2015**, *35*, 174−175; (b) S. Park, H. Lim, Y. Kim, *ACS Catal.*, **2015**, *5*, 3995; (c) A. Lewera, L. Timperman, A. Roguska, N. Alonso-Vante, *N. J. Phys. Chem. C,* **2011**, *115,* 20153; (d) J. Jaksic, F. Nan, G. Papakonstantinou, G. Botton, M. Jaksic, *J. Phys. Chem. C,* **2015,** *119*, 11267; (e) C. Campbell, *C. T. Nat. Chem.*, **2012**, *4*, 597.

[186] (a) E. Fabbri, A. Rabis, R. Kotz, T. J. Schmidt, Phys. Chem. Chem. Phys. 2014, 16, 13672. (b) S. Geiger, O. Kasian, A. M. Mingers, K. J. J. Mayrhofer, S. Cherevko, *Sci. Rep.* **2017**, *7*, 4595.

[187] (a) G. Cognard, G.Ozouf, C. Beauger, I. Jimenez-morales, S. Cavaliere, D. Jones, J. Roziere, M. Chatenet, F. Maillard, *Electrocatalysis,* **2017**, *8*, 51; (b) G. Cognard, G. Ozouf, B. Beauger, G. Berthome, D. Riassetto, L. Dubau, R. Chattot, M., Chatenet, F. Maillard, *Applied Catalysis B: Environmental*, **2017**, *201*, 381-390; (c) G. Cognard, G. Ozouf, C. Beauger, L. Dubau, M. López-Haro, M. Chatenet, F.

Maillard, *Electrochimica Acta, 2017, 245* 993–1004; (d) G. Ozouf, G. Cognard, F. Maillard, M. Chatenet, L.Guétaz, M. Heitzmann, P.Jacques, C. Beauger, *Journal of the Electrochimical Society*, **2018**, *165 (6),* F3036-F3044.

[188] L. Dubau, F. Maillard, M. Chatenet, S. Cavaliere, I. Jiménez-Morales, A. Mosdale, R. Mosdale, *Energies*, **2020**, *13*, 403.

[189] S. Abbou, R. Chattot, V. Martin, F. Claudel, L. Solà-Hernández, C. Beauger, L. Dubau, F. Maillard, *ACS Catalysis*, **2020**, *10 (13)*, 7283–7294

[190] (a) A. Corma, *Chem Rev*, **1997**, *97*, 2373-420. (b) U. Ciesla, F. Schüth, *Microporous Mesoporous Mater*, **1999**, *27*, 131-49. (c) C. Kresge, M. Leonowicz, W. Roth, J. Vartuli, J. Beck, *Nature*, **1992**, *359*, 710. (d) J. Beck, J. Vartuli, W. Roth, M. Leonowicz, C. Kresge, K. Schmitt, C. Chu, D. Olson, E. Sheppard, S. McCullen, *J Am Chem Soc*, **1992**, *114*, 10834-43. (e) P. Celdeira, M. Goncalves, F. Figueiredo, S. Dal Bosco, D. Mandelli, W. Carvalho, *Appl Catal Gen.*, **2014**, *478*, 98–106. (f) M. Moritz, M. Geszke-Moritz, *Mater Sci Eng C.*, **2015**, *49*, 114–51. (g) C. Lee, T. Lin, C. Mou, *Nano Today*, **2009**, *4*, 165–79.

[191] (a) P. Bhanja, B. Mohanty, A. K. Patra, S. Ghosh, B. Jena, A. Bhaumik, B. Asim, *ChemCatChem.*, **2018**, 11 (1), 583-592; (b) K. Kakinuma, M. Uchida, T. Kamino, H. Uchida, M. Watanabe, *Electrochim. Acta*, **2011**, *56*, 2881-2887; (c) D. Lebedev, C. Copéret, *ACS Appl. Energy Mater.*, **2019**, *2*, 1, 196-200; (d) F. Takasaki, S. Matsuie, Y. Takabatake, Z. Noda, A. Hayashi, Y. Shiratori, K. Ito, K. Sasaki, *Journal of The Electrochemical Society*, **2011**, *158*, B1270-1275; (e) G. Ozouf, C. Beauger, *Journal of Materials Science*, **2016**, *51(11)*, 5305-5320.

[192] L. Wang, F. Song, G. Ozouf, D. Geiger, T. Morawietz, M. Handl, P. Gazdzicki, C. Beauger, U. Kaiser, R. Hiesgen, A. Gago, K. Andreas Friedrich, *J. Mater. Chem. A*, **2017***, 5*, 3172-3178.

[193] (a) T. Baumann, S. Kucheyev, A. Gash, J. Satcher Jr., *Advanced Materials*, **2005**, *17(12),* 1546-1548; (b) A. Chizhov, M. Rumyantseva, A. Gaskov, *Inorganic Materials*, **2013**. *49(10)*, 1000-1004; (c) S. Wang, N. Wu, *Journal of Non-Crystalline Solids*, **1998**, *224 (3)*, 259-266.

[194] A. Gaddari, F. Berger, M. Amjou, J.B. Sanchez, M. Lahcini, B. Rhouta, D. Mezzane, C. Mavon, E. Beche, V. Flaud, *Sensors and Actuators B-Chemical*, **2013**. *176*, 811-817.

[195] (a) S. Lekshmy, G. Daniel, K. Joy, *Applied Surface Science*, **2013**. *274*: p. 95-100. 229 (b) N. Ibrahim, *et al.*, *Applied Surface Science*, **2013**, *271*, 260-264. (c) M. Aziz, S. Abbas, W. Baharom, *Materials Letters*, **2013**. *91*, 31-34. (d) M. Aziz, S. Abbas, W. Wan Baharom, W. Wan Mahmud, *Materials Letters*, **2012**. *74*, 62-64. (e) H. Kose, A. Aydin, H. Akbulut, *Applied Surface Science*, **2013**. *275*, 160-167.

[196] A. Ahmed, A. Azam, M. Muhamed Shafeeq, M. Chaman, S. Tabassum, *Journal of Physics and Chemistry of Solids*, **2012**, *73(7)*, 943-947.

[197] R. Huang, L. Hou, B. Zhou, Q. Zhao, S. Ren, *Journal of Non-Crystalline Solids***, 2005**, *351(1)*, 23-28.

[198] (a) S. Mihaiu, L. Marta, M. Zaharescu, *Journal of the European Ceramic Society*, **2007**, *27(2-3)*, 551-555; (b) S. Lee, J. Lee, T. Oh, Y. Kim, *Solar Energy Materials and Solar Cells*, **2003**, *75(3-4),* 481-487;

(c) S. de Monredon, *et al.*, *Journal of Materials Chemistry*, **2002**, *12(8)*, 2396-2400; (d) K. Severin, T. Abdel-Fattah, T. Pinnavaia, *Chemical Communications*, **1998,** *(14)*, 1471-1472; (e) A. Kumar, P. Zhang, A. Vincent, R. McCormack, R. Kalyanaramane, H.Cho, S. Seal, *Sensors and Actuators B-Chemical*, **2011**, *155(2)*, 884-892;

[199] N. Markovic, *et al.*, *Fuel Cells*, **2001**, *1(2)*, 105-116.

[200] J. Correa, A. Agrios, *Appl. Mater. Interfaces,* **2014**, *6 (21)*, 19137-19143

[201] (a) D. John Wright, N. Sommerdijk, *Sol-Gel Materials Chemistry and Applications*, Ed. Gordon and Breach Scinece Publishers, **2001**. (b) C. Jeffrey Brinker, *Sol-Gel Science*, Ed. Academic Press,**1990**.

[202] Guillaume Ozouf, **2017**, *Electrodes à base d'aérogels de SnO2, résistantes à la corrosion pour la réduction de l'oxygène dans les piles à combustible à membrane échangeuse de protons (PEMFC)*, PSL Research University, MINES ParisTech, Sophia Antipolis.

[203] S. Kistler, *Nature*, **1931**, *127*, 741-741.

[204] U. Schubert, N. Husing, *Angew. Chem. Int. Ed,* **1998**, *37*, 22-45

CHAPTER 2: Materials and methods

This chapter presents the materials or reagents, as well as the procedures performed for the synthesis, characterization and evaluation of tin oxide-based aerogels as catalysts supports for the OER in PEMWE cells.

In this study the tin oxide-based materials were prepared by a sol-gel method from a previously prepared tin alkoxide precursor, following the protocol explained in section II.2 of this chapter. Such aerogels were dried with CO_2 under supercritical conditions and calcined under air at 600°C. After the full characterization of this materials with the techniques described among this chapter, Iridium oxide nanocatalysts were deposited over as-prepared aerogels by chemical reduction (described in section II.3 of this chapter) in order to prepare the anode electrocatalyst for Oxygen Evolution Reaction. Once the electrocatalysts were prepared, and fully characterized, the evaluation by electrochemical techniques using a Rotating Disc Electrode (RDE) was performed. The activity and stability of developed electrocatalysts is evaluated and discussed on Chapter 4.
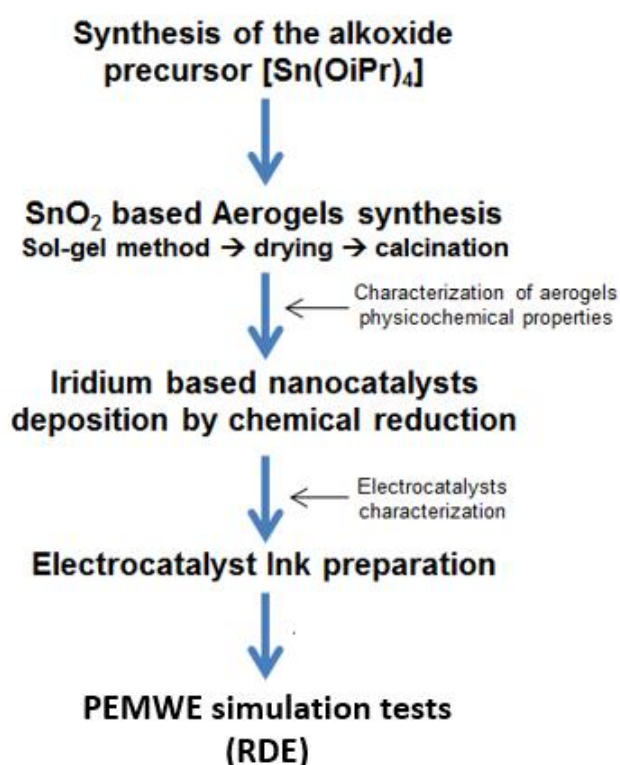
Figure 2.1 Chronological steps of the study.

I Materials

For [Sn(OiPr)$_4$] alkoxide precursor preparation, tin tetrachloride (SnCl$_4$, 99%) was purchased by Across Organics, diethylamine (C$_4$H$_{11}$N, 99%) was delivered by Merck, *tert*-butanol (C$_4$H$_{10}$O, 99.5%) was purchased by Sigma-Aldrich, heptane (C$_7$H$_{16}$, 99%) and isopropanol (C$_3$H$_8$O, 99.5%) were delivered by Fischer Scientific.

For the aerogel synthesis, the [Sn(OiPr)$_4$] alkoxide precursor was previously prepared by our own, the Sb and Ta dopant precursors Antimony(III) isopropoxide (Sb[OCH(CH$_3$)$_2$]$_3$, 99.9%) and Tantalum(V) isopropoxide (Ta[OCH(CH$_3$)$_2$]$_5$, 99.9%) were purchased by Alfa Aesar, Nitric acid (HNO$_3$, 2M) was delivered by Fischer Scientific, Sodium hydroxide (NaOH, 98%) purchased by Alfa Aesar was diluted in Deionized (DI) water (18.2 MΩ·cm), supplied from ultrapure water plants (Smart2Pure, Thermo Scientific).

For Ir deposition over Sn aerogels, or Ir NPs preparation, the metallic iridium(III) chloride precursor (IrCl$_3$, 99.9%) and the stabilizing agent hexadecyltrimethylammonium bromide, CTAB, (C$_{19}$H$_{42}$BrN, ≥98%) were purchased by Sigma Aldrich and the reducing agent Sodium borohydride (H$_4$BNa, 99%) was delivered by Across Organics.

For the catalyst ink preparation, a Nafion® solution (5%w/w in water and 1-propanol), purchased by Alfa Aesar, was used. Electrolyte for electrochemical measurements (HNO$_3$, 95-97%) was purchased by Sigma Aldrich, which was diluted with D.I water (Smart2Pure, Thermo Scientific) for a 0.05M solution.

WO$_3$ aerogel materials were prepared using tungsten(VI) oxychloride (WOCl$_4$, 98%) and Epichlorohydrin (>99%), both purchased by Sigma Aldrich.

II Physicochemical characterization

On this section are presented the different methods and techniques used for characterizing the physicochemical properties of the prepared materials.

II.1 Structure and morphology

II.1.1 X-Ray diffraction (XRD)

XRD analyses were performed using an X'Pert pro-Philips diffractometer (Cu Kα of λ = 1.5405 Å), operating at 45 kV and 30 mA. Data were collected from 20° to 90° in 2-θ mode with a Pixel counter. The crystallites size was determined using the Debye-Scherer method. For tin oxide aerogels we considered the (211 orientation), and for metallic Iridium, (Ir(0), the (111) orientation was selected.

II.1.1.2 Scanning Electron Microscope (SEM)

The morphology of the synthesized aerogels was determined using a Supra 40 SEM equipped with a Gemini column, and operated at 3.00 kV. Samples were deposited onto adhesive conducting carbon tapes and coated with a 7 nm thick platinum layer, using a Quorum (Q150T).

II.1.1.3 Transmission Electron Microscope (TEM)

In order to analyze the Iridium based nanocatalysts, with diameter sized around 2 nm, TEM measurements were performed using a JEOL 2010 operated at 200 kV (point-to-point resolution of 0.19 nm).

These measures were all carried out at CEA / Liten in Grenoble.

II.1.1.4 Nitrogen sorption measurements

Nitrogen sorption analyses were performed with a Micrometrics ASAP 2020. Before analyses, samples were degassed for 120 min at 100 °C and 10 μm Hg. For specific surface area determination, the Brunauer-Emmett-Teller (BET) model was applied. The pore size distributions were determined by applying the Barret-Joyner-Halenda (BJH) method to the desorption branch of the isotherms. The t-plot construction using Harkins-Jura correlation was

used for microporosity assessment. We assumed that the samples were mechanically strong enough after calcination to withstand the pressure applied during the experiment when using this technique. An error of a 10% was considered on the obtained results.

II.2 Chemical composition

II.2.1 Energy Dispersive X-ray Spectroscopy (EDX)

The samples bulk chemical compositions were analyzed by Energy Dispersive X-ray Spectroscopy (EDX) performed during SEM observations with a Philips XL30 operated at 15kV.

II.2.2 X-ray Photoelectron Spectroscopy (XPS)

Insights into the near-surface chemical composition were obtained by X-ray Photoelectron Spectroscopy (XPS) using a Thermo-Scientific K-Alpha system. The spectrometer was equipped with a monochromatic Al $K\alpha$ source and a low energy flood-gun for charge compensation. The ellipsoid spot size is about 350 µm x 700 µm

II.3 Conductivity tests

The electronic conductivity of the synthesized aerogels was determined by using a homemade conductivity cell, made up of two copper electrodes (S = 0,785 cm²) surrounded with a Teflon ring. Approximatively 100 mg of sample were introduced between these two electrodes (see **Figure 2.2**). A potentiostat was used to apply a current of 100, 150, 250 and 400 mA and the voltage was measured for each current. The homemade conductivity cell was placed in a press and measurements were made at room temperature with 1 ton of pressure. The conductivity (σ, S/cm) was calculated with the formula $\boldsymbol{\sigma = (e \cdot I \cdot U^{-1} \cdot S^{-1}_{electrode})}$ where "**e**" is the thickness of the sample (cm), "**I**" the applied current (mA), "**$S_{electrode}$**" the surface of the electrode (cm²) and "**U**" the measured voltage (mV).
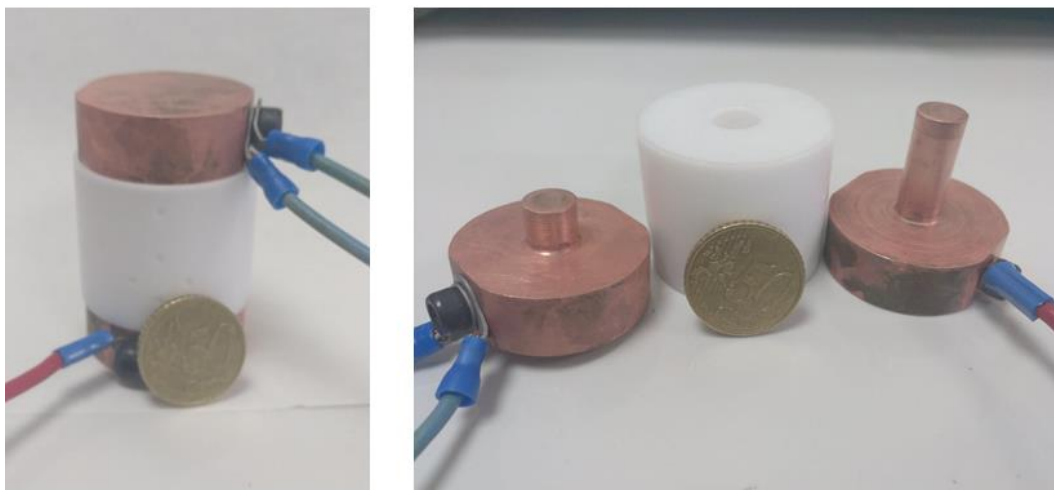
Figure 2.2 Homemade conductivity cell picture assembled (left) and disassembled (right).

III Electrochemical characterization by Rotating Disc Electrode (RDE)

The electrocatalytic performance of the synthesized nanocatalysts towards the OER, based on Iridium nanocatalysts deposited onto tin oxide aerogels, were assessed in rotating disk electrode (RDE).

III.1 Cell presentation

All performed experiments were carried out by using a Biologic-HCP803 potentiostat and a three-electrodes electrochemical cell.

The RDE assembly shown on **Figure 2.3** is made up of:

1. The working electrode (WE), that consists in a glassy carbon (GC) rotating disk electrode (RDE) with a diameter of 0.5 cm and a surface of 0.196 cm^2. It was covered with a thin-layer film of catalyst added by drop casting.

2. The counter electrode (CE), a Pt foil.

3. A reference electrode (Ref), which in our case was a Standard Hydrogen Electrode (SHE). Such electrode consists of a platinum wire in contact with gaseous hydrogen (H_2) and the electrolyte solution (H_2SO_4 0.05 M).

4. A gas inlet that allows the gas injection into the cell in order to degas the electrolyte or just for maintaining a desired atmosphere inside the cell.

5. A bubbler that allows the ejection of injected gas.
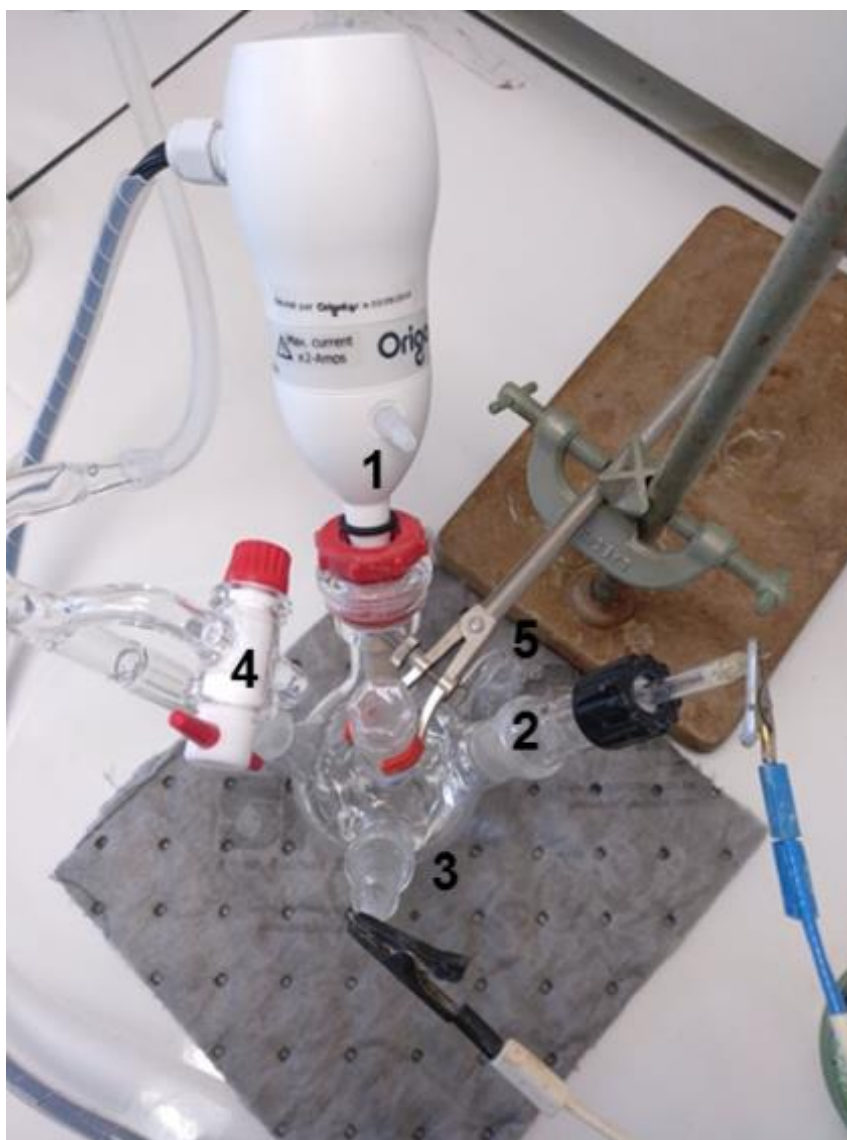
Figure 2.3 Assembly for the electrochemical test measurements by RDE.

III.2 Working electrode preparation

To deposit the catalyst on the surface of the electrode, an ink is first prepared. A precise amount of this ink is then deposited on the glassy carbon disk of the WE in order to obtain the expected Ir loading ($\mu g_{Ir}/cm^2_{geo}$).

III.2.1 Catalytic ink preparation

Catalytic suspensions were made by mixing 3.6 ml of MQ-grade water, 6.7 g of Ir/XTO 30 wt.% catalyst powder corresponding to 2.0 mg of Ir (, 1.45 mL of iPrOH and a calculated volume of a 5.0 wt. % Nafion® solution in order to obtain a constant (mass of Nafion®) / (m² support) ratio equal to 1.19 $mg_{Nafion}/m^2_{support}$ (around 0,014 mL for TO based supports). The inks solutions were sonicated in an ultrasonic bath for 30 min in order to ensure a good dispersion/dissolution of all the elements.
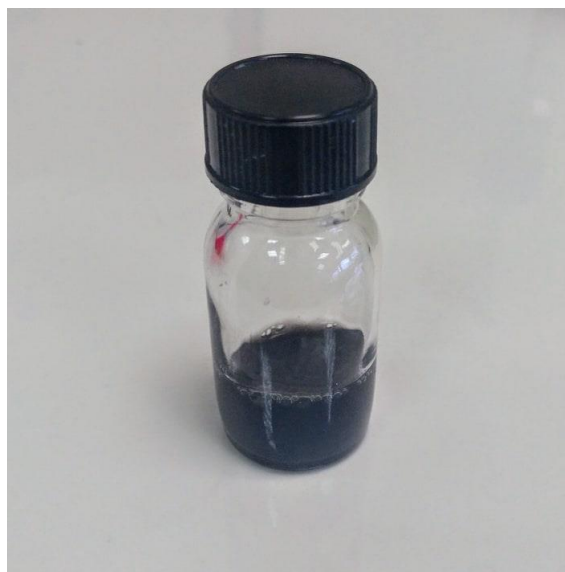
Figure 2.4 Prepared catalytic ink solution after sonication.

III.2.2 Electrode preparation

Before each measurement, the working electrodes were polished in order to obtain a perfectly flat surface without any impurities from the previous measurements. To this end, a 1 µm diamond paste is applied on a polishing cloth and the surface of the electrodes is polished by drawing 8 with the glassy carbon face over the cloth (10 times). Then the electrode is turned 90°, and the procedure is repeated until a full turn of the electrode. Finally, the electrode is washed with acetone, ethanol and D.I water. In time, the electrodes are submerged in the corresponding solvent and ultra-sounded (Elma S40, 140 W) for 15 min.

Once the working electrodes (Glassy Carbon) are well polished, a 10 µl droplet of the as-prepared catalytic ink was deposited on the electrode surface while rotating at 500 rpm, under air atmosphere until complete evaporation of the solvents, leading to the targeted Iridium loading of 20 $\mu g_{Ir}/cm^2_{geo}$. Such procedure is named spin coating, and allows obtaining a flat and homogenous thin layer film of catalysts over the glassy carbon electrode.
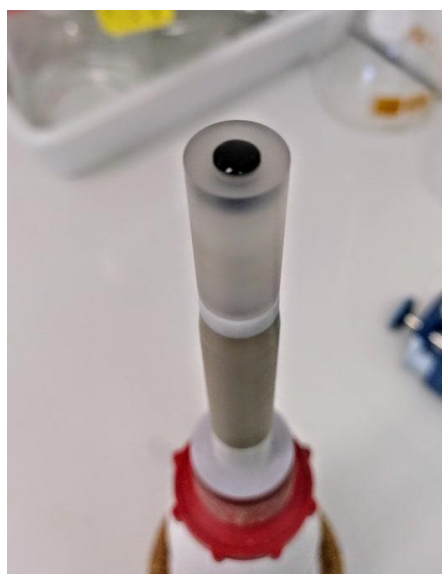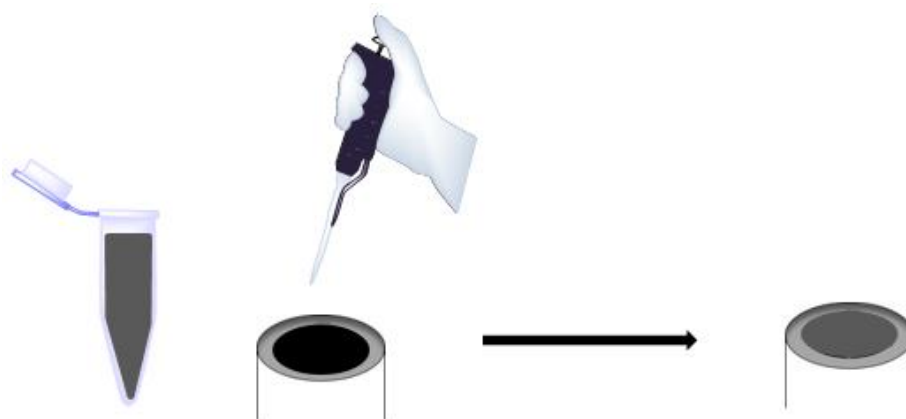
Figure 2.5 Top: representation of the deposition of the catalyst ink over the working electrode by the spin coating procedure. Bottom: 10 µL of the catalytic ink deposited on the tip of the working electrode.

III.3 Cell preparation

For cell preparation, first of all, the glassware was left in Caro's acid (a 50/50 solution of H_2O_2 and H_2SO_4) the day before. The Pt electrode (CE) was immersed only 30 min (because of the Pt corrosion). This duration is also enough for carbon working electrodes, if desired. After acid bath, all the materials were carefully washed with D.I water.

The day before each experiment, the electrolyte solution was prepared. Experiments were run in a 0.05 M H_2SO_4 solution, which was prepared by diluting 1.4 mL of 95-97 % H_2SO_4 with D.I water in total of 500 mL solution.

For starting the experiments, 100 mL of electrolyte solutions were added to the cell and degassed with a N_2 flow for minimum 20 minutes.

Meanwhile the Pt foil used as the CE was washed several times with the electrolyte solution and then placed in the cell and connected to the potentiostat (blue wire **Figure 2.3**).

Then the reference electrode was prepared and placed. **Figure 2.6** illustrates the procedure for SHE preparation.
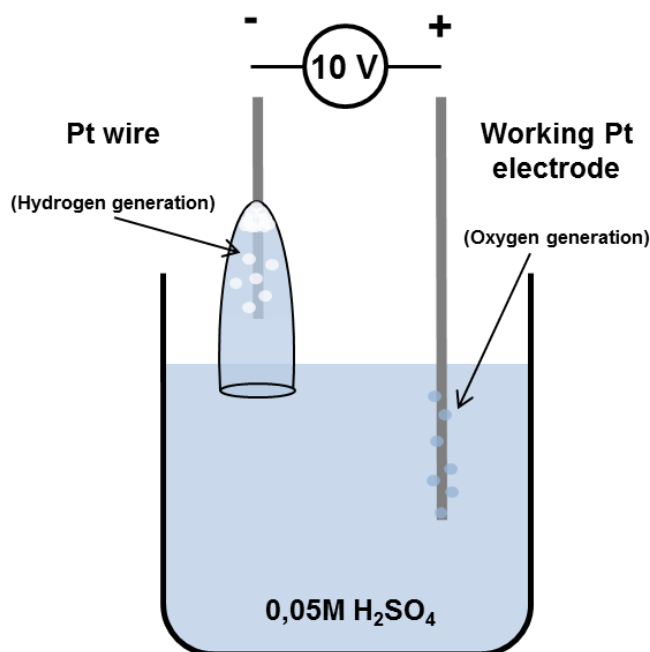
Figure 2.6 Schematic representation of the SHE preparation

For Reference electrode preparation, first of all, the tip of the electrode was filled with the electrolyte solution (by using a syringe), taking care not to leave any air bubbles. Then, the tip was immersed in a beaker filled with the H_2SO_4 0.05M electrolyte. A Pt wire that acts as a working electrode was also introduced into the beaker. A voltage of approximately 10 V was applied between the two electrodes (the + on Pt and the - the reference electrode). Bubbles were formed on both electrodes, O_2 on the Pt cable and H_2 on the reference electrode. The SHE electrode was ready when the amount of generated H_2 is enough to have a sufficient reserve of H_2. It is also necessary that the Pt cable of the electrode is always in contact with the electrolyte. Finally, the electrode was inserted carefully in its guard, placed on the cell and connected to the potentiostat (white wire).

Once the working electrode was prepared (**section IV.1.2.3, chapter 2**) and placed on the cell, experiments were run.

III.4 Activity tests

The electrochemical properties of each catalyst were investigated using the three-electrode electrochemical cell described above with the rotating disk electrode configuration. The OER activity was evaluated by the following protocol (**Table 2.1**) at a 1600 rpm rotation rate. This rotation rate was supposed to be fast enough to remove and limit the oxygen bubble formation at the electrode surface.

The ohmic drop potential (iR) was automatically corrected at 85 % by the Biologic EC-Lab software for all cyclic voltammetry and chronoamperometry measurements. So, the overpotential induced by the resistance of the electrolyte and other interfaces (connectors, surface films, etc.) was corrected.

Table 2.1. Sequences used for electrochemical characterizations

Sequence Number	Starting Potential (V *vs.* SHE)	Potential range (V *vs.* SHE)	Sweep rate (mV s^{-1})	N° Cycles	Purpose
1	1.0	1.0 – 1.6	5	3	OER pre-test
2	OCP	0.0 – 1.6	20	10	Electrochemical conditioning
3	1.0	1.0 – 1.6	5	3	OER activity evaluation

III.5 Stability tests

The long-term stability of each prepared catalyst under OER catalytic conditions was determined using galvanostatic (constant current) electrolysis. The catalyst material was held at a constant current for a selected time at a constant 1600 rpm rotation rate, while potential was measured as a function of time. The increase of the measured potential with the time gave us an evidence of catalyst deactivation. Note that the stability measurement used in this study does not distinguish if the deactivation mechanism is due to corrosion, material degradation, surface passivation, or other processes that our catalyst materials suffered during such stability test.

The stability measurement protocol outlined above is a useful and rapid preliminary screen of the catalyst durability under OER catalytic conditions.

III.6 Electro-Chemically active Surface Area (ECSA) determination

The electro-chemically active surface area (ECSA) for each system was estimated from the electrochemical double-layer capacitance of the catalytic deposited surface, according to the procedure described by Jaramillo *et al.* and Trassati and co-workers.[1,2] The electrochemical capacitance was determined by measuring the non-Faradaic capacitive current associated with the double-layer charging from the scan-rate dependence of cyclic voltammograms (CVs).[1,3]

To measure the double-layer charging via CV, a potential range in which no apparent Faradic or redox process occur (around 0.3 V-0.4V vs SHE for our materials) was determined from static CV. Then the charging current, i_c, is measured from CVs at multiple scan rates (5, 10, 25, 50, 75, 100, 250 and 500 mV s^{-1}), holding the WE at each potential vertex (0,3 and 0,40 V) for 10 seconds before beginning the next sweep, recording just one cycle for each scan rate. The double-layer charging current is equal to the product of the scan rate, v, and the electrochemical double-layer capacitance, C$_{DL}$:

$$i_c = v\ C_{DL}\ \textbf{(eq. 2.1)}$$

Plotting i_c as a function of v yields a straight line whose slope equals C$_{DL}$, **Figure 2.7**.
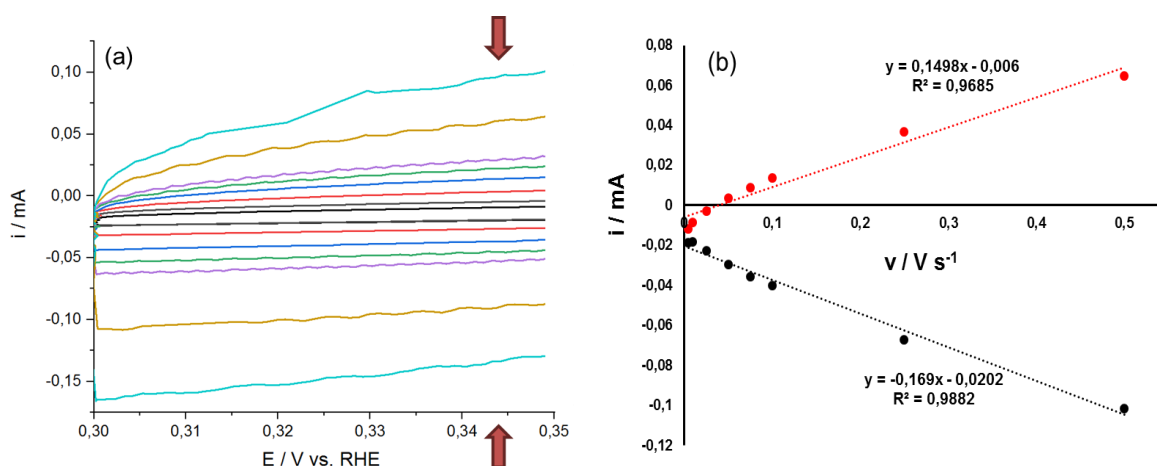
Figure 2.7 Double-layer capacitance measurements for determining electrochemically active surface area for an electrodeposited IrO$_x$ catalyst from voltammetry in 0.05 M H$_2$SO4. (a) Cyclic voltammograms measured in a non-Faradaic region of the voltammogram, between 0.3 and 0.4 V, at different scan rates (mV s^{-1}): black line=0.005, grey =0.01, red =0.025, blue =0.05, green =0.075, purple =0.1, orange =0.25 and cyan =0.5 V/s. The working electrode was held at each potential vertex for 10 s before the beginning the next sweep. (b) The cathode (black marks) and anode (red marks) charging currents measured at 0.344 V vs SHE plotted as a function of scan rate. The determined double-layer capacitance of the system is taken as the average of the absolute value of the slope of the linear fits to the data.

The ECSA was obtained by dividing the calculated capacitance by a tabulated value (C_s), which corresponds to the specific capacitance that depends on the material used and solution, equation **3.2**. Following the protocol described by Jaramillo et *al.,*[1,3] we used the general value of 0,035 mF·cm^{-2},[1] which comes from an average of the specific reported capacitances of different metallic surfaces in acidic media (C, Cu, Au, Pt, Ni or Mo).[1] Of course, it is unclear how appropriate it is to average these literature values since a simple mean gives artificial weight to those materials studied more deeply, but most of the reported materials showed a specific capacitance between 0,022 and 0,040 mF·cm^{-2}, so 0,035 mF·cm^{-2} is chosen as specific capacitance value. We understand that such value is an approximation, but we kept it to compare our results between them.

$$\text{ECSA (cm}^2) = C_{DL} / C_s \qquad \textbf{(Eq. 2.2)}$$

$$RF = \text{ECSA (cm}^2) / 0{,}196 \text{ (cm}^2) \qquad \textbf{(Eq. 2.3)}$$

Finally, the Roughness Factor (RF) was calculated by dividing the ECSA by the geometrical surface area of the electrode (0,196 cm^2), equation **3.3**.

IV Résumé

Dans ce chapitre, les différentes techniques de caractérisation sont présentées.

Des propriétés physiques :

- **Diffraction des rayons X :** détermination de la structure cristalline des matériaux et la taille des cristallites.
- **Adsorption d'azote :** mesure de la surface spécifique des échantillons et la distribution de tailles de pore.
- **Microscopie électronique à transmission et à balayage (MET** et **MEB) :** analyse de la morphologie des supports et catalyseurs préparés, la mesure de la taille des particules.
- **Conductivité :** mesure de la conductivité sous pression (1 tonne) des matériaux préparés.

Des propriétés chimiques :

- **XPS :** détermination de la composition chimique de la surface des matériaux.
- **EDX :** détermination de la composition chimique de l'intérieur des matériaux.

V References

[1] C. McCrory, S. Jung, J. Peters T. Jaramillo, *J. Am. Chem. Soc.,* **2013**, *135*, 16977–16987

[2] S. Trasatti, O. Petrii, *Pure Appl. Chem.,* **1991**, *63*, 711– 734

[3] J. Benck, Z. Chen, L. Kuritzky, A. Forman, T. Jaramillo, *ACS Catalysis*, **2012**, *2*, 1916 –1923

CHAPTER 3. Tin dioxide-based aerogels: synthesis and characterization

This chapter is focused on the preparation and characterization of tin dioxide-based aerogels, with the purpose of developing such materials and improve their key properties as catalyst supports for PEMWE.

The chapter is split into four main sections:

The first one (**section I**) reports the synthesis of the tin alkoxide precursors. A home-made precursor was synthesized so as to avoid any problems in delivery time and quality. This would also allow to modify the metal ligands in order to play on the sol-gel kinetics, and eventually on the aerogels morphology.

The second one (**section II**) concerns the synthesis and characterization of different tin dioxide-based aerogels and their comparison. Pure tin oxide (TO) materials were compared to Antimony-doped tin dioxide (ATO) and Tantalum-doped tin dioxide (TaTO). The work presented in this section was published in the International Journal of Hydrogen Energy.[1]

Sections III and **IV**, are respectively dedicated to the development of novel ATO and TaTO aerogels, where different sol-gel synthesis parameters (ATO and TaTO) and doping ratios (TaTO) were studied in order to improve their intrinsic properties for the final sought-after usage (catalyst supports for the OER).

I Tin alkoxide precursor synthesis and characterization

A tin metal alkoxide precursor [$Sn(OiPr)_4$] was first prepared using the procedure described by Thomas *et al.*[2] First of all, 3.7 mL of tin tetrachloride ($SnCl_4$) were added into a 500 mL dry reactor flask under inert (argon) atmosphere, **Figure 3.1.a**, with 50 mL of previously dried (stored 24 hours with active molecular sieves) and degassed heptane (by argon bubbling for 20 minutes). After 10 minutes of stirring at room temperature, a solution of 17 mL of diethylamine dissolved in 20 mL of dried heptane was added by using a syringe in order to keep the inert atmosphere, and the reactants were kept under stirring for 2 hours.

At this stage of the synthesis,[2] the product obtained is the tin amino chloride $SnCl_4 \cdot 2(HNEt_2)$, where the coordination sphere of tin has changed from 4 to 6, following the reaction **3.1**:

$$SnCl_4 + 2HNEt_2 \rightarrow SnCl_4 \cdot 2(HNEt_2) \text{ (\textbf{Eq. 3.1})}$$

Then, a 17 mL solution of *tert*-butanol dissolved in 70 mL of dried heptane was added to the reactor and kept under stirring for 72 hours.

The reaction medium then consists of an amine hydrochloride precipitate of formula $HNEt_2 \cdot HCl$ dispersed in a solution of tin *tert*-butoxide, according to reaction **3.2**:

$$SnCl_4(HNEt_2)_2 + 4 \text{ } tBuOH + 2 \text{ } HNEt_2 \rightarrow Sn(OtBu)_4 + 4 \text{ } HNEt_2 \cdot HCl \text{ (\textbf{Eq 3.2})}$$
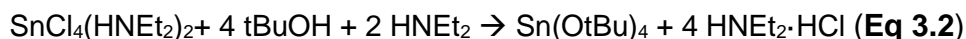
The product was then filtered inside an inert atmosphere glove box, **Figure 3.1.b**, and the filtrate was washed several times with heptane. 30 mL of dried isopropanol were added to the filtrate, and the solution was kept under stirring and inert atmosphere for 24 hours more in order to get the final product, tin isopropoxide [$Sn(OiPr)_4$]:

$$Sn(OtBu)_4 + 4 \text{ } iPrOH \rightarrow Sn(OiPr)_4 + 4 \text{ } tBuOH \text{ (\textbf{Eq 3.3})}$$
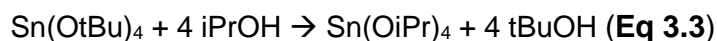
After that, the solution was evaporated under vacuum until an orange-yellow oil is obtained (**Figure 3.2.a**), using a rotary evaporator (**Figure 3.1.c**), in order to eliminate undesirable by-products and solvents.

Figure 3.1 (a) Reactor flask under Argon atmosphere. The reactor flask is connected to a balloon filled with the inert gas in order to maintain the Ar atmosphere; (b) the glove box under inert atmosphere (Argon) where some procedures, as filtrations, were taken place; (c) the rotatory evaporator, used for evaporating the solvent and by-products of the synthesis from the desired product.

Finally, the obtained alkoxide was re-diluted with around 60 mL of isopropanol in order to obtain a solution of $[Sn(OiPr)_4]$ of 10% mass in volume ($w \cdot vol^{-1}$). Finally, the solution keeps the orange-yellow color of the pure alkoxide oil, **Figure 3.2.b**.
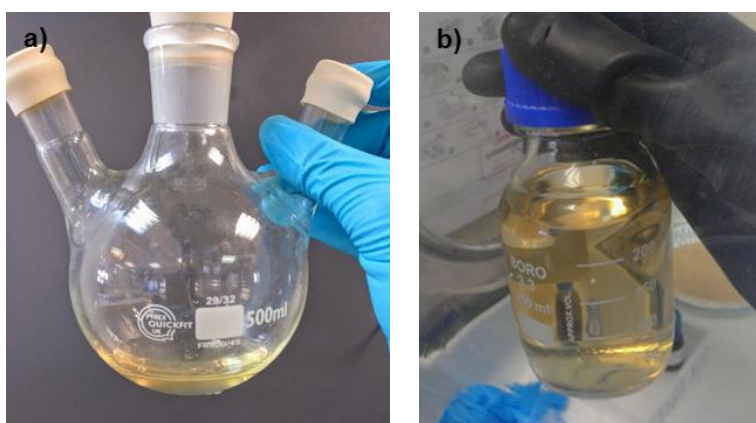
Figure 3.2 (a) The obtained tin alkoxide oil after the evaporation with the rotating evaporator of the solvents and by-products. (b) The solution of the as-prepared alkoxide precursor diluted in isopropanol. In such bottle, various precursor syntheses were mixed together.

The determination of the exact concentration of $[Sn(OiPr)_4]$ in mass per volume was determined with UV, using a UV spectrophotometer UV-1800 Shimadzu.

First of all, a calibration line was made by preparing a solution of 0.2 mL of a commercial $[Sn(OiPr)_4]$ precursor, at 10 % mass in volume (g / 100 mL), in a total solution of 250 mL in isopropanol.

Absorbance of such solution was registered in a range between 800 and 200 nm, with a scan rate of 100 nm/min. The absorbance value measured at 203 nm peak was used as the

reference. The initial solution was then diluted several times in order to have different reference solutions for the calibration (dilution: 7.5 % m·vol⁻¹, 5.0 % m·vol⁻¹, 2.5 m·vol⁻¹, 1.5 m·vol⁻¹ and 1 % m·vol⁻¹). The absorbance of each solution was also measured at 203 nm. The collected data allowed to obtain a calibration line, **Figure 3.3**.

For samples to be analyzed, 0.2 mL of the prepared home-made [Sn(OiPr)$_4$] precursor solutions were diluted in 250 mL of isopropanol. The measured absorbance at 203 nm was to determine the precursor concentration based on the calibration line.
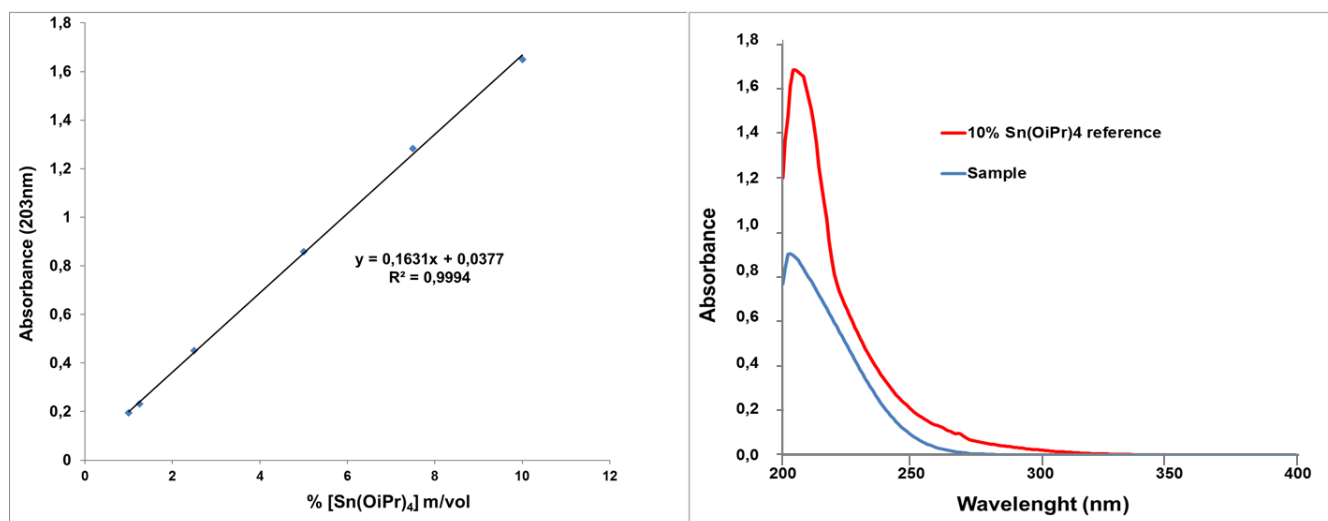
Figure 3.3 On the left, calibration line of [Sn(OiPr)$_4$] precursor. On the right, the UV spectra of the commercial / reference [Sn(OiPr)$_4$] precursor (red) and the home-made one (blue).

Table 3.1 shows the different prepared [Sn(OiPr)$_4$] precursor solutions used among this work, with their respective percentages of mass per volume (% m·vol⁻¹):

Table 3.1. List of used [Sn(OiPr)4] precursor solutions in each section of this work, and their respective mass in volume percentages (% m·vol⁻¹).

Precursor solution	Precursor	Section	% m·vol⁻¹ (g / mL)
1	Home-made	3.II	8.5 %
2	Commercial	3.III.1	10,0 %
3	Home-made	3.III.2	8,0 %
4	Home-made	3.IV.1	5,2 %
5	Home-made	3.IV.2	5,0 %

123

II Tin dioxide-based aerogels: a first comparison between SnO$_2$ (TO), SnO$_2$:Sb (ATO) and SnO$_2$:Ta (TaTO)

In this study, different types of tin oxide-based aerogels (TO, ATO and TaTO) were prepared by a classical sol-gel route, to be used as a catalyst support for PEMWE electrolyzers. By using as a reference the ATO aerogel doped at 10% previously developed by our group,[3] the same protocol was used to prepare non-doped tin dioxide aerogels and 10 at. % Ta-doped ones. Therefore, the effect of the dopant nature on the support properties (such as morphology, structure, electronic conductivity, etc.) was investigated by using a set of physical and chemical techniques.

II.1 Synthesis route

Tin oxide-based aerogels were prepared by the sol-gel method, previously reported by our group,[3] using alkoxide precursors and isopropanol as solvent. By using a secondary alcohol as solvent, isopropanol in our case, alcoholysis reactions after the sol-gel reactions are avoided. As the alkoxide precursors are very sensitive to the humidity of air, all sensitive reactants were stored inside a globe box in argon atmosphere (**Figure 3.1.b**), where all solutions were also prepared.

First of all, two solutions (A & B) were prepared:

On the one hand, solution A consisting of (1) the tin isopropoxide (Sn(OiPr)$_4$) precursor solution dissolved in isopropanol and (2) the corresponding amount of the dopant alkoxide precursor, if desired, in the case of this work: (Ta(OiPr)$_5$ or (Sb(OiPr)$_3$). Once solution A was prepared, it was stirred for few minutes.

On the other hand, solution B consisting of (1) nitric acid, or sodium hydroxide, as the sol-gel reaction catalyst and water (2) were diluted in isopropanol and mixed under magnetic stirring.

When both solutions were prepared, solution B was then slowly added into solution A, while stirring carefully by shaking with hand. In this case, the final solution was not stirred with magnetic stirring in order to avoid breaking of gels while stirring, as the gels are formed after few minutes once solution B is added over A.

The morphology of the gel is controlled by a set of sol-gel parameters: the solvent, the water and the catalyst molar ratio with respect to Sn (S = solvent / Sn, R = H$_2$O / Sn and C = catalyst / Sn).

In this part of the study they were fixed as:

$$S = iPrOH / Sn = 120 \qquad R = H_2O / Sn = 3 \qquad C = HNO_3 \text{ (or NaOH)} / Sn = 0.07$$

Once the gels were formed, they were covered with 10 mL of isopropanol in order to prevent drying (**Figure 3.4.a**), and aged for 72 hours at room temperature before being washed with isopropanol three times a day for three days. This washing procedure is very important as it ensures the elimination of possible impurities and water, which is not soluble with CO_2 in supercritical conditions (SC), meaning that if not eliminated before it will not be evacuated during the SC drying.

After washing, the resulting gels were dried under CO_2 in supercritical conditions (80 bars, 40°C) inside an autoclave (**Figure 3.4.b**). Then an amorphous aerogel is obtained (**Figure 3.5**).

Finally, the amorphous materials were calcined in air at 600°C for 5 hours inside a furnace (Carbolite AAF1100), **Figure 3.4.d**, with a temperature ramp of 10°C min^{-1}.
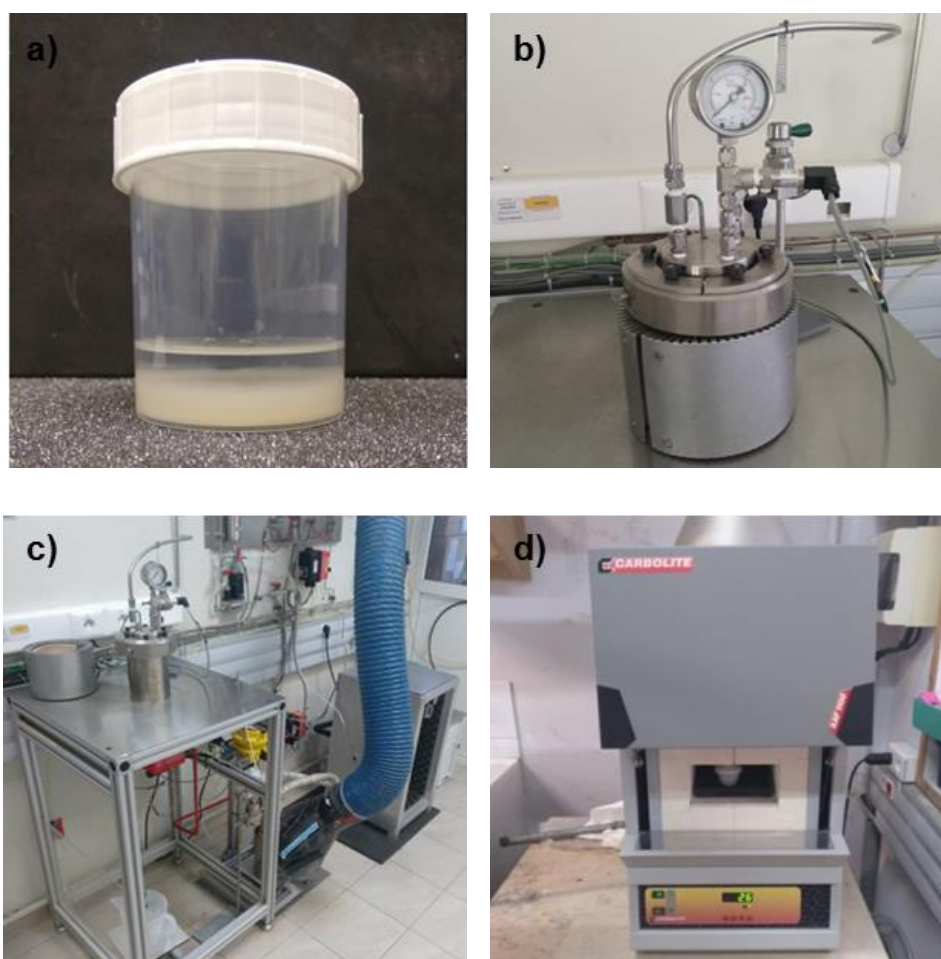
Figure 3.4 (a) A fresh prepared gel covered with 10mL of isopropanol for avoiding air drying of the material; (b) the autoclave where the drying of the gels, using CO_2 in supercritical conditions, takes place; (c) the S.C. CO_2 drying loop; (d) the furnace where aerogels are calcined under air.

As seen on **Figure 3.5**, after the calcination the pure aerogels and the tantalum-doped ones remain white, while the aerogels doped with antimony turned dark blue. This color has been attributed to the presence of extra electrons in the conduction band of the semiconductor, inserted from the Sb dopant. Some authors suggested that Sb^{5+} and Sb^{3+} create impurity levels just below the conduction band of the semiconductor, effectively reducing its bandgap, which results in the blue coloration observed on ATO materials.[4]

Figure 3.5 Same sequence for each material: TO on the top, ATO in the centre and TaTO at the bottom. From left to right: image of the gel, image of the amorphous aerogel after drying with SC CO_2, and image of the calcined aerogel.

Samples were labeled according to a dedicated nomenclature, **Figure 3.6**: the non-doped tin dioxide aerogel was labeled as A6S, the 10 at% Sb-doped SnO_2 (ATO) as A6SS100 and the 10 at% Ta-doped SnO_2 as A6ST100; where A stands for aerogel, 6 for calcination temperature at 600ºC, first S for SnO_2, second S or T for Sb or Ta doping, respectively, and 100 for 10.0 at. % doping.
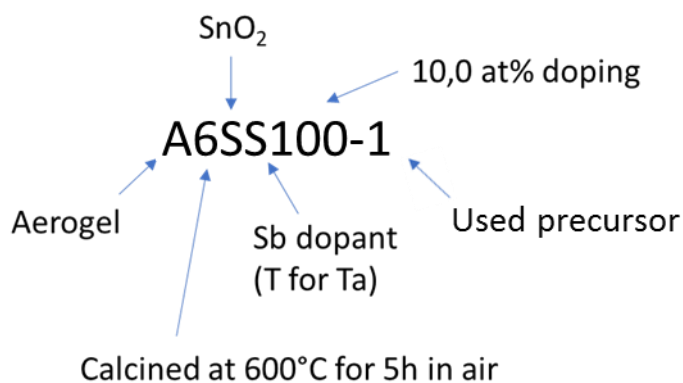
Figure 3.6 Labeling of as-prepared samples.

Table 3.2 presents the synthesis conditions of each sample. All tin dioxide-based aerogels were calcined 5 h at 600°C under air, and the doped aerogels were doped at 10 at. % with Sb or Ta. The ratio between the sol-gel catalyst (HNO_3) and tin was 0.072 for all the aerogels.

Table 3.2. Summary of the as-prepared aerogels. All samples were prepared using a ratio of 3.06 H_2O/Sn and calcined at 600°C for 5 hours.

Aerogel	Sample	Sn alkoxide precursor Sn(OiPr)$_4$	Sb doping (at. %)
TO (SnO_2)	A6S-1	Home-made	-
ATO (SnO_2:Sb)	A6SS100-1	Home-made	10 (Sb)
TaTO (SnO_2:Ta)	A6ST100-1	Home-made	10 (Ta)

II.2 Morphology and structure

The morphology and the structure of the as-prepared aerogels were characterized by SEM, nitrogen sorption measurements and X-ray diffraction analyses.
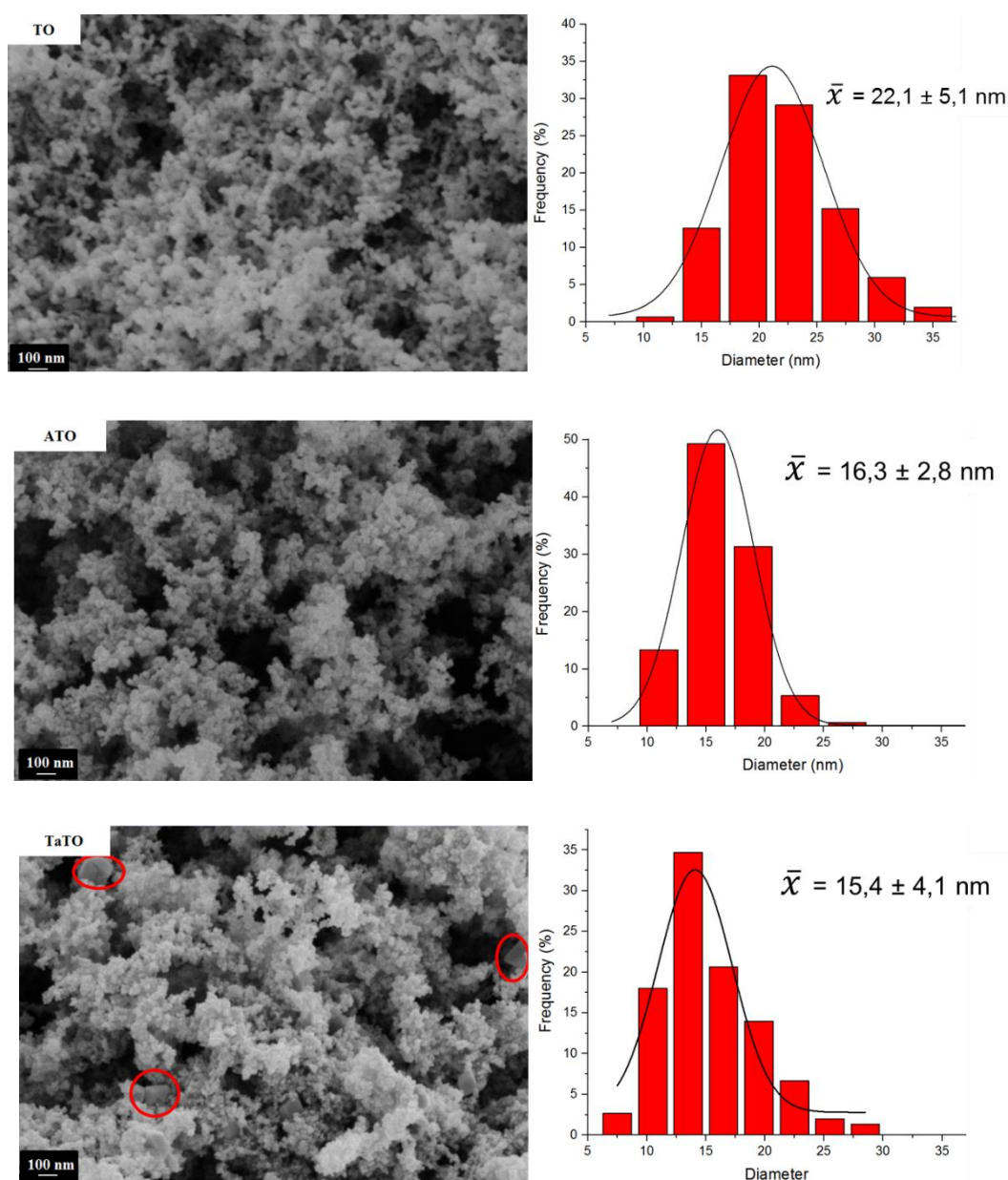
Figure 3.7 SEM images (Magnification = 50000) and associated primary particle size distributions (150 particles analysed using *Image J* software) of: pure tin dioxide aerogel (top), antimony-doped tin dioxide (ATO) (centre), and tantalum-doped tin dioxide (TaTO) (bottom).

SEM images displayed in **Figure 3.7** show that all the aerogels feature a similar airy morphology, lying on a three-dimensional network composed of interconnected primary particles. As already observed in previous studies,[3] doped SnO_2 are made up of smaller

particles than non-doped SnO$_2$ with a diameter distribution respectively cantered around 15 nm and 22 nm). Doping appears to inhibit particle growth during the sol-gel process. This control of the nucleation and growth of SnO$_2$ particles with the addition of a dopant has already been observed and reported. The introduction of foreign agents favours the creation of dislocations or imperfections in the network, interrupting particles growth.[4] Note that some larger particles (100 nm) are also present in the Ta-doped sample. This will be further discussed in **section IV** of this chapter.

Nitrogen sorption measurements were performed to determine the textural properties of the synthesized aerogels.

As shown on **Figure 3.8**, all materials present a typical sigmoidal type IV adsorption isotherm representative of mesoporous materials. Doped tin dioxide aerogels (ATO and TaTO) adsorbed a larger amount of nitrogen on the whole domain of pressure pressures than the pure tin dioxide one. They should present a larger porous volume.
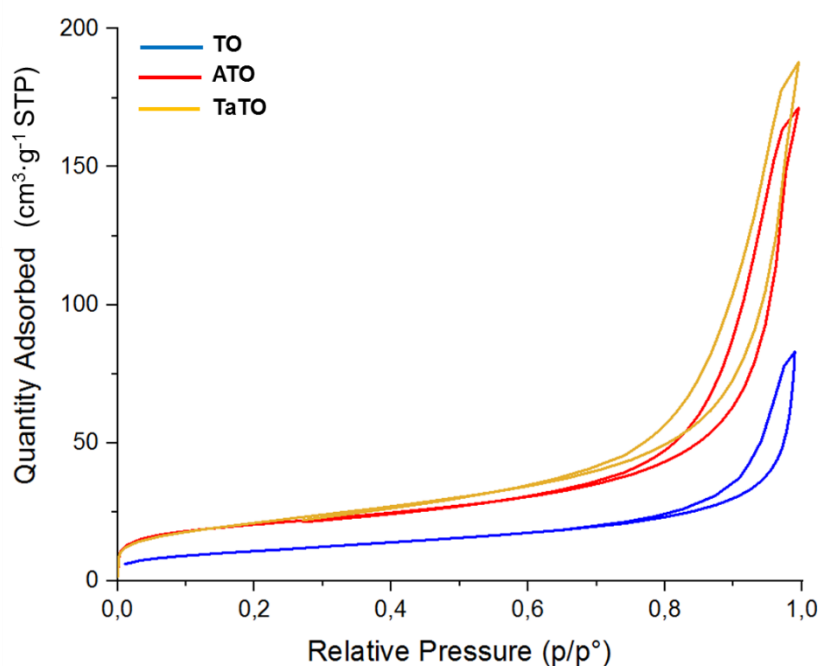
Figure 3.8 Adsorption isotherm of TO (blue curve), ATO (red curve) and TaTO (orange curve).

The analysis of the isotherms allowed to calculate the specific surface area of the samples applying the BET model. Values are reported in **Table 3.3**, along with pore size distribution (BJH model) and pore volume results.

Table 3.3. Nitrogen sorption measurement results for pure and doped SnO_2 aerogels.

Sample	Sp. Surf. Area BET ($m^2\,g^{-1}$)	PSD (BJH, nm)	Pore volume (BJH, $cm^3\,g^{-1}$)	μ-pore volume (BJH, $cm^3\,g^{-1}$)
TO	41.1 ± 4.1	20 — 30 — 40	0.09 ± 0.01	$0.3 \times 10^{-2} \pm 0.03 \times 10^{-2}$
ATO	70.2 ± 7.0	20 — 25 — 35	0.29 ± 0.03	$0.9 \times 10^{-2} \pm 0.09 \times 10^{-2}$
TaTO	74.6 ± 7.5	20 — 25 — 40	0.29 ± 0.03	$0.1 \times 10^{-2} \pm 0.01 \times 10^{-2}$

Due to smaller primary particles, a higher specific surface area was obtained for the doped aerogels, reaching almost twice that of pure SnO_2 aerogel (roughly 75 $m^2 \cdot g^{-1}$ for ATO and TaTO *vs* 40 for TO).

The pore size distribution is presented on **Figure 3.9.** It reveals actually a multimodal distribution with maxima between 20 and 40 nm for all synthesized aerogels which are thus mainly mesoporous.

The presence of mesoporosity with a large specific area is key to efficiently deposit Iridium-based NPs on the aerogel surface and thus ensure higher mass activity towards the OER.

The calculation of the pore volume based on the BJH model confirmed that doping results in a larger pore volume (0.3 vs 0.1 $cm^3 \cdot g^{-1}$). The calculated microporous volume (μ-pore volume) is quite negligible, two orders of magnitude smaller than the total pore volume. Together with the pore size distribution this is confirming that our materials are mainly mesoporous.
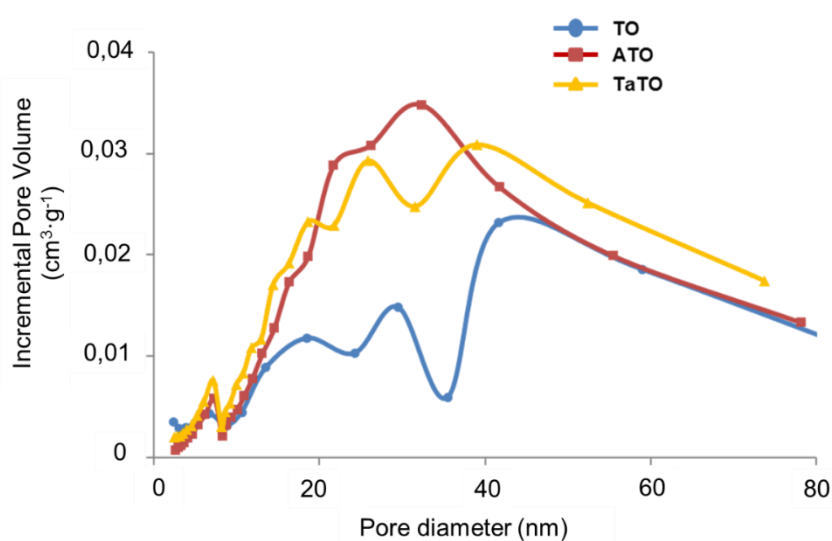
Figure 3.9 Pore size distribution of TO, ATO and TaTO aerogels.

130

Figure 3.10 shows only the characteristic XRD peaks of the rutile structure of SnO_2, (110), (101), (200), (211), (200). No peak signal corresponding to Sb or Ta phases (M, MO, M_2O_3, M_2O_5 with M = Sb or Ta) was found, which may allow to conclude to a real doping and a dopant atoms accommodation in the SnO_2 lattice. The substitution of Sn^{4+} ions (ionic radius = 69 pm) with Sb^{5+} (ionic radius = 60 pm) or by Ta^{5+}(ionic radius = 64 pm) is indeed made possible by their smaller ionic radius. Moreover, as shown in **Table 3.3**, the "*a*" and "*c*" lattice parameters of TaTO or ATO aerogels are unchanged compared to, suggesting no or very little deformation of the rutile cell of SnO_2 due to the insertion of foreign atoms. Others authors have already reported small or undetectable peak shifts resulting in minimal or negligible changes in cell lattice parameters of doped SnO_2 materials.[4d,e] This may indicate that some foreign atoms (Sb or Ta), that are not inserted on the rutile network, could reside between grain boundaries or on the particle surface (dopant atoms segregation).

We can however not exclude possible small amounts of Sb or Ta oxide amorphous phases or the presence of two small particles to be detected.
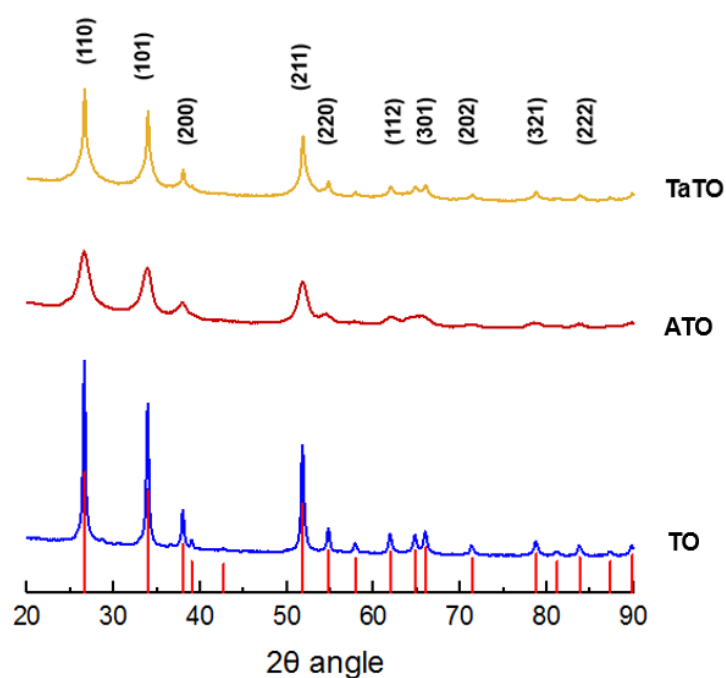
Figure 3.10 X-ray diffraction patterns of TO, ATO and TaTO aerogels. Red bars correspond to the pattern of the rutile structure of tin oxide (JCPDS 14-1445).[5]

The XRD patterns displayed in **Figure 3.10** show that the doped aerogels are less crystalline and feature smaller crystallites than the pure TO material. This is confirmed with the calculation of the crystallite sizes using the Debye-Scherer equation (**Table 3.4**):

Table 3.4. "*a*" and "*c*" lattice parameters, crystallite size determined by XRD (Debye-Scherer) and primary particles size (SEM, 150 particles analysed using *Image J* software) of doped and un-doped samples.

Sample	Measured primary particle size (nm)	Crystallite size (nm)	*a // c* lattice parameters (nm)
TO	22 ± 5	23 ± 3	4.7 // 3.2
ATO	16 ± 3	5 ± 1	4.7 // 3.2
TaTO	15 ± 4	8 ± 1	4.7 // 3.2

TO aerogel exhibits similar particle and crystallite size of 22-23 nm in diameter. It is most probably monocrystalline. On the contrary, for the doped samples we observed that the crystallite size (5 nm in diameter for ATO and 8 nm for TaTO) is systematically smaller than the primary particle size, suggesting that doped aerogels are polycrystalline. Such negative effect of doping on crystallite size is consistent with other reports for doped metal oxide materials. For example Correa *et al.*, found a crystallite size decrease for ATO aerogels (prepared by an epoxide-initiated sol-gel method) when compared with TO ones.[4d] This entails in narrower signals for non-doped SnO_2 aerogels if compared with doped ones, suggesting that the Sb-doped samples are more amorphous and less crystalline than the pure SnO_2 ones. According to bibliography,[3,4d-e,6] doping with foreign atoms of different atomic diameter results in a larger number of smaller grains or crystallites. Considering that some dopant atoms do not substitute tin atoms, they can occupy interstitial sites resulting in a large number of dislocations.[6a] Same trend was observed for Tong *et al.*, and Noonuruk and co-workers,[6b-c] for ATO materials prepared by different methods: soft template method and sonochemical-assisted precipitation, respectively. Both studies attributed such crystallite size decrease to the presence of M^{3+} cations (0.72 pm for Ta^{+3} and 0.76 for Sb^{3+}), which are bigger than the Sn^{4+} ones (69 pm). As M^{5+} are smaller than Sn^{4+} atoms, they easily substitute Sn into the SnO_2 lattice, but the bigger M^{3+} cations could occupy interstitial sites of the SnO_2 rutile lattice, causing a large number of dislocations, and therefore smaller crystallites. Authors relate the formation of M^{3+} cations to the high temperature of crystallization of the tin dioxide lattice and addition of larger amounts of dopant (x > 4 at. %, for Sb).[6d]

II.3 Chemical composition

It is well-established that the electronic conductivity of semiconductors strongly depends on the nature and the content of the doping element as well as on the homogeneity of doping.[3,7,8,9,10]

During the synthesis of doped-SnO_2 aerogels, dopant elements may segregate during the sol-gel process or during the calcination step. The surface segregation layers can strongly affect the properties of the materials obtained., First owing to surface segregation, the bulk concentration of doping elements often differs from the nominal concentration. Second the created surface layers have different properties from those of the bulk material.[6e] To check the dopant concentration and determine the homogeneity of doping in ATO and TaTO aerogels, the bulk and the near-surface chemical compositions were determined by EDX and XPS, respectively.

According to EDX measurements (**Figure 3.11** and **Table 3.5**), the bulk concentration of the doping element was 12 at. % for ATO and 14 at. % for TaTO (targeted value was 10 at. %). Such a difference between the expected doping ratio and the obtained one was attributed to the use of a home-made Sn precursor, which real concentration was not precisely measured yet. The synthesis route was improved later, so in following section the doping at. % was much closer to the expected one.
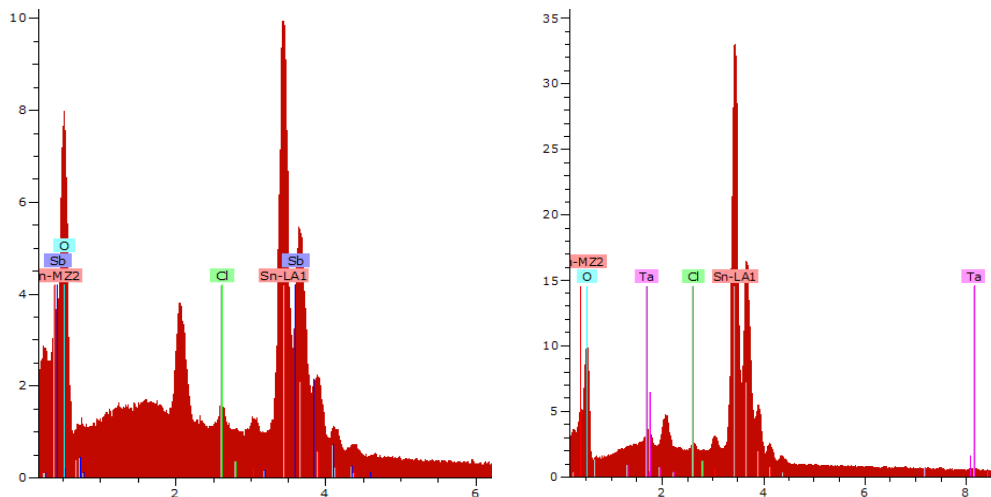
Figure 3.11 EDX graphs of ATO (left) and TaTO (right) aerogels.

Some difficulties appeared to quantify the Sb content by XPS, as the most intense peak of Sb (Sb 3d5) is located at the same binding energy than the O 1s peak (≈530 eV). To avoid interferences, the Sb content was determined using the less intense Sb 3d3 peak at *ca.* 540 eV (**Figure 3.12**). Then for O 1s peak determination, a peak deconvolution was performed in order to differentiate between O 1s signal and Sb 3d$_{5/3}$. For the determination of the near-surface composition of TaTO, Ta 4d5 and Ta 4d3 peaks were used where no interference with Sn or O peak occurs **(Figure 3.13)**.

The near-surface Sb content (**Table 3.5**) measured by XPS was found notably higher than the bulk one, both for ATO (15 at. % *vs* 12 at. %) and TaTO (16 at. % *vs* 14 at. %). This corresponds to segregation percentages of 26% for the ATO sample and 15% for the TaTO one.

Despite results obtained by EDX and XPS should be regarded as semi-quantitative, we believe that the observed trend is significant. Surface and near-surface enrichment by the doping element can be attributed to interatomic diffusion during the calcination step. Indeed, some authors attributed this migration to dopant atoms which could not be inserted in the rutile network and segregate during the calcination step.[4d] Oswald *et al.,* found that such dopant atom diffusion processes can differ for each dopant.[6e] They found that for tin dioxide-doped materials, In-doping present lower segregation percentages than Sb-doping under similar calcination conditions, the activation energy for indium atoms diffusion being higher than for antimony ones.

Unfortunately, this represents a significant limitation in terms of electronic conductivity and has to be mitigated. One option can be to select different alkoxide precursors with similar hydrolysis/condensation kinetics or to modify sol-gel parameters (as for example pH, hydrolysis or solvent ratios) or the calcination temperature.
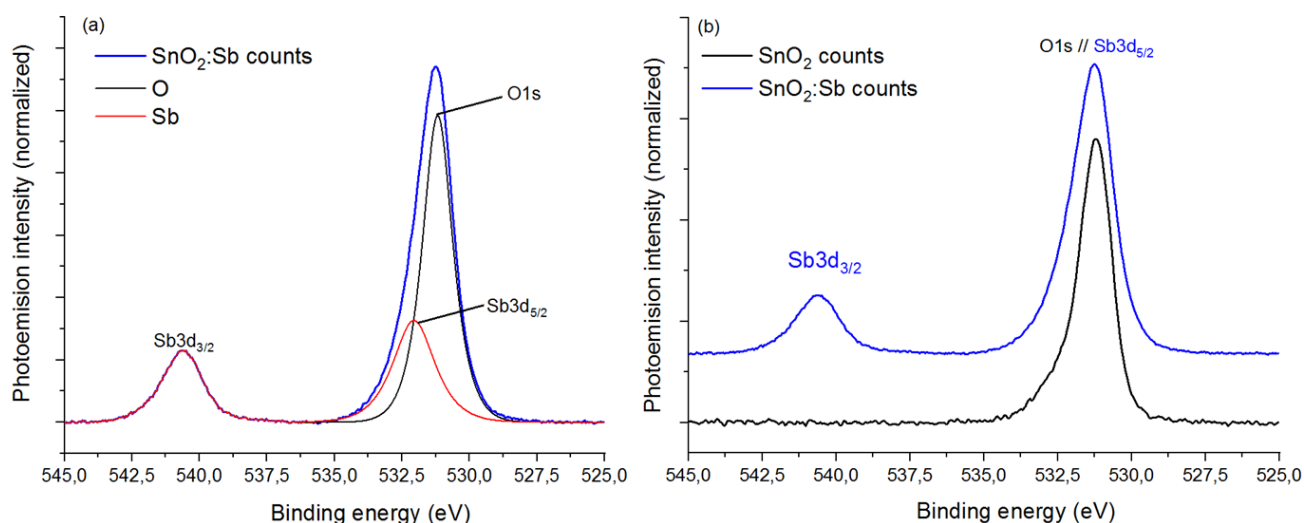
Figure 3.12 (a), deconvolution for Sb 3d and O 1s measurement. (b), XPS spectra comparison between TO and ATO between 525 and 545 eV.
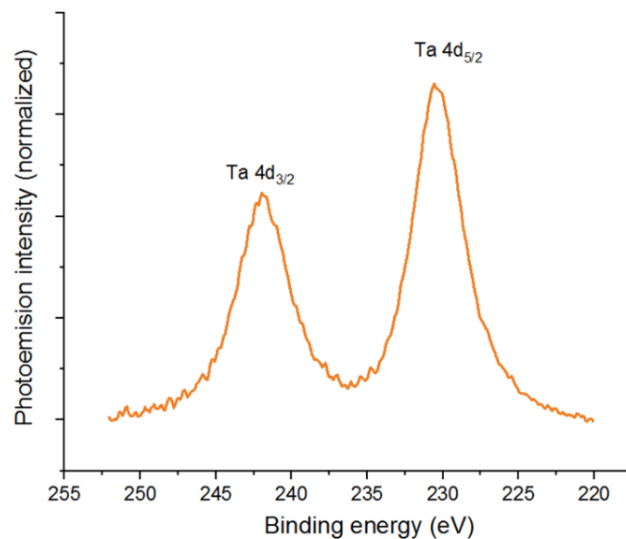
Figure 3.13 XPS spectra focusing on Ta 3d5/3d3. No interference with any Sn or O peak occurs with Ta.

Note that local EDX analyses (see **section II** of **chapter 2**) indicated that the large particles observed in TaTO are actually depleted in Ta. Such domains are believed to be responsible of the higher degree of crystallinity of TaTO *vs*. ATO.

Table 3.5. Bulk and near-surface chemical composition of the as-prepared aerogels determined by EDX and XPS analyses, respectively.

Sample	Dopant / (Dopant + Sn) EDX (at. %)	Dopant / (Dopant + Sn) XPS (at. %)	Segregation % ([Sb]$_{surf}$-[Sb]$_{bulk}$)/ -[Sb]$_{bulk}$
TO	-	-	-
ATO	11.8 ± 2.5	14.9 ± 0.1	26.3
TaTO	14.0 ± 1.9	16.1 ± 0.4	15.0

II.4 Electronic conductivity

A good catalyst support material for PEM Water Electrolysis should present a high electronic conductivity. The conductivity of metal oxides is defined as dielectric, which means that it can only be improved by modifying the electronic configuration of the material. As the bulk conductivity of SnO_2 is considered very low in comparison with other used supports ($0.5x10^{-3}$ $S \cdot cm^{-1}$ for SnO_2 vs. 4 $S \cdot cm^{-1}$ for carbon Vulcan XC-72 support, or the 64 $S \cdot cm^{-1}$ of commercial IrO_2), it should be improved for the foreseen application. An option is doping, as followed by our group in this work and previous ones.[3] It may also be very useful to study how the modifications of the sol-gel route can influence the conductivity of the aerogels. In this section, the electronic conductivity was measured for ATO and TaTO aerogels and compared with that of pure SnO_2. All samples were analyzed in the same conditions, as described in **section II** on **chapter 2**.

As seen in **Table 3.6**, Ta is much less efficient than Sb to enhance the electronic conductivity of the TO aerogels. Indeed, while a four order of magnitude enhancement was reached with 12 at. % of Sb (0.8 $S \cdot cm^{-1}$), a modest 3-fold enhancement of the electronic conductivity was achieved after doping the TO aerogel with 14 at. % of Ta ($1.7 x10^{-3}$ $S \cdot cm^{-1}$), in agreement with former reports in the literature. Note that such a result is consistent with the change in colour observed for ATO while TaTO remained whitish (independently of the Ta at. %). The lower conductivity of TaTO materials in comparison with ATO ones is further discussed later in this chapter. In short, the maximum conductivity for TaTO materials was reached with lower doping ratio, around 2 at. %. For higher values, Sn^{4+} may be substituted by Ta^{3+} instead of Ta^{5+}, causing a decrease in the conductivity of the material.

Despite optimal doping rates depend on the nature of the element,[11] we initially kept similar values for ATO and TaTO so as to limit the impact on the morphology of the support and to allow a straightforward comparison between the different samples.

Table 3.6. Tin dioxide-based Aerogels electronic conductivity determined by resistance measurements obtained with an applied pressure of 1 ton.

Sample	Conductivity ($S \cdot cm^{-1}$)
TO	$0.5 x 10^{-3}$
ATO	0.82 ± 0.01
TaTO	$1.7 x 10^{-3} \pm 0.1 x 10^{-3}$

The electronic conductivity depends on both the charge carriers concentration and their mobility, the latter being notably influenced by grain and domain boundaries.[7] Since ATO and TaTO samples synthesized in this study feature similar particle sizes, we believe that the density of grain boundaries is similar for both materials. Hence, the higher conductivity observed for ATO most likely results from a higher charge carrier's density, in agreement with former claim of Bruneaux *et al.*.[12] Such a statement may result from different oxidation states equilibrium between Sb^{5+} and Sb^{3+}. As already discussed in a previous work,[3] they are impacting the concentration of oxygen vacancies that control the electronic conductivity.

II.5 Conclusions and perspectives

In summary, the morphologies of the different tin dioxide-based aerogels are very similar, showing an airy three-dimensional network composed of interconnected primary particles, moreover very resembling to that of the carbon aerogels previously developed in our group for PEMFC. Agglomeration of these primary particles leads to mainly mesoporous materials, with a notably larger pore volume for doped materials. Such primary particles are significantly smaller for both doped aerogels. Therefore, specific surface areas of doped samples are higher than that of the pure tin dioxide aerogel. After calcination, all aerogels present the rutile structure of pure tin dioxide, without any signal of other crystal phases or, in case of doped samples, Sb or Ta phases. The dopant, Sb or Ta, are thus most probably substituted to Sn, randomly in the rutile network.

Bulk and near-surface chemical composition analyses (EDX and XPS, respectively), showed higher dopant content on the surface of both doped tin-dioxide aerogels, suggesting a segregation of Sb and Ta. Such an enrichment by the doping element can result from the calcination step of the sol-gel procedure, due to the difficulty for some dopants to accommodate the rutile network.

As mentioned on **section IV.1** of **chapter 1**, doping tin dioxide with hypervalent cations, M^{5+}, increases the conductivity of the material. Our results showed an increase of electronic conductivity for the doped samples, the conductivity of Ta-doped samples being 3 times higher than that of the pure oxide, and that of Sb-doped ones four orders of magnitude higher.

In order to improve our aerogel supports, the sol-gel route (calcination time and sol-gel catalyst) was modified for ATO, and TaTO. Results are presented respectively in **section III** and **section IV**, of this chapter.

Preliminary works in the group determined that the optimum Sb concentration was around 10 at% with respect to Sn. A similar study has been performed for Ta, reported in **section IV**, where aerogels with different Ta ratios have been studied.

III Modification of the Antimony-doped tin dioxide aerogels (ATO) synthesis route

Based on ATO aerogel doped at 10 at% as the reference material, different synthesis conditions have been applied in order to improve the desired properties of ATO aerogels and limit the Sb segregation. Two main parameters were investigated: (1) the aerogels calcination time, at 600°C under air atmosphere (the impact of the calcination temperature has already been investigated in a previous study),[13] and (2) the usage of a base NaOH (at different ratios) instead of HNO_3 as the sol-gel catalyst.

III.1 Impact of the calcination time

The impact of the calcination time was investigated based on the reference ATO and varied between 1, 3, 5 and 8 hours. ATO aerogels were synthesized following the same sol-gel route described in **section I**, **chapter 3**, keeping the same solvent, sol-gel catalyst (HNO_3) and hydrolysis ratios, S = 120, C = 0.072 and R = 3 respectively. Only the calcination time was varied.

Aerogel samples were labeled according to the same dedicated nomenclature mentioning in addition the calcination time.
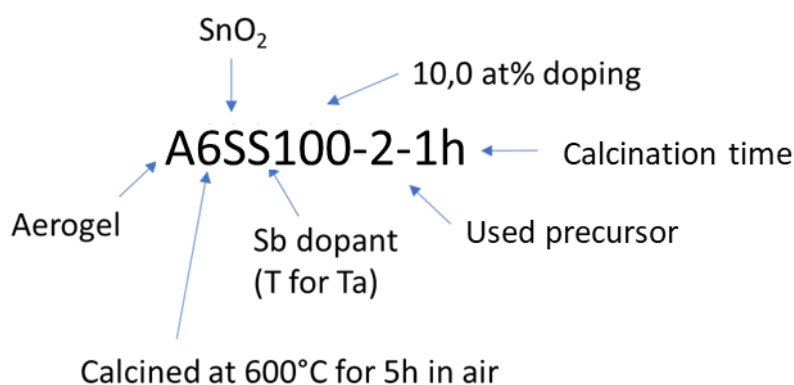
Figure 3.14 Labeling of as-prepared samples.

Table 3.7 presents the synthesis conditions of each sample, atomic doping ratio and calcination time.

Table 3.7. Summary of the as-prepared ATO aerogels with different calcination time. All samples were prepared using same amount of water, HNO$_3$ and solvent and calcined at 600°C.

Aerogel	Sample	Sb doping (at. %)	Calcination time (h)
ATO	A6SS100-2-1h	10%	1 hour
ATO	A6SS100-2-3h	10%	3 hours
ATO	A6SS100-2-5h	10%	5 hours
ATO	A6SS100-2-8h	10%	8 hours

When calcining ATO at 600°C in air at different times it was expected that ATO may present different morphology, crystallinity or Sb repartition inside the SnO$_2$ matrix. Aerogels with shorter calcination times (1 and 3 hours) were expected to be less crystalline and less conductive but with airier morphologies and higher specific surface areas, on top of a more homogeneous Sb repartition, due to limited expected segregation. Longer exposure of the samples at high temperature (8 hours) would normally lead to more crystalline materials, with higher conductivities but lower specific surface areas and a higher surface Sb concentration in comparison with bulk concentration.

III.1.1 Morphology and structure

The morphology of the as-prepared ATO aerogels where characterized by SEM, nitrogen sorption analyzes, while their structure was analyzed by X-ray Diffraction.

ATO aerogels calcined at 600°C under air at different calcination times (1, 3, 5 or 8 hours) showed similar morphologies. As seen on previous sections, **section II** (**chapter 3**), aerogels are made up of an airy network of interconnected particles (named primary particles). Diameter sizes of such particles are similar for all the studied ATO aerogels (**Table 3.9**). The calcination time does not seem to influence their growth, at least at 600°C, **Figure 3.15**. Finally, it seems that the particle growth and the crystallites size are more impacted by the temperature, as reported in previous studies.[4]
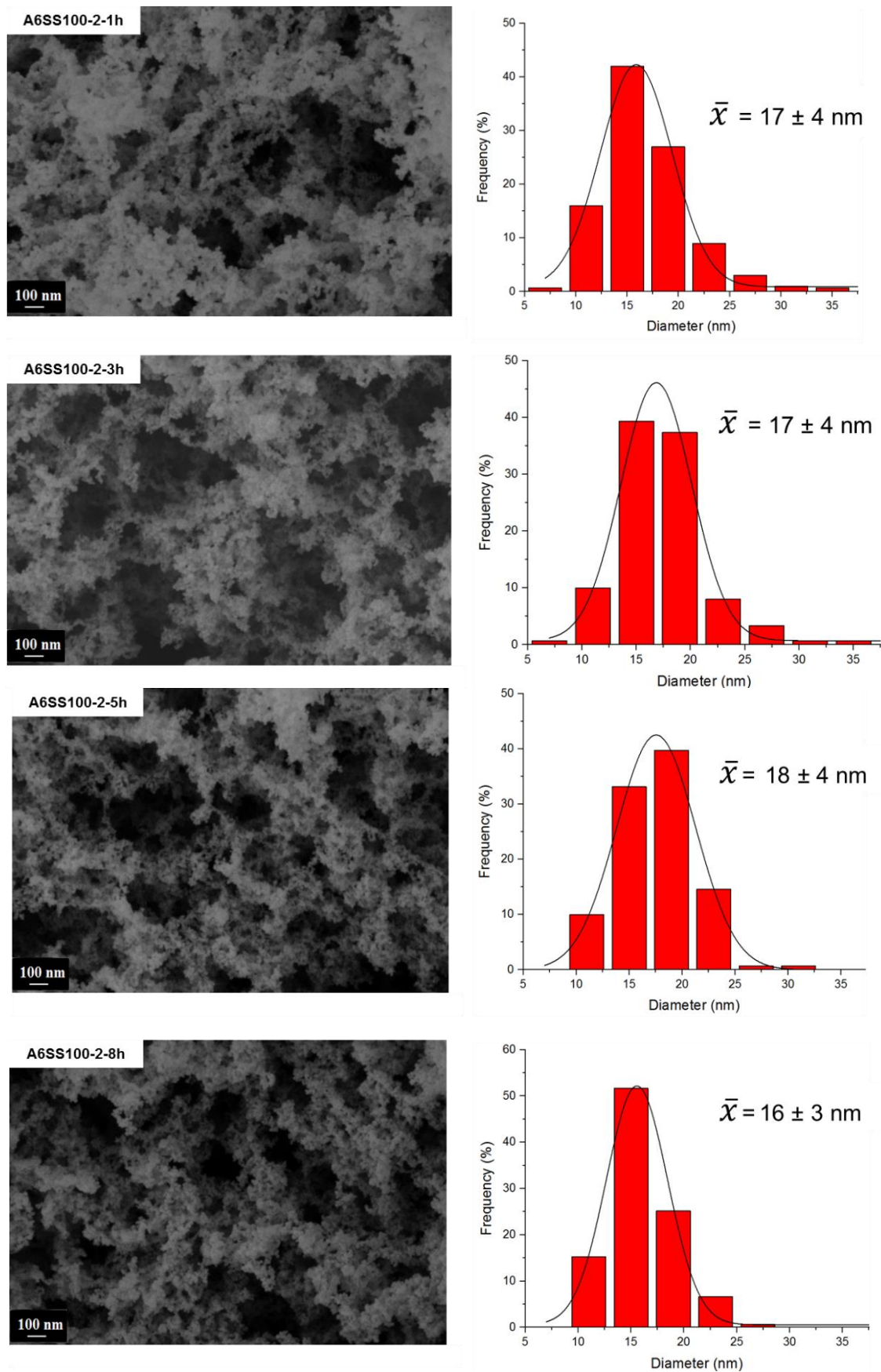
Figure 3.15 SEM images of ATO aerogels (Magnification = 50000 X) and their associated primary particle size distributions (150 particles analysed using *Image J* software).

Adsorption isotherms of all the studied aerogels also present a sigmoidal type IV shape, representative of mesoporous materials. Pore size distribution and adsorption isotherms are shown on **Annex** section of this manuscript. Similar primary particles size and arrangement led up to similar specific surface areas. ATO aerogels, presented also similar pore size distributions and pore volumes. Therefore, no much influence on morphology properties by calcination time were observed in this study.

Table 3.8. Nitrogen sorption measurement results for pure TO and ATO as-prepared aerogels.

Sample	Sp. Surf. Area BET ($m^2 \cdot g^{-1}$)	PSD (BJH, nm)	Pore volume (BJH, $cm^3 \cdot g^{-1}$)	µ pore volume (BJH, $cm^3 \cdot g^{-1}$)
A6SS100-2-1h	76.9 ± 7.7	10 — 20 — 35	0.31 ± 0.03	$0.40 \times 10^{-2} \pm 0.04 \times 10^{-2}$
A6SS100-2-3h	76.9 ± 7.7	15 — 20 — 40	0.29 ± 0.03	$0.20 \times 10^{-2} \pm 0.02 \times 10^{-2}$
A6SS100-2-5h	73.0 ± 7.3	15 — 20 — 30	0.27 ± 0.03	$0.30 \times 10^{-2} \pm 0.03 \times 10^{-2}$
A6SS100-2-8h	74.6 ± 7.5	15 — 20 — 30	0.29 ± 0.03	$0.80 \times 10^{-2} \pm 0.08 \times 10^{-2}$

Table 3.9. Cell parameters of analyzed aerogels obtained after different calcination times, crystallites sizes of pure TO and ATO aerogels and the measured primary particles by SEM.

Sample	Primary particle size (nm)	Crystal size (nm)	a // c lattice parameters (nm)
A6S-1-5h (section II)	22 ± 5	23 ± 3	4.7 // 3.2
A6SS100-2-1h	17 ± 4	6 ± 1	4.7 // 3.2
A6SS100-2-3h	17 ± 4	6 ± 1	4.7 // 3.2
A6SS100-2-5h	18 ± 4	6 ± 1	4.7 // 3.2
A6SS100-2-8h	16 ± 3	6 ± 1	4.7 // 3.2

The structure of ATO aerogels was analyzed by XRD, diagrams are shown on **Figure 3.16**. Unsurprisingly, as mentioned above calcination times shorter than 5 h do not affect the crystallographic phase of the materials whose diffractogram still perfectly fit that of rutile SnO_2. Increasing the calcination time to 8 h neither affect the result.
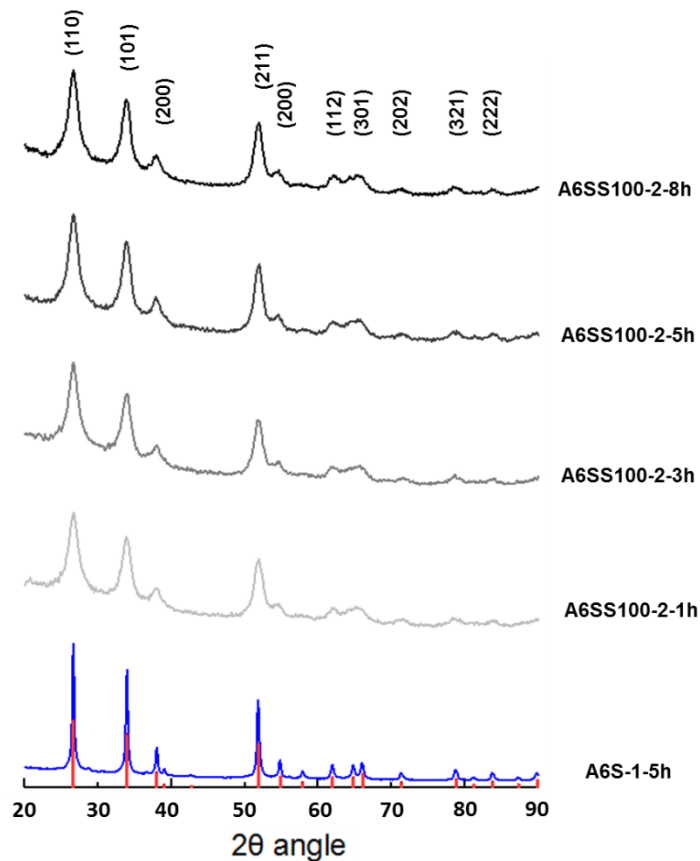
Figure 3.16 X-Ray diffraction diagrams of pure SnO_2 for phase comparing (calcined at 600°C for 5 hours, in blue), and ATO aerogels (calcined at 600°C for 1, 3, 5 and 8 h, grey scale). In red the SnO_2 pattern of rutile structure (JCPDS 14-1445).[5]

Table 3.9 also shows the crystallites size values, determined with the *Debye-Scherer* equation, for comparison with the measured primary particle sizes obtained from SEM analysis. For crystallites size measurements, the peak (211) was selected due to the lower influence of large peaks in the vicinity as for (110) and (101) peaks.

Similar lattice parameters and crystallites sizes were obtained for aerogels calcined for different times, suggesting no influence on samples crystallinity. Previous results obtained in our group showed that calcination temperatures lower than 600°C led to smaller crystallites size. On the contrary, calcination at higher temperature, up to 800°C, highly increases the crystallites' size as well as that of primary particles,[3,13] resulting in lower specific surface areas.[4d] A calcination temperature of 600°C was selected to achieve a good compromise between crystallinity and specific surface area.

The influence of the type of precursor (commercial or home-made) on the synthesis of ATO aerogels was studied by comparing the morphology and the structure of A6SS100-2-5h prepared in this section with that of A6SS100-1 (5h of calcination) prepared in **section II**

(**chapter 3**). Comparing the main properties of both aerogels (**Table 3.10**), we can conclude that very few differences were found: +2 nm in particles size (13%), +1 nm in crystallites size (20%), -4 m²·g⁻¹ in specific surface area (5%) and -0.02 cm³·g⁻¹ in pore volume (7%) when the commercial precursor is used., Using our homemade precursor does significantly impact the morphology of obtained ATO aerogels and if so, in the right direction.

Table 3.10. Comparison of morphology and structure values between ATO aerogels prepared using our home-made Sn precursor vs. a commercial one.

Sn Precursor	(1) Home-made(chapter 3.II)	(2) Commercial
Primary particle size (nm)	16 ± 3	18 ± 4
Crystallites size (nm)	5 ± 1	6 ± 1
Sp. Surf. Area BET ($m^2 \cdot g^{-1}$)	76.9 ± 7.7	73.0 ± 7.3
PSD (BJH, nm)	20-25-35	15-20-30
Pore volume (BJH, $cm^3 \cdot g^{-1}$)	0.295	0.275

III.1.2 Chemical composition

The electronic conductivity strongly depends on the chemical composition of the material.[3,14] As the amount of dopant precursor (Sb) can be controlled during the aerogel preparation, the exact ratio of dopant and its repartition among the final material must be analyzed. The precipitation during the sol-gel reaction of some precursors and the atomic diffusion or segregation during the calcination can induce a heterogeneous repartition of the dopant agent or modify the real dopant amount in the samples.

In order to check the chemical homogeneity of our samples, and investigate the impact of calcination time on the dopant segregation, the bulk and the surface chemical compositions were measured by EDX and XPS respectively (**Table 3.11**). Bulk and surface Sb concentration were respectively equal to 12-13 at. % and 17 at. % for all the samples. As the used commercial tin precursor was quite old, its real Sn concentration could be lower than the expected 10 % mass in volume, due to reaction between tin precursor and air humidity that can generate tin oxides. This could be the reason why we obtained doping ratios larger than the expected 10 at. %.

Nevertheless, results showed high segregation percentages for all samples but no impact of the calcination. These results suggest that if the dopant segregation occurs during the

calcination step, it would depend on the calcination temperature. Cross and co-workers found that the onset of Sb surface enrichment, for ATO materials, starts 400°C.[6f] Correa *et al.,*[4d] found a larger Sb concentration on the surface (XPS analyses) of their ATO materials when calcined at 800°C instead of 450°C. They attributed this observation to segregation procedures. As their ATO aerogels calcined at 800°C presented larger crystallite sizes, the migration of Sb to the surface may be triggered by the elimination of grain boundaries in the course of crystallite growth as the calcination temperature was increased. Herein, as the crystal structure of the different aerogels does not change, no grain boundaries are eliminated with time and similar fractions of Sb are diffused from the bulk to the surface. Here again, the main parameter seems to be the temperature.

Hence, a monitoring of the Sb repartition for different calcination temperatures would be really interesting to be performed in the future.

Table 3.11. Bulk and near-surface chemical composition of the as-prepared aerogels determined by EDX and XPS analyses, respectively.

Sample	Sb / (Sb+Sn) EDX (at. %)	Sb / (Sb+Sn) XPS (at. %)	% segregation (XPS-EDX)/EDX
A6SS100-2-1h	12.1 ± 0.7	16.6 ± 0.2	43.0
A6SS100-2-3h	11.9 ± 1.4	16.8 ± 0.3	47.1
A6SS100-2-5h	12.8 ± 1.0	17.3 ± 0.3	35.2
A6SS100-2-8h	12.8 ± 2.4	17.5 ± 0.2	36.7

III.1.3 Electronic conductivity

The electronic conductivity was measured as mentioned on **section II.3** of **chapter 2**, applying a pressure of 1 ton on powder samples introduced inside a home-made resistance cell.

No important difference in electronic conductivity was found between ATO aerogels calcined at different times, which is in agreement with previously obtained values of Sb concentration measurements (by EDX) and crystallites sizes (measured with XRD). It was supposed than higher calcination times (5h and 8h) may result in larger electronic conductivity, due to higher crystallinity of the samples. However, the conductivity obtained after 5 or 8 h of calcination (0.8 S·cm⁻¹) is not significantly higher than that obtained after 1 or 3 h (0.7 S·cm⁻¹) to be considered as really representative, all the more so that all the previous studied parameters (morphology, BET, crystal size and chemical composition) are similar.

Table 3.12. ATO aerogels conductivity determined by resistance measurements obtained with an applied pressure of 1 ton.

Sample	Sb / (Sb+Sn) EDX (at. %)	Crystal size (nm)	Conductivity (S·cm⁻¹)
A6SS100-2-1h	12.1 ± 0.7	6.2 ± 0.6	0.73 ± 0.07
A6SS100-2-3h	11.9 ± 1.4	5.8 ± 0.6	0.70 ± 0.03
A6SS100-2-5h	12.8 ± 1.0	5.5 ± 0.5	0.79 ± 0.01
A6SS100-2-8h	12.8 ± 2.4	6.2 ± 0.6	0.80 ± 0.01

III.1.4 Conclusions

Exposing ATO aerogels for different times at 600°C does not seem to have any important impact on the main materials properties. The morphology of the aerogels seemed very similar, including the size of the interconnected primary particle that conforms the aerogel network, or specific surface areas.

It was expected that longer calcination exposures may lead up to a better crystallinity. The crystallites size was however also similar for all aerogels. Similar morphologies, together with similar crystallites sizes, entailed similar Sb repartition among the material and same electronic conductivity for all ATO aerogels.

As the calcination time did not seem to impact significantly the samples properties, a 5-hours exposure time was kept for following aerogels synthesis.

III.2 Impact of the sol-gel catalyst, type and concentration

The catalyst used for the sol-gel route was also modified, changing its ratio or type (basic or acid) for the preparation of aerogels (Sb-doped at.10%) Changing the catalyst type or concentration could actually modify the kinetics of the sol-gel reactions. This may lead up to the formation of aerogels with different morphologies or even impact the dopant segregation and therefore the support properties (specific surface area, electronic conductivity, etc.).

ATO aerogels were synthesized following the same sol-gel route described in **section II.1** of **chapter 3**, keeping the calcination for 5 hours at 600°C in air and the same hydrolysis and solvent ratios, S = 120 and R = 3 respectively. The catalyst ratio was varied instead between 0.05, 0.072 and 0.1, both with HNO_3 and NaOH as the catalyst. The tin precursor used for this study was prepared in advance (precursor 3, **Table 3.1**).

Aerogel samples were labeled according to the same dedicated nomenclature used before, mentioning in addition the catalyst ratio as well as the catalyst type when NaOH is used (B for base). Otherwise mentioned, the catalyst is HNO_3.
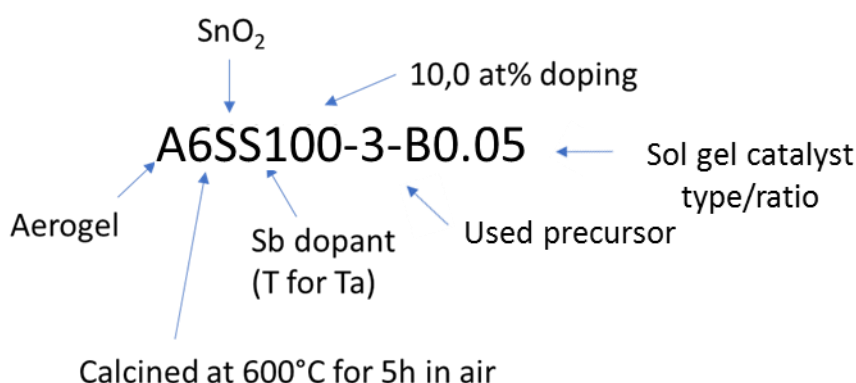
Figure 3.17 Labeling of as-prepared samples.

Table 3.13 presents the synthesis conditions used for each sample (atomic doping ratio and acid or basic sol-gel catalyst). Pure tin dioxide aerogel, A6S-1-0.072 was used as a reference in order to compare properties of new prepared ATO aerogels with the pure TO.

Table 3.13. Summary of the as-prepared aerogels, for which the effect of the ratio of the sol-gel catalyst was investigated. All samples were prepared using same amounts of water and solvent and calcined 5h in air at 600°C.

Aerogel	Sample	Sn alkoxide precursor	Nominal Sb doping (at. %)	Sn atomic ratio - (HNO$_3$ or NaOH) / Sn
TO	A6S-1-0.072	Home - made	-	0.072 – HNO$_3$
ATO	A6SS100-3-0.050	Home - made	10%	0.050 – HNO$_3$
ATO	A6SS100-3-0.072	Home - made	10%	0.072 – HNO$_3$
ATO	A6SS100-3-0.100	Home - made	10%	0.100 – HNO$_3$
ATO	A6SS100-3-B0.050	Home - made	10%	0.050 – NaOH
ATO	A6SS100-3-B0.072	Home - made	10%	0.072 – NaOH
ATO	A6SS100-3-B0.100	Home - made	10%	0.100 – NaOH

III.2.1 Morphology and structure

SEM images of the Sb-doped aerogels prepared with HNO$_3$ as the sol-gel catalyst (**Figure 3.18A**, present similar morphologies, porosities and primary particle sizes (around 17 nm) whatever the HNO$_3$ concentration. The amount of HNO$_3$ does not impact the morphology.

On the contrary the usage of a basic sol-gel catalyst, NaOH, seems to have an impact on the aerogel morphology, **Figure 3.18B**. These aerogels exhibit indeed smaller primary particle sizes (**Table 3.15**), and therefore higher specific surface areas (**Table 3.14**). The higher the catalyst ratio, the higher the specific surface area, reaching 90 m$^2 \cdot$g^{-1} for NaOH/Sn = 0.1. As expected from the theory, increasing the concentration of the sol-gel catalyst favors nucleation to the detriment of growth. Moreover, basic hydrolysis favors faster hydrolysis reactions, resulting in the formation of highly branched polymers with smaller particle sizes.
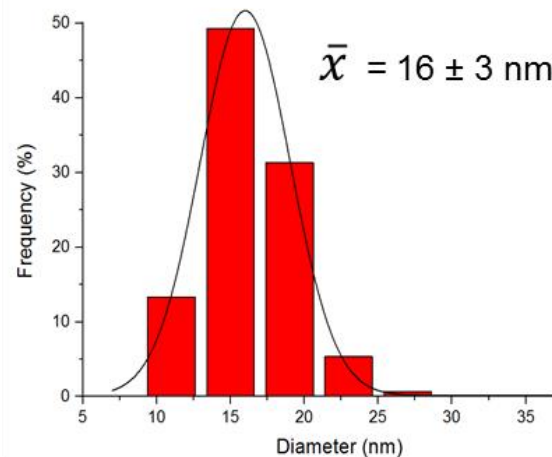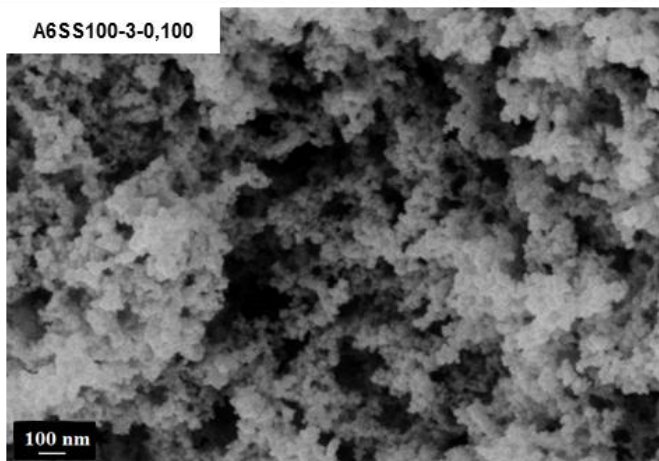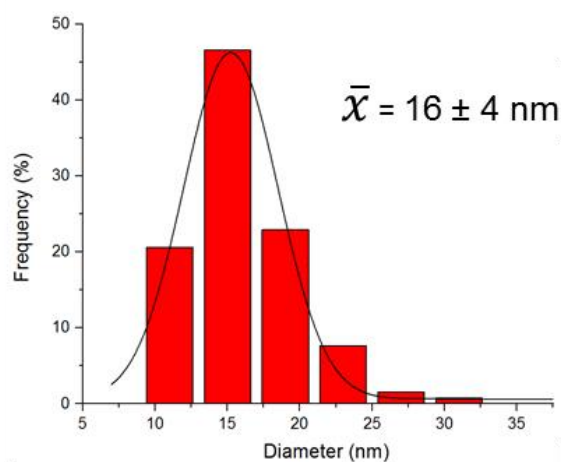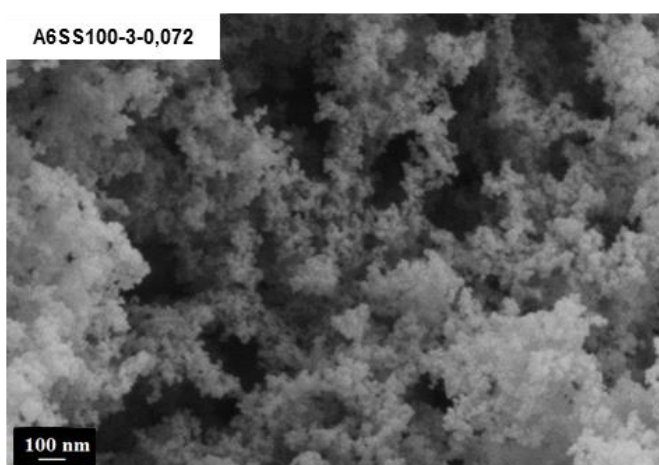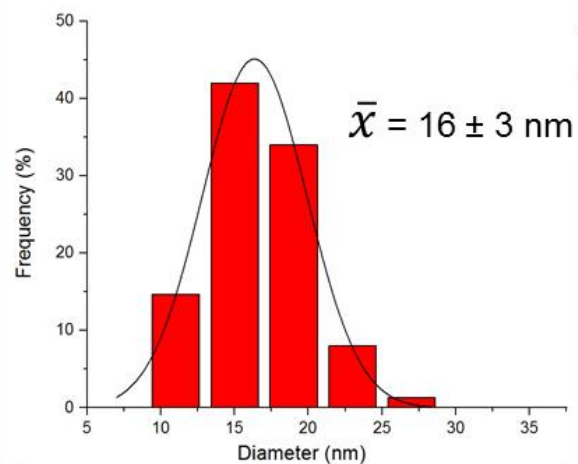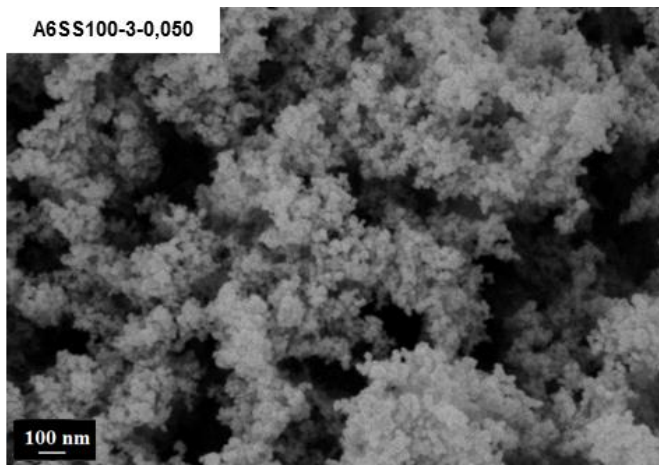
Figure 3.18A SEM images of ATO aerogels, prepared with acid sol-gel catalysts (HNO_3), and their respective particle size distribution (150 particles analyzed using Image J software). Maximization of the images = 50000.
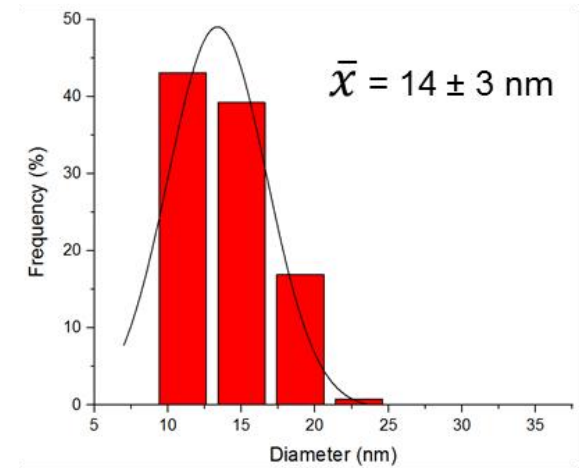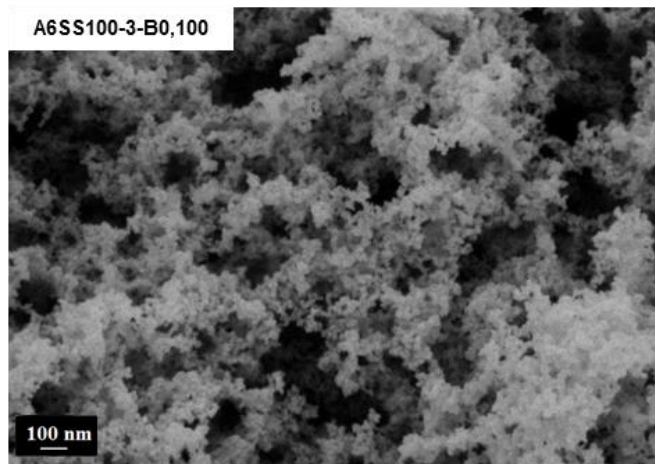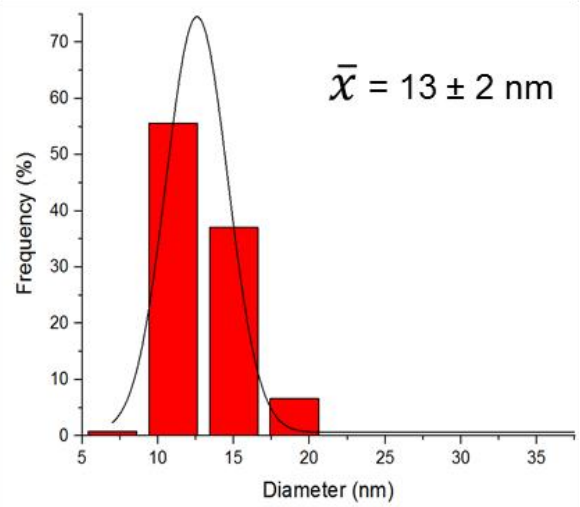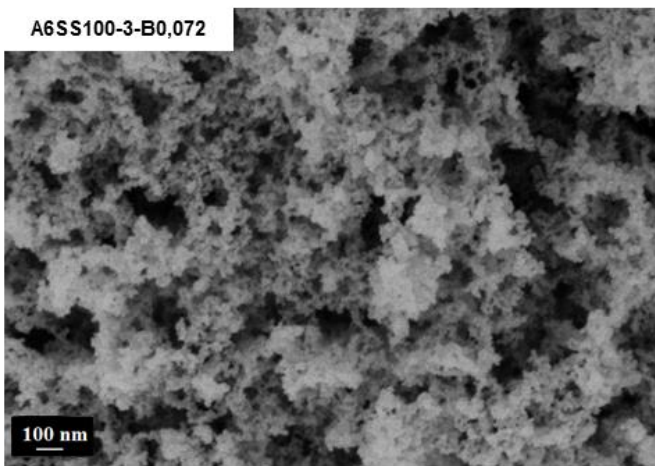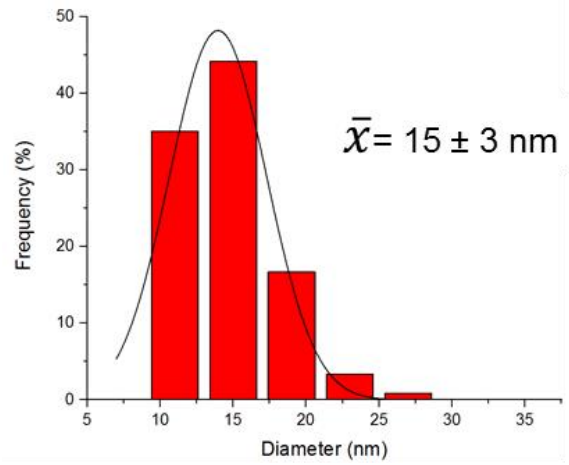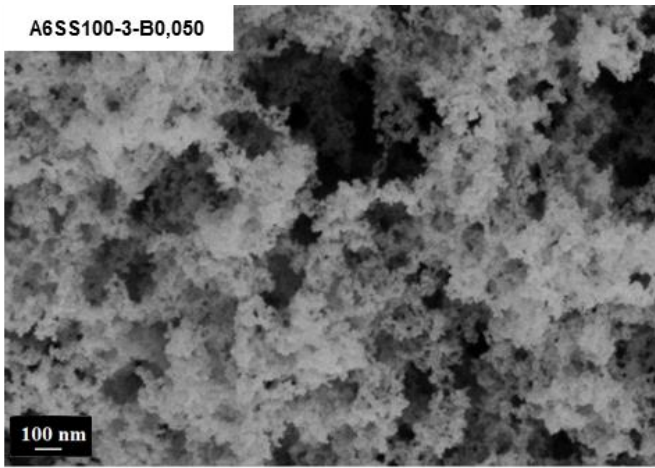
Figure 3.18B SEM images of ATO aerogels, prepared with basic sol-gel catalysts (NaOH), and their respective particle size distribution (150 particles analyzed using Image J software). Maximization of the images = 50000.

Table 3.14. Nitrogen sorption measurement results for pure TO and ATO aerogels prepared with HNO_3 or NaOH as the sol-gel catalyst.

Sample	Specific Surface area BET ($m^2 \cdot g^{-1}$)	PSD (BJH, nm)	Pore volume (BJH, $cm^3 \cdot g^{-1}$)	μ pore volume (BJH, $cm^3 \cdot g^{-1}$)
A6S-1-0.072	41.1 ± 4.1	20 — 30 — 40	0.09 ± 0.01	$0.3 \times 10^{-2} \pm 0.03 \times 10^{-2}$
A6SS100-3-0.050	61.5 ± 6.2	15 — 25 — 30	0.31 ± 0.03	$0.80 \times 10^{-2} \pm 0.08 \times 10^{-2}$
A6SS100-3-0.072	61.4 ± 6.1	15 — 25 — 30	0.29 ± 0.03	$0.20 \times 10^{-2} \pm 0.02 \times 10^{-2}$
A6SS100-3-0.100	64.7 ± 6.5	20 — 25 — 40	0.27 ± 0.03	$0.10 \times 10^{-2} \pm 0.01 \times 10^{-2}$
A6SS100-3-B0.050	73.4 ± 7.3	15 — 20 — 40	0.32 ± 0.03	$0.40 \times 10^{-2} \pm 0.04 \times 10^{-2}$
A6SS100-3-B0.072	83.5 ± 8.3	15 — 20 — 35	0.36 ± 0.04	$0.90 \times 10^{-2} \pm 0.09 \times 10^{-2}$
A6SS100-3-B0.100	89.8 ± 9.0	15 — 20 — 40	0.43 ± 0.03	$0.20 \times 10^{-2} \pm 0.02 \times 10^{-2}$

The adsorption isotherms for both type of aerogels, "basic" and "acid" series, present a sigmoidal type IV shape of mesoporous materials. All isotherms are shown in **Annex**.

Note that the specific surface areas of the "HNO_3" series presented here are slightly lower than that of samples presented in **section II.2**. This may be attributed to the utilization of a different precursor batch. Moreover, the Sn and Sb precursors content were adapted in order to reach doping ratios closer to 10 at. % (12 at. % was obtained in the first series). Decreasing the doping ratio should result in larger particles and smaller specific surface areas.

The "HNO_3" and the "NaOH" series presented here have been prepared with the same Sn precursor and Sb/Sn ratios, making the comparison fair.

As previously observed, the XRD pattern of every sample corresponds to that of rutile SnO_2. Changing the catalyst and its concentration does not impact the crystalline structure, no new phases or peak shift appeared.

Using NaOH instead of HNO_3 as the sol-gel catalyst seems however to result in more amorphous materials, keeping the catalyst concentration constant. As seen for silica aerogels synthesis, acid-catalyzed hydrolysis and condensation lead to weakly branched structures with larger particles sizes, whereas basic conditions results in faster kinetics. Increasing the nucleation rate results in decreased particle size and larger specific surface areas.[15]
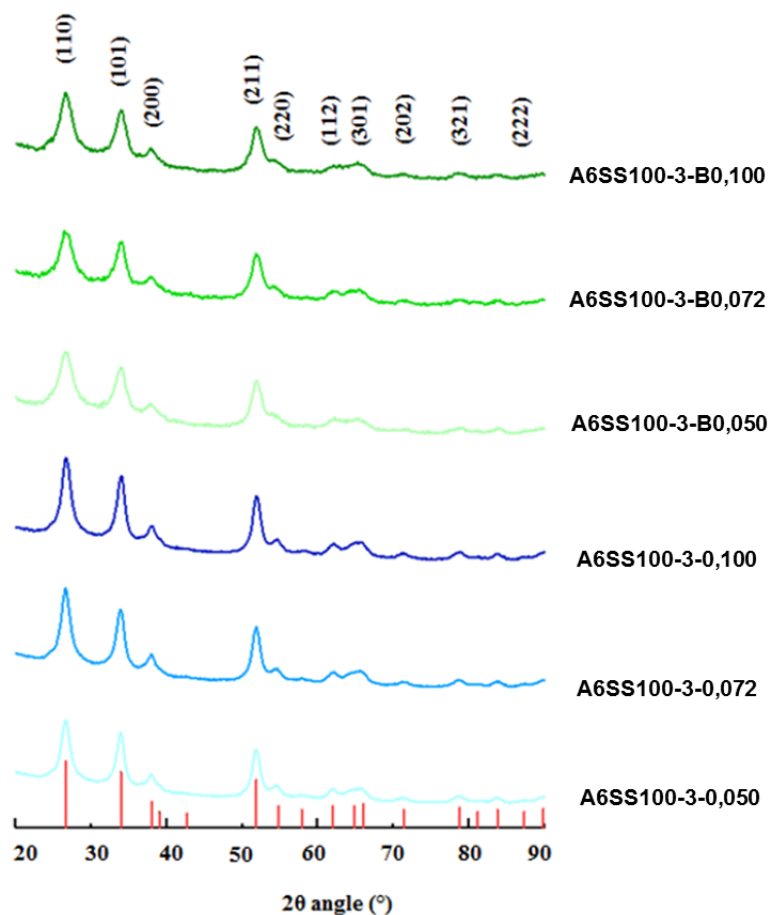
Figure 3.19 X-Ray diffraction diagrams of: ATO aerogels prepared with different ratios of NaOH (green scale) or HNO$_3$ (blue scale). In red the SnO$_2$ pattern of rutile structure (JCPDS 14-1445).[5]

Table 3.15 gathers the crystallites size values, determined with *Debye-Scherer* equation, and the measured primary particle sizes obtained from SEM analysis. For crystallites size measurements, the peak (211) was selected due to lower influence of large peaks close by as for (110) and (101) peaks.

Here again, whatever the catalyst used, primary particles of Sb-doped aerogels are larger than crystallites (**Table 3.15**), suggesting a polycrystalline system. As observed in **section II**, the pure tin oxide sample seems to be monocrystalline. Nucleation and growth control of SnO$_2$ particles with and without dopant has already been observed and reported.[4] Doping inhibits the particle and crystallite growth because foreign atoms do not ideally fit on the Sn^{4+} 6-coordination sites of the rutile network. In case of Sb-doping, Sb^{3+} (76 pm) cations do not fit on the SnO$_2$ (69 pm for Sn^{4+}) rutile network as well as Sb^{5+} (60 pm) ones.

Another interesting point is that the crystallites size of aerogels prepared with the same catalyst (NaOH or HNO_3) are very similar whatever the catalyst ratio. On the contrary, changing HNO_3 for NaOH results in smaller crystallites. This should be linked to the fact that for "basic" prepared aerogels primary particles are smaller, due to the faster nucleation kinetics. Therefore, smaller crystallites are expected for identical synthesis conditions.[4d,15]

Table 3.15. Cell parameters of analyzed aerogels, crystallites sizes (Debye Scherer) and measured primary particles (SEM) of pure TO and ATO aerogels obtained with different catalysts and ratios.

Sample	Primary particle size (nm)	Crystallites size (nm)	a // c lattice parameters (nm)
A6S-1-0.072	22 ± 5	23 ± 2	4.7 // 3.2
A6SS100-3-0.050	16 ± 3	5 ± 0.5	4.7 // 3.2
A6SS100-3-0.072	16 ± 4	5 ± 0.5	4.7 // 3.2
A6SS100-3-0.100	16 ± 3	5 ± 0.5	4.7 // 3.2
A6SS100-3-B0.050	15 ± 3	3 ± 0.5	4.7 // 3.2
A6SS100-3-B0.072	13 ± 2	5 ± 0.5	4.7 // 3.2
A6SS100-3-B0.100	14 ± 3	4 ± 0.5	4.7 // 3.2

III.2.2 Chemical composition

In this study, the respective amounts of Sn and Sb precursors have been adapted to reach the targeted doping ratio of 10 at. %, approximately. **Table 3.16** shows EDX values between 9 and 11 at. % depending on the sample.

It is interesting to notice that the Sb segregation percentage (relative concentration difference between the surface and the bulk of particles, calculated as $[Sb]_{surf}$-$[Sb]_{bulk}$)/ -$[Sb]_{bulk}$) was significantly lower in the case of basic-catalyzed aerogels.

Segregation percentages of the "acid" series present values above 12%, while less than 4% was obtained for the "basic" series. Such segregation percentages are attributed to the different sol-gel kinetics between "basic" and "acid" catalysed sol-gel synthesis. If for "basic" synthesis the sol-gel reaction kinetics are faster than for the "acid" synthesis,[15] entailing a faster nucleation rate of tin dioxide-based particles, more Sb^{5+} (60 pm) can probably substitute Sn^{4+} (69 pm) in the SnO_2 network . Therefore, in "basic" synthesis; less unsubstituted Sb remain between the grain boundaries, lowering the segregation to the particles surface during

calcination. A better Sb repartition is thus supposed in the case of the "basic" synthesis due to better Sb integration in the rutile network.

Hopefully, this may increase the material chemical stability. Indeed, as mentioned before, several studies published in the literature reported that antimony dissolution has been observed under potentials around OER working conditions.[7,16] This is impacting some properties of the catalyst support, the major one being the electronic conductivity. With lower segregation, slower dissolution during the OER can be expected.

Table 3.16. Bulk and near-surface chemical composition of the as-prepared aerogels determined by EDX and XPS analyses, respectively.

Sample	Nominal dopant-rate (at. %)	Sb / (Sb+Sn) EDX (at. %)	Sb / (Sb+Sn) XPS (at. %)	Segregation % ($[Sb]_{surf}-[Sb]_{bulk}$)/ - $[Sb]_{bulk}$
A6S-1-0.072	-	-	-	-
A6SS100-3-0.050	10	8.7 ± 1.0	9.8 ± 0.1	12.6
A6SS100-3-0.072	10	9.5 ± 0.3	11.8 ± 0.1	24.2
A6SS100-3-0.100	10	9.0 ± 1.5	10.1 ± 0.1	12.2
A6SS100-3-B0.050	10	10.9 ± 0.3	11.3 ± 0.1	3.7
A6SS100-3-B0.072	10	11.0 ± 0.7	11.1 ± 0.1	0.9
A6SS100-3-B0.100	10	10.6 ± 0.4	10.8 ± 0.3	1.9

III.2.3 Electronic conductivity

When comparing electronic conductivity between both aerogels series (**Table 3.17**) it was found that the electronic conductivity of aerogels prepared with NaOH is slightly lower than that of the "acid" series. This may be ascribed to their smaller crystallites and primary particles, which induce more grain boundaries, interfaces and defects.

However, the difference in conductivity remains reasonable and ATO basic catalyzed aerogels are interesting due to the lower Sb surface segregation, which could, as mentioned above, induce less Sb dissolution and, probably, a higher corrosion resistance during OER.

Table 3.17. ATO aerogels electronic conductivity determined by resistance measurements obtained with an applied pressure of 1 ton.

Sample	Sb / (Sb+Sn) EDX (at. %)	Sb / (Sb+Sn) XPS (at. %)	Crystallites size (nm)	Conductivity (S·cm^{-1})
A6S-1-0.072	-	-	23 ± 2	5 x 10^{-4*}
A6SS100-3-0.050	8.7 ± 1.0	9.8 ± 0.1	5 ± 1	1.17 ± 0.02
A6SS100-3-0.072	9.5 ± 0.3	11.8 ± 0.1	5 ± 0.5	1.02 ± 0.02
A6SS100-3-0.100	9.0 ± 1.5	10.1 ± 0.1	5 ± 0.5	0.83 ± 0.02
A6SS100-3-B0.050	10.9 ± 0.3	11.3 ± 0.1	3 ± 0.5	0.65 ± 0.05
A6SS100-3-B0.072	11.0 ± 0.7	11.1 ± 0.1	4.5 ± 0.5	0.77 ± 0.02
A6SS100-3-B0.100	10.6 ± 0.4	10.8 ± 0.3	4 ± 0.5	0.67 ± 0.04

It is difficult for our samples to find a relation between Sb segregation and conductivity. If we compare results of both series (acid and basic), we can imagine that if for larger Sb surface enrichment, the conductivity is higher, maybe the electron mobility goes through the particles surface of the aerogel. Such hypothesis is difficult to contrast with other obtained results with our materials, as the used tin precursor is different, and therefore, the synthesis conditions are different too.

We can also think that, higher segregation percentages of Sb dopant can also decrease the Sb^{5+} / Sb^{3+} on the surface, being the electron mobility reduced among all the material.

Normally higher dopant segregation is related to the presence of higher crystallites sizes, which during calcination facilitates non-inserted dopant atoms diffusion.[4,6] But higher crystallinity of the material favors electron mobility.

Therefore, in this case we relate the higher conductivity of the "acid" ATO aerogels to the presence of larger crystallites. As said before, we attribute the presence of larger particles and crystallites sizes for "acid" ATO materials to the acid sol-gel synthesis, which is slower than the basic one.

III.2.4 Electrochemical corrosion evaluation tests

As mentioned in bibliography, Sb segregation on ATO materials has already been widely reported,[17] causing a modification of the Sb repartition among the material and modifying its intrinsic properties. A general segregation/dissolution mechanism for ATO materials has been proposed by Fabbri *et. all.*:[16a] where calcination temperature, calcination time, and potential cycling produced an initial Sb surface enrichment. Sb surface segregation can then further proceed until the formation of a Sb oxide layer (Sb_2O_4 phase).[6d,e,f] Finally, Sb is leached out from the tin oxide surface (being dissolved in the case of potential cycling in aqueous media), leaving a bulk material poorer in dopant, resulting in a loss of conductivity.

It was thus worth comparing the electrochemical stability of ATO samples presenting different Sb segregation. Samples A6SS100-3-0.072 and A6SS100-3-B0.072 were selected, due to very different segregation % (1% and 24% respectively). Stability tests were carried out on RDE recording the current under a constant applied voltage of 1.58 V for 2 hours.
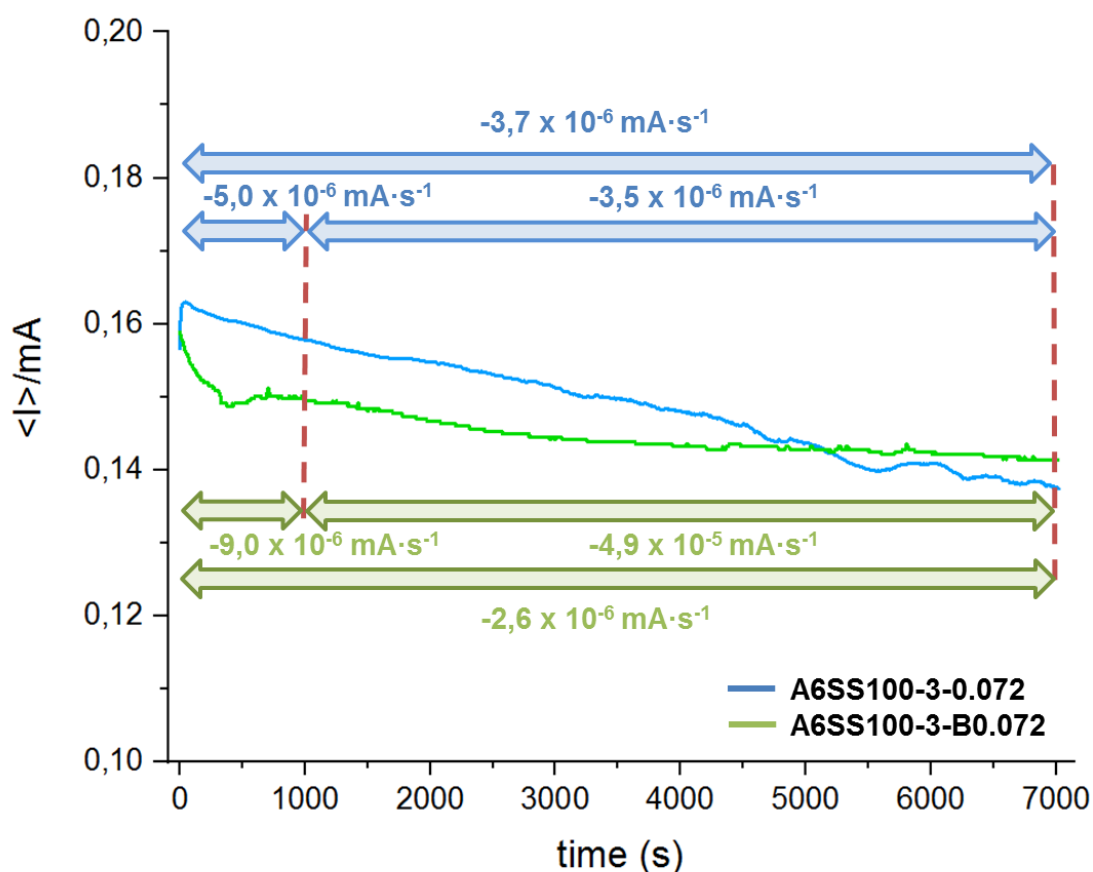
Figure 3.20 2-hours chronoamperometry profiles recorded for ATO aerogels (blue: A6SS100-3-0.072, green: A6SS100-3-B0.072) with their corresponding current loss at different times (from 0 to 1.000 s, from 1.000 to 7.000 s and from 0 to 7.000 s). Measurements were carried out on a 1M solution of H_2SO_4 under N_2 atmosphere and a constant applied voltage of 1.58 V vs. RHE.

Chronoamperometry profiles of both ATO aerogels show no drastic loss of current intensity during the 2-hours experiment (**Figure 3.20**). First, this, suggests that our ATO aerogels are promising candidates as catalyst supports for OER. Second, it is noteworthy that the profile recorded for A6SS100-3-B0.072 showed less current loss than that recorded for A6SS100-3-0.072.," Basic" ATO aerogels may then be less prone to degradation.

Figure 3.21 shows the cyclic voltammograms recorded between 0.05 and 1.40 V vs RHE, at a potential sweep rate of 50 mV·s^{-1}, before and after the 2 hours chronoamperometry.
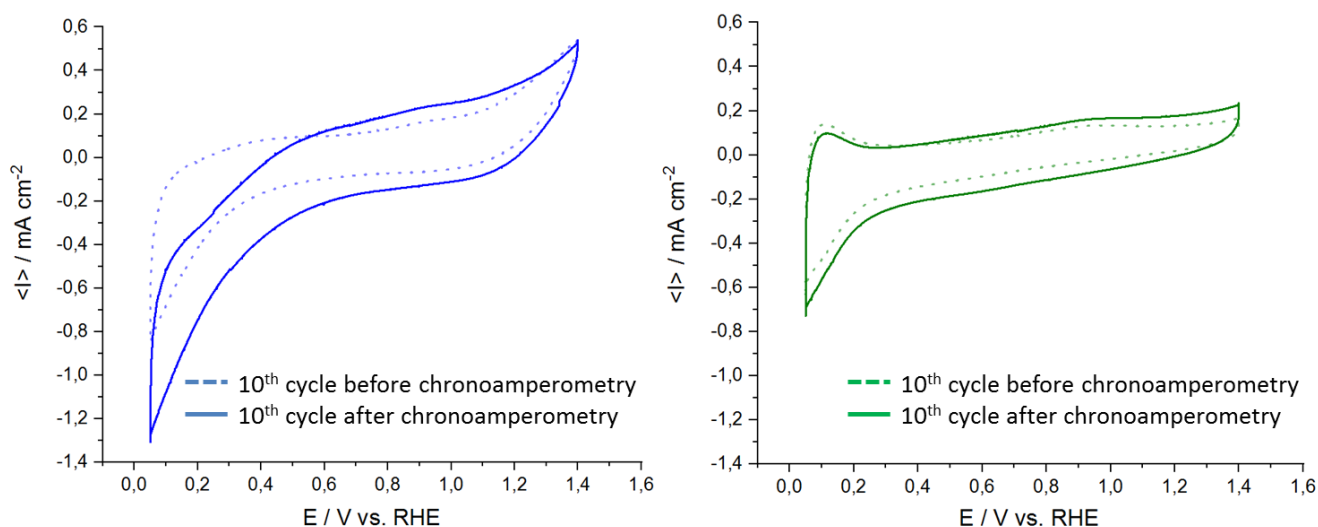
Figure 3.21 Cyclic voltammograms of ATO doped with 10% of Sb. Left: the tenth cycle before (dotted) and after the 2-hour chronoamperometry obtained with A6SS100-3-0.072 (HNO$_3$). Right: the tenth cycle before (dotted) and after the 2-hour chronoamperometry obtained with A6SS100-3-B0.072 (NaOH). Measurements were carried out on a 1M solution of H$_2$SO$_4$ under N$_2$ atmosphere.

The comparison of the cyclic voltammograms recorder for both ATO aerogels seem to confirm the better stability under OER conditions of basic catalyzed ATO aerogels. The two CVs recorded for A6SS100-3-B0.072 (basic catalyzed aerogel), the one before the stability test and the one after, are very similar, suggesting a low degradation of the material during the two-hours under 1.58 V. On the contrary, the voltammograms recorded for A6SS100-3-0.072 (acid catalyzed aerogel) are quite different. The higher intensity of the cathodic current recorded after the stability tests suggests that a non-reversible process is occurring at the surface of the material. This may correspond to Sb dissolution.

In the following chapter, Ir will be supported on the developed ATO aerogels and a more detailed comparison of corrosion resistance between both aerogels will be performed.

III.3 Conclusions and perspectives

Antimony tin oxide (ATO) aerogels were synthesized by a sol-gel route starting with metal alkoxide precursors ($Sn(OiPr)_4$). Herein we varied the calcination time at 600ºC and the type of sol-gel catalyst used during the sol-gel process: acid (HNO_3) versus basic (NaOH).

To sum up, it was not found any effect of the calcination time on ATO aerogels.

ATO aerogels prepared with a basic catalyst seemed to be more promising and stable under OER conditions than aerogels prepared with HNO_3 as a sol-gel catalyst.

All aerogel samples showed an interconnected primary particle network with bimodal mesoporous pore size distributions. ATO aerogels prepared with NaOH present smaller primary particles than those prepared with HNO_3, giving to the first ones a superior airy morphology with higher specific surface areas reaching values of 90 $m^2 \cdot g^{-1}$ for the ratio NaOH/Sn = 0.1.

All calcined ATO aerogels presented the SnO_2 rutile crystal phase only, without any peaks shift. Moreover, no visible Sb oxide crystal phase was detected, suggesting no modification of the rutile network.

No difference in crystallinity was observed between aerogels calcined at different times. Temperature mostly rules the crystallinity instead of time. On the contrary, higher specific surface areas and lower crystallites sizes, give to ATO aerogels prepared with NaOH conductivities lower than the acid ones (0.8 $S \cdot cm^{-1}$ versus 1 $S \cdot cm^{-1}$ respectively for A6SS100-3-B0.72 and A6SS100-3-0.72). We related such results to the faster sol-gel kinetics under basic conditions, that leads to the formation of smaller particles, and therefore; larger surface areas, smaller crystallites and lower conductivities. We also ascribed to the faster kinetics the lower Sb segregation percentage of "basic" series compared to "acid" ones (1% versus 24% respectively for A6SS100-3-B0.72 and A6SS100-3-0.72).

Finally, our chronoamperometry tests showed a greater resistance of basic ATO aerogels suggesting more interest for such oxide materials as catalyst support.

It is noteworthy that preparing an ATO material with a high surface area, a good electronic conductivity and a long-term stability under OER conditions, all desired properties in one, is rather difficult. Indeed, high surface area materials lead up to small primary particle, generally resulting in low conductivities due to more grain boundaries. Hence it is necessary to find the best compromise between all the desired properties.

Generally speaking, the higher the catalyst ratio the higher the specific surface area but the lower the electronic conductivity. Hence, for the following studies and the deposition of iridium, we decided to keep the catalyst ratio to 0.072 for a better compromise between both properties.

IV Modification of the Tantalum-doped tin dioxide aerogels (TaTO) synthesis route

Herein a similar study as for ATO aerogels (**section III**) was carried out, where the preparation route of TaTO (Tantalum-doped tin dioxide) was modified in order to get a deeper knowledge of such Ta-doped materials. Using as the reference the sol-gel method protocol previously developed by our group,[3] different synthesis conditions have been tested in order to improve the desired properties of TaTO aerogels. Following obtained results for ATO aerogels, two main parameters were investigated: (1) the catalyst used for the sol-gel reaction (NaOH *vs* HNO$_3$) injected at different ratios, and (2) the Ta doping ratio. The effect of these parameters on the sol-gel route in the final TaTO aerogels properties (such as the morphology, specific surface area, chemical repartition of Ta atoms or electronic conductivity), is discussed in this section.

IV.1 Synthesis of novel TaTO aerogels: impact of the sol-gel catalyst, type and concentration

Since NaOH proved to be beneficial in the case of ATO, it has also been used for the synthesis of TaTO. Therefore, different aerogels (Ta-doped with 10% at.) were prepared by the sol-gel route described in **section II.1**, with different sol-gel catalyst ratios (basic or acid). **Table 3.18** presents the synthesis conditions followed for each sample. All aerogels where calcined for 5 hours at 600°C in air, keeping the same hydrolysis and solvent ratios, S = 120 and R = 3 respectively.

A similar kind of nomenclature as that proposed for ATO was used to identify the samples.
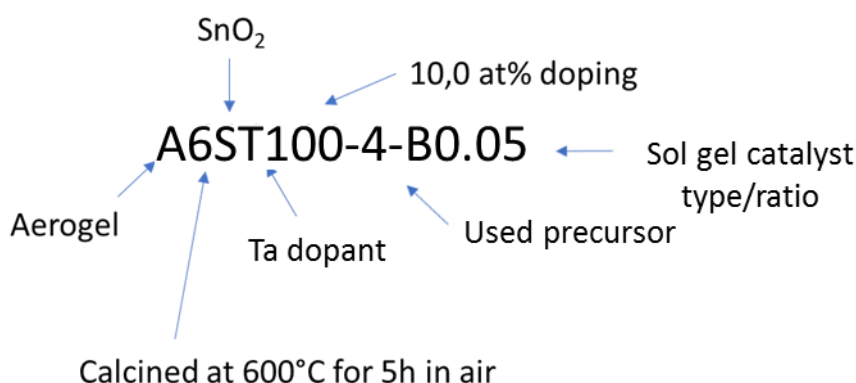
Figure 3.22 Labeling of as-prepared TaTO samples.

Table 3.18. Summary of the as-prepared Ta-doped aerogels.

Aerogel	Sample	Nominal Sb doping (at. %)	Sol-gel catalyst	(HNO$_3$ or NaOH) / Sn atomic ratio
TaTO	A6ST100-4-0.050	10	HNO$_3$	0.050
TaTO	A6ST100-4-0.072	10	HNO$_3$	0.072
TaTO	A6ST100-4-0.100	10	HNO$_3$	0.100
TaTO	A6ST100-4-B0.050	10	NaOH	0.050
TaTO	A6ST100-4-B0.072	10	NaOH	0.072
TaTO	A6ST100-4-B0.100	10	NaOH	0.100

IV.1.1 Morphology and structure (impact of sol-gel catalyst)

SEM images of the Ta-doped aerogels showed morphologies similar to that of pure TO and previously prepared doped-TO aerogels, as seen in **section II**. Herein (**Figures 3.23A and 3.23B**) we observe the same agglomeration or aggregation of rather small primary particles (around 12 nm in diameter for all analyzed samples, **Table 3.20**), smaller than those of pure TO aerogels (22 nm). Therefore, as seen for our doped-TO aerogels, the presence of Ta as a doping agent seems to inhibit the particle growth during the sol-gel procedure. Such a nucleation and growth control of SnO$_2$ particles with dopant has already been studied and reported by other groups.[3,4,6]

The main difference between the different TaTO aerogels prepared here stands in the presence or not of big grains (between 50 and 100 nm), with geometrical shapes, that seem to be trapped inside the aerogel network. Their evolution seems to be related to the amount of the Ta doping agent (Ta at. %). It is discussed in the following section (**section IV.2**). Such grains are largely present for 10 at. % doped TaTO, as seen on SEM images, whatever the type of catalyst (acid or basic) and its concentration in the sol.
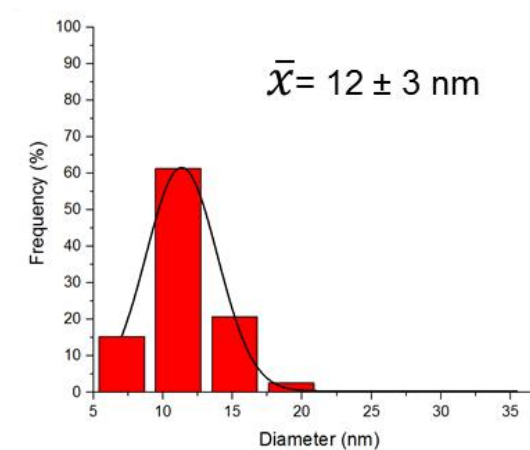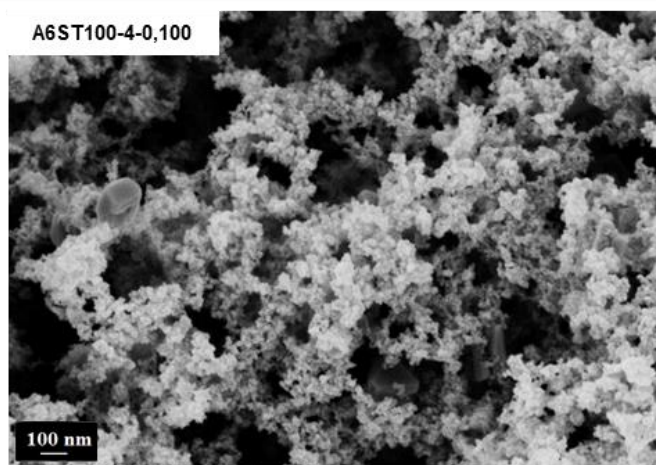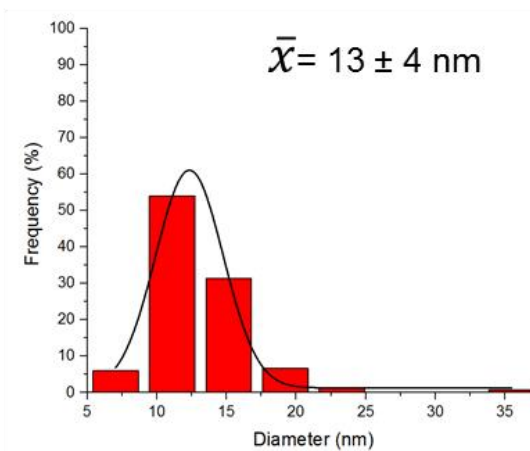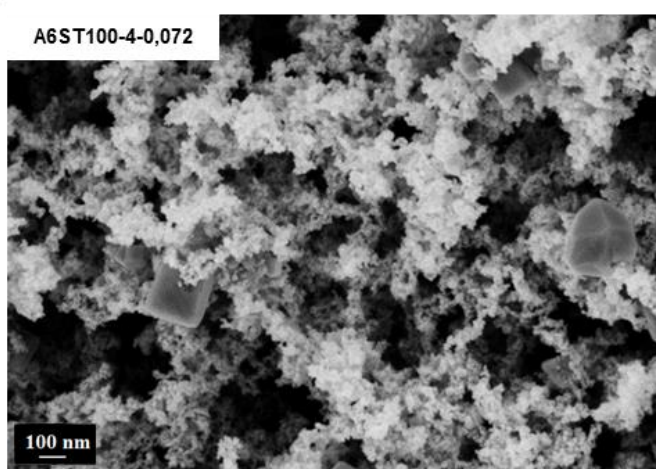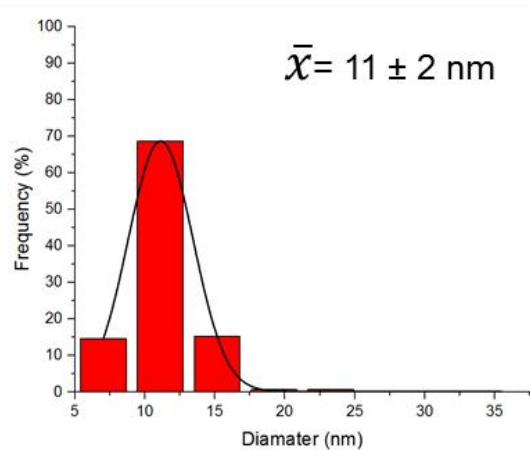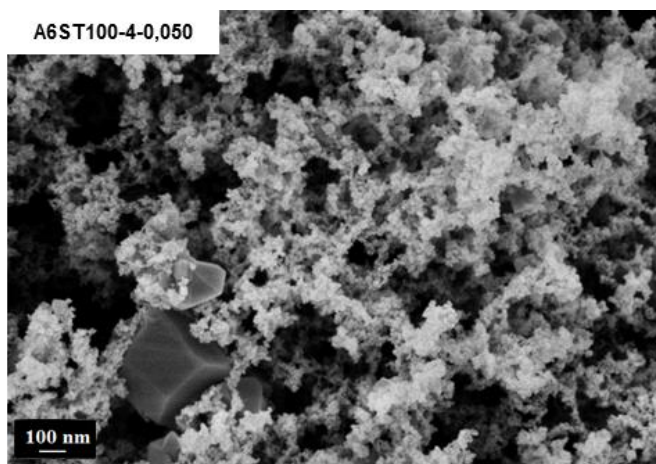
Figure 3.23A SEM images of TaTO aerogels, prepared with acid sol-gel catalyst (HNO$_3$), and their respective particle size distribution (150 particles analysed using *Image J* software). Maximization of the images = 50000.
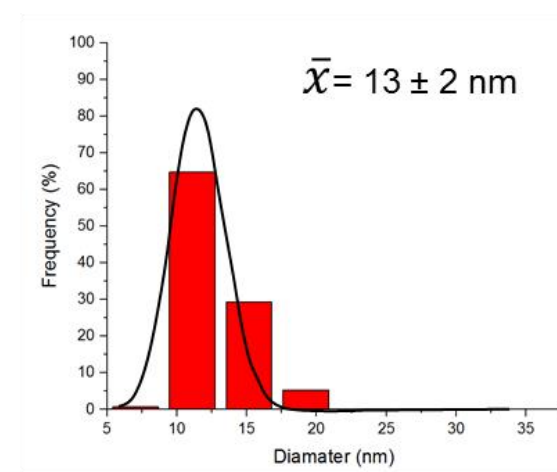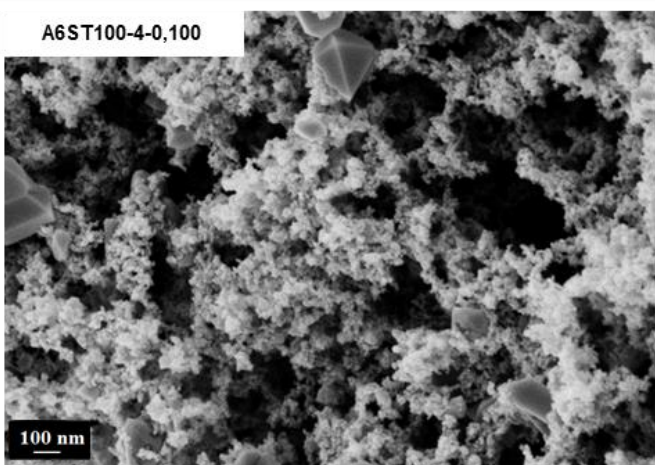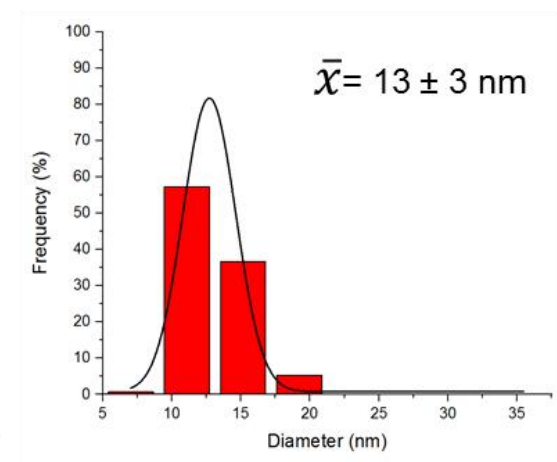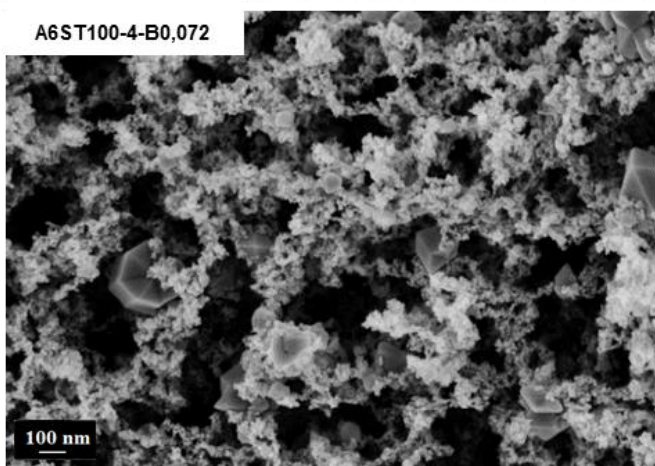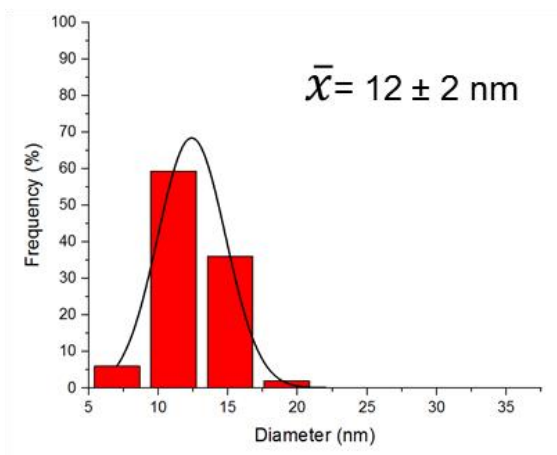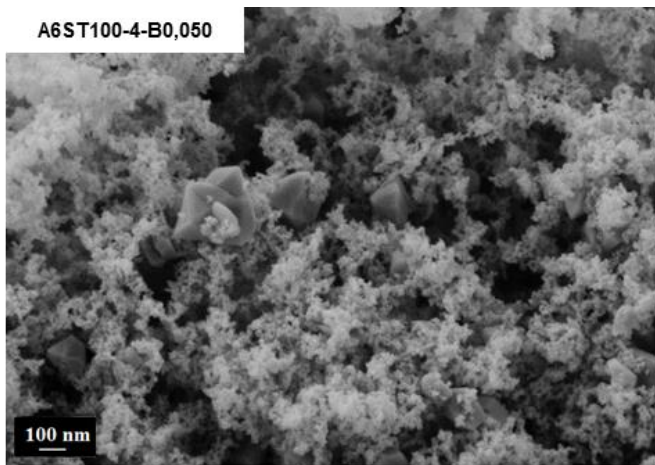
Figure 3.23B SEM images of TaTO aerogels, prepared with basic sol-gel catalyst (NaOH), and their respective particle size distribution (150 particles analysed using *Image J* software). Maximization of the images = 50000.

They have already been observed on previous of our studies. Fabien Labbé found similar structures when coating carbon materials with tin dioxide, starting from $SnCl_2$ as a precursor.[18] In this study, it was found that adjusting the initial pH above the point of zero charge of such carbon materials, the favorable electrostatic attractions allowed to optimize the coating level. Then, it was possible to reduce the presence of such pure SnO_2 big grains, obtaining a more homogeneous tin dioxide coating.

In our case, EDX analyzes focused on the big grains showed an almost pure SnO_2 composition. It was surprising to find such big grains for Ta-doped materials, and not for Sb-doped samples. Their presence may be ascribed to different sol-gel kinetics. These grains could be formed due to a preferential growing of Sn-O-Sn chains, at the beginning of the sol-gel reactions. However, since in "basic" conditions, the kinetics of sol-gel reactions (hydrolysis and condensation) are supposed to be faster, a more homogeneous aerogel was expected. Unfortunately, we don't see such an effect on our materials. Hence, if we stick to this interpretation, we can hypothesize that Ta may slow the reaction down compared to Sb. This would impact the segregation and will discussed later.

Additional morphological data were obtained by nitrogen sorption analysis. As for previous studied aerogels, all the obtained adsorption isotherms correspond to mesoporous materials with a sigmoidal isotherm of type IV (see **Annex**). As previously, the calculated specific surface area was based on the BET model, and the Pore Size Distributions (PSD) and mesoporous volumes on the BJH model.

Results gathered in **Table 3.19**, show no significant differences between all our Ta-doped aerogels. The specific surface areas and pore volume of the aerogels are similar between both series. Here again we can notice a difference with the results obtained for Sb-doped aerogels, which showed smaller particles in basic conditions. Herein the modification of the sol-gel media seems to have no, or negligible effect on the primary particle size. Therefore, the starting sol-gel kinetics should be different for Ta-doped samples than for Sb, confirming our previous statement. Should it be more difficult for Ta than for Sb to be integrated in the SnO_2 rutile network? This should not be a question of size since Ta^{5+} and Sn^{4+} have similar ionic radii (64 pm and 69 pm respectively).

As seen on **Figure 3.24**, the XRD diffraction diagrams of TaTO materials fit perfectly with the SnO_2 rutile structure. No peak shifts or characteristic peak of novel Ta-based phases are observed. As for Sb-doped aerogels, *a*/*c* lattice parameters are not impacted by the catalyst and its concentration (**Table 3.20**).

Table 3.19. Nitrogen sorption measurement results for TaTO aerogels.

Sample	Specific surface area BET ($m^2 \cdot g^{-1}$)	PSD (BJH, nm)	Pore volume (BJH, $cm^3 \cdot g^{-1}$)	µ-pore volume (BJH, $cm^3 \cdot g^{-1}$)
A6ST100-4-0.050	62.6 ± 6.3	10--25--50	0.40 ± 0.04	$0.10 \times 10^{-2} \pm 0.01 \times 10^{-2}$
A6ST100-4-0.072	75.3 ± 7.5	10--20--30	0.36 ± 0.04	$0.40 \times 10^{-2} \pm 0.04 \times 10^{-2}$
A6ST100-4-0.100	68.2 ± 6.8	10--25--40	0.27 ± 0.03	$0.30 \times 10^{-2} \pm 0.04 \times 10^{-2}$
A6ST100-4-B0.050	67.6 ± 6.8	10--20--35	0.33 ± 0.03	$0.40 \times 10^{-2} \pm 0.04 \times 10^{-2}$
A6ST100-4-B0.072	57.7 ± 5.8	10--25--30	0.29 ± 0.03	$0.80 \times 10^{-2} \pm 0.08 \times 10^{-2}$
A6ST100-4-B0.100	65.4 ± 6.35	10--20--30	0.34 ± 0.03	$0.40 \times 10^{-2} \pm 0.04 \times 10^{-2}$

Previous results reported in **sections II** and **III**, suggest a polycrystalline system for each primary particle of the doped-TO aerogel. The same phenomenon is observed for to the Ta-doped samples prepared in this part of the work. However, the presence of big geometrical grains inside the aerogel made it difficult to confirm applying the Debye-Scherer equation on peak (211).

Table 3.20. Measured primary particles (SEM), crystallites sizes (Debye Scherer) and cell parameters of analyzed aerogels.

Sample	Measured primary particle size (nm)	Crystallites size (nm)	a // c lattice parameters (nm)
A6ST100-4-0.050	11 ± 2	31 ± 4	4.7 // 3.2
A6ST100-4-0.072	13 ± 4	20 ± 1	4.7 // 3.2
A6ST100-4-0.100	12 ± 3	26 ± 2	4.7 // 3.2
A6ST100-4-B0.050	12 ± 2	23 ± 2	4.7 // 3.2
A6ST100-4-B0.072	13 ± 3	20 ± 2	4.7 // 3.2
A6ST100-4-B0.100	13 ± 2	18 ± 2	4.7 // 3.2
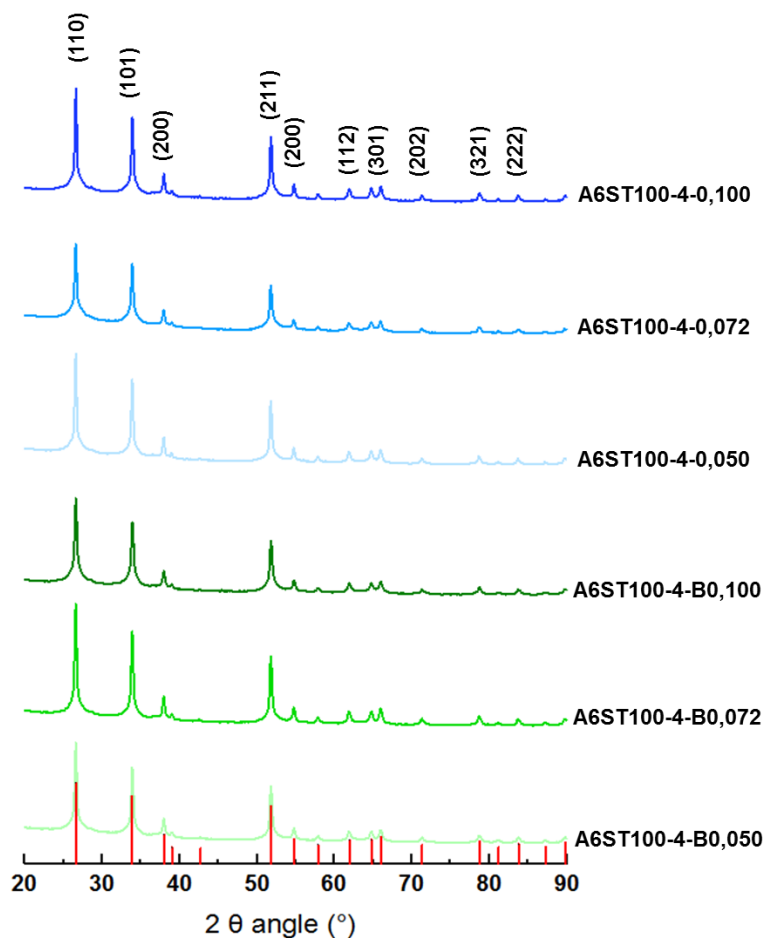
Figure 3.24 X-Ray diffraction diagrams of TaTO aerogels prepared with different ratios of NaOH (green scale) or HNO₃ (blue scale). In red the SnO₂ pattern of rutile structure (JCPDS 14-1445).[5]

IV.1.2 Chemical composition (impact of sol-gel catalyst)

The chemical composition affects the electronic conductivity. Despite the amount of Ta dopant precursor can be controlled at the beginning of the sol-gel process, the exact concentration of the Ta and, more importantly, its repartition inside the final aerogel particles has to be analyzed. There are many possible causes that can modify the final dopant amount in samples, such as: the homogeneity of the primary solution linked to the Ta precursor dissolution, the precipitation of precursors during sol-gel reactions or the pH of the media. Different sol-gel kinetics can also induce a different repartition of the doping agent through the particles, and affect its integration in the rutile network. Moreover, during calcination the thermal energy can induce segregation of the dopant (Ta) from the bulk to the surface.

As supposed for Sb-doped aerogels, the catalyst type can modify the kinetics of sol-gel reactions, hydrolysis and condensation reactions, and therefore the composition of the doped SnO₂. Compared EDX and XPS analysis (**Table 3.21**) highlighted a pronounced segregation

of Ta from the bulk to the surface for all samples, whatever the catalyst type or ratio. The segregation is even more important than for Sb, thus confirming the slower kinetics induced by Ta hypothesized in **section IV.1.1**. As in the case of Sb doping, the percentage of segregation seems to be less important when NaOH is used as the sol-gel catalyst. This is ascribed to the faster sol-gel reaction kinetics under basic media, as seen for Sb-doped materials (**section III.1** and **III.2**).

Table 3.21. Bulk and surface chemical composition results, measured by EDX and XPS analysis.

Sample	Dopant-rate (at. %)	Ta/(Ta+Sn) EDX (at.%)	Ta/(Ta+Sn) XPS (at.%)	% segregation ($[Ta]_{surf}$-$[Ta]_{bulk}$)/ -$[Ta]_{bulk}$
A6ST100-4-0.050	10.0	10.0 ± 0.6	18.1 ± 0.7	81.0
A6ST100-4-0.072	10.0	11.8 ± 2.7	15.1 ± 0.4	28.0
A6ST100-4-0.100	10.0	11.6 ± 2.4	18.5 ± 1.8	59.5
A6ST100-4-B0.050	10.0	10.2 ± 2.3	15.8 ± 0.7	54.9
A6ST100-4-B0.072	10.0	10.7 ± 0.3	17.2 ± 1.0	17.2
A6ST100-4-B0.100	10.0	12.2 ± 2.7	15.3 ± 0.3	15.3

IV.1.3 Electronic conductivity (impact of sol-gel catalyst)

Herein, the electronic conductivity of TaTO aerogels was measured using the same home-made cell, as described in **section III.3** of **chapter 2**. Unfortunately, the electronic conductivity was too low to be measured *i.e.* lower than 1 mS·cm^{-1}, the detection limit of our device. The difference with the sample characterized in **section II** of this chapter, (similar at. %) was ascribed to the margin of error of our technique associated to the vicinity of the conductivity with the detection limit of the device.

In the case of Ta, higher electronic conductivities have been reported for much lower doping ratio, the optimum being between 1 and 4 at.%.[19, 20, 21]

Such a small conductivity obtained for 10 at. % Ta-doping can be attributed to several causes: (1) small grain size inducing numerous grain boundaries and interfaces resistances (as the higher the Ta concentration, the smaller the primary particles size), (2) structural imperfections and relatively large number of dislocations due to high Ta doping ratio, (3) Ta ions on interstitial

lattice positions, (4) reduction of Ta^{5+} ions into Ta^{3+} that can induce a decrease of the number of oxygen vacancies and electron concentration, leading to a conductivity decrease.[3]

The impact of Ta ratio is studied in the following section.

IV.1.4 Conclusions

In this section TaTO aerogels doped with a Ta content of 10 at. % were prepared with different sol-gel catalysts (NaOH and HNO_3) at different ratios, as done for ATO materials in **section III**.

The morphology of aerogels did not change with the sol-gel catalyst type or ratio, keeping the 3D-airy morphology based on interconnected particles. Primary particles did not change in size resulting in similar specific surface areas. The presence of big grains that appeared in the TaTO aerogels network was not affected by the modification of the sol-gel catalyst, meaning that it may not be related to the medium pH.

As seen for ATO aerogels, NaOH sol-gel catalyst seemed to reduce the dopant segregation (difference between the surface and bulk concentration). For TaTO aerogels lower segregation percentages were found for the "basic" series when compared to the "acid" ones. Despite that, the segregation was still high if compared to ATO materials. The faster sol-gel reaction kinetics that have a visible effect for ATO materials, as seen in **section III**, is less pronounced herein. Therefore, it seems that Ta has less affinity than Sb for the SnO_2 rutile network.

As no improvement of the TaTO aerogels was obtained when playing with the sol-gel catalyst, it was decided to keep HNO_3 at a ratio of 0.072 for the following TaTO synthesis study, dedicated to the influence of the Ta ratio on the properties of TaTO.

IV.2 Synthesis of novel TaTO aerogels: impact of the Ta doping ratio

Here is reported a study on the impact of the Ta content on the main aerogel properties: specific surface area and conductivity. A set of Ta-doped tin dioxide aerogels with Ta concentrations ranging from 0.5 to 20 at. %, were prepared following the sol-gel route described in **section II.1**. A home-made tin alkoxide precursor was specifically prepared and the main synthesis parameters were kept constant: S = iPrOH / Sn = 120, R = H_2O / Sn = 3, C = HNO_3 / Sn = 0.07. The aerogels obtained were calcined 5-hour at 600°C in air.

Samples were labeled according the same mentioned dedicated nomenclature, **Figure 3.25**: the non-doped tin dioxide aerogel was labeled as A6S, and the 10 at% Ta-doped SnO_2 as A6ST100; where A stands for aerogel, 6 for calcination temperature (600ºC), S for SnO_2, T for Ta doping, and 100 for 10.0 at. % doping.
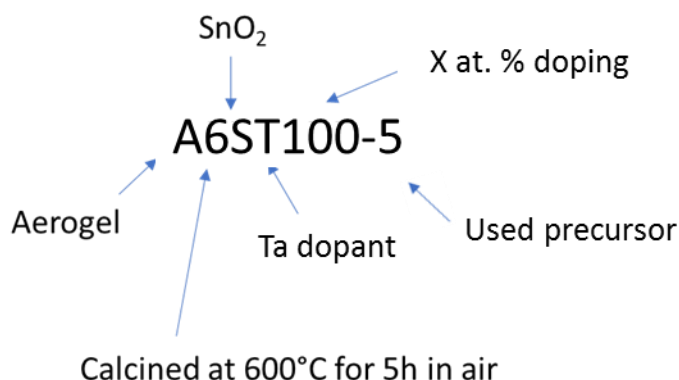
Figure 3.25 Labeling of as-prepared TaTO samples.

Table 3.22 presents the synthesis conditions of each sample:

Table 3.22. Summary of the as-prepared Ta-doped aerogels.

Aerogel	Sample	Nominal Sb doping (at. %)
TaTO	A6ST005-5	0.5
TaTO	A6ST010-5	1.0
TaTO	A6ST025-5	2.5
TaTO	A6ST050-5	5.0
TaTO	A6ST075-5	7.5
TaTO	A6ST100-5	10
TaTO	A6ST150-5	15
TaTO	A6ST200-5	20

IV.2.1 Morphology and structure

SEM images of the Ta-doped aerogels show the presence of the already discussed big grains inside the network made up of primary particles. As said before, the size of the grains seems to be heterogeneous for each sample, as well as their location random through the aerogel network. By observing SEM images (**Figure 3.26**) the presence and the size of this grains seem to be related to the Ta content as their number and size increase for low doping ratios. The number of such large grains of pure SnO_2 becomes residual for 15 and 20 at. % of Ta. We can imagine that for lower Ta doping concentrations, larger number of pure tin dioxide particles are formed due to a preference of creating Sn-O-Sn chains than Sn-O-Ta on the network. Therefore, as the number of Ta dopants increase, it is necessary for the aerogel mesh to form Sn-O-Ta chains, as the ratio Sn/Ta decrease.

Another possibility is that the surface segregation of Ta entails the formation of amorphous Ta_2O_5 phase on the particle surface, which inhibits the particle growth of the tin dioxide-based primary particles. Such an effect has been reported to be promoted by calcination, or by potential cycling.[22]

At the same time, larger dopant ratios have a negative effect on particle and crystallites growth, as seen for ATO aerogels (**Table 3.24**).[4,6]

A6ST005 (a) $\bar{x}$ = 19 ± 5 nm

A6ST010 (b) $\bar{x}$ = 16 ± 4 nm

A6ST025 (c) $\bar{x}$ = 14 ± 3 nm

A6ST050 (d) $\bar{x}$ = 13 ± 3 nm
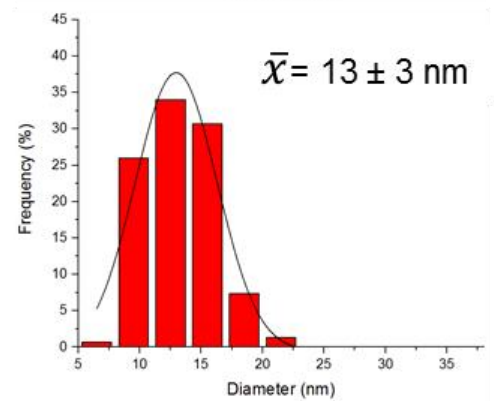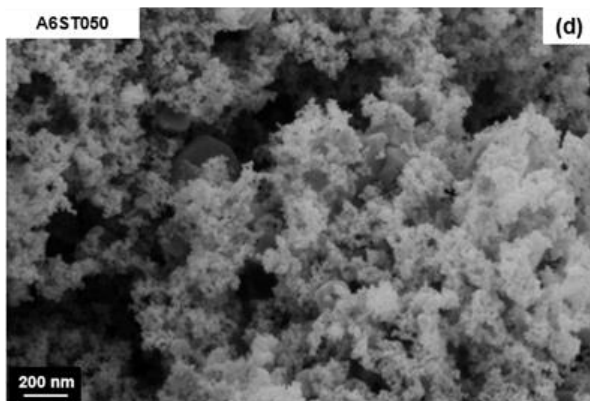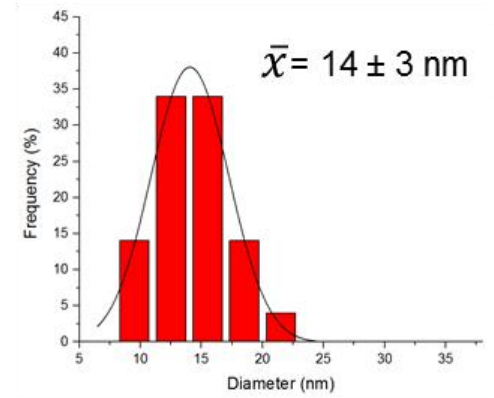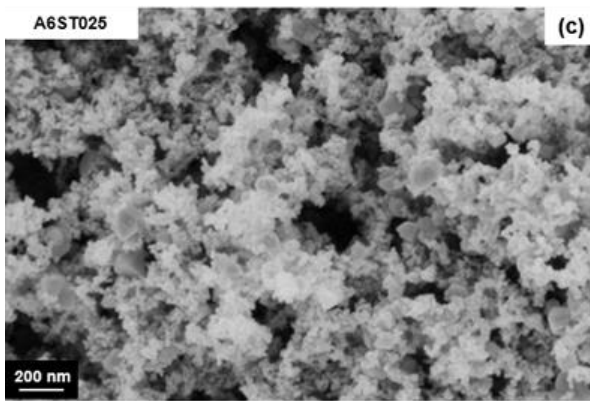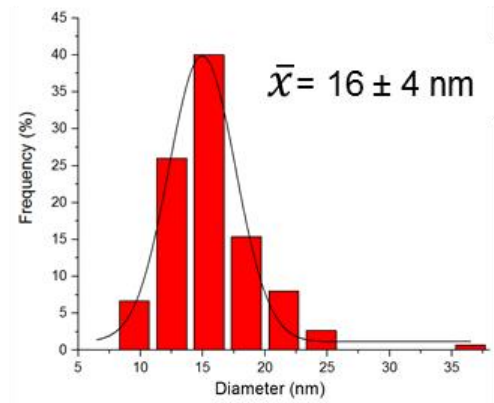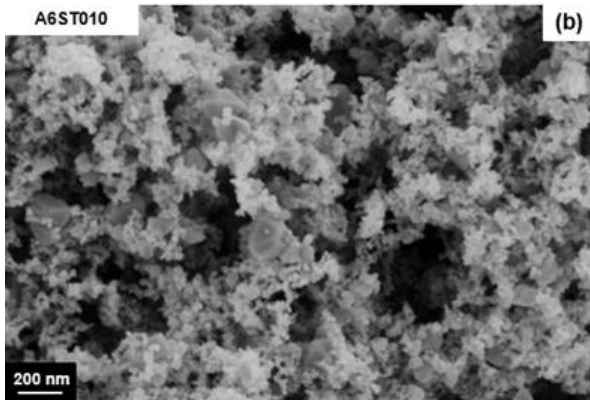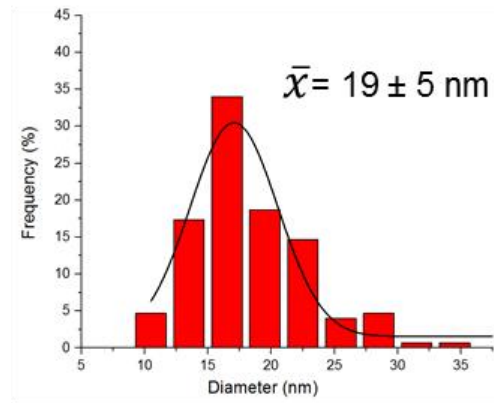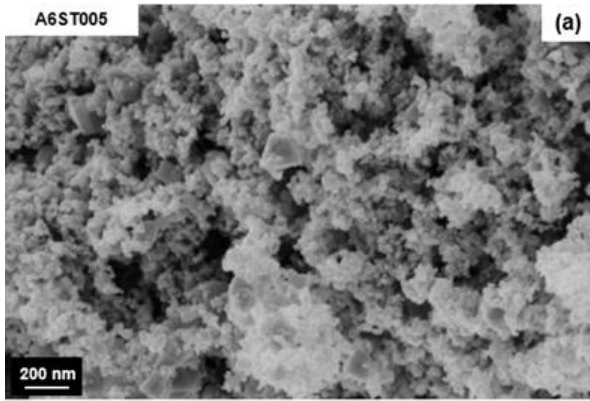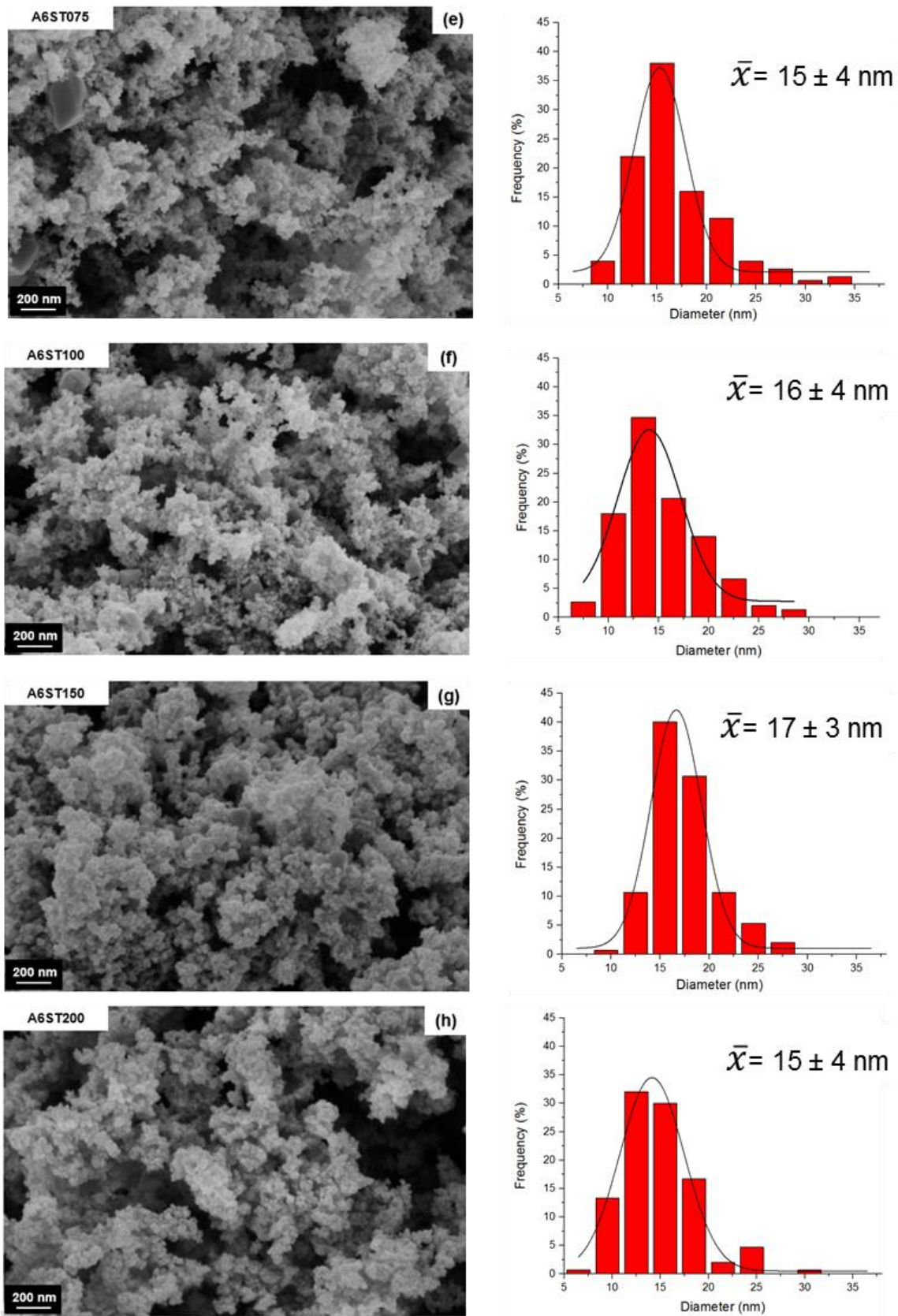
Figure 3.26 SEM images of TaTO aerogels and their respective size distributions (150 particles analysed using *Image J* software), from 0.5 to 20 at.%. Maximization of the images = 50000.

170

For additional morphological data, nitrogen sorption analyses were performed and obtained results are reported in **Table 3.23**. All the obtained isotherms correspond to mesoporous materials with type IV adsorption isotherms, as seen for TO and ATO aerogels. The adsorption isotherms of all the studied aerogels are shown in the **Annex** of this manuscript. The calculated specific surface area was based on the BET model, and the Pore Size Distributions (PSD) and mesoporous volumes on the BJH model.

Table 3.23. Nitrogen sorption measurement results for TaTO aerogels.

Sample	Specific surface area BET ($m^2 \cdot g^{-1}$)	PSD (BJH, nm)	Pore volume (BJH, $cm^3 \cdot g^{-1}$)	µ-pore volume (BJH, $cm^3 \cdot g^{-1}$)
A6ST005-5	34.1 ± 3.4	10--20--30	0.19 ± 0.02	$0.10 \times 10^{-2} \pm 0.01 \times 10^{-2}$
A6ST010-5	41.8 ± 4.2	10--20--25	0.19 ± 0.02	$0.10 \times 10^{-2} \pm 0.01 \times 10^{-2}$
A6ST025-5	50.1 ± 5.0	10--15--20	0.23 ± 0.02	$0.10 \times 10^{-2} \pm 0.01 \times 10^{-2}$
A6ST050-5	60.0 ± 6.0	10--20--30	0.28 ± 0.03	$0.40 \times 10^{-2} \pm 0.04 \times 10^{-2}$
A6ST075-5	74.6 ± 4.5	15--20--25	0.29 ± 0.03	$0.10 \times 10^{-2} \pm 0.01 \times 10^{-2}$
A6ST100-5	78.9 ± 7.9	10--15--20	0.30 ± 0.03	$0.50 \times 10^{-2} \pm 0.05 \times 10^{-2}$
A6ST150-5	84.2 ± 8.4	10--20--25	0.30 ± 0.03	$0.40 \times 10^{-2} \pm 0.04 \times 10^{-2}$
A6ST200-5	77.1 ± 7.7	10--15--25	0.25 ± 0.02	$0.30 \times 10^{-2} \pm 0.03 \times 10^{-2}$

As in **section III.1**, TaTO aerogels XRD diffraction diagrams (**Figure 3.27**) showed a perfect rutile SnO_2 structure without any peak shift or presence of novel Ta phases, such as: Ta(0), Ta_2O_3, Ta_2O_5, or SnO, even with the variation of Ta at. %. "a" and "c" lattice parameters of the obtained rutile structures indicate no structure modification of the SnO_2 rutile network after doping with tantalum (**Table 3.24**).
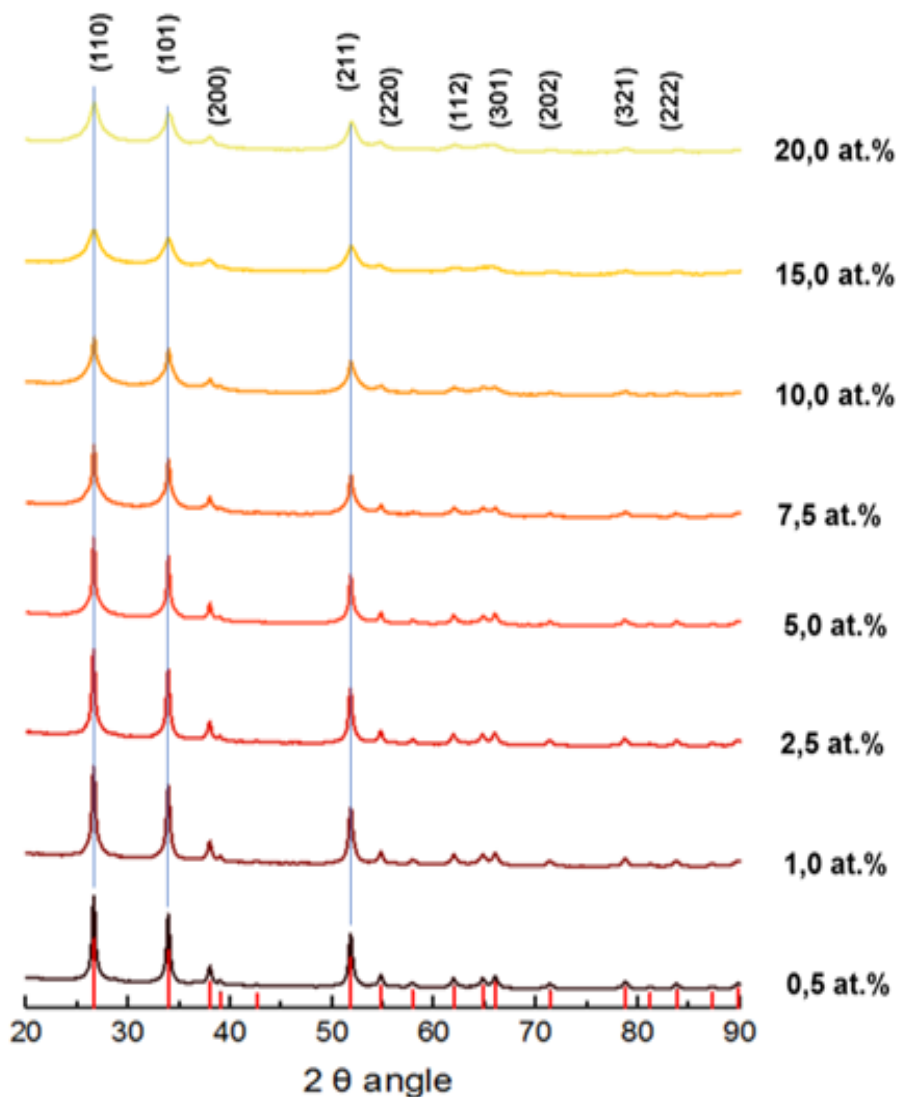
Figure 3.27 X-Ray diffraction diagrams of SnO_2 aerogels doped with different Ta content. In red the SnO_2 pattern of rutile structure (JCPDS 14-1445).[5]

As seen in **Figure 3.27**, the larger the Ta amount, the lower the intensity of the XRD peaks. Accordingly, small crystallite sizes are measured for high Ta amounts (**Table 3.24**). Increasing the Ta amount in the rutile network, increases the number of defects which could then impede the crystallites growth. Larger Ta ratios generally also involve a lower Ta^{5+}/Ta^{3+} ratio. If Ta^{5+} are able to substitute Sn^{4+} because of similar diameter (0.64 vs. 0.69 pm), Ta^{3+} with bigger diameter (0.72 pm) tends to occupy interstitial sites, favoring the development of dislocations. Therefore, increasing the doping ratio results in more polycrystalline materials, with smaller crystallite sizes. Such a negative effect of doping on crystallite size is consistent with other reports on doped metal oxide materials.[6]

Table 3.24. Cell parameters of analyzed aerogels, crystallites sizes and primary particles diameters.

Sample	Primary particle diameter (nm)	Crystallites size (nm)	a // c lattice parameters (nm)
A6ST005-5	19 ± 5	17 ± 1	4.7 // 3.2
A6ST010-5	16 ± 4	14 ± 1	4.7 // 3.2
A6ST025-5	14 ± 3	15 ± 1	4.7 // 3.2
A6ST050-5	13 ± 3	13 ± 3	4.7 // 3.2
A6ST075-5	15 ± 4	8 ± 1	4.7 // 3.2
A6ST100-5	16 ± 4	6 ± 1	4.7 // 3.2
A6ST150-5	17 ± 3	5 ± 1	4.7 // 3.2
A6ST200-5	15 ± 4	6 ± 1	4.7 // 3.2

IV.2.2 Chemical composition (impact of the Ta doping ratio)

Chemical composition of the TaTO aerogels was analyzed by EDX (bulk composition) and XPS (surface composition) in order to study the impact of the Ta content on its segregation from the bulk to the surface of particles.

Both XPS and EDX values were much higher than expected whatever the nominal Ta ratio (**Figure 3.28**). Such big differences, see **Table 3.25**, were attributed to the used commercial Ta precursor (Ta(OiPr)$_5$, whose concentration is suspected to be higher than expected. This however did not affect too much our study, just shifting the range of doping ratio. As a consequence, new aerogels have been synthesized in order to reach lower Ta contents and complete the series.

It was found that for very low Ta doping ratios, the Ta segregation percentages are negatives, the Ta content being higher on the bulk than on the surface. This does not agree with the dopant diffusion during calcination. Such negative values may result from inaccuracy in the calculations. Indeed, as seen on **Figure 4.29**, the Ta 4d peaks recorded for low Ta-content are very small compared to those obtained for larger doping ratios. Hence   the quantification is much more difficult and the calculated segregation cannot be very precise below 2.5 at. %. For high Ta at. %, as usually observed in this work, the tantalum concentration was generally speaking higher on the surface of the particles than on the bulk, suggesting again a segregation of Ta during calcination.

Table 3.25. Bulk and surface chemical composition results, measured by EDX and XPS analysis.

Sample	Expected dopant-rate (at. %)	Ta/(Ta+Sn) EDX (at.%)	Ta/(Ta+Sn) XPS (at.%)	% segregation ([Ta]$_{surf}$-[Ta]$_{bulk}$)/ -[Ta]$_{bulk}$
A6ST005-5	0.5	2.4 ± 0.7	1.8 ± 0.1	- 25.0
A6ST010-5	1.0	4.8 ± 0.2	2.9 ± 0.1	- 39.5
A6ST025-5	2.5	6.6 ± 0.1	6.8 ± 0.4	3.0
A6ST050-5	5.0	10.3 ± 0.9	11.9 ± 0.4	15.5
A6ST075-5	7.5	14.0 ± 2.0	16.1 ± 0.4	15.0
A6ST100-5	10.0	17.9 ± 0.7	19.3 ± 0.4	7.8
A6ST150-5	15.0	24.5 ± 1.6	26.8 ± 0.4	9.4
A6ST200-5	20.0	31.6 ± 5.6	36.3 ± 0.3	14.8
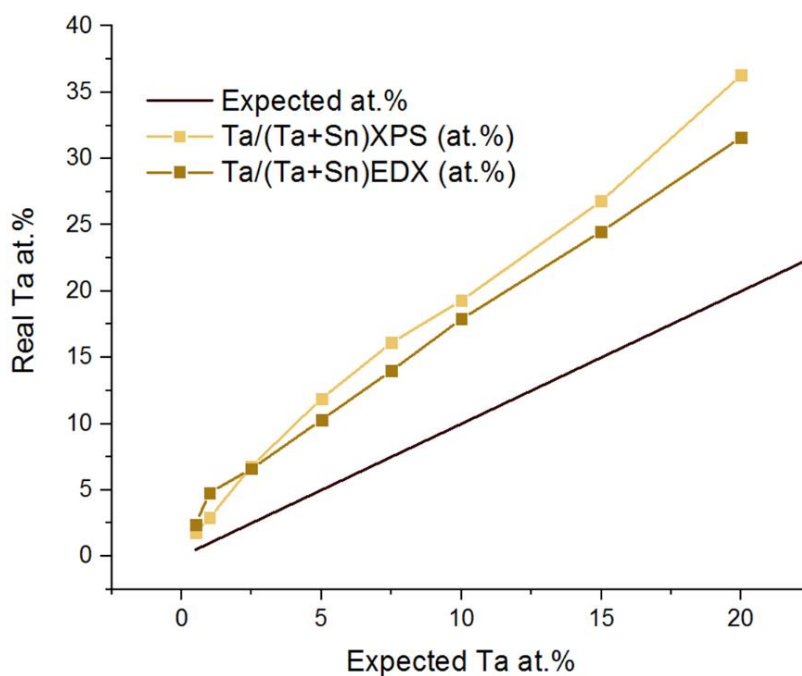
Figure 3.28 Expected Ta at. % concentration *vs.* real Ta at. % measured by XPS and EDX.
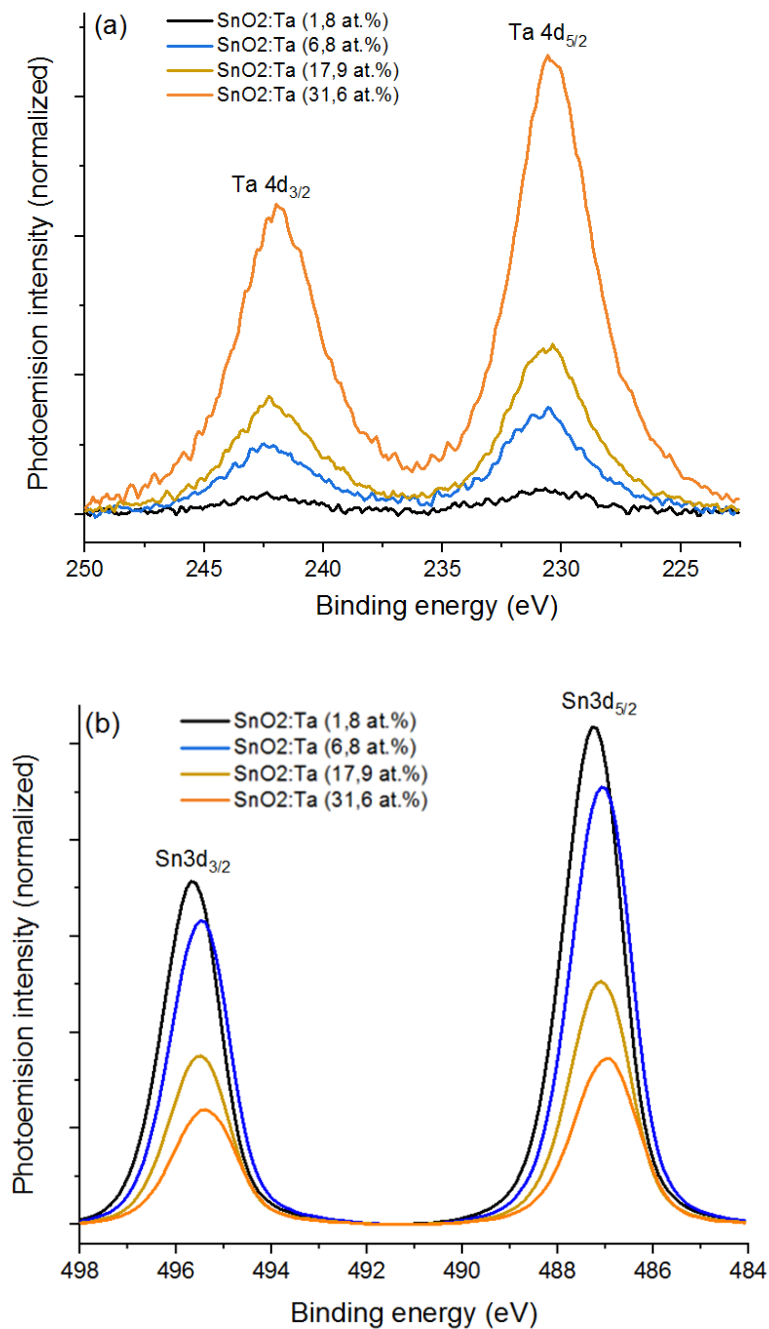
Figure 3.29 XPS spectra of TaTO aerogels with different doping levels: (a) scans of the Ta 4d region, (b) scans of the Sn 3d region.

It is noteworthy that, for both elements, XPS spectra show peak shifting to lower binding energies as far as the Ta at. % increases. Sn signals ($3d_{3/2}$ and $3d_{5/2}$) and Ta ($4d_{3/2}$ and $4d_{5/2}$) are shifted to the right. As mentioned before, increasing the Ta doping ratio results in an increase of Ta^{3+} with respect to Ta^{5+}. Such oxidation state reduction impacts on the global chemical environment, modifying the columbic interaction between photo-emitted electrons and the ion cores, and resulting in a peak shifting.

IV.2.3 Electronic conductivity (impact of the Ta doping ratio)

The electronic conductivity of TaTO aerogels was measured with the same home-made cell, as described in **section III.3**. Obtained results are gathered in **Table 3.26**.

Table 3.26 TaTO aerogels conductivity and Ta repartition (EDX and XPS).

Sample	Ta/(Ta+Sn) EDX (at.%)	Ta/(Ta+Sn) XPS (at.%)	Conductivity $(S \cdot cm^{-1})$	Crystallites size (nm)
A6ST005-5	2.4	1.8 ± 0.1	3.2×10^{-3}	17.0
A6ST010-5	4.8	2.9 ± 0.1	2.9×10^{-3}	14.1
A6ST025-5	6.6	6.8 ± 0.4	3.3×10^{-3}	15.1
A6ST050-5	10.3	11.9 ± 0.4	2.1×10^{-3}	13.3
A6ST075-5	14.0	16.1 ± 0.4	$1.\,7 \times 10^{-3}$	8.2
A6ST100-5	17.9	19.3 ± 0.4	$< 1 \times 10^{-3}$	6.0
A6ST150-5	24.5	26.8 ± 0.4	$< 1 \times 10^{-3}$	5.0
A6ST200-5	31.6	36.3 ± 0.3	$< 1 \times 10^{-3}$	5.6

Comparing **Table 3.26** with **Figure 3.30**, we see that both the specific surface area and the electronic conductivity of Ta-doped samples are strongly related to the doping level of the material, as seen for Sb or Nb doped SnO_2 aerogels.[3]

In the case of TaTO aerogels and in agreement with other studies,[21] the electronic conductivity was one order of magnitude higher for low amounts of Ta. The maximum of conductivity (6 $mS \cdot cm^{-1}$) was measured between 0,5 and 5 at. %. It remains however far from that reported for ATO aerogels (800 $mS \cdot cm^{-1}$), what may be ascribed to the lower density of charge carriers at such low doping ratios.

According to Turgut *et al.*,[21] discussed the impact of doping on the conductivity based on point defects theory. They argued that: (1) the presence of M^{5+} and its substitution to Sn^{4+} ions in SnO_2 lattice, or location in interstitial positions in the lattice, increases the concentration of free electrons in the matrix. For such a situation, M atoms act as a donor.[23] (2) M with multivalence states, like Sb or Ta, (3+ or 5+) can induce presence of oxygen vacancies. The substitution of Sn^{4+} with M^{5+} increases the conductivity of the material by changing the concentration of oxygen vacancies and increasing the concentration of electrons (**Eq. 3.5**). If Sn^{4+} are

substituted with M^{3+} (**Eq. 3.6**) the electronic conductivity is decreased due to a left shift on the equilibrium **3.7**, which decrease the electron concentration. Therefore, the higher the ratio M^{5+} / M^{3+}, the higher the electronic conductivity:[3,13]

$$2 \; M_2O_5 \rightarrow 4 \; M_{Sn}{}^{\circ} + 10 \; O^x{}_o + V_{Sn}{}^{4'} \quad (\textbf{Eq. 3.5})$$

$$M_2O_3 \rightarrow 2 \; M_{Sn}{}^{'} + 3 \; O^x{}_o + V^{\circ\circ}{}_O \quad (\textbf{Eq. 3.6})$$

$$2 \; O^x{}_o \leftrightarrow O_{2(g)} + 4 \; e^- + 2 \; V^{\circ\circ}{}_O \quad (\textbf{Eq. 3.7})$$

Figure 3.30, shows the compared evolution of the electronic conductivity and the specific surface area as a function of doping level for TaTO aerogels.
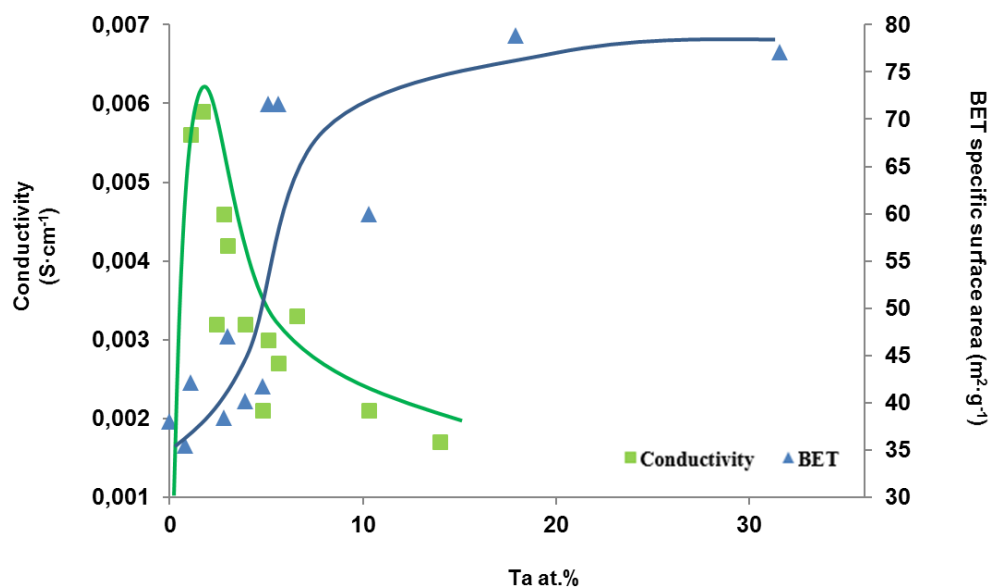
Figure 3.30 Conductivity ($S{\cdot}cm^{-1}$) and specific surface area ($m^2{\cdot}g^{-1}$) evolution as a function of Ta at. %.

In order to determine the optimum Ta content, a complementary study was carried out with Ta at. % ranging from 0.5 to 5. The main results of this second study are shown in **Table 3.27**, and on **Figure 3.31**.

Note that Ta-doped aerogels presented hereafter have been prepared with a different Ta-precursor than those from the previous series.

Figure 3.31 plots both the conductivity and specific surface area values of all samples as a function of Ta content between 0,5 and 7 at.%. Both properties present a tendency (blue for BET and green for conductivity) in agreement with the first series. Considering that the specific surface area reached on the whole range (40-50 $m^2 \cdot g^{-1}$) is acceptable, it is preferable to select the Ta at. % based on the electronic conductivity. From our point of view, the optimum stands between 1 and 3 at. %. The highest electronic conductivities reported in the literature were obtained for Ta at. % between 1 and 4 at.%.[19,20, 21,16b]

Table 3.27. TaTO aerogels doped with Ta at. % ranging from 0.5 to 5% and their main properties (bulk Ta at. %, specific surface area and electronic conductivity).

Sample	Dopant ratio (at. %)	Ta/(Ta+Sn) EDX (at. %)	Specific surface area BET ($m^2 \cdot g^{-1}$)	Electronic conductivity ($S \cdot cm^{-1}$)
A6ST005-5 (2)	0.5	0.8	35.5	Not measured
A6ST010-5 (2)	1.0	1.1	42.1	5.6×10^{-3}
A6ST015-5	1.5	1.7	34.6	5.9×10^{-3}
A6ST020-5	2.0	2.8	38.4	4.6×10^{-3}
A6ST025-5 (2)	2.5	3.0	47.0	4.2×10^{-3}
A6ST035-5	4.0	3.9	40.14	3.2×10^{-3}
A6ST040-5	4.0	5.1	Not measured	3.0×10^{-3}
A6ST050-5 (2)	5.0	5.6	71.6	2.7×10^{-3}

Ta-doped SnO_2 aerogels exhibit quite low electronic conductivities, three order of magnitude lower than that of ATO or carbon black materials, and four with commercial IrO_2. However, IrO_x NPs deposition may result in a reduction of the charge carrier depletion layer, created by oxygen species adsorbed on the tin dioxide surface (O_2^-, O^{2-} or O^-). Thus, as reported for Pt,[24] we can expect an improvement in electronic conductivity after deposition of Iridium NPs.

Despite quite a low electronic conductivity, we decided to select TaTO aerogels doped at 3 at. %, along with ATO doped at 10 at%, as catalyst supports for Iridium NPs, for further electrochemical characterization in RDE configuration.
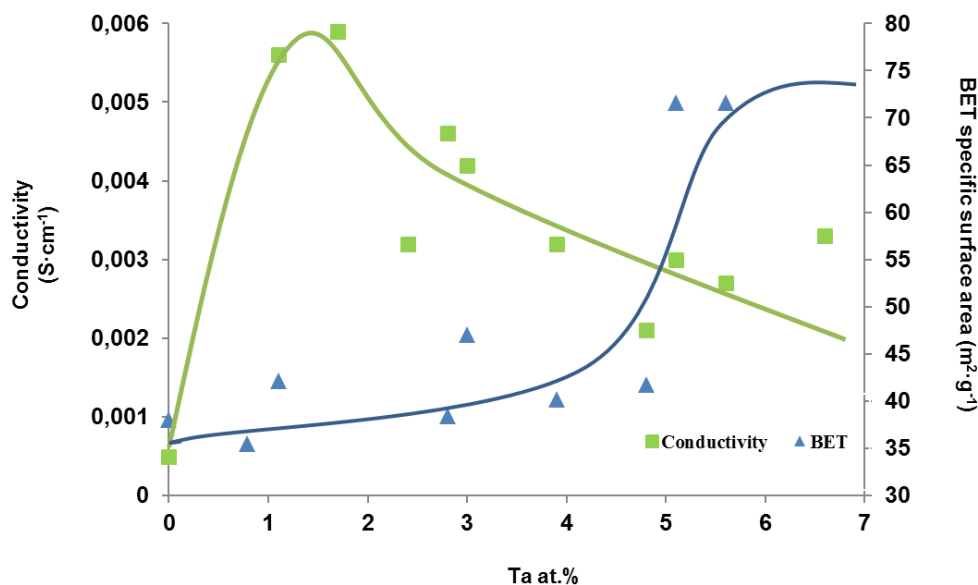
IV.3 Conclusions and perspectives

Tantalum-doped tin oxide (TaTO) aerogels were synthesized by a sol-gel route starting with metal alkoxide precursors, prepared with different sol-gel catalyst (HNO$_3$ or NaOH). TaTO aerogels were doped with different Ta ratios (from 0.5 to 32 at. %).

Calcined TaTO aerogels present the SnO$_2$ rutile crystal phase (as observed for ATO aerogels), without any shift of peaks due to the presence of tantalum and no visible Ta crystalline phases, meaning an excellent fit of Ta inside the rutile crystal phase of tin oxide. SEM images show a very interesting airy morphology lying on a three-dimensional network made up of interconnected particles, similar to the one obtained for TO and ATO aerogels. Large geometric particles were also observed inside the doped-tin dioxide aerogel network. The presence of such large grains seems to be related to the Ta at. % level, as they are disappearing for high doping levels. Their presence makes difficult the determination of crystallites sizes.

Using NaOH instead of HNO_3 as a sol-gel catalyst does not significantly impact the sol-gel process contrary to ATO aerogels. Surface segregation of Ta was slightly less important with NaOH but in a much lower extent than for ATO.

The Ta content strongly affects the electronic conductivity and the specific surface area. The best compromise was reached for low doped samples, in accordance with several reported studies.

SnO_2 doped with 3 at. % of Ta was finally selected for Ir deposition and evaluation as a catalyst support for water splitting in PEMWE conditions.

V General Conclusions

Antimony and Tantalum doped tin dioxide aerogels have been synthesized by sol-gel method from metal alkoxides precursors. After a calcination step in air at 600 °C for 5 h, only the rutile crystalline phase of SnO_2 was detected by XRD for all prepared tin dioxide-based aerogels.

Due to their unique morphology, aerogels seem to be perfectly suitable as catalyst supports. These materials exhibit a three-dimensional network of interconnected primary particles, that present different diameters depending on the dopant. Such particles appear to be smaller for doped materials (around 15 nm), than for un-doped aerogels (around 20 nm), resulting in larger specific surface areas, 80 $m^2 \cdot g^{-1}$ *vs.* 40 $m^2 \cdot g^{-1}$. Aerogels also present a bimodal pore size distribution in the mesoporous range, centred on 20 nm and 45 nm, with few micropores and some macropores. This is beneficial because it avoids the pore obstruction after the deposition of the catalyst particles (size < 5 nm) on one hand and allows a rapid gas diffusion and flow during the oxygen evolution reaction on the other hand. For both doped aerogels, the higher the doping agent atomic ratio (Sb or Ta) the higher the specific surface area of the material.

The doped tin dioxide aerogel samples presented a significant improvement of the measured electronic conductivity. Specially Sb-doped samples showed an increase in electronic conductivity of about 4 orders of magnitude in comparison with pure SnO_2 (1 $S \cdot cm^{-1}$ for 10 at. % Sb-doped vs. 5×10^{-4} $S \cdot cm^{-1}$ for pure SnO_2). Doping with Ta resulted in an increase of "only" 1 order of magnitude (6×10^{-3} $S \cdot cm^{-1}$) for tantalum doping ratio between 1 and 2 at.%. It is noteworthy that low electronic conductivities can be improved after catalyst deposition.

Large doping ratios results in higher specific surface area but lower electronic conductivity. The best compromise was obtained for 10 at. % in the case of Sb-doped aerogels and 2 at. % for TaTO aerogels.

Both doped tin dioxide aerogels suffer from dopant segregation (higher dopant concentration on the surface than in the bulk). Such a surface enrichment of the dopant is extremely unfavourable as it will probably result in an accelerated leaching and dissolution of the dopant during PEMWE operation and subsequent loss of conductivity and activity. ATO aerogels prepared in an alkaline sol-gel media showed lower Sb surface enrichment than aerogels prepared in acid media, giving place to possible increased resistance under PEMWE operation conditions. The impact was much less pronounced in the case of TaTO.

In conclusion, doped tin dioxide aerogels present interesting properties as catalyst supports for PEMWE applications. They will now be used for Ir deposition. The obtained catalysts will then be evaluated as alternatives to pure Ir oxide for oxygen evolution in PEMWE working conditions.

VI Résumé

Des aérogels de dioxyde d'étain dopés à l'antimoine et au tantale ont été synthétisés par la méthode sol-gel à partir de précurseurs d'alkoxide métallique. Après une étape de calcination à 600°C pendant 5 h, seule la phase cristalline rutile de SnO_2 a été détectée par XRD pour tous les aérogels préparés.

En raison de leur morphologie unique, les aérogels semblent parfaitement convenir comme supports de catalyseur. Ces matériaux présentent un réseau tridimensionnel de particules interconnectées, qui ont des diamètres différents en fonction de l'agent dopant. Ces particules apparaissent plus petites pour les matériaux dopés (environ 15 nm) que pour les aérogels non dopés (environ 20 nm), ce qui donne des surfaces spécifiques plus importantes de l'ordre de 80 $m^2 \cdot g^{-1}$ contre 40 $m^2 \cdot g^{-1}$. Les aérogels ont également une distribution de taille de pores bimodale centrée à 20 nm et 45 nm. Ils sont donc principalement mésoporeux, avec peu de micropores et quelques macropores. Ceci est avantageux car, d'une part, cela évite le colmatage des pores après le dépôt des particules de catalyseur (taille < 5 nm), tout en permettant une diffusion et un écoulement de gaz rapides lors de la réaction de dégagement d'oxygène. Pour les deux aérogels dopés, plus le rapport atomique de l'agent dopant (Sb ou Ta) est élevé, plus la surface spécifique du matériau est grande et plus la taille des cristallites est petite.

Les échantillons d'aérogel de dioxyde d'étain dopés ont montré une amélioration significative de la conductivité électronique mesurée. Les échantillons dopés au Sb ont montré une augmentation de la conductivité électronique d'environ 4 ordres de grandeur par rapport au matériau pur (1 $S \cdot cm^{-1}$ pour 10 at.% dopé avec Sb vs $5 \times 10^{-4}\, S \cdot cm^{-1}$ pour SnO_2 pur). Le dopage au Ta a entraîné une augmentation de "seulement" 1 ordre de grandeur ($6 \times 10^{-3}\, S \cdot cm^{-1}$) pour un taux de dopage compris entre 1 et 2 at.%. Il est à noter que la conductivité électronique pourrait être améliorée après le dépôt du catalyseur.

Les deux aérogels de dioxyde d'étain dopés subissent une ségrégation de l'agent dopant (concentration en dopants plus élevée en surface qu'en volume). Un tel enrichissement de la surface du dopant est extrêmement défavorable car il entraînera vraisemblablement une lixiviation et une dissolution du dopant pendant le fonctionnement de l'électrolyseur, et une perte de conductivité et d'activité du catalyseur.

Afin d'améliorer les propriétés intrinsèques des aérogels, différents paramètres de synthèse sol-gel ont été modifiés, tels que : le catalyseur sol-gel, le temps de calcination ou la concentration de l'agent dopant.

Les aérogels ATO préparés en milieu sol-gel alcalin ont montré une diminution de l'enrichissement en surface de Sb par rapport aux aérogels préparés en milieu acide,

conduisant à une augmentation possible de la durée de vie dans les conditions de fonctionnement PEMWE. Le phénomène est beaucoup moins marqué pour les aérogels dopés au Ta, où les pourcentages de ségrégation restent élevés.

Des rapports de dopage élevés se traduisent par une surface spécifique plus élevée mais une conductivité électronique inférieure. Le meilleur compromis a été obtenu avec 10 at. % dans le cas des aérogels dopés Sb et 2 at. % pour les aérogels dopés au Ta.

En conclusion, les aérogels de dioxyde d'étain dopés ont des propriétés intéressantes en tant que supports de catalyseurs pour les applications PEMWE. Deux formulations ont été sélectionnées pour dépôt d'Ir. Les catalyseurs obtenus seront ensuite évalués comme des alternatives à l'oxyde d'Ir pur pour le dégagement d'oxygène dans les conditions de travail des électrolyseurs PEM.

VII Reference

[1] L. Sola-Hernandez, F. Claudel, F. Maillard, Christian Beauger, *International Journal of Hydrogen Energy*, **2019**, *44*, 24331-24341

[2] I. Thomas, Method for producing stannic tertiary alkoxide. **1976**, Google Patents

[3] G. Ozouf, C. Beauger, *J. Mater. Sci.*, **2016**, *51*, 5305.

[4] (a) D. Szczuko J. Werner S. Oswald G. Behr, K. Wetzig, *Appl Surf Sci*, **2001**, *179(1–4)*, 301–306; (b) S. Cavaliere, S. Subianto, I. Savych, M. Tillard, DJ. Jones DJ, J. Roziere, *J Phys Chem C*, **2013**, *117*, 18298; (c) E. Leite, I. Weber, E. Longo, J. Varela, Adv Mater, 2000, 12, 965; (d) J. Correa, A. Agrios, *Appl. Mater. Interfaces,* **2014**, *6 (21)*, 19137-19143; (e) D. Woo, C. Koo, H. Ma, H. Lee, Trans. *Electr. Electron. Mater.*, **2012**, *13*, 241-244.

[5] W. Baur, *Acta Crystallographica*, **1956**, *9*, 515-20.

[6] (a) A. Babar, S. Shinde, A. Moholkar, C. Bhosale, J. Kim, K. Rajpure, *J. of alloys and compounds*, **2010**, *505*, 416-422; (b) R. Noonuruk, N. Vittayakorn, W. Mekprasart, J. Sritharathikhun, W. Pecharapa, *J Nanosci Nanotechnol*, **2015**, *15*, 2564–2569; (c) J. Tong, Y. Liu, Q. Peng, W. Hu, *Journal of Materials* Science, **2017**, *52(8)*, 13427–13443; (d) F. Berry, *J. Catal*, **1982**, *73*, 349-356; (e) S. Oswald, G. Behr, D. Dobler, J. Werner, K. Wetzig, W. Arabczyk, *Anal. Bioanal. Chem.*, **2004**, *378*, 411; (f) Y. Cross, D. Pyke*, J. Catal.*, **1979**, *58*, 61.

[7] G. Cognard, G. Ozouf, C. Beauger, G. Berthome, D. Riassetto, L. Dubau, R. Chattot, M. Chatenet, F. Maillard, *Applied Catalysis B: Environmental*, **2017**, *201*, 381-390; (b) G. Cognard, G. Ozouf, C. Beauger, L. Dubau, M. López-Haro, M. Chatenet, F. Maillard, *Electrochimica Acta*, **2017**, *245*, 993–1004

[8] (a) G. Cognard, G. Ozouf, C. Beauger, I. Jiménez-Morales, S. Cavaliere, D. Jones, J. Rozière, M. Chatenet, F. Maillard, *Electrocatalysis*, **2017**, *8*, 51-58; (b) G. Ozouf, G. Cognard, F. Maillard, M. Chatenet, L. Guétaz, M. Heitzmann, P. Jacques, C. Beauger, *Journal of the Electrochimical Society*, **2018**, *165 (6)*, 3036-44.

[9] C. Beauger, L. Testut, S. Berthon-Fabry, F. Georgi, L. Guétaz, *Microporous and Mesoporous Materials*, **2016**, *232*, 109-118.

[10] D. Abbott, D. Lebedev, K. Waltar, M. Povia, M. Nachtegaal, E. Fabbri, C. Copéret, T. Schmidt, *Chem. Mater.*, **2016**; *28*, 6591-6604.

[11] E. Fabbri, A. Rabis, Y. Chino, U Uchida, T. Schmidt, *Electrochemistry Communications*, **2017**, *83*, 90-95

[12] J. Bruneaux, H. Cachet, M. Froment, A. Messad, *Electrochim. Acta*, **1994**, *39*, 1251

[13] Guillaume Ozouf, **2017**, *Electrodes à base d'aérogels de SnO2, résistantes à la corrosion pour la réduction de l'oxygène dans les piles à combustible à membrane échangeuse de protons (PEMFC)*,

Université de recherche Paris Sciences et Lettres - PSL Research University, MINES ParisTech, Sophia Antipolis, France.

[14] (a) M. Ouattara-Brigaudet, C. Beauger, S. Berthon-Fabry, P. Achard, *Fuel Cells*, **2011**, *6*, 726; (b) M. Ouattara-Brigaudet, S. Berthon-Fabry, C. Beauger, M. Chatenet, N. Job, M. Sennour, P. Achard, *Int J Hydrog Energy*, **2012**, *12*, 9742

[15] A. Dorcheh, M. Abbasi, *J. Mater. Process. Technol.*, **2008**, *199*, 10-26.

[16] (a) E. Fabbri, A. Rabis, R. Kotz, T. J. Schmidt, Phys. *Chem. Chem. Phys.*, **2014**, *16*, 13672; (b) S. Geiger, O. Kasian, A. M. Mingers, K. J. J. Mayrhofer, S. Cherevko, *Sci. Rep.,* **2017**, *7*, 4595.

[17] (a) D. Dobler, S. Oswald, J. Werner, W. Arabczyk, G. Behr, K. Wetzig, *Chem. Phys.*, **2003**, *286*, 375; (b) V. Dusastre, D. E. Williams, *J. Phys. Chem. B*, **1998**, *102*, 6732; (c) D. G. Stroppa, L. A. Montoro, A. Beltran, T. G. Conti, R. O. da Silva, J. Andres, E. R. Leite, A. J. Ramirez, *Chem. – Eur. J.*, **2011**, *17*, 11515; (d) D. Szczuko, J. Werner, G. Behr, S. Oswald, K. Wetzig, *Surf. Interface Anal.*, **2001**, *31*, 484; (e) D. Szczuko, J. Werner, S. Oswald, G. Behr, K. Wetzig, *Appl. Surf. Sci.*, **2001**, *179*, 301.

[18] Fabien Labbé, **2018**, *Carbones revêtus de dioxyde d'étain comme supports cathodiques plus durables dans les piles à combustible à membrane échangeuse de protons (PEMFCs)*, Université de recherche Paris Sciences et Lettres - PSL Research University, MINES ParisTech, Sophia Antipolis, France.

[19] S. Nakao, Y. Hirose, T. Fukumura, T. Hasegawa, *Japanese J. Appl. Phys.*, **2014**, *53*, 05FX04

[20] Y.-W. Kim, S.W. Lee, H. Chen, *Thin Solid Films,* **2002**, *405*, 256-262

[21] (a) G. Turgut, *Thin Solid Films*, *594*, **2015,** 56; (b) S. Nakao, N. Yamada, T. Hitosugi, Y. Hirose, T. Shimada, T. Hasegawa, *Appl. Phys. Exp.,* **2010**, *3*, 031102.

[22] (a) R. J. Brook, in Ceramic Fabrication Process, Vol. 9 (Ed. F. F. Y. Wang), Academic Press, New York **1976**, *Ch. 17*; (b) S. Abbou, R. Chattot, V. Martin, F. Claudel, L. Solà-Hernández, C. Beauger, L. Dubau, F. Maillard, *ACS Catalysis*, **2020**, *10 (13)*, 7283–7294

[23] (a) N. Greenwood, A. Earnshaw, Chemistry of the Elements, 2nd ed., p. 1341, Reed Educational and Professional Publishing, Oxford, **1997**; (b) Y. Muto, S. Nakatomi, N. Oka, Y. Iwabuchi, H. Kotsubo, Y. Shigesato, *Thin Solid Films*, **2012**, *520*, 3746-3750; (c) S. Nakao, N. Yamada, T. Hitosugi, Y. Hirose, T. Shimada, T. Hasegawa, *Appl. Phys.*, **2010**, *3*, 031102.

[24] (a) N. Barsan, U. Weimar, *Journal of Electroceramics*, **2001**. *7(3)*, 143-167; (b) Y. Senoo, K. Kakinuma, M. Uchida, H. Uchida, S. Dekia, M. Watanabe, *Rsc Advances*, **2014**, *4(61)*, 32180-32188.

CHAPTER 4: OER activity and stability of IrO$_x$/XTO (X = Sb or Ta)

This chapter is focused on the deposition of Iridium-based nanoparticles (NPs) over some selected aerogels of **Chapter 3** and their characterization in RDE. The prepared catalysts, Ir/XTO (X = A or Ta), have been characterized by a set of techniques and tested with RDE in simulated PEMWE electrolyzer conditions.

The chapter is splitted into four sections:

The first **section I** is dedicated to the description of the Ir NPs deposition route. The same protocol has been used for each catalyst support.

In the second section, **section II**, the aerogels studied on **section 3.II** (TO, ATO and TaTO) were decorated with the Iridium-based NPs. The results after the full characterization are discussed. The work of this section was published in the International Journal of Hydrogen Energy together with the results presented on **section II**, **chapter 3**.[1]

In **section III**, Iridium was deposited over ATO aerogels prepared with acid (HNO$_3$) or basic (NaOH) sol-gel catalyst. The aim of this study was to evaluate a possible effect of the lower Sb segregation in ATO-b aerogels on the OER performance of the catalysts, especially on the resistance under PEMWE conditions.

On **section IV** the same deposition method was used for the decoration of a selected TaTO aerogel (Ta doping = 2 at. %) with Iridium NPs. Characterization of the catalysts and comparison with Ir/ATO catalysts is presented.

Finally, on **section V** a deeper study on the stability and possible causes of the catalyst deactivation are discussed.

I Iridium deposition route

IrO_x based nanocatalysts were deposited *in-situ* onto the previously as-prepared aerogel supports, following the procedure previously described by Wang *et al.*[2] A 30 wt.% Ir loading (Ir/(Ir+XTO)) was selected as optimum target based on the work of De Pauli *et al.* and Balko and co-workers.[3] It was calculated after deposition for each sample with EDX and XPS measurements for double checking.

First of all, 1,17 g of hexadecyltrimethylammonium bromide (CTAB), 0.095 g of as-prepared aerogel and 0,075 g of the Ir precursor ($IrCl_3 \cdot xH_2O$) were dispersed in 120 mL of anhydrous ethanol. The obtained green-brown solution, color (**Figure 4.1.a**), was then stirred for 4 hours under Argon atmosphere. Meanwhile 0.114 g of reducing agent, sodium borohydride ($NaBH_4$), were dissolved in 50 mL of anhydrous ethanol under Argon atmosphere. The sodium borohydride solution was then added slowly to the first solution, maintaining a vigorous stirring and keeping the system under Argon atmosphere. The reaction mixture was kept overnight in order to ensure a complete reduction. The color of the mixture turned from initial green-brown to black with time, after the addition of the reducing agent (**Figure 4.1.b**)

Afterwards, the suspension containing the electrocatalysts Ir/XTO was centrifuged and rinsed with large amounts of pure ethanol and deionized water in order to remove CTAB and the residual non-reduced reagents, as for example $IrCl_3$. Finally, the synthesized catalyst was dried overnight at 80°C in air for solvents evaporation and a black powder was collected (**Figure 4.1.c**).

Unsupported iridium nanoparticles were also synthesized following the same procedure suppressing the support from the route.

The oxidation state of the Ir NPs depends on several factors like the synthesis conditions and history of the samples. Since it can hardly be predicted, NPs will be labeled IrO_x with 0<x<2.
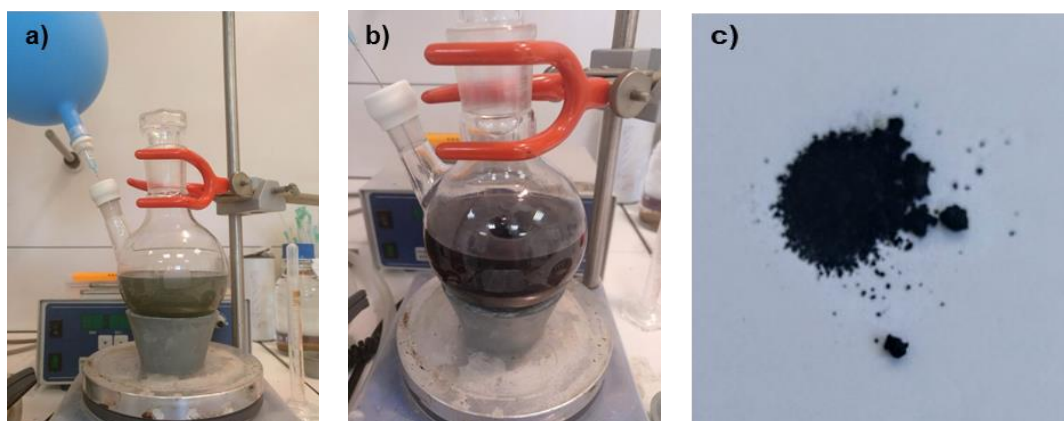
Figure 4.1 Images of the reaction solution (a) before and (b) after the addition of the reducing agent. (c) the electrocatalysts powder obtained after the solvent evaporation.

II Compared OER activity of IrO$_x$/TO, IrO$_x$/ATO and IrO$_x$/TaTO)

In this study, Iridium nanocatalysts were prepared *in-situ* over the prepared and characterized aerogels of **section I**, **chapter 3**. The effect of the composition of each tin dioxide-based aerogel (non-doped, Ta-doped or Sb-doped) on the activity and stability towards the OER was compared and discussed.

Aerogel samples decorated with Iridium nanocatalysts were labeled as: IrO$_x$/TO (for Ir on A6S-1), Ir/ATO (for iridium on A6SS100-1) and IrO$_x$/TaTO (for Ir on A6ST100-1). Unsupported iridium nanoparticles were labeled IrO$_x$ NPs.

Properties and synthesis conditions of aerogel supports are reminded in **Table 4.1**. Once the catalysts NPs were deposited onto such aerogels, they were characterized by a set of physiochemical techniques and later electrochemically characterized in RDE configuration (**section III**, **chapter 2**).

Table 4.1. Summary of the main properties of selected TO-based aerogels.

Aerogel	Sample	Particle size (nm) - SEM	Crystallites size (nm) XRD	Bulk doping (at. %) XPS	Surface doping (at. %) EDX	Sp. Surf. Area (m^2·g^{-1})	Conductivity (S·cm^{-1})
TO	A6S-1	22.1 ± 5.1	23.0	-	-	41.1 ± 4.1	0.5 x 10^{-3}
ATO	A6SS100-1	16.3 ± 2.8	5.1	14.9 ± 0.1	11.8 ± 2.5	70.2 ± 7.0	0.82
TaTO	A6ST100-1	15.4 ± 4.1	8.2	16.1 ± 0.4	14.0 ± 1.9	74.6 ± 7.5	1.70 x 10^{-3}

II.1 Physicochemical characterization

TEM images of unsupported and aerogel-supported IrO_x NPs are displayed on **Figure 4.2**. Images of supported IrO_x NPs over TO-based aerogels (**Figures 4.2.b-d**) show the presence of two type of particles: big particles with a grey colour, corresponding to tin dioxide primary particles of the aerogel network, and small dark particles that correspond to Iridium NPs. Such IrO_x deposited NPs present a diameter of around 2 nm. Despite they are not homogenously distributed, their agglomeration is limited (**Figure 4.2.a**).
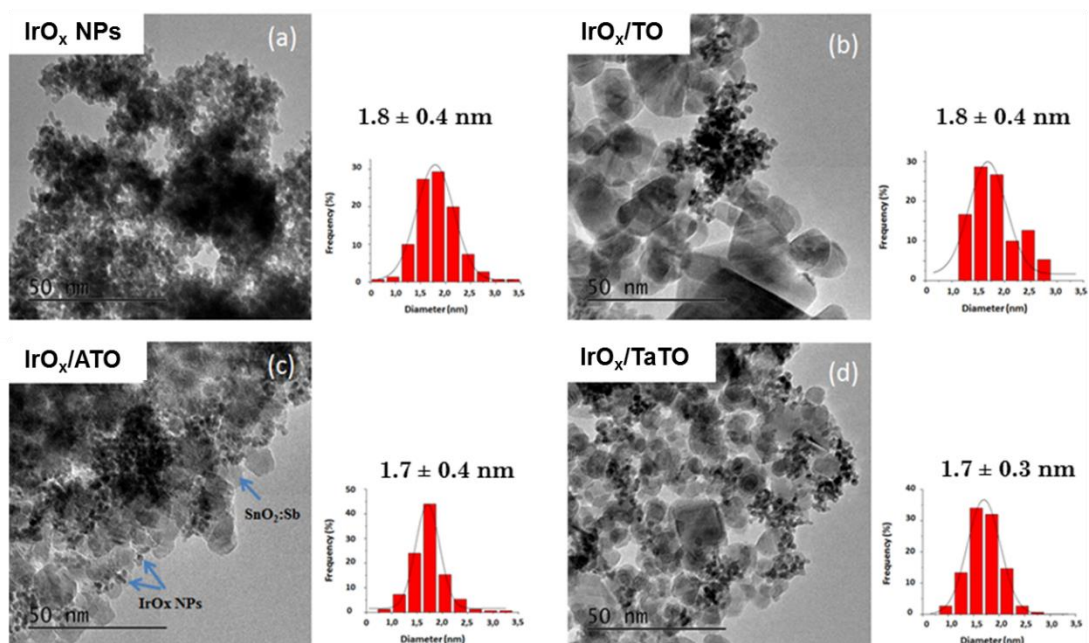
Figure 4.2 TEM images of (a) IrO_x NPs, (b) IrO_x/ TO, (c) IrO_x/ ATO and (d) IrO_x/TaTO and their associated IrO_x particle size distribution (150 particles analysed using *Image J* software).

Figure 4.3 shows the X-ray diffractograms of un-supported and supported IrO_x NPs. IrO_x NPs feature a face-centred cubic structure representative of metal Ir. Because the synthesis was performed at low temperature and in air-free atmosphere, we did not observe typical reflections of IrO_2. A thin oxide layer may cover the NPs but cannot be detected with XRD. For supported IrO_x NPs over tin-dioxide-based aerogels, X-ray diffractograms confirmed the presence of Ir(0) on the catalysts supports, as the patterns of Ir(0) clearly appears.

In the case of supported catalysts, the size of IrO_x particles, measured from TEM observation and that of crystallites, calculated with the Debye-Scherer equation, are very similar (**Table 4.2**). IrO_x NPs deposited onto the aerogels are thus most probably single crystalline. On the contrary, the crystallites of un-supported IrO_x NPs surprisingly appeared to be much larger than the particles. This has been attributed to the formation of bigger IrO_x NPs that were not detected during TEM observation.
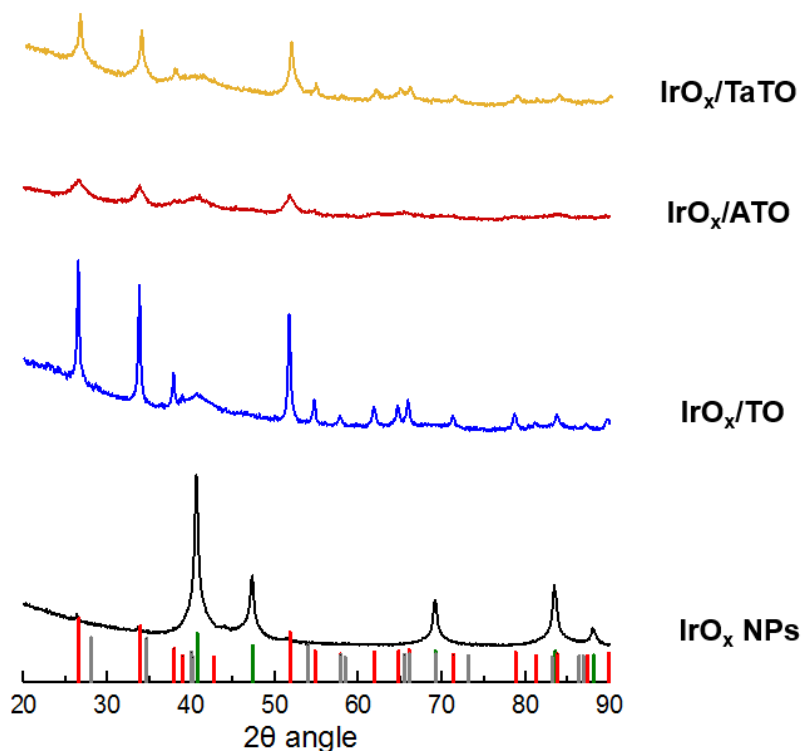
Figure 4.3 X-ray diffractograms of unsupported IrO_x NPs (black), IrO_x/TO (blue), IrO_x/ATO (dark red) and IrO_x/TaTO (yellow). Red bars correspond to the rutile structure of pure TO, grey bars to IrO_2 and green ones to Ir(0) pattern.[4,5,6]

Table 4.2. Crystallite and particle sizes of unsupported and supported IrO_x nanocatalysts.

Sample	IrO_x particle size (nm)	IrO_x crystallite size (nm)
Unsupported IrO_x NPs	1.8 ± 0.4	8.9
IrO_x/TO	1.8 ± 0.4	1.6
IrO_x/ATO	1.7 ± 0.4	1.9
IrO_x/TaTO	1.7 ± 0.3	1.9

EDX and XPS analyses were used to gain insights into the weight fraction (wt. %) and the valence of Ir in each catalyst (**Table 4.3**).

The Ir wt. % determined by EDX was close to the nominal value (30 wt. %), thus reflecting that the vast majority of the $IrCl_3$ salt was reduced and deposited on each support material. For Ir detection, the peak at 9.17 eV (Ir Lα emission) was selected, due to the overlapping of the

peak at 1.98 eV with the Pt loading signal (note that the samples were covered by a thin film of Pt for EDX analyses).
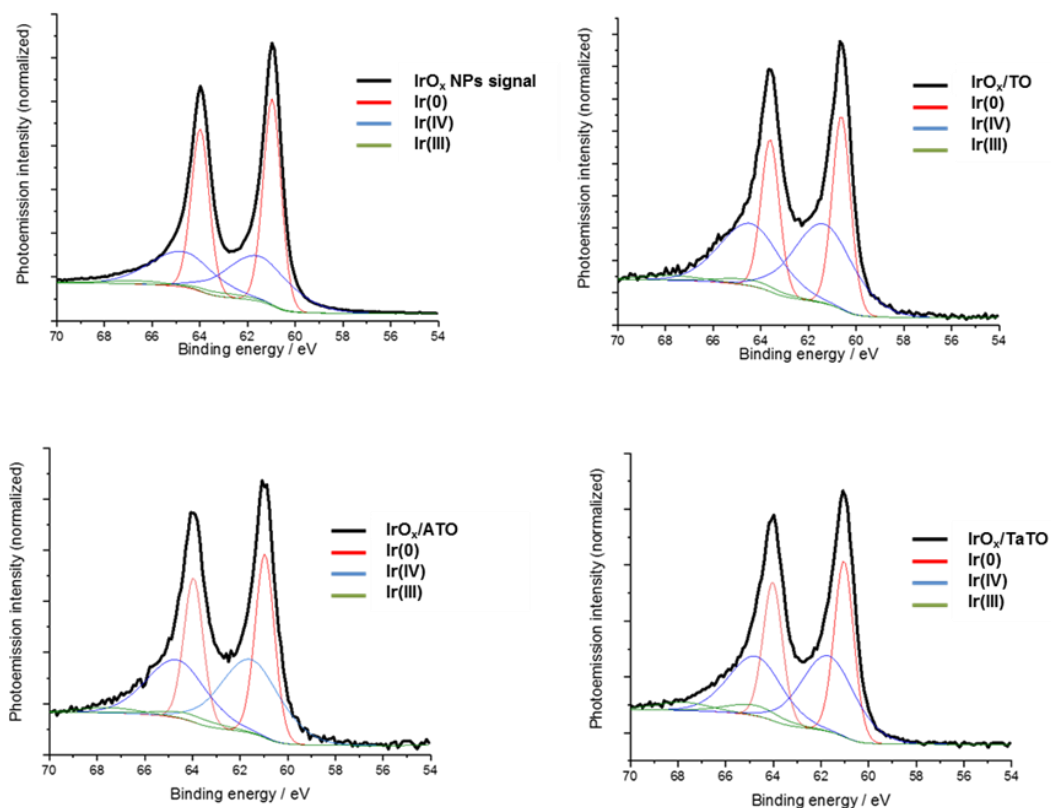
Figure 4.4 Detailed Ir 4f spectra of (a) IrO_x NPs, (b) IrO_x/TO, (c) IrO_x/ATO and (d) IrO_x/TaTO catalysts, showing the contribution of each Ir oxidation state.

The Ir4f peak was fitted using the parameters and the line shapes proposed by Freakley *et al.*[7] Three contributions were considered: metallic Ir(0), Ir(IV) and Ir(III).

Table 4.3 gathers data obtained from the XPS peaks analysis. They show that the IrO_x nanocatalysts are composed of both metallic Ir and Ir oxide in approximately the same amount. This was no surprise as nanocatalysts are prone to formation of an amorphous IrO_x layer (with $x < 2$) resulting from oxidation in air. Regarding the deposited nanocatalysts over the aerogels, all IrO_x NPs present similar particle and crystallite sizes (**Table 4.2**), and similar metallic and oxide contributions. We suggest a crystalline metallic core covered with a thin oxide layer, probably amorphous, composed with $Ir^{3+/4+}$ that can be attributed to an Ir oxohydroxide phase (IrO_x).[3]

The unsupported IrO_x NPs featured a higher Ir metallic content than the aerogel-supported IrO_x nanocatalysts. This higher metallic content is mostly a consequence of the bigger particles size assumed for this material, the volume/surface ratio of particles increasing with their diameter.

Table 4.3. Chemical composition of the IrO_x/TO-based aerogels determined by EDX and XPS measurements.

Sample	Ir wt. % (EDX) (Ir/(Ir+ATO)	Ir(0) at. % (XPS) 60.8 eV ($4f_{7/2}$)	Ir(IV) at. % (XPS) 61.6 eV ($4f_{7/2}$)	Ir(III) at. % (XPS) 62.9 eV ($4f_{7/2}$)
Unsupported IrO_x NPs	96.3 ± 2.4*	53.6 ± 5.9	42.6 ± 3.9	3.8 ± 1.4
IrO_x/TO	30.0 ± 1.3	41.2 ± 4.0	49.9 ± 5.6	8.9 ± 2.4
IrO_x/ATO	29.0 ± 1.5	42.7 ± 1.9	50.4 ± 1.9	6.9 ± 2.2
IrO_x/TaTO	33.0 ± 2.0	41.9 ± 2.6	49.6 ± 2.5	8.6 ± 1.4

*complement to 100% with O and possibly Cl and/or C

II.2 OER electrocatalytic activity and stability

The OER activity and stability of the four prepared catalysts were studied in RDE configuration at room temperature, using as electrolyte solution of H_2SO_4 at 0,05 M (pH ≈ 1). The analysis protocol is summarized in **Table 4.4**.

Table 4.4. Sequences used for electrochemical characterizations

Sequence Number	Starting Potential (V *vs.* RHE)	Potential range (V *vs.* RHE)	Sweep rate (mV·s^{-1})	N° Cycles	Purpose
1	1.0	1.0 – 1.6	5	3	OER pre-test
2	OCP	0.0 – 1.6	20	10	Electrochemical conditioning
3	1.0	1.0 – 1.6	5	3	OER activity evaluation
4	Chronopotentiometry at 1 mA·cm^{-2} for 24 hours				Stability test

First of all, the cell and the electrodes were prepared as described in the experimental part, section III, chapter 2. Three different electrodes were prepared and analysed with the same ink solution. Conditioning of the electrodes was first carried out by performing a series of 10 cyclic voltammograms (CV) between 0.0 and 1.6 V *vs.* RHE and another of 3 CV cycles between 1.0 and 1.6 V. A 24-hour chronopotentiometry at 1 mA·cm^{-2} was used to determine the stability of each catalyst under OER conditions. The current obtained at 1.51 V ($\eta = 0.28$V) in the last sequence step, was normalized either by the mass of Ir initially deposited on the electrode (mass activity, j_{mass}) or by the anodic charge measured between 0.40 and 1.40 V vs. RHE, which is known to be proportional to the amount of Ir oxide (specific activity, j_{spec}).[8,9] It is of real interest to compare both activities (j_{mass} and j_{spec}). Indeed, the mass activity may not be really accurate since the total amount of Ir deposited on the working electrode is difficult to know precisely. The ink solution dispersion may not be completely homogeneous and the deposited volume could be approximate. On the contrary, the specific activity which depends on the measured current and the measured anodic charge, should be more accurate.

The results, displayed on **Figure 4.5**, show a 5-fold enhancement of the OER mass activity at 1.51 V (nearly 10-fold at 1.58 V) for the aerogel-supported IrO$_x$ NPs compared to unsupported IrO$_x$ NPs. This can be ascribed first to the larger particle size of the IrO$_x$ NPs, presenting a lower surface to volume ratio.

Then the relative ratio between the two main detected Ir oxidation degrees (0/IV) is inversed for unsupported IrO$_x$ NPs (1.26) and supported ones (0.82, 0.85 and 0.85 for TO, ATO and TaTO respectively). It is well stablished by literature that Iridium oxide species appear to be much more active for OER than Ir(0), due to the presence of iridium oxohydroxides.[3,10] This is in agreement with the two main OER mechanisms currently considered, where the cationic centre Ir(III) plays a key role for the transitions Ir (III)-Ir (IV)-Ir (V).[11] Therefore, in agreement with our results, the higher the amount of Ir(IV) compared to Ir(0), the higher the activity. However, since this ratio is relatively close to unity, we can reasonably consider that the main factor here is the catalyst particle size and the larger aggregation of the non-supported NPs.

The stability of the IrO$_x$ NPs was also enhanced by the presence of the aerogel support, as the lifespan of the materials was improved from 1 hour for unsupported IrO$_x$ NPs up to 17 hours for the IrO$_x$/TO catalyst (**Figure 4.6** and **Table 4.5**). Such a result may temptingly be ascribed to metal-metal oxide interactions with the support (MMOSI) which could stabilize the supported IrO$_x$ NPs. However, without further evidence the only reason we can propose here stands again in the difference in particle size between unsupported and supported IrO$_x$ NPs. With larger NPs size, the unsupported IrO$_x$ is indeed subjected to a higher potential during the chronopotentiometry accounting for the lower durability observed.

Surprisingly, despite very different electronic conductivity of their supports (**Table 4.1**), similar geometric, OER mass and specific activities were measured for the three aerogel-supported IrO_x catalysts. Even more surprising, IrO_x/TO was found to be the best-performing material. These results may however be rationalized by considering that, in RDE configuration, a very thin film of catalyst covers a glassy carbon disk with high electronic conductivity. Since supported IrO_x/TO-based aerogel and carbon Fermi levels, of RDE glassy carbon, align upon contact, any effect on the OER activity because different conductivity of the catalysts is not possible to been observed in RDE configuration. The situation will be very different for *ca.* 150-200-fold thicker PEMWE anodes, in which the electronic conductance of XTO-based aerogels will be determined by their intrinsic conductivity, the contact resistances, and their volume density. In that frame, it was also no surprise to note that the time during which a current density of 1 $mA \cdot cm^{-2}$ could be sustained (cut-off voltage of 2 V) almost did not depend on the nature of the aerogel (**Table 4.1**). We thus conclude that quantifying the impact of the nature of the XTO-based aerogel (non-doped *vs.* Sb or Ta doped SnO_2) is hardly possible in RDE configuration.
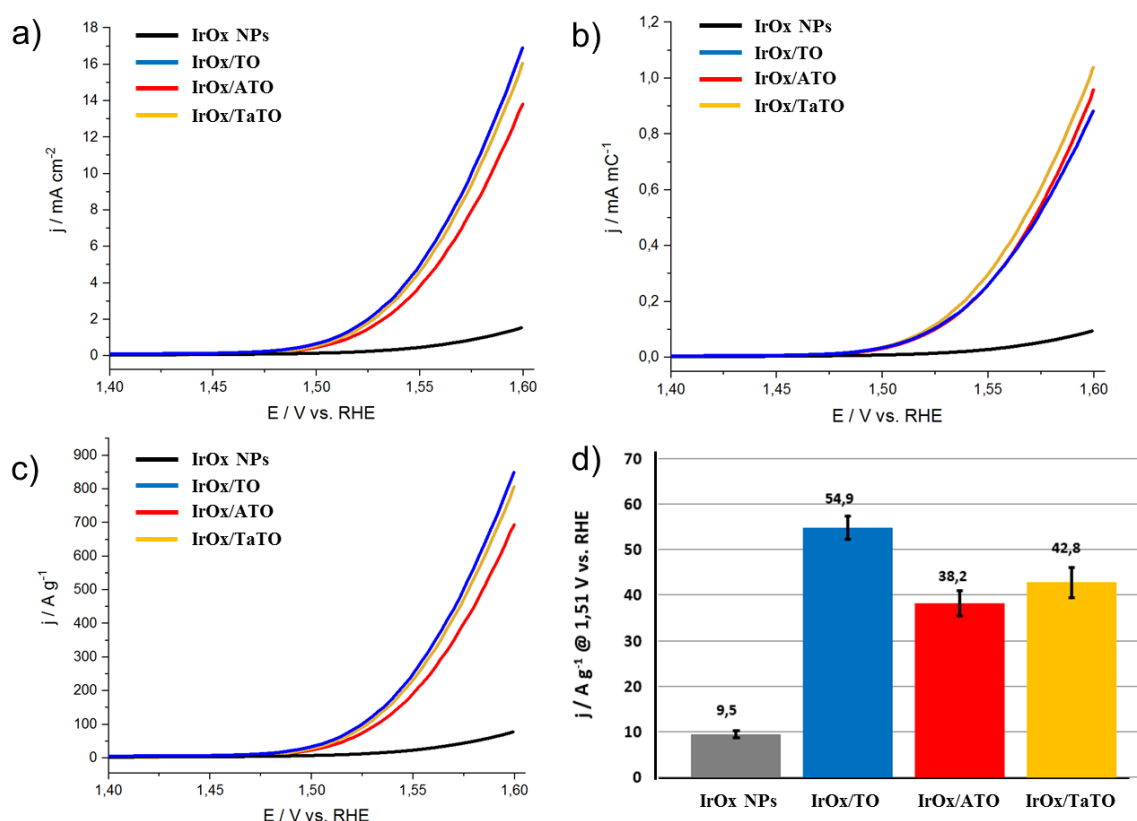
Figure 4.5 Electrocatalytic performance and durability of the different catalysts: (a) geometric activity (b) specific activity (c) mass activity and (d) mass activity comparison at 1.51 V vs RHE. All measurements were performed at 25°C in N_2-saturated 0.05 M H_2SO_4 using a potential sweep rate of 5 $mV \cdot s^{-1}$ and a rotation rate of 1600 rpm. The Ir loading was 20 $\mu g\ cm^{-2}$ for all electrodes (3.9 μg Ir per RDE tip).

Table 4.5. Stability tests results for the synthesized catalysts (24-hour chronopotentiometry using a constant current density of 1 mA·cm^{-2} and a cut-off voltage of 2.0 V.

Sample	Durability (@ 1 mA cm^{-2})
Unsupported IrO$_x$ NPs	1.0 ± 0.5 h
IrO$_x$/TO	17.0 ± 2.5 h
IrO$_x$/ATO	16.0 ± 1.0 h
IrO$_x$/TaTO	14.5 ± 2.0 h
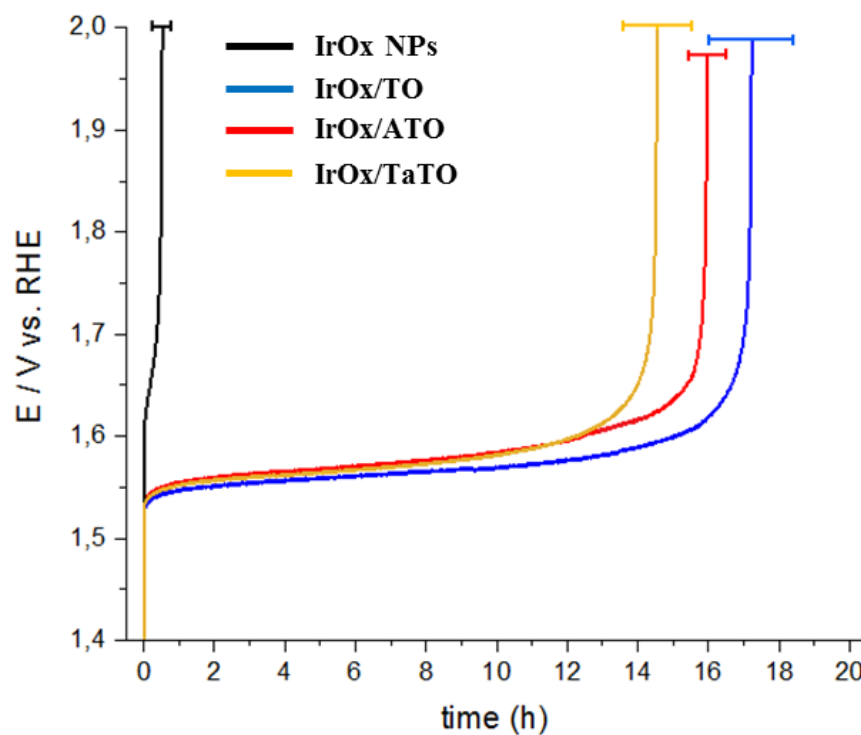
Figure 4.6 Stability tests results for the synthesized catalysts (24-hour chronopotentiometry using a constant current density of 1 mA·cm^{-2} and a cut-off voltage of 2.0 V).

II.3 Conclusions

In conclusion, we showed that supporting IrO_x nanoparticles on tin oxide aerogels allows enhancing their OER activity and stability. Despite very different electronic conductivity, the OER mass and specific activities of IrO_x nanoparticles deposited onto tin oxide-based aerogels were found similar in thin-film electrode configuration. This is in agreement with the recent results obtained by the group of Professor Uchida on different types of tin dioxide support. On top of a better OER activity, all aerogel supported IrO_x/XTO-based catalysts also exhibited enhanced durability compared to unsupported IrO_x nanoparticles.

Considering the promising results reported in this study, specific studies have been carried out in order to optimize the doping element concentration of doped tantalum dioxide-based aerogels.

The impact of the sol-gel catalyst used for the ATO gel formation on the performance of the electrocatalyst will first be evaluated in the next section.

III Impact of the sol-gel catalyst used for the ATO synthesis on the performance of the IrO$_x$/ATO electrocatalyst

The study of Sb-doped aerogels in **section III.2** of **chapter 3**, showed that the aerogels prepared in a basic sol-gel media seemed to be more promising, as catalysts supports for PEMWE, than those prepared in acid media, due to lower Sb segregation. In order to confirm such a hypothesis, Iridium oxide NPs were deposited over selected ATO aerogels prepared in acid or basic conditions (HNO$_3$ or NaOH respectively) by chemical reduction of IrCl$_3$ salt, as described in **section I, chapter 3**. Selected aerogels were A6SS100-3-0.07 (ATO-a) and A6SS100-3-B0.07 (ATO-b), already characterized and discussed in **section III.2, 3rd chapter**. The main properties of selected ATO aerogels are summarized in **Table 4.6**.

Once the catalysts NPs were deposited onto aerogels, they were characterized by a set of physiochemical techniques and their OER activity evaluated in RDE configuration as well as their durability.

Table 4.6. Summary of the main properties of selected aerogels ATO-a (HNO$_3$) and ATO-b (NaOH)

Sample	Particle size (nm) - SEM	Crystallites size (nm) - XRD	Bulk doping (at. %) EDX	Surface doping (at. %) XPS	Specific surface area (m$^2 \cdot$g^{-1})	Conductivity (S$\cdot$cm^{-1})
ATO-a	16.1 ± 3.7	4.9	9.5	11.8	61.4	1.0
ATO-b	12.9 ± 2.2	6.3	11.0	11.1	83.5	0.8

III.1 Physicochemical characterization

Iridium-based NPs, prepared by chemical reduction of salt precursor $IrCl_3$, shown typical face-centred cubic structure of Ir(0) without any presence of IrO_2 phases (**Figure 4.7**). If any presence of Iridium oxide, it should be either amorphous or as too thin a layer to be detected.
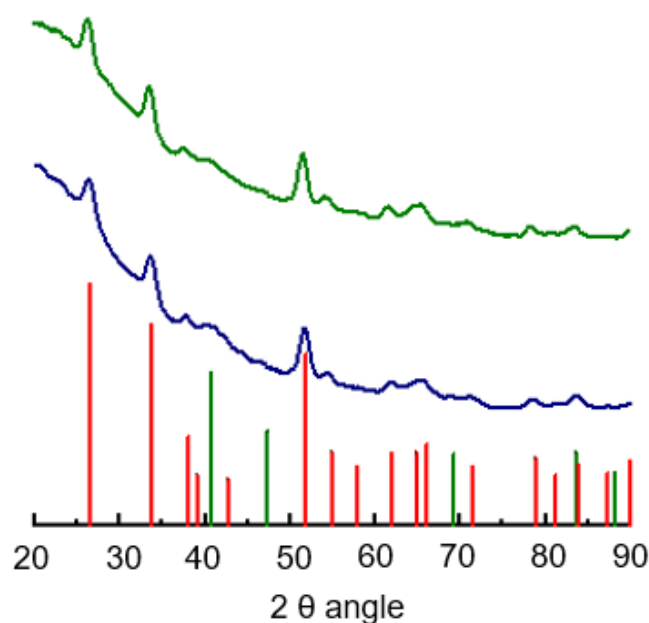
Figure 4.7 X-ray diffractograms of IrO_x/ATO-a (blue) and IrO_x/ATO-b (green). Red bars correspond to the rutile structure of pure TO and green coloured ones correspond to Ir(0) pattern.[4,5]

Iridium NPs were successfully deposited onto the aerogels with a homogeneous distribution over the ATO-based aerogels, and similar particles size of around 2 nm in diameter for both prepared catalysts, (**Figure 4.8** and **Table 4.7**). The crystallites size of Ir(0), obtained by XRD measurements, is very similar to that of IrO_x NPs, as observed previously (**section 4.II**).

Table 4.7. Crystallite and particle sizes of supported IrO_x nanocatalysts.

Sample	IrO_x NPs size (nm)	Ir(0) crystallites size (nm)
IrO_x/ATO-a	2.0 ± 0.5	2.1
IrO_x/ATO-b	2.0 ± 0.5	2.8
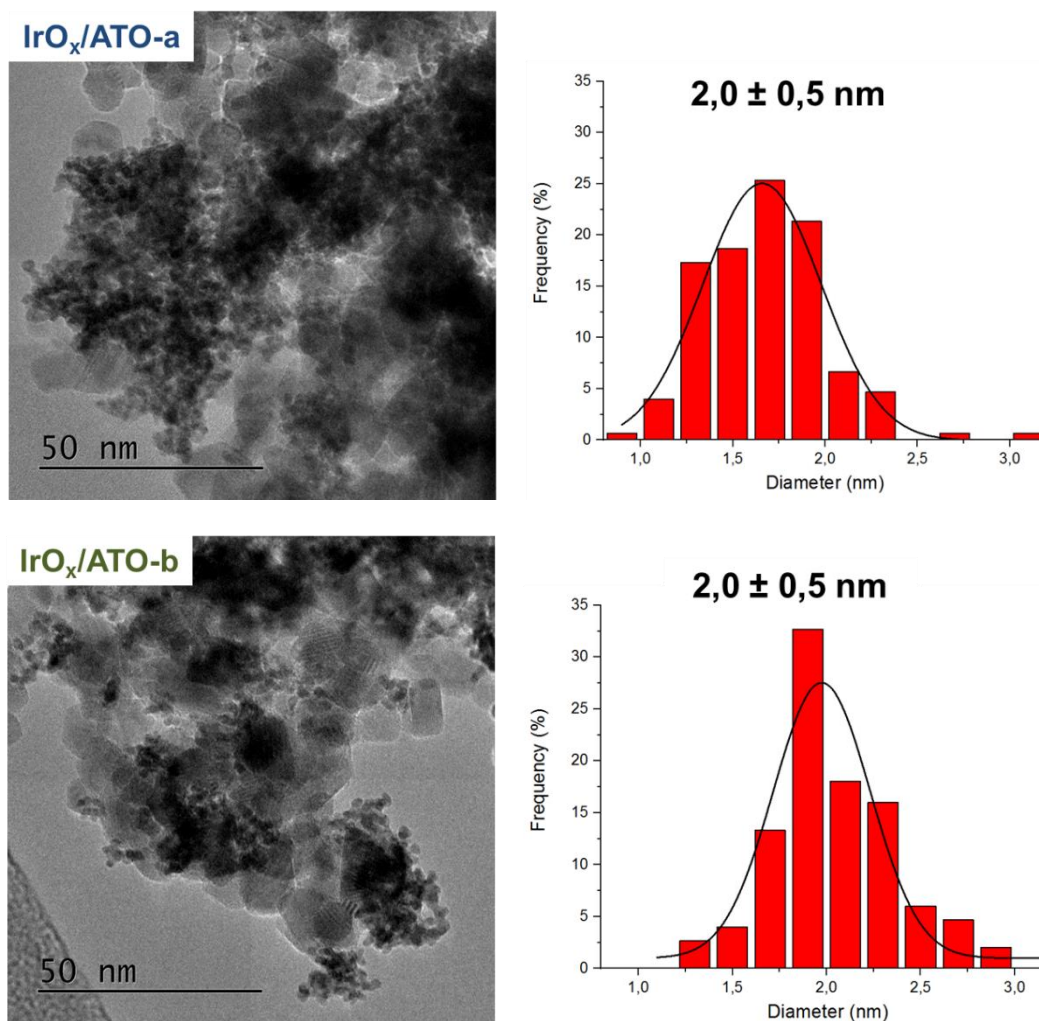
Figure 4.8 TEM images of (a) IrO$_x$/ATO-a and (b) IrO$_x$/ ATO-b, and associated IrO$_x$ particle size distribution (150 particles analysed using *Image J* software).

The real Ir weight fraction (wt. %) and the valence of Ir were measured by XPS and EDX analyses for both catalysts, as seen on **Table 4.8**.

The determined Ir wt. % (EDX) was close to the nominal value (30 wt. %) for both samples: 31 wt. % for IrO$_x$/ATO-a and 25 wt. % for IrO$_x$/ATO-b. The peak at 9.1 eV (Ir Lα emission) was selected for the measurement, as the most intense Ir peak at 1.98 overlaps with the Pt signal (a Pt loading is needed for SEM analyses).

Table 4.8. Chemical composition of the IrO$_x$/ATO aerogels determined by EDX and XPS.

Sample	Ir wt. % (EDX)	Ir(0) at. % (XPS) 60.8 eV (4f$_{7/2}$)	Ir(IV) at. % (XPS) 61.6 eV (4f$_{7/2}$)	Ir(III) at. % (XPS) 62.9 eV (4f$_{7/2}$)
IrO$_x$/ATO-a	31.0 ± 1.8	37.4 ± 1.8	53.0 ± 1.7	9.8 ± 0.4
IrO$_x$/ATO-b	25.0 ± 2.3	35.6 ± 1.3	53.4 ± 2.2	10.8 ± 0.6

Table 4.8, shows the composition of supported typical IrO$_x$ NPs,[12] which are composed of a mix of Ir(0), Ir(III) and Ir(IV). As previously supposed, the oxide phase is probably resulting from oxidation under air exposition. The Ir4f peak was fitted using the same procedure as in **section II**.[7] When comparing at. % between both catalysts, we can see a similar metallic Ir(0) contribution for both samples, as well as similar particle and crystallite sizes, suggesting a crystalline metallic core for Ir NPs for both catalysts covered with an amorphous surface oxohyydroxide layer composed of Ir(IV) and Ir(III).

III.2 OER electrocatalytic activity and stability

The OER activity and stability of the four prepared catalysts were studied in RDE configuration, at room temperature, using as electrolyte solution of H$_2$SO$_4$ at 0,05 M (pH ≈ 1). The analysis protocol is summarized in **Table 4.9**.

Table 4.9. Sequence used for electrochemical characterizations

Sequence	Test
1	OER Activity evaluation
2	Chronopotentiometry at 1 mA·cm^{-2} for 10 hours
3	OER Activity evaluation

Four experiments were run for each catalyst, with four different electrodes prepared for each catalytic ink, and the average values with their respective variations were plotted on **Figure 4.9** and **Table 4.10**.

The results, show similar mass and specific activities for both catalysts, IrO$_x$/ATO-a and IrO$_x$/ATO-b, before the chronopotentiometry, despite the different conductivities between both aerogels. The similar registered activities are attributed to: (1) similar morphologies and particle and crystallites sizes of the deposited NPs (expected to be the same as they were prepared following the same synthesis route) and (2) similar chemical surface composition for both catalysts, i.e. same oxidation state for both samples.

The chronopotentiometry parameters chosen here were adapted from previous preliminary tests, **section II**, where the lifespan of IrO$_x$/ATO catalysts under 1 mA·cm^{-2} was determined to be around 20 hours. Therefore, a first 10 hours-test was carried out to compare the activity of both catalysts before and after the chronopotentiometry test but before any deactivation. Aliquots of electrolytes were sampled during the experiment for further ICP-MS analysis in order to follow any possible leaching of Ir, Sn or Sb. Since the Sb repartition was more homogeneous for ATO-b aerogels than for ATO-a ones, which showed larger surface Sb segregation, less Sb leaching was expected. This may impact the IrO$_x$ NPs detachment during the experiment and, as a result the durability of the catalysts.
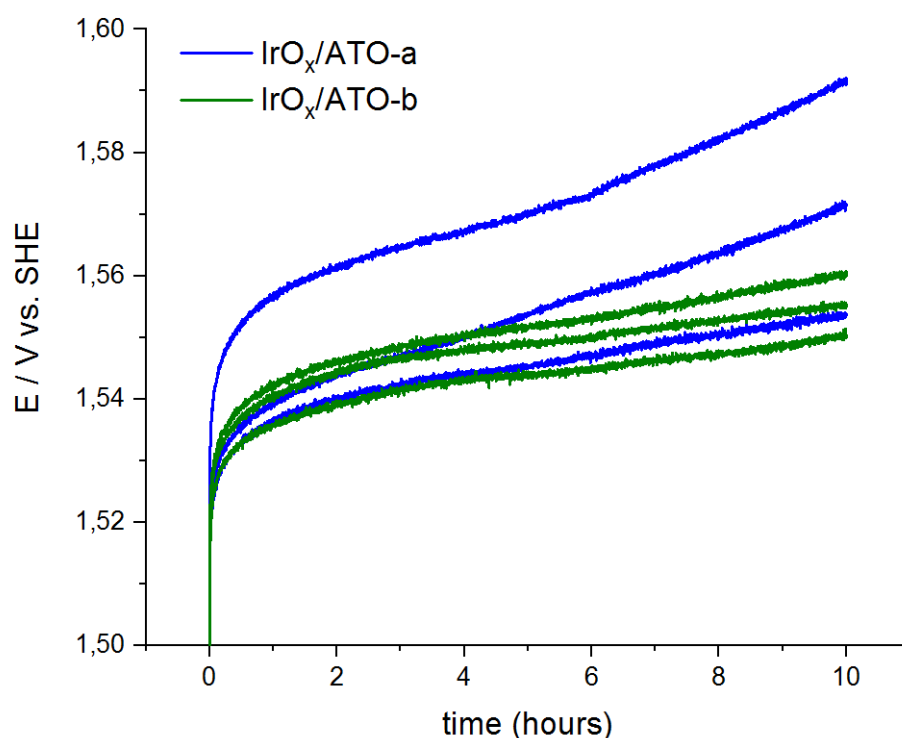
Figure 4.9 Registered 10-hours chronopotentiometry at 1 mA·cm^{-2} for different IrO$_x$/ATO-a (blue) and IrO$_x$/ATO-b (green) electrodes.
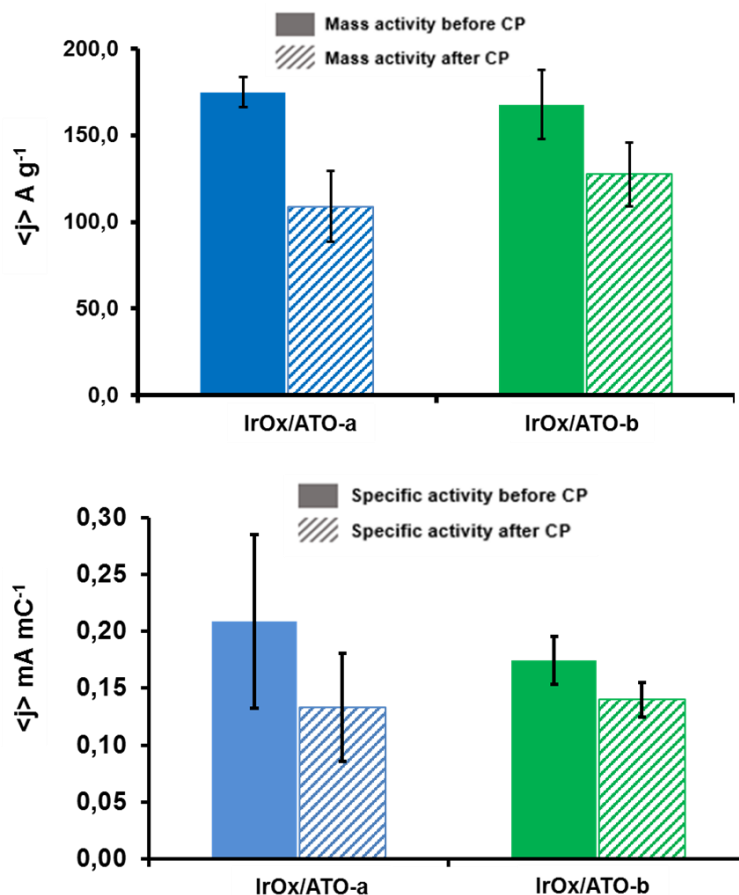
Figure 4.10 Comparison of mass activities (top) and specific activities (bottom) of both catalysts before and after the chronopotentiometry (CP) test (10-hours at 1 mA·cm^{-2}) at 1.53 V. All measurements were performed at 25°C in N$_2$-saturated 0.05 M H$_2$SO$_4$ using a potential sweep rate of 5 mV·s^{-1} between 1.0 and 1.6 V and a rotation rate of 1600 rpm. The Ir loading was 20 µg·cm^{-2} for all electrodes (3.9 µg Ir per RDE tip).

Table 4.10. Mass and Specific activity values, at 1.53 V vs. SHE, of the IrO$_x$/ATO catalysts before (initial, $_i$) and after (final, $_f$) the 10-hours CP test, together with ECSA and RF obtained values.

Sample	Initial Mass Activity (A·g^{-1})	Final Mass Activity (A·g^{-1})	Initial Specific Activity (mA·mC^{-1})	Final Specific Activity (mA·mC^{-1})	ECSA (cm^2)
IrO$_x$/ATO-a	178.8 ± 8.5	108.9 ± 20.5	2.1E^{-4} ± 0.8E^{-4}	1.3E^{-4} ± 0.8E^{-4}	4.5 ± 1.5
IrO$_x$/ATO-b	167.7 ± 19.9	127.5 ± 18.3	1.7E^{-4} ± 0.2E^{-4}	1.4E^{-4} ± 0.2E^{-4}	4.3 ± 0.7

The initial mass and specific activities are both lower for IrO$_x$/ATO-b than for IrO$_x$/ATO-a.

Note that the initially measured Electro-Chemically Active Surface Area (ECSA) of IrO_x/ATO-a was slightly higher than that of IrO_x/ATO-b. This could partly explain the differences observed in initial mass and specific activities between both catalysts.
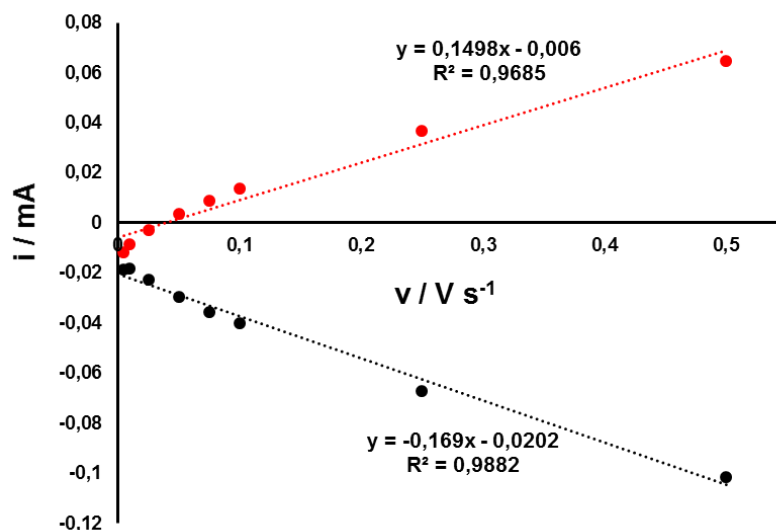
Figure 4.11 Cathodic (black) and anodic (red) charging currents measured at 0.344 V vs. SHE plotted as a function of scan rate. The determined double-layer (C_{DL}) capacitance of the system was took as the average of the absolute values of the slope of the linear fits to the data. Then the obtained C_{DL} (mF) value is divided by the C_S (0.035 mF·cm^{-2}) in order to obtain the ECSA values (cm^2).

When comparing mass activity and specific activity, before and after the chronopotentiometry test, the activity loss is systematically smaller for IrO_x/ATO-b compared to IrO_x/ATO-a. Such lower decrease is clearer for mass activity, where a 24% activity loss was observed for IrO_x/ATO-b compared to 38% for IrO_x/ATO-a (**Table 4.10**). Strasser *et al.*,[8b] observed similar mass activity loss, 21.4 %, after 15h chronopotentiometry test under similar conditions (1 mA·cm^{-2} at pH = 1), for IrO_x-based nanocatalysts supported on ATO particles.

The difference observed in the case of the specific activity (12% loss for IrO_x/ATO-b compared to 36% for IrO_x/ATO-a) is more difficult to analyse, due to a larger variance between measured values. The evolution trend tends however to confirm results obtained for mass activity. Such a lower activity decrease is reflected on the lower increase of the potential during the 10-hours chronopotentiometry compare to that of IrO_x/ATO-a (**Figure 4.9**). If the potential increases less with time, then the deactivation of active sites is slower and the stability better.

In order to measure the Ir, Sn, and Sb possible losses during the stability test, ICP-MS analyses were carried out on electrolyte solution aliquots sampled during the experiment. Three electrolyte aliquots were taken for each experiment: one after the first activity test, just before the chronopotentiometry, a second one after 6 hours of chronopotentiometry, and a

third one at the end of the experiment. ICP-MS analysis results are gathered in **Table 4.11 and Figure 4.12**.

Table 4.11. ICP-MS results for analysed aliquots sampled during the electrochemical tests for each catalyst.

Sample	Element	Aliquot nº1	Aliquot nº2	Aliquot nº3
IrO$_x$/ATO-a	Ir	2.4 ± 0.4	3.8 ± 0.2	5.5 ± 0.1
IrO$_x$/ATO-b	Ir	2.5 ± 0.1	3.7 ± 0.1	5.2 ± 0.2
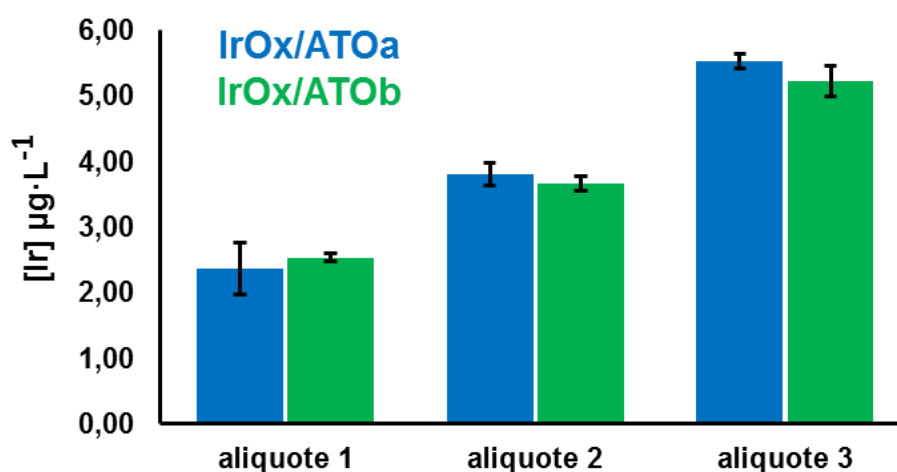
Figure 4.12 Ir concentration measured, in the electrolyte solution during stability tests. Each aliquot sampled at t=0, 6 and 10 h, for each catalyst, IrO$_x$/ATO-a (blue), and IrO$_x$/ATO-b (green).

Only Ir could be detected with ICP-MS. Results (**Figure 4.12**) suggest that the activity decrease for both catalysts was caused by an Ir dissolution in the electrolyte solution, or IrO$_x$ NPs detachment, during the OER tests. Notoriously, the Ir leaching from both ATO aerogels were similar. The better durability of IrOx/ATO-b may thus come from a better stability of the support. Sb and Sn dissolution, if ever present, were however too low to be quantified, the quantification being limited to 2 µg·L^{-1} for Sb and 20 µg·L^{-1} for Sn. Therefore, it was not possible the discriminate between both aerogels.

About *et al.*[14] also measured the Ir dissolution from IrO$_x$ particles prepared *ex-situ* and deposited over our ATO aerogel materials and compared it to that of Sn and Sb during AST cycling, between 0.9 and 1.4 V vs. SHE. at 5 mV·s^{-1}. They found Ir dissolution rates higher than Sb and around one order of magnitude higher than Sn ones. Based on the same ATO aerogels support, our Sb dissolution would be expected around 2-3 µg·L^{-1}, and Sn dissolution

around 0.5 - 1 µg·L^{-1}. Such values are lower than the quantification limit of the ICP-MS utilized for the analysis.

We assumed that ATO-b aerogel could be more stable under OER conditions. Lower Sb leaching was indeed expected because of a lower initial Sb segregation. No Sb nor Sn could be detected in the several aliquots. Since it is also the case for IrOx/ATO-a, we cannot completely conclude concerning the relative stability of ATO-b compared to that of ATO-a.

Measured values of dissolved Ir cannot be compared with other Ir dissolution values from literature, as different stability protocols are used. For example: Da Silva et co-workers cycled IrO$_x$ NPs deposited over an ATO support between 1.1 and 1.6 V vs. SHE. at 5 mV·s^{-1}.[13a] They found that Sb dissolution was 4 times higher than Ir, and around 10 times higher than Sn leaching. Savinova *et al.*,[Erreur ! Signet non défini.b] observed that supported IrO$_x$ NPs over ATO materials suffered less Ir dissolution than non-supported ones under galvanostatic conditions at 1 mA·cm^{-2} in 0.1 M H$_2$SO$_4$. They related such slower dissolution to the interactions between the support and the Ir nanocatalysts. A decrease of the Ir(III) species on the supported Ir NPs, compared to the non-supported Ir NPs, was a key factor for the stability increase. They also detect a preferential Sb dissolution than Sn.

III.3 Conclusions

In conclusion, similar IrO$_x$ particle properties (size, structure and crystal size) have been obtained whatever the ATO supports, the "basic" or the "acid" one.

Concerning the OER performance, it was found that IrO$_x$/ATO-b presented higher resistance than IrO$_x$/ATO-a under OER operations, as its mass and specific activity losses after a stability test were lower. These results are in accordance with our previous results obtained on the bare support.

Unfortunately, the ICP-MS measurements showed similar Ir dissolution for both catalysts. Therefore, it is eventually difficult to conclude if and why ATO-b aerogels would provide higher stability to IrO$_x$/ATO system. In order to prove our previous hypothesis, similar tests performed on a longer period of time would be necessary. The detection of Sb and Sn in the electrolyte would indeed be very interesting for the comparison between ATO-a and ATO-b aerogels.

IV OER activity and stability of IrO_x/TaTO after selection of a better support A6ST028 (2.8 at% Ta)

The study of Ta-doped aerogels on **section IV, chapter 3,** showed that the Ta-doped aerogels with an atomic doping ratio between 1 and 3 at. % present the best compromise between specific surface area and electronic conductivity. Herein, Iridium oxide NPs were deposited over a selected TaTO aerogel, doped at 2.8 at. %, and the resulting IrO_x/TaTO catalyst was fully characterized by a set of physiochemical techniques. Then the OER activity and durability were compared in RDE configuration to those of IrO_x/ATO-a of **section III**.

The Iridium NPs were deposited *in-situ* over the selected TaTO aerogel by chemical reduction of $IrCl_3$ salt, as described on **section I, chapter 3**. Selected aerogel was A6ST028-5 (TaTO), whose main properties are summarized in **Table 4.12**.

Table 4.12. Summary of the main properties of the selected aerogel, A6ST020-5(TaTO).

Sample	Particle size (nm) - SEM	Crystallites size (nm) - XRD	Bulk doping (at. %) EDX	Surface doping (at. %) XPS	Specific surface area ($m^2 \cdot g^{-1}$)	Conductivity ($S \cdot cm^{-1}$)
TaTO	16.1 ± 3.7	13.2	2.8	5.4	38.4	0.0046

IV.1 Physicochemical characterization

Figure 4.14, shows the XRD diffractogram of IrO_x/TaTO. The deposited Ir-based NPs present a face-centred cubic structure of Ir(0), with no presence of crystalline IrO_2 phases.

TEM images show that Iridium NPs were successfully deposited onto the aerogels with a less homogeneous distribution, some regions of the catalysts showing no IrO_x nanoparticles. IrO_x particles sizes similar to previous samples (around 2 nm in diameter) were measured (**Figure 4.13** and **Table 4.13**).

Crystallites size of Ir(0), obtained by XRD measurements, is very close to that of IrOx NPs, as previously.

Table 4.13. Crystallites and particles sizes of supported IrO_x nanocatalysts.

Sample	IrOx NPs size (nm)	Ir(0) crystallite size (nm)
IrO_x/ATO-a	2.0 ± 0.5	2.0
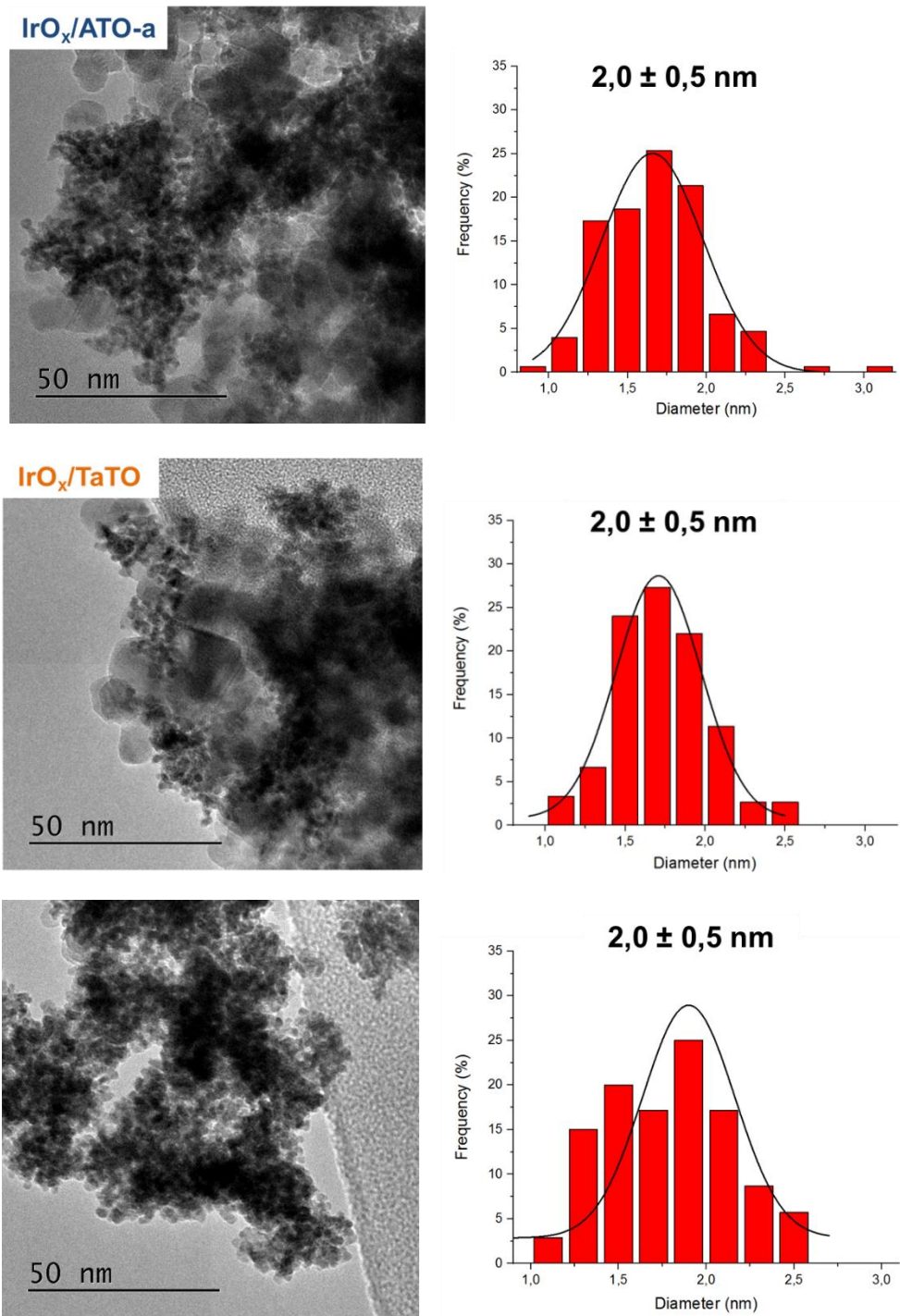
Figure 4.13 TEM images of (a) IrO$_x$/ATO-a and (b) IrO$_x$/ TaTO and associated IrO$_x$ particle size distribution. (c) region where IrO$_x$ NPs are not supported on the TaTO aerogel, with its respective particle size distribution. 150 particles were measured for the (a) and (b) particle size distribution graphs, 35 for (c).
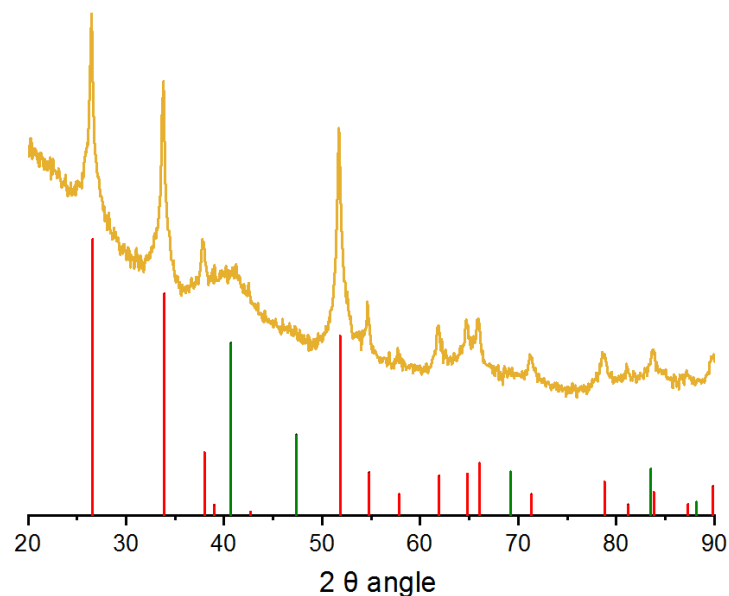
Figure 4.14 X-ray diffractograms of IrO$_x$/TaTO. Red bars correspond to the rutile structure of pure TO and green colour ones correspond to Ir(0) pattern.[4,5]

About the catalyst chemical composition, the Ir weight fractions (wt. %) and oxidation states of IrO$_x$/TaTO and IrO$_x$/ATO-a are reported in **Table 4.14**. The Ir wt. % determined by EDX was very close to the nominal value (30 wt. %). The peak at 9.17 keV was selected for Ir detection by XPS as in previous sections.

Table 4.14. Chemical composition of the IrO$_x$/TaTO aerogels determined by EDX and XPS.

Sample	Ir wt. % (EDX)	Ir(0) at. % (XPS) 60.8 eV (4f$_{7/2}$)	Ir(IV) at. % (XPS) 61.6 eV (4f$_{7/2}$)	Ir(III) at. % (XPS) 62.9 eV (4f$_{7/2}$)
IrO$_x$/ATO-a	31.0 ± 1.8	37.4 ± 1.8	53.0 ± 1.7	9.8 ± 0.4
IrO$_x$/TaTO	30.8 ± 1.8	38.9 ± 3.9	51.2 ± 3.9	9.9 ± 1.3

The composition of IrO$_x$ NPs supported over the selected TaTO aerogel present a mix of Ir(0), Ir(III) and Ir(IV) with a similar repartition than on IrO$_x$/ATO-a. Together with the XRD data, this suggests a crystalline metallic core of Ir covered with an amorphous surface oxide layer.

IV.2 OER electrocatalytic activity and stability

The OER activity and stability of the prepared $IrO_x/TaTO$ catalyst was studied in RDE configuration by using the same method as in **section III** for IrO_x/ATO catalysts. In brief, tests were performed at 25°C, in a 0.05 M electrolyte solution of H_2SO_4 and the OER activity was measured before and after a 10-hours chronopotentiometry at 1 mA·cm^{-2}. Measured activity values, before and after the chronopotentiometry test, were analysed and compared to those obtained for IrO_x/ATO-a with the aim to determine and compare the stability of each aerogel under simulated PEMWE operation conditions.

Four experiments were run for $IrO_x/TaTO$, with four different electrodes prepared from one catalytic ink, and the average values with their respective variations were plotted on **Figure 4.15** and **Table 4.15**.

The results show a higher mass activity for the IrO_x/ATO-a catalyst than for the $IrO_x/TaTO$, but similar specific activities for both catalysts. Previous results on **section II** showed that the electronic conductivity of the aerogels does not impact the activity in RDE configuration. Since the specific activity of both catalysts is similar, such a difference in mass activity should result from a lower loading on the electrode. This could actually be attributed to a difference in Ir concentration in the catalytic ink or in the homogeneity of the suspension. Whatever, the specific activities of both catalysts, which depends on the current density and is known to be proportional to the amount of Ir oxide,[8,9] were similar.

Comparing mass and specific activities before and after the chronopotentiometry step, for both catalysts (**Table 4.15** and **Figure 4.15**), we observed a better stability of the $IrO_x/TaTO$ (loss of 28%) compared to IrO_x/ATO-a (loss of 39%). The same behaviour was observed for the specific activity: 25% loss for the $IrO_x/TaTO$ compared to 38% for IrO_x/ATO-a. Despite a larger variance calculated for the specific activities, the evolution trend for both aerogels are similar. Observing the chronopotentiometry profiles between both catalysts (**Figure 4.16**), we observed a smaller increase of the potential for the $IrO_x/TaTO$, suggesting again a better stability under OER conditions. Then, it seems than the stability of IrO_x NPs is increased if using a TaTO aerogel, thus confirming the results recently reported by Abbou *et al.*,[14] also obtained on our aerogel supports, as further discusses below.
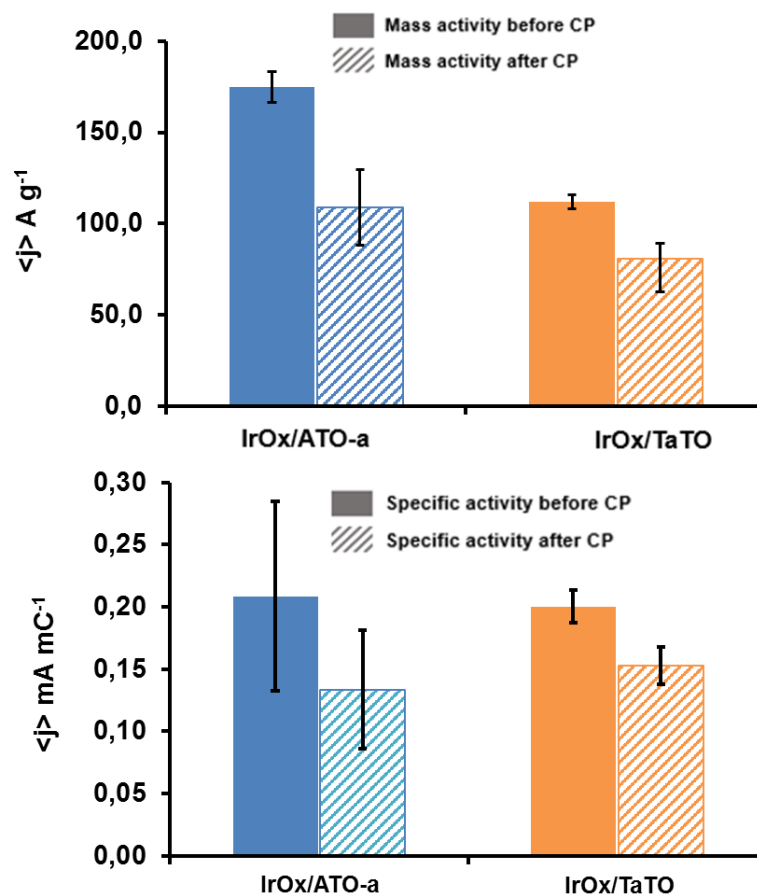
Figure 4.15 Comparison of mass activities (top) and specific activities (bottom) at 1.53 V, between IrO$_x$/ATO-a, and IrO$_x$/TaTO catalysts, before and after the chronopotentiometry (CP) test (10-hours at 1 mA·cm^{-2}). All measurements were performed at 25°C in N$_2$-saturated 0.05 M H$_2$SO$_4$ using a potential sweep rate of 5 mV·s^{-1} between 1.0 and 1.6 V and a rotation rate of 1600 rpm. The Ir loading was 20 µg·cm^{-2} for all electrodes (3.9 µg Ir per RDE tip).

Table 4.15. Mass and Specific activity values, recorded at 1.53 V, of the IrO$_x$/ATO-a and IrO$_x$/TaTO catalysts before (initial - i) and after (final - f) the 10-hours CP test, together with ECSA and RF obtained values.

Sample	Initial Mass Activity (A·g^{-1})	Final Mass Act. (A·g^{-1})$_f$	Initial Sp. Act. (mA·mC^{-1})$_i$	Final Sp. Act. (mA·mC^{-1})$_f$	ECSA (cm^2)	RF
IrOx/ATO-a	178.8 ± 8.5	108.9 ± 20.5	2.1E^{-4} ± 0.8E^{-4}	1.3E^{-4} ± 0.8E^{-4}	4.5 ± 1.5	22.9 ± 7.6
IrOx/ATO-b	111.9 ± 3.9	80.9 ± 8.8	2.0E^{-4} ± 0.1E^{-4}	1.5E^{-4} ± 0.2E^{-4}	3.2 ± 1.3	16.4 ± 6.8
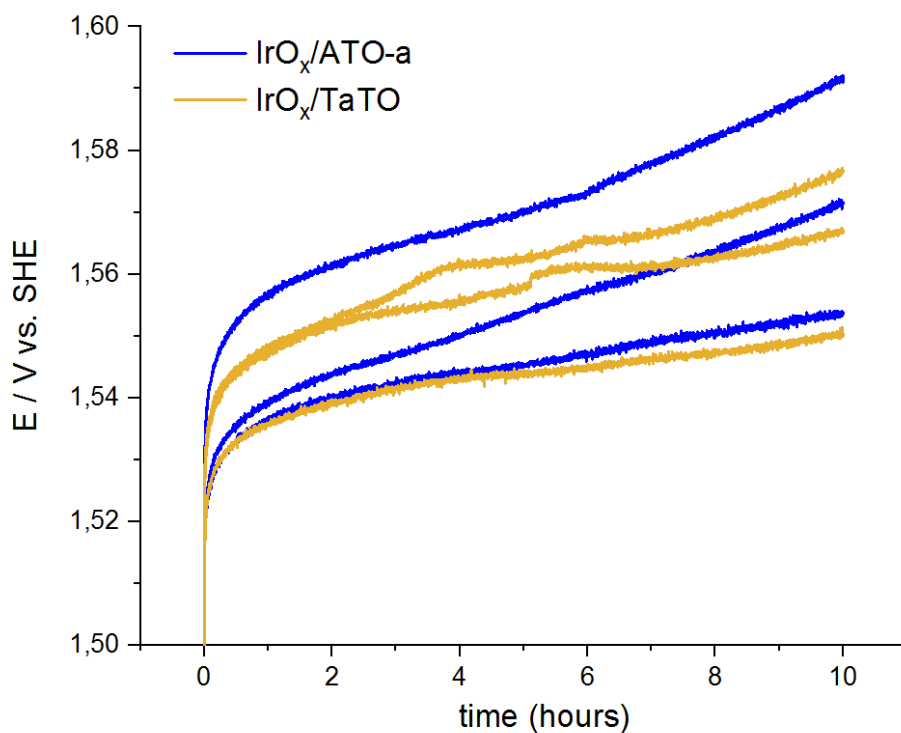
Figure 4.16 Registered 10-hours chronopotentiometry at 1 mA·cm^{-2} for different IrO$_x$/ATO-a (blue) and IrO$_x$/TaTO (orange) electrodes.

As done in **section III** for the ATO supports comparison, aliquots of the electrolyte were sampled during the chronopotentiometry step for ICP-MS analysis in order to follow possible leaching of Ir, Sn or Ta. Since the Ta concentration in TaTO (2 at. %) is much lower than that of Sb in ATO aerogels (10 at. %), its repartition through the material and, therefore, its possible segregation and leaching would differ. This may impact the IrO$_x$ NPs detachment during the experiment and, as a result the durability of the catalysts. ICP-MS results are gathered in **Table 4.16 and Figure 4.17**.

Table 4.16. ICP-MS results for analysed aliquots sampled during the electrochemical tests for each catalyst.

Sample	Element	Aliquot nº1	Aliquot nº2	Aliquot nº3
IrO$_x$/ATO-a	Ir	2.4 ± 0.4	3.8 ± 0.2	5.5 ± 0.1
IrO$_x$/TaTO	Ir	1.7 ± 0.7	2.4 ± 0.2	3.2 ± 0.2
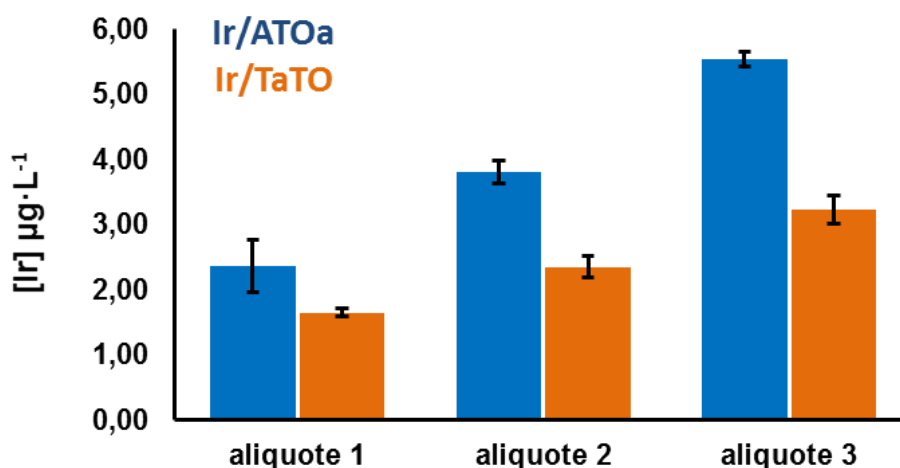
Figure 4.17 Ir concentration measured in the electrolyte solution during stability tests. Each aliquot sampled at t=0, 6 and 10 h for each catalyst, IrO_x/ATO-a (blue) and IrO_x/TaTO (orange).

ICP-MS results (**Figure 4.17**), showed a lower Ir dissolution with time for IrO_x/TaTO than for IrO_x/ATO. As mentioned above, we attributed the lower mass-activity of the IrO_x/TaTO to a lower catalyst loading on the RDE, meaning that a lower dissolution is expected if there is less Ir amount. Despite that, the Ir dissolution rate is lower for IrO_x/TaTO than for IrO_x/ATO, suggesting a higher stability of Ir NPs over TaTO aerogels.

Note that no Ta nor Sn could be detected in the electrolyte (limit of quantification of 2 and 20 $\mu g \cdot L^{-1}$, respectively). The impossibility of quantifying the Ta and Sn dissolution prevents us to completely conclude concerning the relative stability of TaTO and ATO aerogels.

As seen on **section III** for IrO_x/ATO aerogels, ICP-MS analyses link the OER activity decrease to an Ir dissolution. As the IrO_x NPs distribution over the ATO aerogel was much more homogeneous than over the TaTO-supported ones, where some regions with non-supported NPs were found, a larger Ir dissolution or NPs detachment was expected for the IrO_x/TaTO catalyst than for the IrO_x/ATO one. Contrary to expectations, a lower Ir dissolution was found for the IrO_x NPs deposited over the TaTO aerogels. If part of the Ir detected in the electrolyte comes from unsupported Ir, then IrO_x/TaTO may even be a much more stable catalyst than IrO_x/ATO, confirming here again the results reported by Abbou *et al.*.[14] They attributed such a higher stability to the formation of a protective Ta_2O_5 shell around the TaTO aerogel support, which could prevent Sn dissolution in the acidic electrolyte, thus lowering the risk of IrO_x NPs detachment. On the contrary, ATO aerogels were found to suffer from antimony dissolution, which enhances the Ir loss during the OER. In the case of TaTO, they reported that the Ta concentration is key to achieve such stable core@shell structure. Too low the Ta content, there is a risk of Sn dissolution and subsequent IrO_x NPS detachment before the Ta_2O_5 shell is

214

formed. Too much Ta in SnO_2 and the electronic conductivity of the doped aerogel is too low, with possible electrical insulation of the support.

IV.3 Conclusions

IrO_x NPs deposited over TaTO aerogel present similar physical (diameter size, structure and crystallites size) and chemical (surface composition) properties than NPs deposited over TO or ATO aerogels.

When testing the IrO_x/TaTO as catalysts material for the OER evaluation in RDE configuration, it was found that the loss of activity with time was lower than that observed for IrO_x/ATO. Such improved stability of the IrO_x/TaTO catalyst was observed for both, mass and specific activities. This was confirmed by a lower amount of Ir detected in the electrolyte solution, despite the presence of some unsupported IrO_x NPs in the initial material. Such a better stability of TaTO aerogel support was also confirmed after the work of Abbou *et al*. who worked on our material with a different Ir deposition route.

V   OER electrocatalytic activity and stability, complementary information:

Regarding the stability of OER catalysts, it has been largely assumed in the literature that galvanostatic (chronopotentiometry tests) RDE stability tests provide a reliable data about the stability of the catalysts, where the increase of potential during the test is considered as an evidence of catalyst "deactivation". The observation of a potential jump after several hours of galvanostatic test was attributed to the complete degradation of the catalyst. However, such lifespan results disagree with stability results obtained in real PEM electrolyzers, where the same catalyst can be used much longer under similar operating conditions (current density, pH, temperature, etc.).[15] Many authors attributed that this discrepancy can be a result from: the passivation of the RDE electrode substrate, the physical detachment of the catalyst material or the accumulation of oxygen bubbles at the surface of the catalyst.[16]

El-Sayed *et al.*, provided evidence that such "deactivation" is mainly caused by the accumulation of oxygen bubbles within the catalyst layer and/or near its interface with the electrolyte, thus isolating the catalytic sites. The active catalyst surface area is progressively decreased, and the OER potential gradually increases, ultimately leading to a sudden jump to very high potentials, commonly interpreted as a complete degradation of the catalyst.[17] To provide such results they proposed a set of RDE experiments, where galvanostatic tests were carried out using different Ir/ATO catalysts loadings and applying different current densities. They showed that the degradation rate was dependent on the geometric current density and not on the mass or specific current density. That, under the point of view of the authors, suggests that the influence of evolved O_2 bubbles was smaller at low geometric current densities. They provided more evidence of that when a gradual activity decrease was observed in polarization curves during OER activity. Such decrease was a function of the number of total cycles, and the accumulation of oxygen bubbles during cycling performing. The accumulation of bubbles also depends on the rotation speed of the RDE, as faster rotation favors bubble diffusion from the active sites. After several polarization cycles, they purged the electrolyte solution with argon for 30 minutes, and observed a recovery of the lost activity. Authors concluded that such microbubbles and/or nanobubbles could not be removed by rotation of the electrode only.[17]

In order to check whether our catalyst "deactivation" was due to the accumulation of oxygen bubbles over the Ir catalyst active sites, a set of electrochemical tests were carried out. The impact of the catalyst loading was also quickly studied in a second stage.

V.I Impact of O₂ bubbles

The electrochemical tests mentioned above consist in different activity test measurements (sequences 1 to 3, 5 and 7 to 9 and 11 of **Table 4.17**), separated with N_2 purge or vacuum treatment (0.3 b) in order to check their impact on the activity recovery through better dissolution and diffusion of the O_2 bubbles from the active sites.

Table 4.17. Sequence of electrochemical tests run at 25°C in a 0.05 M sulfuric acid electrolyte solution. Electrode Iridium loading was 20 µg·cm^{-2}.

Seq. Numb.	Experiment
1	OER evaluation test
2	**CP, 2h at 10 mA·cm^{-2}**
3	OER evaluation test
4	**30 min N₂ bubbling.**
5	OER evaluation test
6	**30 min vacuum (0.3 bar).**
7	OER evaluation test
8	**CP, 2h at 10 mA·cm^{-2}**
9	OER evaluation test
10	**30 min N₂ bubbling.**
11	OER evaluation test

Experiments of this section were performed on a new batch of ATO aerogel doped at 6 at. % synthesized in basic conditions (A6SS060-6-b) and characterized by the main set of techniques described on **section III**, **chapter 4**. If the doping ratio was lower than the usual nominal one (10 at. %), this does not impact the conclusion of the study. The Sb segregation percentage ($[Sb]_{surf}$ - $[Sb]_{bulk}$)/ $[Sb]_{bulk}$) confirm the poor segregation under basic sol-gel synthesis.

The main properties of the support are presented on **Table 4.18**:

Table 4.18. Main properties of the aerogel support.

Sample	Crystallites size (nm) - XRD	Particles size (nm) - SEM	Doping ratio (at. %) XPS	Doping ratio (at. %) EDX	Specific surface area ($m^2 \cdot g^{-1}$)	Conductivity ($S \cdot cm^{-1}$)
A6SS060-6-b	5.3	13.0 ± 2.5	6.6	6.4	96.3	0.44

Iridium-based NPs were then deposited by chemical reduction, described on **section I**, as for previous studies. Then, the resulting catalyst IrO_x/A6SS060-6-b was characterized before performing activity and stability tests in RDE configuration.

Table 4.19. Main properties of IrO_x/A6SS060-6-b.

Sample	IrO_x NPs size (nm)	Ir(0) crystallites size (nm) - XRD	Ir wt.% EDX	Ir(0) at. % (XPS) 60.8 eV ($4f_{7/2}$)	Ir(IV) at. % (XPS) 61.6 eV ($4f_{7/2}$)	Ir(III) at. % (XPS) 62.9 eV ($4f_{7/2}$)
IrO_x/A6SS060-6-b	2.0 ± 0.5	2.5	26.7 ± 1.2	40.3 ± 2.9	50.2 ± 2.5	9.6 ± 0.9

IrO_x/A6SS060-6-b presented similar properties than our previous IrO_x/ATO catalysts, with particles and crystallites size respectively around 2.0 nm and 2.5 nm. Chemical composition consists on a 40 at. % of Ir(0) and a oxohyydroxide amorphous phase composed of Ir(III) and Ir(IV), 10 and 50 at. % respectively.

Our results didn't follow those obtained by El-Sayed *et al.*, since no OER activity could be recovered after N_2 bubbling. On the contrary, the OER activity measured on polarization curves, was slightly lower after N_2 bubbling (sequence 5, blue continuous line on **Figure 4.18**) than before (sequence 3, red continuous line). Note that the potential was regularly increasing during the first chronopotentiometry phase (**Figure 4.19**, CP1), accounting for the drop of performance from one sequence to the other on **Figure 4.19**. Such a small decrease may be attributed either to a catalyst degradation, such as Ir dissolution or NPs detachment, or to the accumulation of oxygen bubbles at the surface of the catalyst as claimed by El-Sayed *et al.*, (sequences 1 to 3 of **Table 4.17**). It is not possible to differentiate between both hypotheses here. If O_2 bubbles were accumulating, the nitrogen purge may not be efficient enough in our case to remove them. What about vacuum?

Submitting the electrodes, submerged into electrolyte solution, to a vacuum treatment (P = 0.3 atm) in order to extract hypothesized oxygen bubbles from active sites neither gave better

results. The measured activity (sequence 7, green continuous line), was again lower than the previous sequence (5).

Therefore, no improvement could be obtained neither by nitrogen bubbling nor degassing the electrode under vacuum.
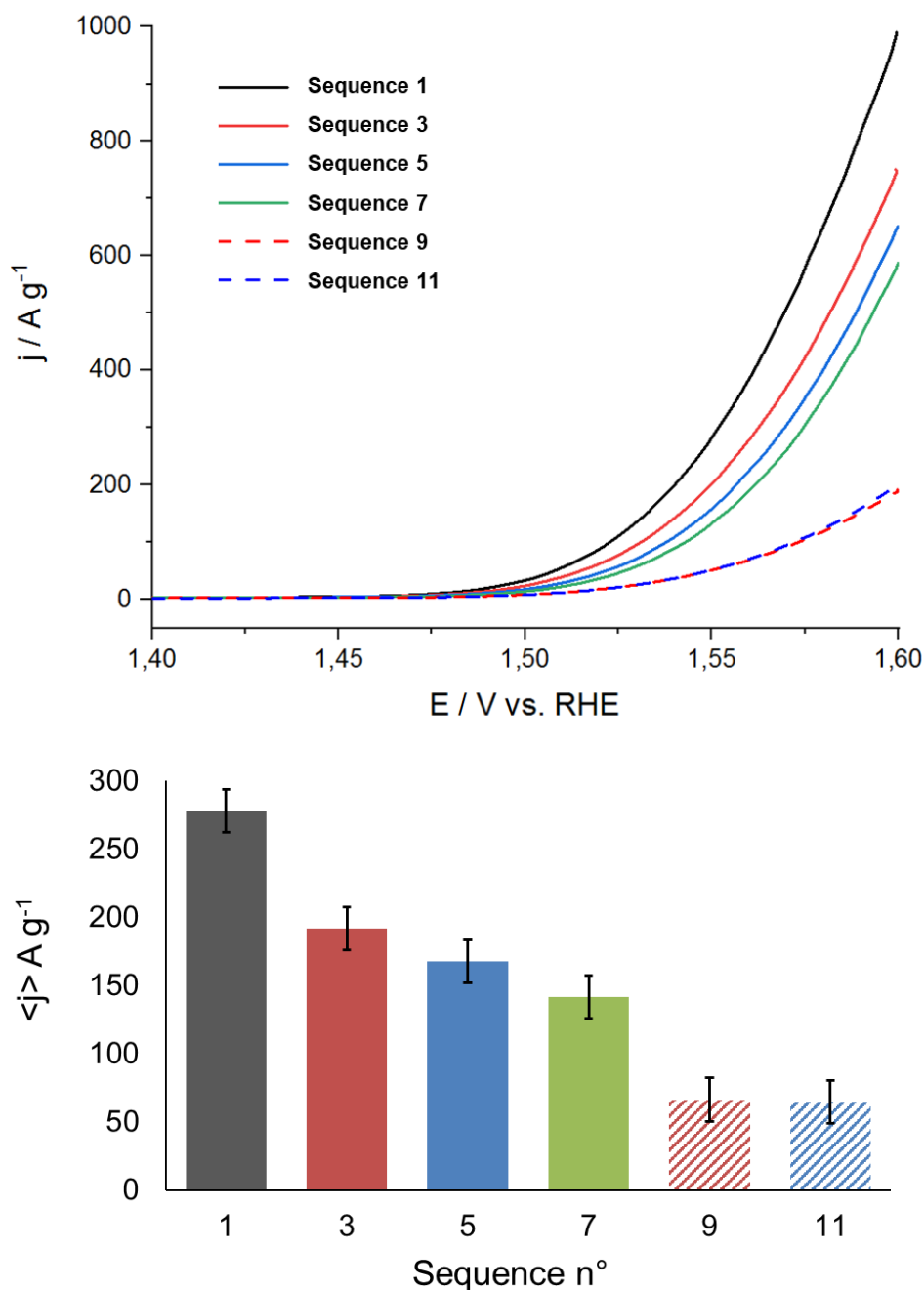
Figure 4.18 Top, polarization curves recorded during sequences 1 (initial OER activity evaluation), 3 (activity after 1st CP), 5 (activity after 1st N_2 bubbling), 7 (activity after vacuum), 9 (activity after 2nd CP) and 11 (activity after a 2nd N_2 bubbling). Bottom, registered mass activities at 1.55 V vs. SHE of each sequence.

IrO_x supported catalyst was quite stable during the first CP test, 2 hours at 10 mA·cm^{-2} (sequence 2 in **Table 4.17 and Figure 4.19**). A relative stability was observed for another 1h or so during the second CP, after which a sudden increase of potential was recorded, sign of end of life. As a result, the activity recorded afterwards was really lower (**Figure 4.18**, sequence 9) and could not be recovered after N_2 purge (**Figure 4.18**, sequence 11).

Based on such results, we found that if O_2 bubbles were accumulating on catalysts active sites, we were not able not remove them following the protocol inspired by El-Sayed *et al.*.[17]

Since the activity loss after the chronopotentiometry tests was so high, we decided to repeat the same procedure with two times the catalyst loading on the RDE electrode. Therefore, the mass-specific current density would be two times lower, and as reported by El-Sayed *et al.*[17] the stability of the catalyst was expected to be higher.
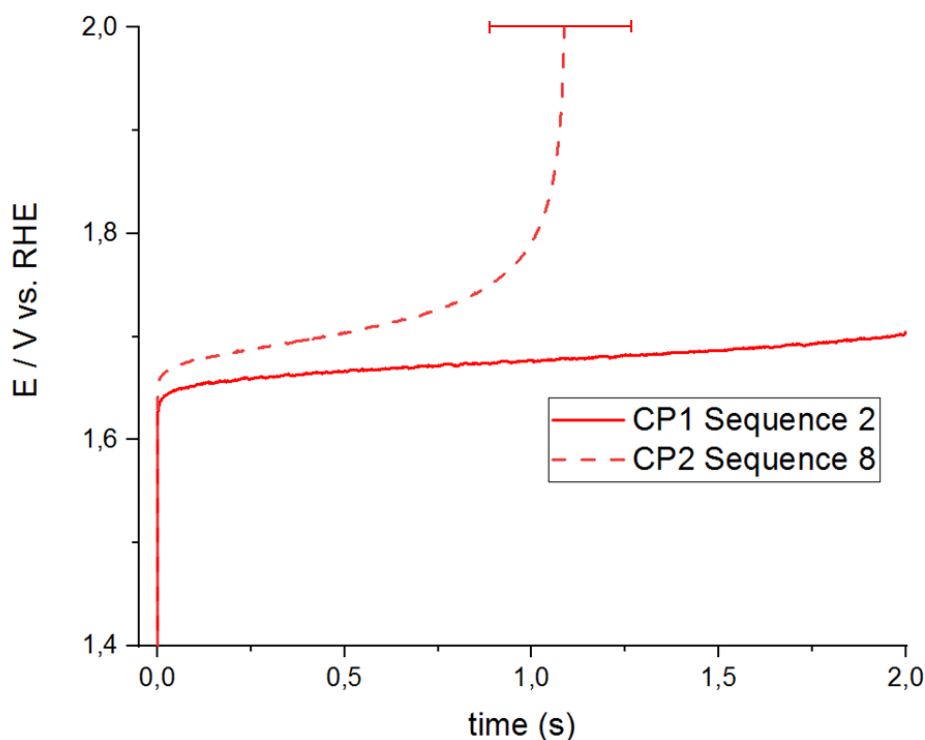
Figure 4.19 Registered chronopotentiometry at 10 mA·cm^{-2}. Continuous line, registered CP of sequence 2, dash line, registered CP of sequence 8.

V.II Impact of anode loading

When repeating same electrochemical tests for an Iridium loading of 40 µg·cm^{-2}, twice the loading used in previous experiments, a decrease of the mass activity was registered, but the lifespan showed a three-fold increase, **Table 4.20**.

Despite the geometric activity of the electrode was higher, the mass activity of the catalyst was lower due to the lower ratio between active Iridium sites and Iridium loaded mass. With a loading of 40 µg·cm^{-2}, it is supposed that a larger amount of IrO$_x$ is initially not active because more or less isolated (white part of the electrodes schematically represented on **Figure 4.20**).

Table 4.20. Mass activity and lifespan at 10 mA·cm^{-2} of IrO$_x$ supported catalyst in a solution of 0.05 M sulfuric acid for an Iridium loading of 20 and 40 µg·cm^{-2}.

Loading	Activity at η = 0,35 V	Lifespan at 10 mA/cm^2
20 µg/cm^2	189.0 ± 21.3 A/g	2.4 ± 0.5 hours
40 µg/cm^2	125 ± 18.1 A/g	7.0 ± 1.1 hours

The increased durability may thus result from a larger reserve of catalyst (white part) which is made progressively accessible through degradation of the initial active part of the catalyst (colored part). It most probably results also from a slower degradation of the catalyst due to a lower operating voltage, consequence of a smaller current density. If O$_2$ bubbles were the main reason for deactivation, then, since the increase of surface is smaller than the increase of volume, we would not expect such an increase of durability. It should be less than twice. It is multiplied by more than 3.

As seen in **Figure 4.21**, for an Iridium loading of 40 µg·cm^{-2} only sequences from 1 to 7 seven were run. Since the lifespan of the electrode was measured to be longer than 7 hours, the effect of a second chronopotentiometry didn't make much sense. In any case, the small loss of measured signal observed from one polarization curve to the other did not show any recovery after N$_2$ bubbling or vacuum treatment. Such results, together with those obtained for an Iridium loading of 20 µg·cm^{-2}, suggests that oxygen bubbles may not be the main cause of our catalysts "deactivation".
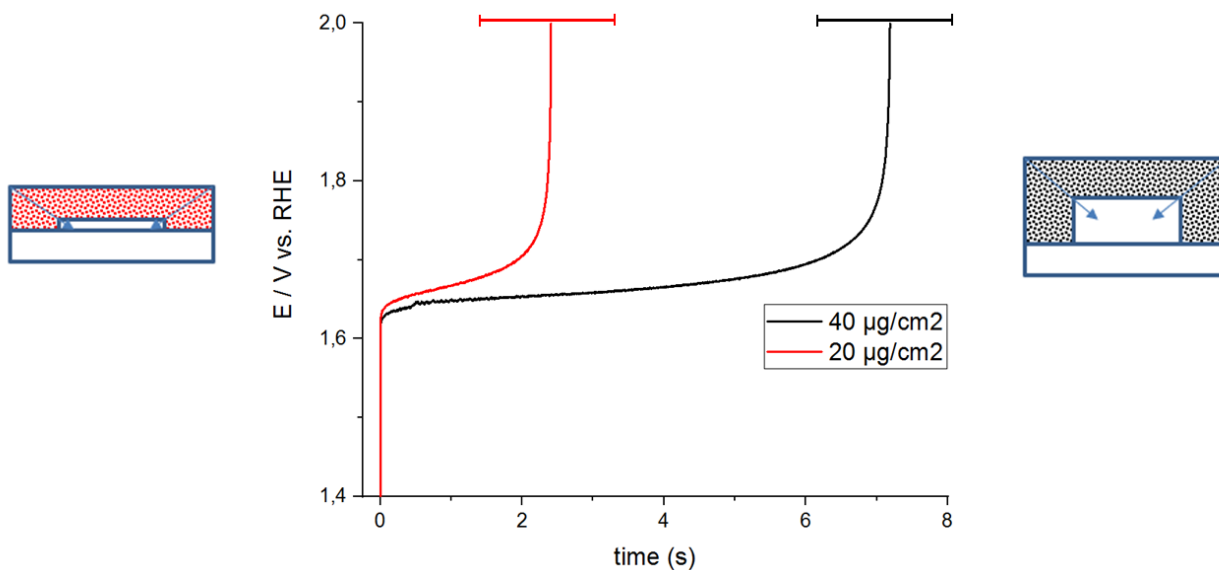
Figure 4.20 Chronopotentiometry curves recorded for different Ir loadings, 20 µg·cm^{-2} (red) and 40 µg·cm^{-2} (black) and schematics of corresponding electrodes (white part supposed inactive).

Following similar experiments of Al-Sayed *et at.*,[17] we concluded that the accumulation of evolved microbubbles between the Ir active sites and the aqueous electrolyte may not be the main cause of our catalyst "deactivation", which can be induced by many other causes (such as glassy carbon electrode passivation, Ir catalyst detachment or degradation, etc.). Our experimental tests didn't show any recovery of the OER activity after bubbling or purging the electrolyte solution with an inert gas, such as nitrogen, for 30 minutes. Such results were obtained for both Iridium electrode loadings, 20 and 40 µg·cm^{-2}.

Passivation of the glassy carbon may be another cause of deactivation. For further investigation one option would be to repeat such electrochemical protocol using a gold RDE.
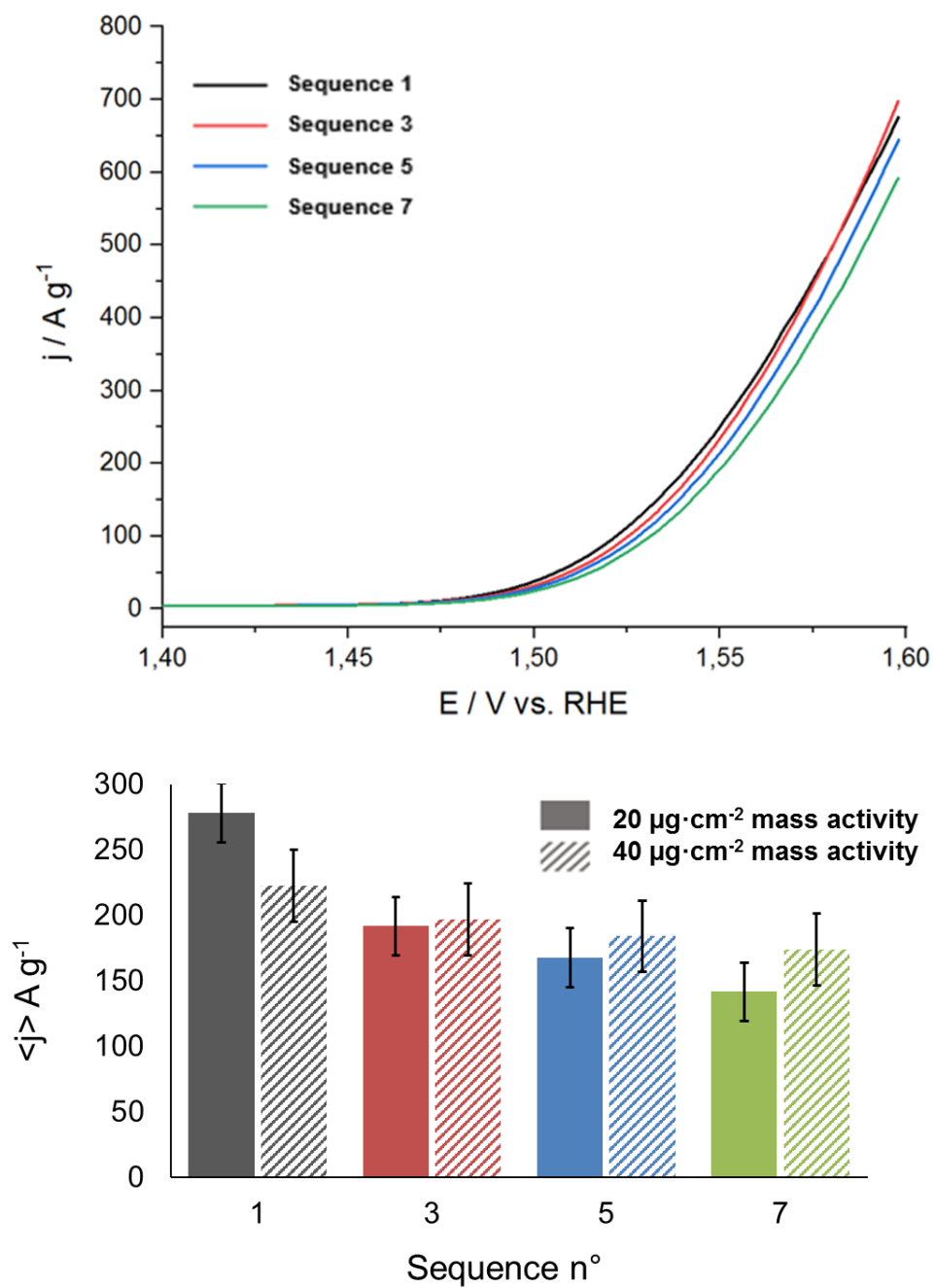
Figure 4.21 Top, polarization curves recorded for 40 µg·cm^{-2} loading during sequences: 1 (initial OER activity), 3 (activity after CP), 5 (activity after N$_2$ bubbling) and 7 (activity after vacuum). Experiments were performed at 25°C in a solution of 0.05 M of sulfuric acid, and a current density of 10 mA·cm^{-2} for the chronopotentiometry (CP) tests. Bottom, registered mass activities at 1.55 V of each sequence for a Ir loading of 20 µg·cm^{-2} (filled bars) and 40 µg·cm^{-2} (triggered bars).

V.IV Conclusions

In order to detect if the "deactivation" observed under operating OER conditions was not only caused by the catalyst degradation, as supposed previously, experiment protocols inspired by El-Sayed *et at.*, were followed to "detect" possible O_2 bubbles accumulation near the surface active sites of the catalyst. By a set of mixed experiments, we found that the "deactivation" of our catalysts may not be caused by O_2 micro-bubbles, as the activity after submitting the working electrode to a continuous flow of nitrogen bubbling or low vacuum, was never recovered.

When the loading of the electrode was doubled in order to decrease twice the mass current density (same controlled current), the lifespan of the catalyst was increased while its mass activity was decreased. Then, the loss of activity was much more limited, but never recovered after N_2 bubbling or vacuum.

VI General Conclusions and perspectives

On this chapter Iridium oxide nanoparticles, IrO_x NPs, were deposited over tin dioxide-based aerogels by chemical reduction of an Iridium precursor salt, $IrCl_3$.

Physical properties of the IrO_x nanocatalysts were similar independently of the used support: particle sizes around 2.5 nm with similar crystallites size for Ir(0) crystalline structures. Differences appear on the near-surface chemical composition, where the ratio $Ir(0)/IrO_2$ was found to be 0.8 for supported NPs and 1.25 for non-supported ones. Comparing XPS results with the crystal structure found by XRD analyses, we imagine the IrO_x NPs as a metallic Ir(0) crystalline core covered with an amorphous layer of IrO_2.

It was found that supporting the IrO_x NPs on the SnO_2 based aerogels enhanced the OER activity and its stability. Concerning the measured activity for the prepared catalysts with different support material, the OER mass and specific activities were found to be similar in RDE configuration, in spite of different electronic conductivities measured for pure TO, ATO and TaTO aerogels.

By ICP-MS analyses of the electrolyte solution during OER evaluation in RDE configuration, it was found that the "deactivation" of our catalysts, or activity loss, was caused by Ir dissolution. It has been noted that the Ir dissolution was similar for IrO_x/ATO-b than for IrO_x/ATO-a, meaning that the stability of IrO_x was not specifically higher supported on ATO-b. Further investigations concerning Sb and Sn dissolution during OER operation should be performed in future in order to determine whether ATO-b is more stable than ATO-a in such conditions. Similar results were obtained for IrO_x/TaTO and IrO_x/ATO. The analyses of Ta and Sn in the electrolyte solution should allow to determine if the higher stability is caused by a higher aerogel stability.

By a set of mixed experiments, the possible effect of oxygen bubbles accumulation, near the active sites of the IrO_x NPs, on the "deactivation" was investigated for our catalysts. Such micro bubbles were tried to be removed by a continuous inert gas flow (nitrogen) on the electrolyte solution and by summiting the RDE electrode at low vacuum conditions. The OER activity was never recovered because this procedures, meaning that microbubbles do not contribute to the catalysts deactivation. Catalyst deactivation was attributed to Ir dissolution, as seen by ICP-MS analyses.

Lowering the total mass current density, by using higher Ir loading amounts, increased the stabilization among time of the IrO_x/XTO catalysts.

VII Résumé

Dans ce chapitre, des nanoparticules (NPs) d'oxyde d'iridium, ont été déposées sur des aérogels à base de dioxyde d'étain par réduction chimique d'une sel précurseur d'iridium, $IrCl_3$.

Les propriétés physiques des nanocatalyseurs IrO_x étaient similaires indépendamment du support utilisé : des tailles de particules d'environ 2,5 nm avec des tailles de cristaux similaires de structures cristallines Ir(0). Des différences apparaissent sur la composition chimique près de la surface, où le rapport $Ir(0)/IrO_2$ était de 0,8 pour les NP supportées et de 1,25 pour celles non supportées. En comparant les résultats XPS avec la structure cristalline trouvée par les analyses XRD, nous imaginons les NPs IrO_x comme un noyau cristallin métallique Ir(0) avec une phase amorphe d'IrO_2 sur la surface. L'oxydation superficielle plus importante des NPs supportées a donc été attribuée à la présence de l'oxyde métallique, du dioxyde d'étain, du support des catalyseurs.

Il a été constaté que le support des NP IrO_x sur les aérogels à base de SnO_2 améliorait l'activité par rapport à l'OER et sa stabilité dans le temps. En ce qui concerne l'activité mesurée pour les catalyseurs préparés avec différents matériaux de support, la masse OER et l'activité spécifique se sont avérées similaires, malgré la conductivité électronique différente entre les aérogels TO, ATO et TaTO purs, pour une configuration RDE.

Par des analyses ICP-MS de la solution électrolytique lors de l'évaluation de l'OER par configuration RDE, il a été constaté que la « désactivation » de nos catalyseurs, ou perte d'activité, était causée par la dissolution de l'Ir. Il a été noté que la dissolution de l'Ir était similaire pour IrO_x/ATO-b que pour IrO_x/ATO-a, ce qui signifie qu'il n'y a pas de stabilité plus élevée d'IrOx par rapport à ATO-b. D'autres études concernant la dissolution de Sb et Sn pendant le fonctionnement de l'OER devraient être effectuées à l'avenir afin de déterminer la stabilité plus élevée de l'ATO-b en tant que catalyseur de support pour l'OER que l'ATO-a. Des résultats similaires ont été obtenus pour le catalyseur IrO_x/TaTO par rapport à IrO_x/ATO. Des analyses Ta et Sn de la solution d'électrolyte doivent être effectuées afin de déterminer si la stabilité mesurée plus élevée à travers l'OER est causée par une stabilité plus élevée de l'aérogel.

Par une série d'expériences mixtes, il a été étudié l'effet possible de l'accumulation de bulles d'oxygène à proximité des sites actifs des NP d'IrO_x, qui collaboreraient à la « désactivation » de nos catalyseurs. On a essayé d'éliminer ces microbulles par un flux continu de gaz inerte (azote) sur la solution d'électrolyte et en sommant l'électrode RDE dans des conditions de vide faible. L'activité OER n'a jamais été récupérée à cause de ces procédures, ce qui signifie que si des bulles utilisent "désactiver" notre catalyseur, la majeure partie devrait être causée par des procédures de dégradation telles que la dissolution de l'Ir.

VIII References

[1] L. Sola-Hernandez, F. Claudel, F. Maillard, Christian Beauger, *International Journal of Hydrogen Energy*, **2019**, *44*, 24331-24341

[2] (a) L. Wang, P. Lettenmeier, U. Golla-Schindler, P. Gazdzicki, N. A. Cañas, T. Morawietz, R. Hiesgen, S. S. Hosseiny, A. S. Gago and K. A. Friedrich, *Phys. Chem. Chem. Phys.*, **2016**, *18*, 4487-4495; (b) L. Wang, F. Song, G. Ozouf, D. Geiger, T. Morawietz, M. Handl, P. Gazdzicki, C. Beauger, U. Kaiser, R. Hiesgen, A. S. Gago, K. A. Friedrich, *J. Mater. Chem. A*, **2017**, *5*, 3172

[3] (a) C. De Pauli, S. Trasatti, *J. Electroanal. Chem.*, **1995**, *396*, 161– 168 : (b) C. De Pauli, S. Trasatti, *J. Electroanal. Chem.*, **2002**, *538 – 539*, 145 – 151 ; (c) E. Balko, P. Nguyen, *J. Appl. Electrochem.*, **1991**, *21*, 678– 682 ; (d) J. Tong, Y. Liu, Q. Peng, W. Hu, Q. Wu, *J. Mater. Sci.*, **2017**, *52*, 13427–13443 ; (e) C. Massué, V. Pfeifer, X. Huang, J. Noack, A. Tarasov, S. Cap, R. Schlögl, *ChemSusChem*, **2017**, *10*, 1943–1957 ; (f) D. Böhm, M. Beetz, M. Schuster, K. Peters, A. G. Hufnagel, M. Döblinger, B. Böller, T. Bein, D. Fattakhova-Rohlfing, *Adv. Funct. Mater.*, **2019**, *19*, 6670

[4] W. Baur, Acta *Crystallographica*, **1956**, *9*, 515-20.

[5] A. Bolzan, C. Fong, B. Kennedy, C. Howard, *Acta Crystallographica*, **1997**, *B53*, 373-380

[6] R. Wyckoff, Crystal Structures, Vol. 1. (Ed. Interscience Publishers), New York **1963**.

[7] S. Freakley, J. Ruix-Esquius, D. Morgan, *Surf. Interface Anal.*, **2017**, *49*, 794-99.

[8] T. Reier, Z. Pawolek, S. Cherevko, M. Bruns, T. Jones, D. Teschner, S. Selve, A. Bergmann, H. Nong, H. Schlögl, J. Mayrhofer, P. Strasser, *J. Am. Chem. Soc.*, **2015**, *137*, 13031-40; (b) H.-S. Oh, H. N. Nong, D. Teschner, T. Reier, A. Bergmann, M. Gliech, J. Ferreira de Araújo, E. Willinger, R. Schloegl, P. Strasser, *J. Am. Chem. Soc.*, **2016**, *138*, 12552-12563.

[9] S. Ardizzone, G. Fregonara, S. Trasatti, *Electrochim. Acta*, **1990**, *35*, 263-67.

[10] (a) R. Kötz, H. Neff, S. Stucki, *J. Electrochem. Soc.*, **1984**, *131 (1)*, 72-77; (b) S. Gottesfeld, S, Srinivasan, *J. Electroanal. Chem. Interfacial Electrochem.,* **1978**, *86 (1)*, 89-104.

[11] (a) A. Minguzzi, O. Lugaresi, E. Achilli, C. Locatelli, A. Vertova, P. Ghigna, S. Rondinini, *Chem. Sci.*, **2014**, *5 (9)*, 3591-3597; (b) H. Sanchez-Casalongue, M. Ng, S. Kaya, D. Friebel, H. Ogasawara, A. Nilsson, *Angew. Chem.*, **2014**, *53 (28)*, 7169-72. (c) A. Minguzzi, C. Locatelli, O. Lugaresi, E. Achilli, G. Cappelletti, M. Scavini, M. Coduri, P. Masala, B. Sacchi, A. Vertova, P. Ghigna, S. Rondinini, *ACS Catal.*, **2015**, *5 (9)*, 5104-5115; (d) O. Kasian, J. Grote, S. Geiger, S. Cherevko, K. Mayrhofer, *Angew. Chem.*, Int. Ed. Engl., **2018**, *57 (9)*, 2488-2491.

[12] F. Claudel, L. Dubau, G. Berthomé, L. Sola-Hernandez, C. Beauger, L. Piccolo, F. Maillard, *ACS Catal.*, **2019**, *9(5)*, 4688-98.

[13] (a) G. da Silva, S. Venturini, S. Zhang, M. Löffler, C. Scheu, K. J. J. Mayrhofer, E. Ticianelli, S. Cherevko, *ChemElectroChem*, **2020**, *7*, 2330 ; (b) V. Saveleva, L. Wang, O. Kasian, M. Batuk, J. Hadermann, J.-J. Gallet, F. Bournel, N. Alonso-Vante, A. Gago, G. Ozouf, C. Beauger, K. J. J.

Mayrhofer, S. Cherevko, A. S. K. A. Friedrich, S. Zafeiratos, E. R. Savinova, *ACS Catal.*, **2020**, *10*, 2508−2516.

[14] S. Abbou, R. Chattot, V. Martin, F. Claudel, L. Solà-Hernández, C. Beauger, L. Dubau, F. Maillard, *ÀCS Catalysis*, **2020**, *10 (13)*, 7283–7294

[15] S. Geiger, O. Kasian, A. M. Mingers, S. S. Nicley, K. Haenen, K. J. J. Mayrhofer, S. Cherevko, *ChemSusChem*, **2017**, *41*, 15.

[16] (a) A. S. Aricò, S. Siracusano, N. Briguglio, V. Baglio, A. Di Blasi, V. Antonucci, *J Appl Electrochem*, **2013**, *43(2)*, 107; (b) C. Rakousky, U. Reimer, K. Wippermann, M. Carmo, W. Lueke, and D. Stolten, *Journal of Power Sources*, **2016**, *326*, 120; (c) K. E. Ayers, E. B. Anderson, K. Dreier, and K. W. Harrison, *ECS Transactions*, **2013**, *50(49)*, 35; (d) S. M. Alia, B. Rasimick, C. Ngo, K. C. Neyerlin, S. S. Kocha, S. Pylypenko, H. Xu, B. S. Pivovar, *J. Electrochem. Soc.*, **2016**, *163(11)*, F3105.

[17] H. El-Sayed, A. Weiß, L. Olbrich, G. Pratomo, H. Gasteiger, *Journal of The Electrochemical Society*, **2019**, *166(8)*, F458-F464.

GENERAL CONCLUSIONS AND PERSPECTIVES

For proton exchange membrane water electrolysis cells (PEMWE) to be economically viable two major improvements must be made in membrane-electrode assemblies (MEAs): reduce the amount of noble metal catalysts and increase their durability.

To achieve this, in this thesis we have deployed the strategy of supporting Iridium-based NPs over a metal oxide support stable under the operation conditions of PEMWE cells. Due to the promising results obtained on PEMFC, the choice fell on tin dioxide-based aerogels.

The work of this thesis goes from the synthesis of the catalyst support (Chapter 3) to the deposition of Ir-based NPs and their characterization in terms of performance and durability in RDE configuration (Chapter 4).

The catalyst support must allow an optimal distribution of the iridium nanoparticles, between 2 and 3 nm in diameter, as well as a good transport of fluids (gas and water). Then, this support material has to present a large specific surface area with a mesoporous pore size distribution. Additionally, electrons produced on the anode side by the OER, must be able to be delivered to the cathode side for the HER. Therefore, the catalyst support must be electronically conductive.

To obtain a suitable morphology and an appropriate electronic conductivity, doped tin dioxide aerogels with hypervalent cations (Ta^{5+} and Sb^{5+}) have been prepared in this work.

Aerogels have been prepared by following a sol-gel method previously developed by our group, and modification on the synthesis parameters have been applied in order to optimize the intrinsic properties of the material. The nature and concentration of the sol-gel catalyst, the dopant concentration (at. %) and the calcination time (under air at 600 °C), were the modified parameters.

The use of NaOH instead of HNO_3 as sol-gel catalysts for the aerogel synthesis, allowed to increase the specific surface area of the antimony-doped tin dioxide aerogels (ATO), up to 90 $m^2 \cdot g^{-1}$. A more homogeneous Sb distribution was also observed throughout the material, limiting the Sb segregation observed for the acid synthesis. Such better Sb repartition is expected to result in lower dopant dissolution, and therefore better support stability, for the OER.

Concerning Tantalum-doped tin dioxide aerogels (TaTO), they showed a much lower electronic conductivity than ATO (4 orders of magnitude lower). It was found that the conductivity value, together with the specific surface area, depends on the Ta concentration.

The optimal compromise between both propertied was found for a doping concentration of 2 at. % (40 m²·g^{-1} and 4.6 mS·cm^{-1}).

Iridium nanoparticles (Ir NPs) where then deposited *in situ* over the selected tin dioxide-based aerogels by the chemical reduction of an Ir salt precursor (IrCl$_3$). Ir-based NPs where homogeneously deposited on the TO aerogels with a noble metal loading of 30%, and a particle size around 2 nm.

Ir NPs present a core-shell structure, with a crystalline core of metallic Ir and an amorphous oxide layer made of Ir(III) and Ir(IV), IrO$_x$.

The performances of the catalysts were assessed on rotating disk electrode (RDE), and compared to those of non-supported NPs, which were prepared by the same protocol by without any tin dioxide support.

Developed catalysts reached similar mass activity values (175 A·g^{-1}$_{Ir}$ at 1.53 V *vs* RHE) than those reported in the literature for different tin dioxide morphologies, preparation methods and Ir catalysts deposition. The supported IrO$_x$ NPs presented much higher mass activities (x5) and stabilities (x16) than the non-supported NPs. It was also found that the IrO$_x$ NPs supported over different catalysts supports (TO, ATO and TaTO), featured, for thin film RDE configuration, similar mass activity and stabilities despite their very different electronic conductivity (0.05, 80 and 4.6 mS, respectively).

Observed deactivation with time of the catalyst under OER working conditions was attributed to an Ir detachment from the electrode, or dissolution, measured by ICP-MS. Possible catalyst deactivation by oxygen micro-bubbles accumulation near the active sites of the IrO$_x$ NPs, as proposed by bibliography, was investigated. It was rather attributed to the anode electrode materials degradation.

In addition, although we have successfully synthesized a very promising material, it is always interesting to think about ways of improving and optimizing its intrinsic properties, as well as a better dopant distribution among the SnO$_2$ matrix. Different solutions can be considered.

On the one hand, a solution could be to chemically modify one or more functional groups of the metal alkoxide precursors which will directly modify the kinetics of hydrolysis and condensation reactions during the initial sol-gel stages as well as the resulting morphology of the aerogels. Another possible solution could be the preparation of mixed doped tin dioxide aerogels, with Ta and Sb. Therefore, the enhanced conductivity by Sb atoms could improve the electron flow of the more resistant Ta-doped aerogels. An optimal compromise between both doping ratios and the desired properties of the material should be found.

On the other hand, different deposition methods of the noble metal catalyst (Ir or Ru) can be considered to be used over our aerogel materials. It is well known that despite the support

properties and morphology is of great importance, the nature of the deposited catalyst, as well as it's morphology, structure or chemical composition is key for an optimal design of an electrocatalyst. A deposition of IrO_x NPs, prepared by the polyol method, have been already realized over our materials by the group of Frédéric Maillard in LEPMI (Grenoble). Many other deposition methods can be proposed (such as: hydrothermal, solvothermal, organometallic approach, organometallic chemical deposition, Adams' fusion, microwave-assisted, colloidal method, etc.). Another interesting strategy could be the direct preparation of Ir-based aerogels or Ir-doped metal oxide aerogels. By this way, deposition of the catalyst would not be necessary, while maintaining the advantages of the aerogel morphology for catalysis.

Finally, it would be very interesting to develop MEAs with electrocatalysts synthesized on this work in order to compare their performance with those of commercial MEAs, or other from bibliography. This achievement is currently underway.

ANNEXES

Supporting information

A.1 Adsorption isotherms (chapter 3, section III.1)
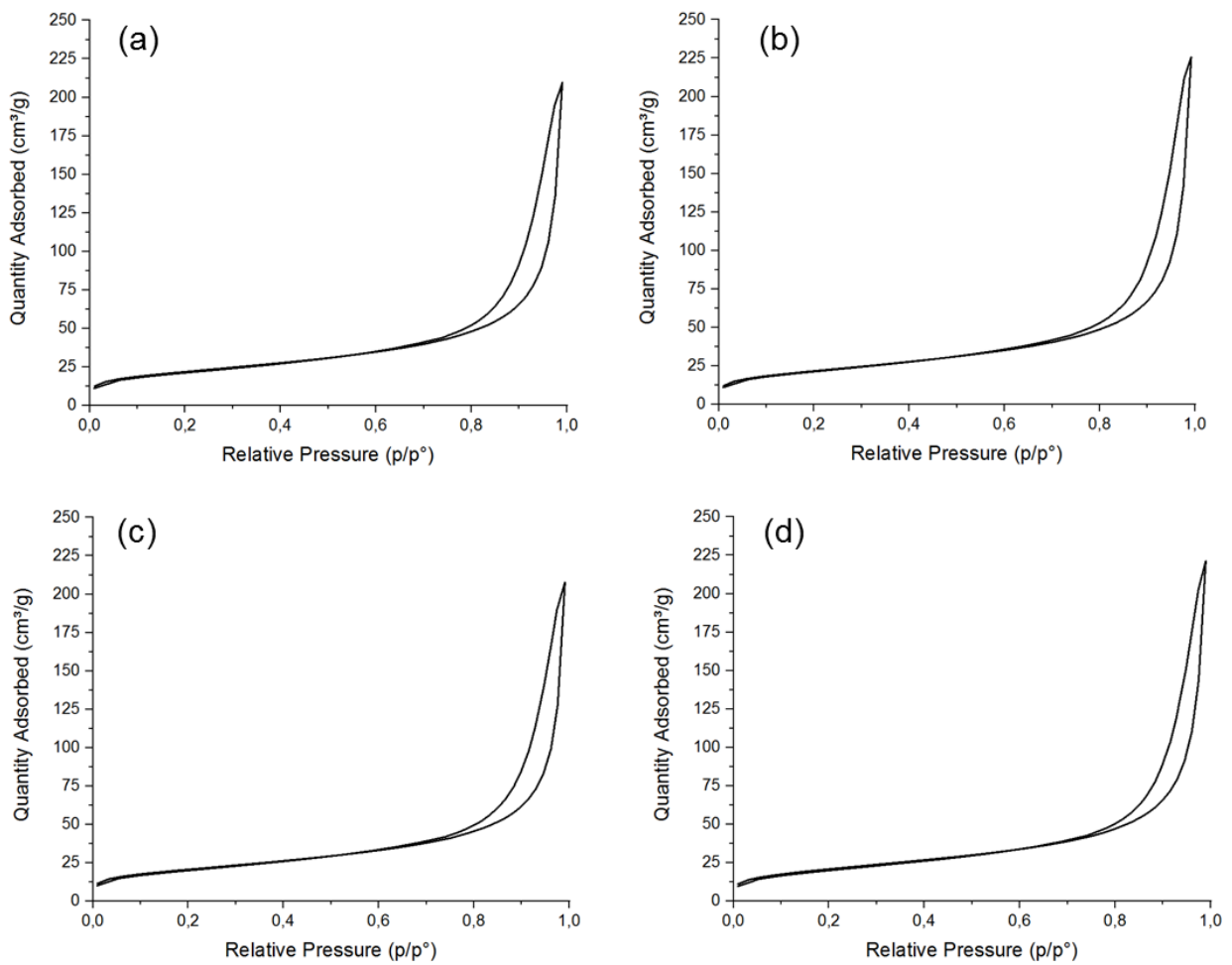
Figure A.1 Adsorption isotherms of ATO aerogels calcined at 600°C under air conditions at different times: (a) 1 hour, (b) 3hours, (c) 5 hours and (d) 8 hours.

Figure A.2 Pore size distribution of ATO aerogels calcined at 600°C under air conditions at different times: (blue) 1 hour, (yellow) 3hours, (purple) 5 hours and (red) 8 hours.

A.3 Adsorption isotherms (chapter 3, section III.2)
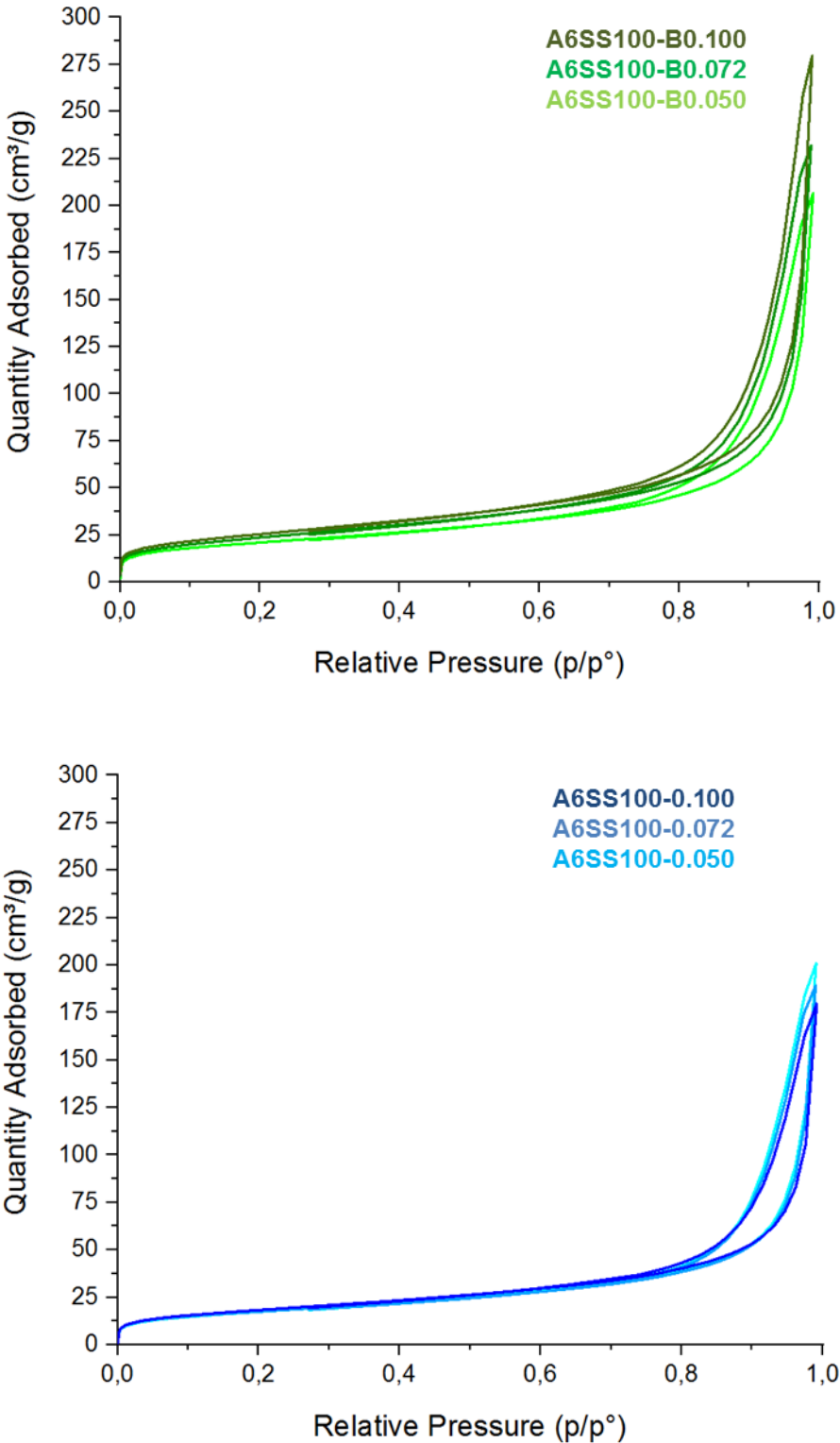
Figure A.3 Adsorption isotherms of ATO aerogels prepared with different sol-gel catalysts (NaOH, top figure, and HNO$_3$, bottom figure) and ratios.

Figure A.4 Pore size distribution of ATO aerogels prepared with different sol-gel catalysts (NaOH, top figure, and HNO$_3$, bottom figure) and ratios.

A.5 Adsorption isotherms (chapter 3, section IV.1)
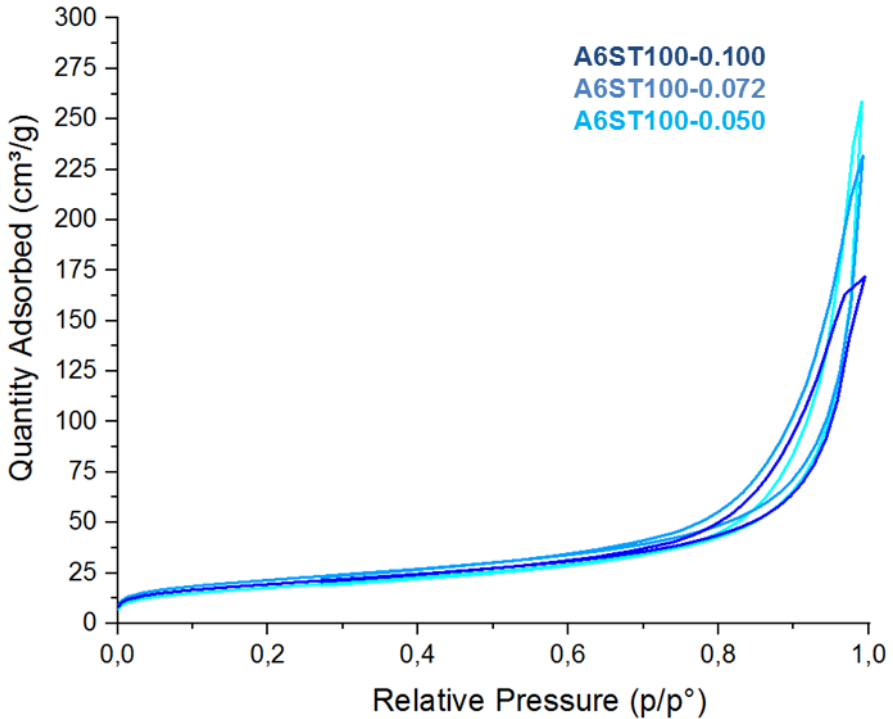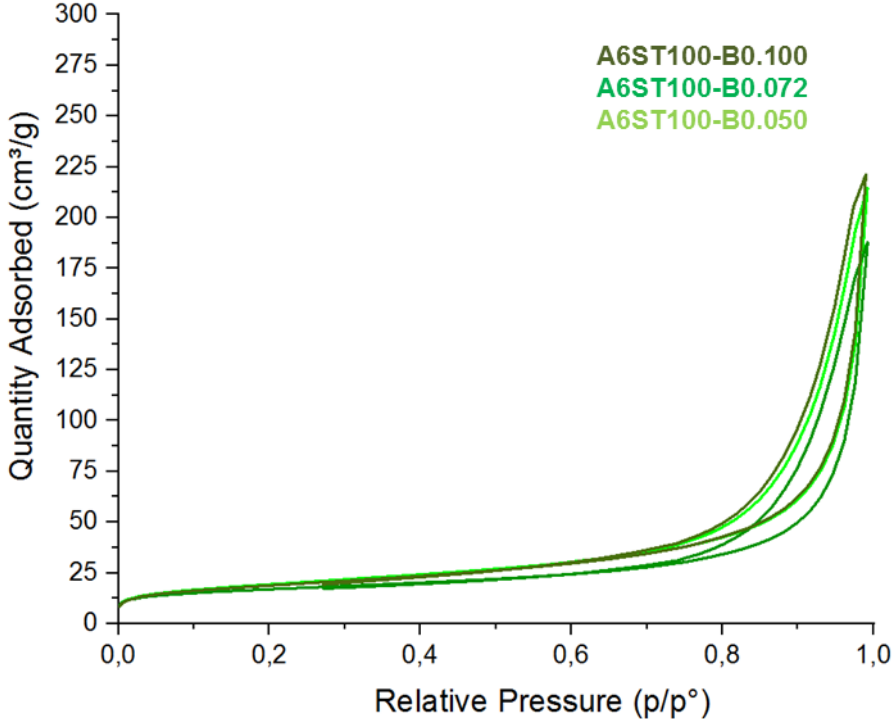
Figure A.5 Adsorption isotherms of TaTO aerogels prepared with different sol-gel catalysts (NaOH, top figure, and HNO₃, bottom figure) and ratios.

A.6 Pore size distribution (chapter 3, section IV.1)
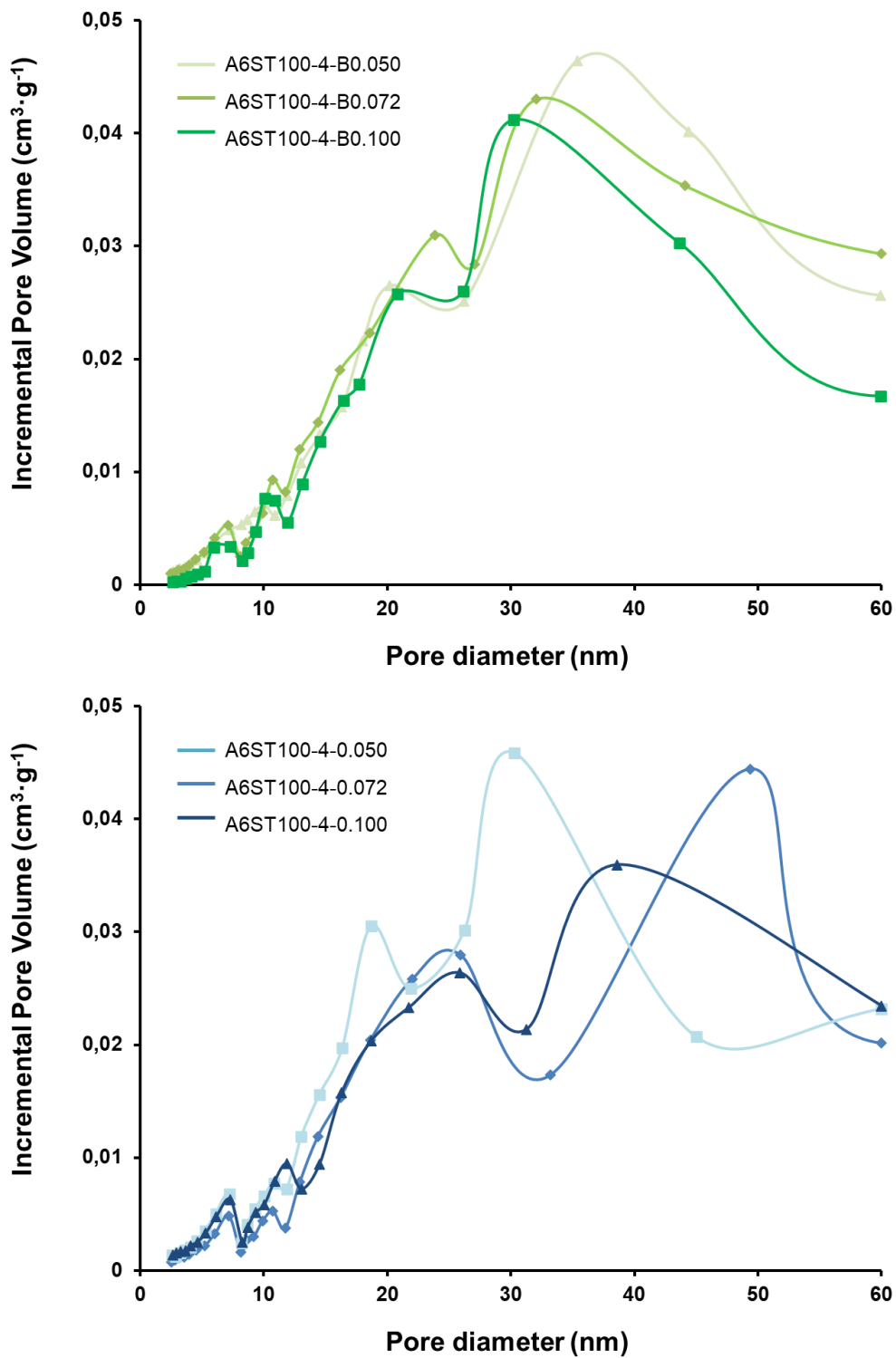
Figure A.6 Adsorption isotherms of TaTO aerogels prepared with different sol-gel catalysts (NaOH, top figure, and HNO$_3$, bottom figure) and ratios.

A.7 Adsorption isotherms (chapter 3, section IV.2)
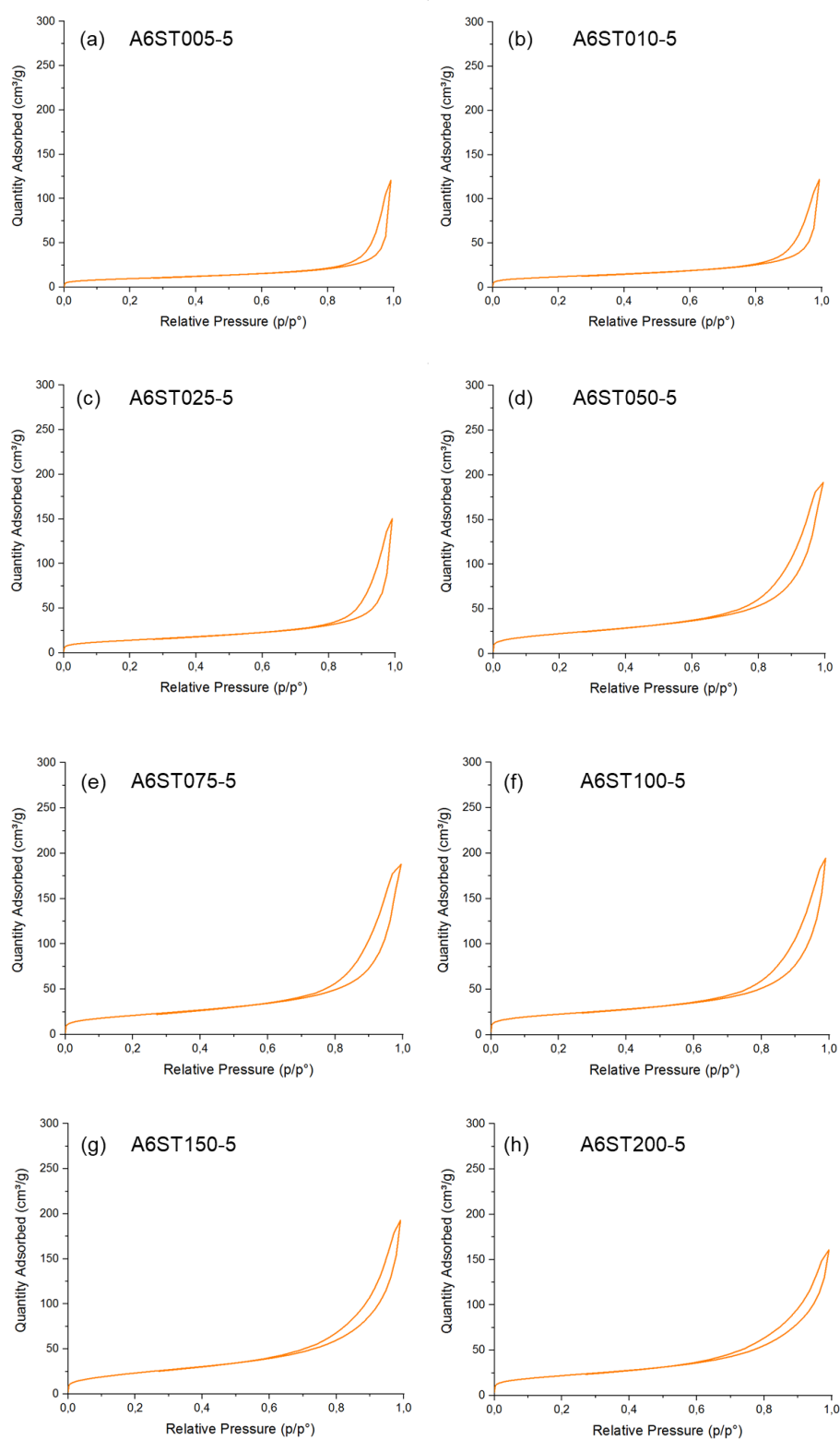
Figure A.7 Adsorption isotherms of TaTO aerogels prepared with different Ta at. % ratios.

A.8 Pore size distribution (chapter 3, section IV.2)
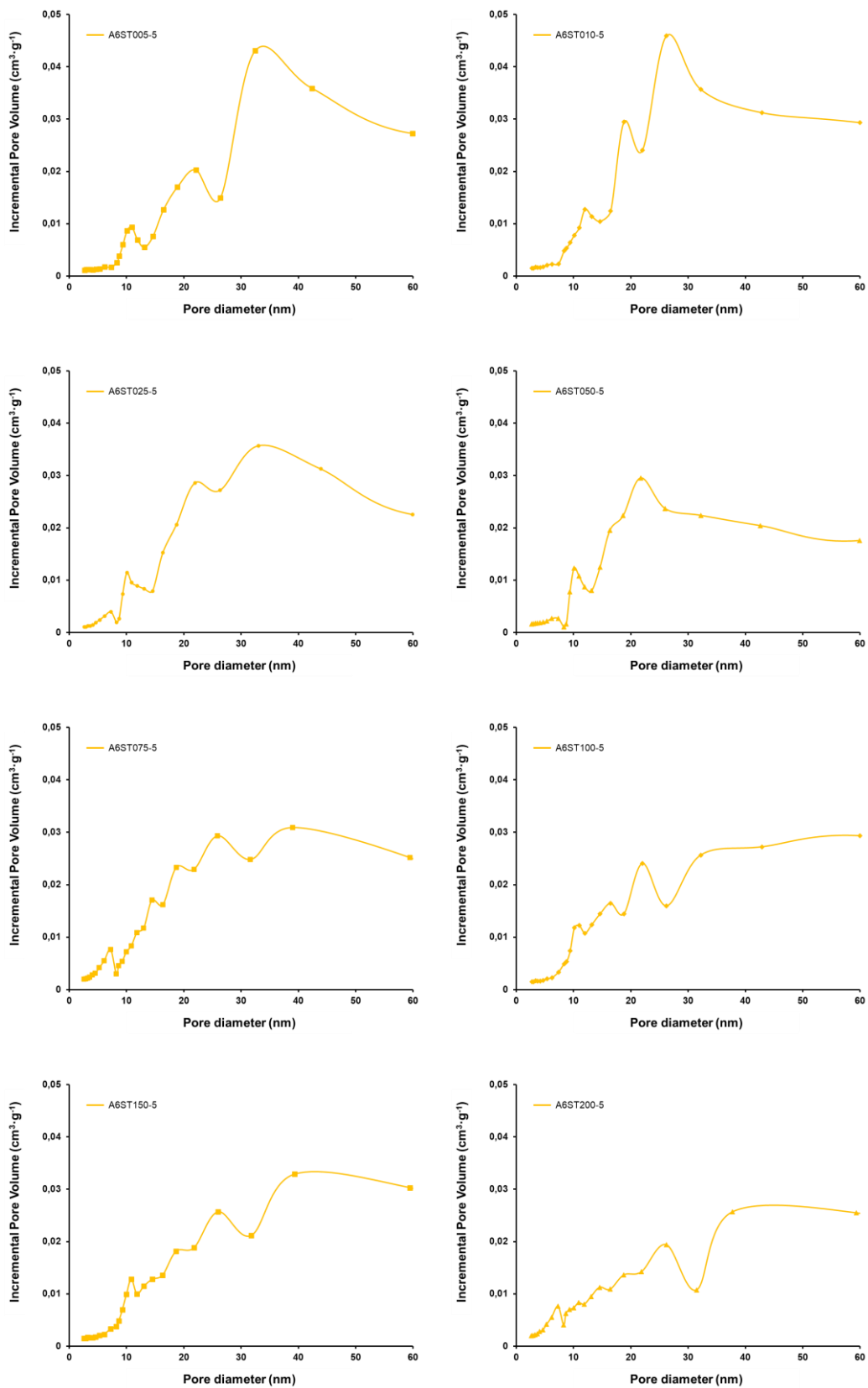
Figure A.8 Pores size distribution of TaTO aerogels prepared with different Ta at. % ratios.

Index of figures

RÉSUMÉ

Les aérogels de dioxyde d'étain dopés à l'antimoine (aérogels ATO) ont montré des résultats prometteurs en tant que supports de catalyseurs résistants à la corrosion pour les piles à combustible à membrane échangeuse de protons (PEMFC). Imitant cette stratégie pour réduire la charge d'iridium dans les cellules d'électrolyse de l'eau à membrane échangeuse de protons (PEM-WE), des nanoparticules d'Ir (NPs) ont été déposées sur des aérogels à base de dioxyde d'étain synthétisés comme supports de catalyseurs. La morphologie mésoporeuse et la surface spécifique élevée des aérogels sont en effet particulièrement bien adaptées à une dispersion optimale des nanoparticules de catalyseur. La voie de synthèse des aérogels à base de SnO_2 a ainsi été étudiée plus avant afin d'améliorer les propriétés attendues. En plus de l'antimoine, le tantale a également été évalué comme autre agent dopant pour augmenter la conductivité électronique du dioxyde d'étain (TO) et la stabilité du catalyseur.

Les paramètres de la méthode sol-gel utilisée comme voie de synthèse des aérogels ont été modifiés de manière à optimiser le catalyseur sol-gel, le temps de calcination ou la concentration en dopant.

L'utilisation de l'hydroxyde de sodium (NaOH) au lieu de l'acide nitrique (HNO_3) comme catalyseur sol-gel a permis d'augmenter la surface spécifique (jusqu'à 90 m²·g^{-1}) des aérogels de dioxyde d'étain dopés à l'antimoine (ATO). Un impact bénéfique a également été observé sur la limitation de la ségrégation du dopant. Une meilleure répartition dans le matériau devrait entraîner une dissolution plus faible et une meilleure stabilité pendant le dégagement d'oxygène (OER).

Les aérogels de dioxyde d'étain dopés au tantale (TaTO) ont montré une conductivité électronique beaucoup plus faible que l'ATO. La valeur dépend de la concentration en Ta, tout comme la surface spécifique. Le meilleur compromis pour les deux propriétés a été obtenu pour 2 %at. (40 m²·g^{-1} et 4.6 mS·cm^{-1}).

Des nanoparticules d'iridium ont ensuite été déposées in situ par réduction chimique d'un sel d'iridium sur les aérogels de dioxyde d'étain sélectionnés. Leurs performances ont été évaluées sur électrode à disque tournant (RDE) et comparées à celles de NPs d'Ir non supportées, préparées selon le même protocole mais sans support. Les électrocatalyseurs développés ont atteint des valeurs d'activité massique similaires à celles rapportées dans la littérature pour différentes morphologies de dioxyde d'étain. Les NPs d'iridium supportées présentent des activités (x5) et des stabilités (x 16) beaucoup plus élevées que les NPs d'Ir non supportées. Elles présentent également des activités massique et spécifique similaires quel que soit le support de catalyseur employé (aérogels de TO, ATO ou TaTO), malgré leur conductivité électronique très différente. La désactivation des catalyseurs observée avec le temps dans les conditions de travail OER, est provoquée par un détachement ou une dissolution de l'Ir de l'électrode. Des contre-mesures sont actuellement à l'étude afin de limiter ce phénomène.

MOTS CLÉS

PEM-WE, oxydes métalliques, aérogels, matériaux nanostructurés, électrolyse, dopage

ABSTRACT

Sb-doped tin dioxide aerogels (ATO aerogels) showed promising results as corrosion resistive Pt catalyst supports for proton exchange membrane fuel cells (PEMFC). Mimicking this strategy to reduce the iridium loading in proton exchange membrane water electrolysis (PEM-WE) cells, Ir nanoparticles (NPs) were deposited on tin dioxide-based aerogels synthesized as catalysts supports. The mesoporous morphology and high specific surface area of aerogels is indeed particularly well adapted for an optimal dispersion of catalyst nanoparticles. The synthesis route of SnO_2-based aerogels was thus further studied in order to improve the sought-after properties. On top of antimony, tantalum was also evaluated as another doping agent to increase the tin dioxide (TO) electronic conductivity as well as the catalyst stability.

The sol-gel method parameters of the aerogel synthesis route were modified so as to optimize the sol-gel catalyst, the calcination time or the dopant concentration.

Using sodium hydroxide (NaOH) instead of nitric acid (HNO_3) as the sol-gel catalyst allowed to increase the specific surface area (up to 90 m2·g^{-1}) of Sb-doped tin dioxide aerogels (ATO). A beneficial impact was also observed on limiting the Sb segregation. A better Sb repartition in the material is expected to result in lower dissolution and a better stability during oxygen evolution (OER).

Tantalum-doped tin dioxide aerogels (TaTO) showed a much lower electronic conductivity than ATO. The value is depending on the Ta concentration as is the specific surface area. The best compromise between both properties was obtained for 2 at. % (40 m²·g^{-1} and 4.6 mS·cm^{-1}).

Iridium nanoparticles where then deposited in-situ by chemical reduction of an iridium salt on the selected tin-dioxide aerogels. Their performance were assessed on rotating disk electrode (RDE) and compared to those of non-supported Ir NPs, prepared following the same protocol but without any support. The developed electrocatalysts reached similar mass activity values than those reported in the literature for different tin dioxide morphologies. Supported iridium NPs presented much higher activities (x5) and stabilities (x16) than non-supported Ir NPs. They also featured similar mass and specific activity whatever the catalyst support (TO, ATO or TaTO aerogels), despite their very different electronic conductivity. The deactivation of the catalysts observed with time under OER working conditions, was caused by an Ir detachment, or dissolution, from the electrode. Countermeasures are now under investigation in order to limit this phenomenon.

KEYWORDS

PEM-WE, metal oxides, aerogels, nanostructured materials, electrolysis, doping